Catalyst-Assisted Low-Temperature Growth of ZnO Field Emitters on Free-Standing Nanomembranes

Dissertation
zur Erlangung des Doktorgrades
an der Fakultät für Mathematik, Informatik und Naturwissenschaften
Fachbereich Physik
der Universität Hamburg

vorgelegt von
Stefanie Haugg

Hamburg
2021

Gutachter der Dissertation:	Prof. Dr. Robert H. Blick Prof. Dr. Zlatan Aksamija
Zusammensetzung der Prüfungskommission:	Prof. Dr. Robert H. Blick Prof. Dr. Zlatan Aksamija Prof. Dr. Jochen Liske Prof. Dr. Alexander Lichtenstein Dr. Robert Zierold
Vorsitzender der Prüfungskommission:	Prof. Dr. Jochen Liske
Datum der Disputation:	22.09.2021
Vorsitzender des Fach-Promotionsausschusses PHYSIK:	Prof. Dr. Wolfgang Hansen
Leiter des Fachbereichs PHYSIK:	Prof. Dr. Günter H. W. Sigl
Dekan der Fakultät MIN:	Prof. Dr. Heinrich Graener

Abstract

Inherently large emission current densities and no need for external heating devices are major advantages of field emission based electron sources over conventional thermionic emitters. Moreover, two-dimensional arrays of electron field emitters are proposed as highly sensitive displacement sensors when positioned on a flexible base, because of the strong dependence of the field emission current on the emitter-anode distance.

This thesis presents the catalyst-assisted synthesis of high aspect ratio zinc oxide (ZnO) nanowires by metal organic chemical vapor deposition. Two individual approaches are tailored to provide a catalyst distribution that allows for the ZnO nanowire growth on free-standing nanomembranes. On the one hand, a sputter shadow mask is employed to affect the constitution of a thin gold film during deposition, and on the other hand, a porous silicon oxide (SiO_2) template is used to guide the thermally induced agglomeration of catalyst particles. The morphology of the randomly distributed ZnO structures is investigated for both synthesis approaches to identify possible growth mechanisms.

Prior to studying the field emission properties of the ZnO emitters, three high vacuum setups are optimized to enhance the reproducibility of the field emission measurements. For the first synthesis approach with the sputter shadow mask, the field emission behavior of the ZnO nanowires is examined regarding the variation of the ZnO growth conditions on silicon membranes and is analyzed in dependence on the lateral dimensions of silicon nitride membranes posing as substrates. For the second synthesis approach, the processing route of the porous SiO_2 template is initially optimized on bulk silicon and subsequently, the transfer to silicon nitride membranes is achieved by adjustment of the fabrication routine. Then, the field emission characteristics of the ZnO structures deposited on bulk silicon as well as of the ZnO emitters on the free-standing silicon nitride substrates, are examined.

In summary, a notable field emission current from the ZnO emitters grown within this thesis is already obtained at an applied electric field of 1.6 V/µm, which is about eighteen times lower than for ZnO structures deposited by a similar, but catalyst-free process using the same precursor. Combined with the sufficient stability of the emission current over several hours, which is demonstrated for both synthesis approaches, the ZnO nanowires on flexible bases offer the potential to be utilized in future sensor applications.

Zusammenfassung

Von Natur aus große Emissionsstromdichten und die Vermeidung eines externen Heizgerätes sind die bedeutendsten Vorteile von feldemissionsbasierten Elektronenquellen verglichen mit konventionellen, thermischen Emittern. Darüber hinaus werden zweidimensionale Anordnungen von Elektronenfeldemittern, die auf einer flexiblen Basis platziert sind, als hoch-sensitive Abstandssensoren vorgeschlagen wegen der starken Abhängigkeit des Feldemissionsstroms von der Emitter-Anoden Distanz.

In der vorliegenden Dissertation wird die katalysatorunterstütze Synthese von Zinkoxid (ZnO) Nanodrähten mit hohem Aspektverhältnis durch metallorganische chemische Gasphasenabscheidung präsentiert. Zwei individuelle Ansätze werden entwickelt, um eine Katalysatorverteilung zu erzeugen, die das Wachstum von ZnO Nanodrähten auf freistehenden Nanomembranen ermöglicht. Einerseits wird eine Sputter Schattenmaske verwendet, um die Beschaffenheit eines dünnen Goldfilms während der Abscheidung zu beeinflussen, und andererseits wird eine poröse Siliziumoxid (SiO_2) Schicht eingesetzt, um die thermisch induzierte Agglomeration von Katalysatorpartikeln zu lenken. Die Morphologie der zufällig angeordneten ZnO Strukturen wird für beide Synthese Ansätze untersucht, um mögliche Wachstumsmechanismen zu identifizieren.

Vor der Analyse der Feldemissionseigenschaften der ZnO Emitter sind drei Hochvakuum Aufbauten optimiert worden, um die Reproduzierbarkeit der Feldemissionsmessungen zu gewährleisten. Für den ersten Synthese Ansatz mit der Sputter Schattenmaske wird das Feldemissionsverhalten der ZnO Nanodrähte hinsichtlich der Variation der ZnO Wachstumsbedingungen auf Silizium Membranen erforscht und in Abhängigkeit von den lateralen Dimensionen der Siliziumnitrid Membranen, die als Substrate fungieren, analysiert. Für den zweiten Synthese Ansatz wird zunächst die Herstellung von porösem SiO_2 auf Bulk-Silizium optimiert und anschließend wird die Übertragung des Prozesses auf Siliziumnitrid Membranen durch die Anpassung des Fabrikationsablaufs erreicht. Danach werden die Feldemissionseigenschaften der ZnO Strukturen auf Bulk-Silizium sowie der ZnO Emitter auf den freistehenden Siliziumnitrid Substraten betrachtet.

Zusammenfassend konnte ein Feldemissionsstrom von den ZnO Emittern bereits ab einem angelegten elektrischen Feld von 1.6 V/µm detektiert werden, welches achtzehn Mal geringer ist als für die ZnO Strukturen die mit einem ähnlichen, aber katalysatorfreien Prozess unter Verwendung des gleichen Präkursors abgeschieden wurden. Kombiniert mit der hinreichenden Stabilität des Emissionsstroms über mehrere Stunden, die für beide Synthese Ansätze demonstriert wird, haben die ZnO Nanodrähte auf den flexiblen Substraten das Potenzial zukünftig in Sensoranwendungen eingesetzt zu werden.

Abbreviations

1D, 2D, 3D	one-, two-, three-dimensional
AC	alternating current
CNT	carbon nanotube
CVD	chemical vapor deposition
DAQ	data acquisition
DC	direct current
ECD	emission current density
EDX	energy-dispersive X-ray spectroscopy
FE	field emission
FEA	field emitter array
FEF	field enhancement factor
FIB	focused ion beam
FN	Fowler-Nordheim
HV	high voltage
ICP-RIE	inductively coupled plasma-reactive ion etching
LPCVD	low-pressure chemical vapor deposition
MCP	microchannel plate
MG	Murphy-Good
MHV	miniature high voltage
MOCVD	metal organic chemical vapor deposition
NASA	National Aeronautics and Space Administration
NM	nanomembrane
NW	nanowire
PECVD	plasma-enhanced chemical vapor deposition
PEEK	polyetheretherketone
PLC	power line cycles
PTFE	polytetrafluoroethylene
PVD	physical vapor deposition
RI	refractive index
SEM	scanning electron microscopy
SHV	safe high voltage
Si	silicon

SiN	silicon nitride
SiO_2	silicon oxide
SN	Schottky-Nordheim
SOI	silicon-on-insulator
TEM	transmission electron microscopy
TML	total mass loss
VLS	vapor-liquid-solid
VPB	vacuum potential barrier
VS	vapor-solid
VSS	vapor-solid-solid
XRD	X-ray diffraction
ZnO	zinc oxide

Contents

1 Introduction

The research on field emission (FE) cathodes is continually evolving, driven by the demand for electron sources with low energy consumption as well as by miniaturization efforts for vacuum micro- and nanoelectronics [1–3]. FE based cathodes naturally offer a larger emission current density (ECD) than purely thermionic electron sources because of the considerable reservoir of electrons near the Fermi level, which can theoretically be emitted by FE. Experimentally obtained ECDs close to the theoretical limit of about 10^{11} A/cm^2 proposed for ideal metal field emitters, have already been reported [1, 3]. In addition, no external energy needs to be supplied to the emitter material—by heating or irradiation—to sustain the electron emission because of the quantum mechanical nature of the FE process. Combined with the exponential dependence of the emission current on the applied electric field, field emitters are attractive electron sources for a number of applications [1–3]. On the one hand, FE cathodes are employed as electron beam sources for surface science techniques, such as field emission microscopy, scanning electron microscopy (SEM) and transmission electron microscopy (TEM). On the other hand, the group of FE based devices includes, for instance, flat display screens, X-ray tubes, ionizers in mass spectrometers as well as sensors [1, 3, 4]. However, the strong sensitivity of the FE cathode to the slightest variation of its electronic or structural surface properties and the relatively short life span compared to other electron sources often impede the integration in commercial equipment [2, 3].

The future replacement of well-established thermionic electron sources by FE cathodes may be improbable, since they offer superior emission current stability and longer lifetimes compared to field emitters [3]. However, it can be beneficial to exploit the unique features of FE sources that are not provided by other electron generation mechanisms. Especially, the strong dependence of the emission current on the electric field—which is inversely proportional to the distance between the cathode and the current collector, namely the anode—allows for the usage of FE electron sources in highly sensitive displacement sensors. Besides pressure and tactile sensors, accelerometers and integrated microphones are proposed applications for FE based displacement detection [5–7]. In general, the sensor function relies on the correlation of FE current with the emitter-anode distance that is controlled by an external applied force. For the operation of a FE based pressure sensor, a flexible, freely suspended anode is deformed by an externally applied pressure, which leads to a change of the electric

field by variation of the spacing towards the field emitter. Consequently, the magnitude of the external force is revealed by modification of the FE current in accordance with the membrane's deflection [1, 8, 9]. Over the last thirty years, field emitter arrays (FEAs) made from silicon (Si), diamond, and more recently also from carbon nanotubes (CNTs) were reported for pressure sensing approaches. Yet, the flexible membranes were predominantly comprised from thinned, freely suspended Si [10–12] and exceptionally also from free-standing diamond films [13]. Suggested by simulations and by experimental results, the sensitivity of a FE based pressure sensor is enhanced by tailoring the constitution of the elastic membrane as well as by optimization of the cathode's FE properties. Firstly, the reduction of the membrane's thickness and at the same time the enlargement of its lateral dimensions increase the maximum displacement of the suspended film, which leads to an enhancement of the sensor's sensitivity, namely a larger change of the emission current is expected for an equal variation of the external load [10, 14, 15]. Secondly, the response is assumed to be stronger for the same applied force when the sensing device is operated with emission currents as large as possible because of the exponential current-field relation [8, 15, 16]. Certainly, with increasing emission current, prior characterization and precise control of the cathode's FE properties are indispensable prerequisites because of the growing risk for electrical discharge in the device.

Among theses studies, there are two main configurations, on the one hand with an elastic membrane posing as anode [5, 9, 15] and on the other hand, with the FEA sitting upon a flexible base [13], as displayed in Figure 1.1. However, only the latter version allows for the triode configuration with a macroscopic grid as control electrode between cathode and anode, because of the inevitable dependence of the emission current on the distance variation between emitter and an opposing electrode. Additionally, the insertion of electron multiplying microchannel plates (MCPs) in the grid-anode gap is only feasible in the triode-type

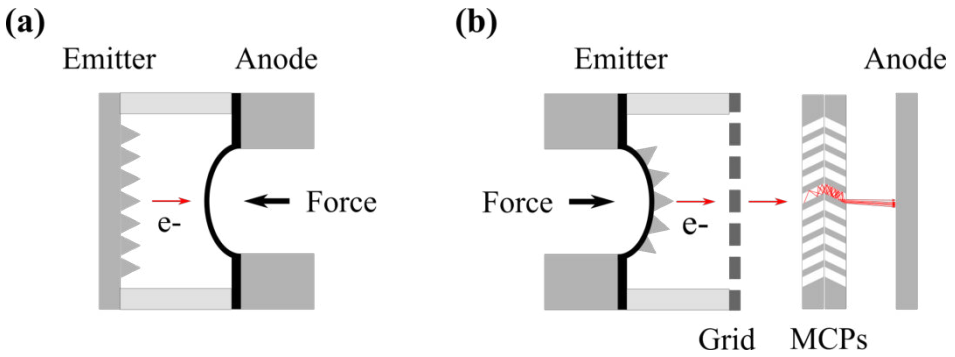

Figure 1.1: The two main configurations of the FE based displacement sensor are shown, namely **(a)** with an elastic membrane as anode and **(b)** with the membrane as base for the FEA. The latter version allows for the insertion of a macroscopic grid as control electrode and of MCPs for current amplification. The electrons, which are generated by FE from the emitter (cathode), are indicated by red arrows.

arrangement, as suggested for a novel FE based detector for mass spectrometry of heavy proteins. In this detection system, the external force is provided by ionized proteins impinging onto an electron emitting nanomembrane (NM) [17–19]. Note, the term nanomembrane herein refers to freely suspended films with less than a few hundred nanometers in thickness and with lateral dimensions at least two orders of magnitude larger. Compared to their bulk versions, NMs offer several unique features, such as a reduced flexural rigidity and the possibility of their thermomechanical excitation [20, 21]. Strong variation of the natural surface constitution of the NMs that were used as electron sources in previous work and their inherent need for high operation voltages reduced the reproducibility of the current-field dependence and enhanced the risk for emitter destruction by electrical discharge, respectively.

This thesis focuses on the synthesis and characterization of ZnO emitter arrays on free-standing NM substrates for the geometrically enhanced FE. Zinc oxide (ZnO) nanowires (NWs) are well known for their excellent FE properties as they can be fabricated with large aspect ratios, especially when the growth process can be combined with catalyst particles [22].

Prior to examination of the emitters' FE properties, three FE measurement setups are optimized to increase the reproducibility of the FE acquisition (chapter 3) and hence, to allow for the detection of changes regarding the FE characteristics caused by variation of the emitters' synthesis conditions. The FE data is analyzed with the conventional and well-established Fowler-Nordheim theory and for comparison, with the recently developed Murphy-Good plot (chapter 2).

Herein, the ZnO NWs are grown by a metal organic chemical vapor deposition (MOCVD) process directly on commercially bought Si membranes as well as on in-house fabricated silicon nitride (SiN) NMs. The catalyst-assisted chemical vapor deposition (CVD) of ZnO is possible at a comparatively low temperature of 580 °C because of the low melting point of the utilized precursor substance (137 °C), namely zinc acetylacetonate hydrate [23, 24]. Two approaches are presented that yield gold particle distributions that allow for the catalyst-assisted MOCVD growth of ZnO NWs on bulk and also on freely suspended NMs. The first method applies a shadow mask to affect the gold film constitution during sputter deposition (chapter 4) and the second approach uses a porous silicon oxide (SiO_2) template to influence the catalyst particle formation during the thermally driven agglomeration (chapter 5). The morphology of the FEAs is investigated with regard to the different substrate types and possible growth mechanisms are suggested for both synthesis approaches.

For the sputter shadow mask technique, the change of FE properties is investigated in dependence on the synthesis parameter variation for the growth of ZnO NWs on Si NMs. Moreover, the effect of the lateral dimensions of the in-house produced SiN NMs on the FE behavior of the ZnO emitters is studied. For the second approach, namely the porous SiO_2

template, a subtractive preparation route is initially developed on bulk Si and subsequently, the process is transferred to free-standing SiN membranes by modification of the fabrication procedure. The FE properties are analyzed for both synthesis approaches in dependence on the utilized substrate type and furthermore, the stability of the emission current over time is examined.

Suggested by the results in this thesis, tailoring of the FE characteristics by adjustment of the synthesis conditions for the ZnO NW array as well as further scaling of the NM dimensions is feasible. In summary, the ZnO emitters on flexible NM substrates may have the potential to be applied as FE electron sources in future displacement sensing devices because of the favorable combination of the observed FE properties.

2 Field Electron Emission Theory

Herein, the theory of field electron emission is presented that is relevant to the cathode types studied in this thesis, namely thin films and field emitter arrays (FEAs). In the first section, the fundamental Fowler-Nordheim (FN) theory of FE from metallic emitters is introduced as starting point and significant effects beyond the assumptions of FN theory are gradually included throughout this chapter. The second section is devoted to the impact of emitter geometry on FE from single isolated emitters as well as from multi-apex arrays. In the third section, semiconductors are contemplated as emitter material instead of metals and a separate part is used to explain distinct features of the FE from ZnO emitters as they constitute the examined cathodes. The fourth part is thought to merge the considerations of the three previous sections by presenting a scheme for the analysis of experimentally acquired FE data. The fifth and sixth part are dedicated to effects that arise from ad-layers on the emitter's surface and from the electrostatic field-induced deformation of the cathode's flexible base, respectively.

2.1 Field Emission from Metals

Field electron emission describes the mechanism of electron release from condensed matter into vacuum stimulated by an applied electric field. If the electric field at the emitter's surface is sufficiently high—typically in the order of 1 to 10 V/nm—the potential barrier at the metal-vacuum interface becomes narrow enough so that electrons have a significant probability for traversing through the vacuum potential barrier (VPB) by quantum mechanical tunneling [1]. Typically, the relationship between the emission current density (ECD) J and the local electric field F is used to describe the electron extraction by FE. In the following, a quantitative representation for FE from metal emitters is given by the FN model, which will be further evolved by inclusion of the image charge effect and the influence of emitter temperature.

2.1.1 Fowler-Nordheim Theory

In general, the ECD is expressed as product of the electron tunneling probability $D(E_\mathrm{x})$ through the VPB, which is also called transmission coefficient, and the supply function $N(E_\mathrm{x})$, multiplied by the magnitude of the electron charge e. With E_x being the kinetic energy com-

ponent normal to the metal-vacuum interface, the ECD is written as [25]:

$$J = e \int_0^\infty N(E_\mathrm{x}) D(E_\mathrm{x}) dE_\mathrm{x}, \tag{2.1}$$

A number of assumptions are indispensable to obtain an analytical solution for $J_\mathrm{FN}(F)$—namely the FN equation—which was first derived by Fowler and Nordheim in 1928 [26]. In FN theory, the emitter is modeled as follows:

(i) The electrons in the metal are assumed to behave effectively as free particles (Sommerfeld's free electron model) and to obey the Fermi-Dirac distribution.

(ii) The VPB has a triangular shape and its width is reduced by F, which is defined as the external electric field on the surface of the emitter at electron emission site.

(iii) The external electric field can be considered as uniform along the surface, because the VPB thickness is usually much smaller than conventional emitter radii for $F > 1$ V/nm. Therefore, the electron tunneling can be treated as a one-dimensional (1D) mechanism.

(iv) The emitter surface is considered to be microscopically smooth and effects that might arise from impurities or the emitter's geometrical shape are disregarded.

(v) Electron states inside the metal experience a constant (zero) potential, which is not affected by the external electric field. For instance, the work function ϕ—the minimum energy required to transfer an electron from bulk to field-free vacuum (typically in the order of 2–5 eV for metals)—is not a function of F.

(vi) Temperature effects are neglected (T = 0 K).

Note, that $J = J_\mathrm{l}$ always refers to the local ECD as a function of the (local) external electric field $F = F_\mathrm{l}$ at electron emission site, unless otherwise stated [1, 4, 26]. According to assumption (ii) and (iii), the VPB has a triangular shape and the electron current moves along x-direction traversing through the yz-plane, which constitutes the metal-vacuum interface. The triangular VPB function is described as energy at vacuum level E_0 reduced by the potential energy caused by the external electric field on the emitter's surface:

$$V_\mathrm{triangular}(x) = E_0 - eFx. \tag{2.2}$$

The vacuum energy level $E_0 = E_\mathrm{F} + \phi$ is defined as sum of Fermi energy E_F and the material's work function value ϕ. Electrons are typically emitted by FE from energy states near Fermi energy under the zero-temperature assumption. Figure 2.1 (a) presents the VPB in FN approximation for different external electric fields. To obtain a solution for equation 2.1,

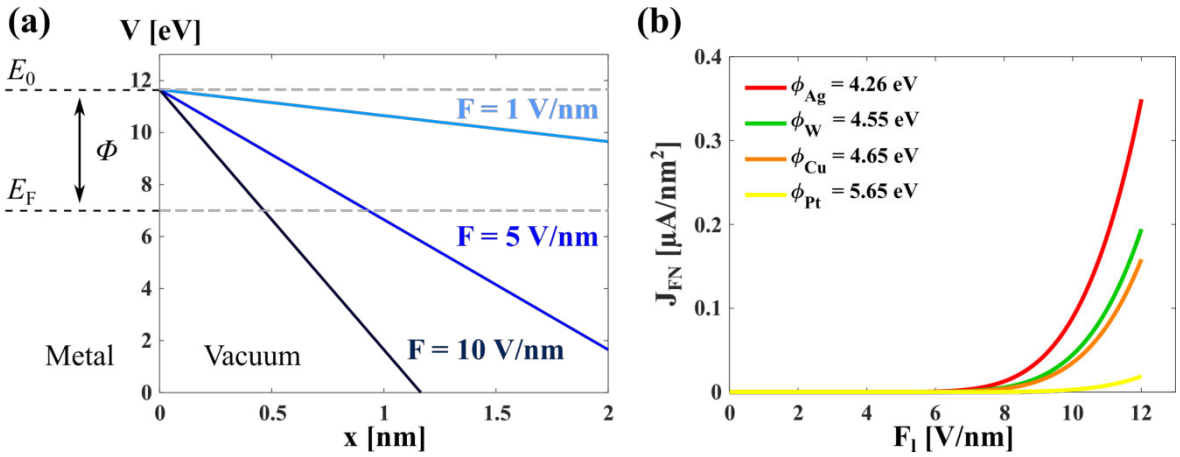

Figure 2.1: (a) Illustration of the triangular VPB at metal-vacuum interface plotted for the potential energy V in dependence on the distance x from the metal surface ($x = 0$). The barrier shape according to $V_{\text{triangular}}(x)$ was calculated for copper with $\phi_{\text{Cu}} = 4.65\,\text{eV}$ [27] and with $E_{\text{F,Cu}} = 7\,\text{eV}$ [28] for external electric fields of $F = 1$, 5 and 10 V/nm (light blue, blue and dark blue lines). The tunneling probability for electrons from metal to vacuum increases with rising electric field, since the VPB width decreases gradually with rise of F. Figure freely adapted from [29]. **(b)** Variation of the ECD with electric field for different values of ϕ according to the FN equation 2.9. Reduction of the work function value facilitates electron emission at lower electric fields. The work functions for polycrystalline films of silver $\phi_{\text{Ag}} = 4.26\,\text{eV}$ (red), tungsten $\phi_{\text{W}} = 4.55\,\text{eV}$ (green), copper $\phi_{\text{Cu}} = 4.65\,\text{eV}$ (orange) and platinum $\phi_{\text{Pt}} = 5.65\,\text{eV}$ (yellow) were taken from [27].

the transmission coefficient and supply function are separately derived. First, $D(E_{\text{x}})$ is defined as the ratio of transmitted to incident probability current densities, which are obtained by solving the Schrödinger equation for the incident as well as for the transmitted electron wave functions. According to assumption (iii), only the x-component normal to the metal-vacuum interface needs to be considered in the Schrödinger equation. In FN approximation, the transmission coefficient for the triangular barrier is given by:

$$D(E_{\text{x}}) = D_{\text{F}} \exp\left(\frac{E_{\text{x}} - E_{\text{F}}}{d_{\text{F}}}\right), \tag{2.3}$$

with the following work function- and field-dependent variables:

$$D_{\text{F}} = \exp\left(-\frac{b_{\text{FN}}\phi^{3/2}}{F}\right) \quad \text{and} \tag{2.4}$$

$$\frac{1}{d_{\text{f}}} = g_{\text{e}}\frac{\phi^{1/2}}{eF}. \tag{2.5}$$

The constants are defined by $b_{\text{FN}} = \frac{2}{3e}g_{\text{e}}$ and by $g_{\text{e}} = 2\left(\frac{2m_{\text{e}}}{\hbar^2}\right)^{1/2}$ with the electron mass m_{e} and the reduced Planck constant $\hbar$. Second, the probability of an electron state with energy E

being occupied in thermal equilibrium is described by the Fermi-Dirac distribution function for calculation of the supply function:

$$f(E) = \frac{1}{1 + \exp\left(\frac{E - E_\mathrm{F}}{k_\mathrm{B} T}\right)}, \tag{2.6}$$

with k_B and T being the Boltzmann constant and the absolute temperature, respectively. According to the Sommerfeld model, the energy component for electrons with wave vector k_x normal to the VPB, is written as:

$$E_\mathrm{x} = \frac{\hbar^2 k_\mathrm{x}^2}{2 m_\mathrm{e}}. \tag{2.7}$$

The supply function—giving a measure of the number of electrons crossing an unit area (yz-plane) per unit time with the normal energy in x direction between E_x and $E_\mathrm{x} + dE_\mathrm{x}$—results in the following expression:

$$N(E_\mathrm{x}) = \frac{m_\mathrm{e} k_\mathrm{B} T}{2\pi^2 \hbar^3} \ln\left(1 + \exp\left(-\frac{E_\mathrm{x} - E_\mathrm{F}}{k_\mathrm{B} T}\right)\right). \tag{2.8}$$

The well-known FN formula is found by substitution of 2.3 and 2.8 into equation 2.1:

$$J_\mathrm{FN} = a_\mathrm{FN} \frac{F^2}{\phi} \exp\left(-\frac{b_\mathrm{FN} \phi^{3/2}}{F}\right), \tag{2.9}$$

with the FN constants a_FN and b_FN being defined as:

$$a_\mathrm{FN} = \frac{e m_\mathrm{e}}{2\pi^2 \hbar^3} \left(\frac{e}{g_\mathrm{e}}\right)^2 = \frac{e^3}{16\pi^2 \hbar} \approx 1.541434 \left[\mu\mathrm{A} \cdot \mathrm{eV}/\mathrm{V}^2\right], \tag{2.10}$$

$$b_\mathrm{FN} = \frac{2}{3e} g_\mathrm{e} = \frac{4}{3} \frac{(2 m_\mathrm{e})^{1/2}}{e\hbar} \approx 6.830890 \left[\mathrm{V}/(\mathrm{nm} \cdot \mathrm{eV}^{3/2})\right]. \tag{2.11}$$

Detailed derivations of the FN equation can be found elsewhere [4, 25]. For theoretical considerations, it was chosen to express the current density in $\mu\mathrm{A}/\mathrm{nm}^2$ and the electric field in V/nm, following the suggestions by Liang [4] and Forbes [30]. On the one hand, the tunneling barrier width is also on the nanometer scale for electric fields that are necessary to enable FE, as illustrated in Figure 2.1 (a). On the other hand, this notation allows for the convenient assessment of the ECD as a function of F and ϕ without handling of large exponents, as shown in Figure 2.1 (b). Clearly, a significant exponential increase of the ECD is already observed for electric fields below 10 V/nm and smaller work function values facilitate the electron emission at lower electric fields. However, experimental results are rather discussed in $\mu\mathrm{A}/\mathrm{cm}^2$ for the ECD and in V/µm for the electric field because of the actual properties and dimensions of the FE cathode and of the measurement geometry. The

Tables A.1 and A.2 in the appendix list physical constants in the magnitude for calculation of a_{FN} as well as of b_{FN} and other FE customized values.

2.1.2 Beyond the Fundamental Model

The triangular potential barrier is a highly simplified approximation that enables derivation of an analytical FE equation. However, it disregards the impact of potential barrier rounding by the image charge effect, which can lead to a considerable underestimation of the ECD by the FN equation [30]. Additionally, FE experiments are usually conducted at room temperature, which puts the zero-temperature approximation into question.

Image Charge Potential

According to classical electrostatics, an electron placed at finite distance from a conductive plane is attracted to the surface by induction of an effective image potential. Assuming the metal-vacuum interface as perfect conductor, the image charge potential is given by:

$$V_{\mathrm{image}} = -\frac{e^2}{16\pi\varepsilon_0 x} \approx -0.36\,\frac{1}{x}\,[\mathrm{nm}\cdot\mathrm{eV}]\,, \tag{2.12}$$

with vacuum permittivity ε_0 [29]. Figure 2.2 (a) exemplifies the shape modification of the triangular VPB through addition of the image charge effect, which is described by the Schottky-Nordheim (SN) barrier function [4]:

$$V_{\mathrm{SN}}(x) = E_0 - eFx - \frac{e^2}{16\pi\varepsilon_0 x}. \tag{2.13}$$

A comprehensive derivation of the FE equation for the image charge affected VPB was given by Murphy and Good in 1956 [31] and yielded the so called Murphy-Good (MG) FE equation:

$$J_{\mathrm{MG}} = a_{\mathrm{FN}}\frac{F^2}{\phi\,\tau(y)^2}\exp\left(-\nu(y)\frac{b_{\mathrm{FN}}\phi^{3/2}}{F}\right). \tag{2.14}$$

The *J*-*F* relation has the characteristic form of the FN equation supplemented by the two field- and work function-dependent correction factors $\tau(y)$ and $\nu(y)$ [4, 25]. Already for this slight modification of the triangular VPB, the exact values for the correction factors can only be obtained numerically, as it was done by Burgess *et al.* [32]. More recently, analytical approximations for the correction factors were developed by Forbes *et al.*, which were found

to be in good agreement with numerical values and are expressed as follows [33, 34]:

$$\tau_F(y) \approx 1 + \frac{y^2}{9} - \frac{y^2}{18}\ln\left(y^2\right), \tag{2.15}$$

$$\nu_F(y) \approx 1 - y^2 + \frac{y^2}{6}\ln\left(y^2\right). \tag{2.16}$$

The Nordheim parameter y is defined as the ratio of the field-induced lowering of the VPB, namely $\Delta\phi_{SN} = c \cdot F^{1/2}$, to the unreduced barrier height, which equals the material's work function in zero-temperature assumption [33, 34]:

$$y^2 = c^2 \frac{F}{\phi^2} \text{ , with } c^2 = \frac{e^3}{4\pi\varepsilon_0} \approx 1.44 \left[\text{nm} \cdot \text{eV}^2/\text{V}\right]. \tag{2.17}$$

The term $\Delta\phi_{SN}$ describes the reduction of the barrier height at the maximum of the SN barrier as indicated in Figure 2.2 (a). The parameter $\tau_F(y)$ varies in a narrow range from 1 to 1.1111 for $0 < y < 1$, which corresponds to electron energies below the maximum of the VPB, namely only electron emission through tunneling. Hence, $\tau_F(y)$ is in practice often set to unity. However, $\nu_F(y)$ changes more significantly with the Nordheim parameter y and therefore, with variation of the work function and of the electric field, which can lead to a considerable deviation of the ECD from the prediction by the FN equation [29, 33, 34]. In Figure 2.2 (b),

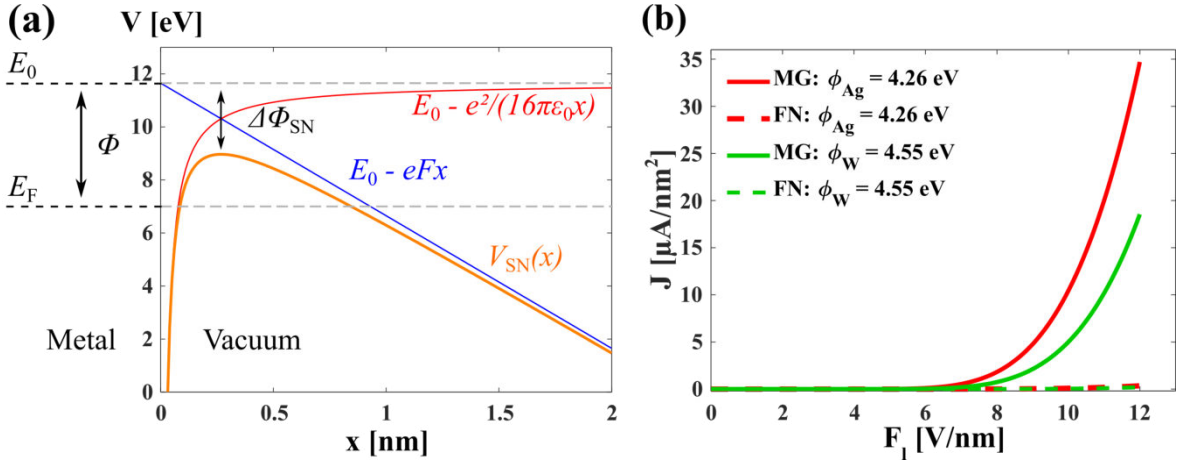

Figure 2.2: (a) Illustration of the SN barrier showing the potential energy V as a function of the distance x from the metal surface. The SN barrier (orange) is presented for copper with ϕ_{Cu} = 4.65 eV [27], $E_{F,Cu}$ = 7 eV [28] and for a medium electric field of 5 V/µm. The triangular barrier height (blue) is reduced by a value of $\Delta\phi_{SN}(Cu) \approx 2.68$ eV by the image charge potential (red). Figure freely adapted from [29]. **(b)** J-F curves for silver ϕ_{Ag} = 4.26 eV (red) and tungsten ϕ_W = 4.55 eV (green), plotted for MG (solid lines) as well as for FN equation (dashed lines). The work function values were taken from [27]. The ECDs calculated with the MG equation are larger by a factor of 117 for silver and of 112 for tungsten at a constant electric field of 10 V/nm compared to the values predicted by the FN formula.

the current densities for MG and FN equation are presented as a function of the electric field for two different work function values. As expected, the predicted ECD from MG formula is larger by a factor of more than 100, which is caused by the increased electron tunneling probability for the image charge reduced barrier [4, 25].

Thermionic Emission and Thermal-Field Emission

The MG FE equation describes the emission of electrons by tunneling through the VPB from energy levels near the Fermi energy and is valid in the limit of high electric fields and zero temperature. If additional energy is supplied to the electrons in a metal by heating, the charge carriers can be excited to higher energy states. For sufficiently high temperatures, enough energy is provided for electrons to overcome the VPB and escape into vacuum, which is well known as thermionic emission and the current density-temperature relation is given by the following formula:

$$J_{\text{thermionic}}(F,T) = A_{\text{R}} T^2 \exp\left(-\frac{\phi - \Delta\phi_{\text{SN}}}{k_{\text{B}} T}\right). \tag{2.18}$$

The pre-exponential factor is defined by $A_{\text{R}} = \frac{e m_{\text{e}} k_{\text{B}}^2}{2\pi^2 \hbar^3}$ and for zero electric field, the term $\Delta\phi_{\text{SN}}$ vanishes and the equation represents pure thermionic emission [4, 25]. Note, the expected contribution from thermionic emission to the total ECD is insignificant compared to the predicted ECD from FE for emitter temperatures below 1500 K, which is sometimes declared as threshold for thermionic emission [4]. For instance, the ECD for thermionic emission (equation 2.18, ϕ = 4.55 eV, F = 10 V/µm) at an emitter temperature of 1500 K is smaller by a factor of 640 compared to the ECD from FE derived with the MG model (equation 2.14) in zero-temperature approximation for the same electric field.

In FE experiments, field and thermionic electron emission are usually intermixed and a distinct separation is not possible [4]. Murphy *et al.* gave boundary conditions to distinguish between the regions that are either dominated by thermionic emission or by FE as well as for an intermediate range [31]. In the intermediate region, namely in the so called thermal-field emission regime, electrons are thermally excited to states above Fermi energy where the VPB is thinner, which corresponds to electrons having a higher tunneling probability. In contrast to thermionic emission, which considers only electron emission above the VPB, the thermal-field emission model contemplates the influence of temperature on FE. At low electric field and work function values, the impact of temperature on FE is typically larger, but decreases considerably with increasing electric field. For instance, for a constant emitter temperature of 1000 K and a work function of 4.5 eV, the ECD that considers the temperature effect is about 5 times larger for an electric field of 2 V/µm compared to the zero-temperature case. Yet, for F = 3 V/µm, the temperature affected ECD is only 1.7 times larger than at T = 0 K [1].

Note, the FE process itself causes usually an inevitably temperature raise at electron emission site. The self-heating of the emitter is dominated by the interplay of Joule and Nottingham effects, which are shortly introduced in the following [1].

(i) Joule Heating

The Joule effect describes the resistive heating by a flow of electrical current through the material, here caused by FE. According to Joule's law for an ohmic conductor, the generated heat per unit volume Q is proportional to the current density J and the specific electric resistivity ρ_{res} of the material: $Q = J^2 \rho_{\mathrm{res}}$. The temperature increase of the emitter by FE is typically dominated by Joule heating because of its quadratic dependence on the ECD [35, 36].

(ii) Nottingham Effect

The Nottingham effect is a pure quantum mechanical energy exchange process. At low temperatures, electrons emitted from a metal originate mainly from energy levels equal to or below the Fermi energy. Electron emission is considered to be in thermal equilibrium, namely electrons emitted from the surface are immediately replaced by negative charge carriers from the metal having energies approximately equal to the Fermi energy. If the average energy of emitted electrons is compared to the average energy of replacing charge carriers, less energy is carried away by FE than supplied from electrons within the metal, which results in local heating of the cathode. However, with increasing temperature, energy states above the Fermi level are gradually populated and the average emitted energy can shift to values larger than Fermi energy. This effect causes local emitter cooling because more energy is released from the emitter by FE than supplied by replacement electrons [4, 35, 37].

The Nottingham heating is the dominant process at low electric fields that initialize FE, but Joule heating takes over as main source for temperature raise with increasing F because of the corresponding rise of the ECD. The inset of Nottingham cooling can delay physical destruction of the emitter structure, which would otherwise occur at lower ECDs by temperature-induced melting or vaporization of the material caused by Joule heating [35]. The prediction of the emitter temperature is rather complicated because the strongly localized Nottingham and Joule mechanisms depend, among other things, on the material's band structure, its thermal conductivity, the emitter's geometrical shape and radiation losses [1].

Moreover, vacuum space charge can be generated by accumulation of emitted electrons close to the emitter, which shield the cathode's surface from the external electric field. In addition to emitter self-heating, vacuum space charge is another pronounced source for deviations of experimental FE data from the previously described theory that arise for large

ECDs and correspondingly strong local electric fields [1]. Typically, the impact of space charge becomes significant at ECDs that are larger than 10^6 A/cm^2, which corresponds to a local electric field greater than 5 V/nm for a work function value of 4.5 eV [25].

2.2 Effect of Emitter Geometry

The *J-F* relation is highly dependent on the shape of the VPB at emission site, which determines the electron tunneling probability and which is strongly influenced by the external electric field. Hence, a differentiation between the applied (macroscopic) electric field F_M and the actual, local electric field F_l on the cathode's surface is necessary because of the effect of the emitter's geometrical shape. Here, most of the initial assumptions of FN model are still considered, but the influence of emitter shape will be included from this section on.

2.2.1 Single-Apex Emitter

Typically, a FE experiment is composed of the emitting cathode and an adjacent electrode for applying an electric field, resembling a capacitor structure. To reach intense electric fields, which are necessary to enable FE before electrical discharge occurs between the two electrode plates, field emitters are often built as sharp tips to enhance the local electric field. The total electric potential corresponds to the sum of potential distributions from the individual charges on the cathode's surface by law of superposition. Since the arrangement of charges varies with surface curvature of the metallic structure, the local electric field changes with position on the emitter. The distortion of the applied electric field by the presence of an emitter causes an amplification of the local electric field, namely the geometric field enhancement effect [29]. Herein, the applied electric field is defined as the ratio of applied (measured) voltage V_m between emitter and adjacent electrode to the inter-electrode spacing d, as shown in Figure 2.3 (a):

$$F_\mathrm{M} = \frac{V_\mathrm{m}}{d}. \tag{2.19}$$

The relation of the electric fields with and without distortion by an emitter, namely the field enhancement factor (FEF), is given by [4]:

$$\gamma = \frac{F_\mathrm{l}}{F_\mathrm{M}}. \tag{2.20}$$

Field Enhancement Models

Several models are available for prediction of the field enhancement effect from emitter shape. A summary of the herein presented, highly simplified models is given in Figure 2.3 (b). Typically, the FEF at emitter apex γ_apex is considered because the local electric field amplification

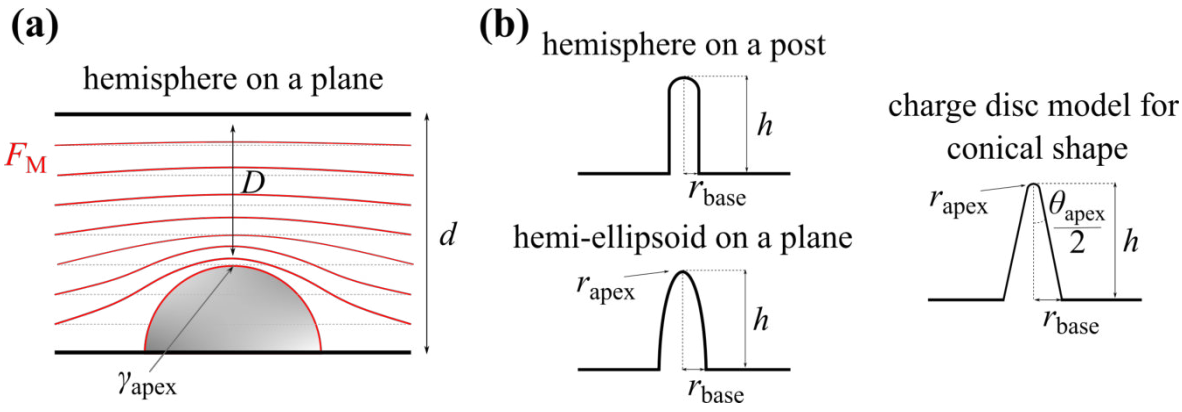

Figure 2.3: (a) Schematic presentation of the geometrical field enhancement effect for a hemispherical conductor in a homogeneous electric field F_M between two electrodes with distance d ("hemisphere on a plane"). The electric field is amplified most at the apex of the protrusion because of the accumulation of charges in dependence on the surface curvature, which is illustrated by stronger bending of the equipotential field lines. Figure freely adapted from [29]. **(b)** Overview of different models for calculation of the apex FEF γ_{apex}. The following models are shown here: "hemisphere on a post" ($\gamma_{apex}(1)$, $\gamma_{apex}(2)$), "hemi-ellipsoid on a plane" ($\gamma_{apex}(3)$) [38], and a cone shaped emitter for $\gamma_{apex}(5)$ [39, 40] and for γ_{c-disc} [41], with apex radius r_{apex}, base radius r_{base}, inclination angle θ_{apex} and emitter height h.

is the strongest at emitter tip, which is caused by dense accumulation of charges as a function of surface curvature. In general, γ_{apex} is proportional to the reciprocal of the radius of apex curvature [29]. The simplest model is a "hemisphere on a plane" with the exact result of $\gamma_{apex} = 3$, which represents a conductive sphere sitting on an equipotential plane. Another often used model for cylindrical emitters is the "hemisphere on a post" model that considers the emitter's base radius r_{base}—being equal to its apex curvature radius r_{apex}—and the distance h of the conductive plane to the emitter's tip. For small ratios of emitter height to base radius, namely $1 < n \equiv \frac{h}{r_{base}} < 10$, the following approximation can be used to predict the apex FEF [38]:

$$\gamma_{apex}(1) = 2 + n. \tag{2.21}$$

However, for larger protrusions, equation 2.21 overestimates the apex FEF. For ratios in the range of $4 \leq n \leq 3000$, the following formula is suggested in literature [38]:

$$\gamma_{apex}(2) = 1.2 \cdot (2.15 + n)^{0.90}. \tag{2.22}$$

For emitter structures having an apex radius smaller than its base radius and for $n > 1$, the

"hemi-ellipsoid on a plane" model describes the FEF as follows [38]:

$$\gamma_{\text{apex}}(3) = \frac{f^3}{((n \cdot \ln(n+f)) - f)}, \text{ with} \tag{2.23}$$

$$f = (n^2 - 1)^{1/2}. \tag{2.24}$$

An universal formula for the FEF of a single emitter is given in the following form [42]:

$$\gamma_{\text{apex}}(4) = \frac{2\frac{h}{r_{\text{apex}}}}{\ln\left(4\frac{h}{r_{\text{apex}}}\right) - \alpha_{\text{base}}}. \tag{2.25}$$

Thereby, α_{base} depends on the emitter base and was found to be 0 for hyperboloid, 0.88 for conical, 2 for ellipsoid and about 2.6 for cylindrical emitter shapes [42]. Moreover, the following equation for a cone shaped emitter considers the inclination angle θ_{apex} [39, 40]:

$$\gamma_{\text{apex}}(5) = \frac{1.7D}{\left(r_{\text{apex}}\, r_{\text{base}} \tan\left(\frac{\theta_{\text{apex}}}{2}\right)\right)^{1/2}}. \tag{2.26}$$

Here, $D = d - h$ refers to the distance between the tip of the emitter and the opposing electrode as shown in Figure 2.3 (a). Recently, another model was developed for quasi-1D field emitters with the intention to examine FEAs composed of ZnO structures. The so called "charge disc" model assumes the emitter shape as a cone with a base radius that is much smaller than the height of the tapered emitter. The FEF is expressed as follows [41]:

$$\gamma_{\text{c-disc}} = \frac{h}{R_{\text{c-disc}}}. \tag{2.27}$$

The radius $R_{\text{c-disc}}$ of the "charge disc" that is used to account for the charge distribution of the cone-shaped emitter, is defined as [41]:

$$R_{\text{c-disc}} = r_{\text{apex}} \left(1 + \frac{r_{\text{base}} - r_{\text{apex}}}{h} \cdot \frac{\sqrt{h^2 + (r_{\text{base}} - r_{\text{apex}})^2}}{h} + \frac{(r_{\text{base}} - r_{\text{apex}})^2}{h^2}\right). \tag{2.28}$$

According to Zhang *et al.*, the model can also be employed for other materials with metallic properties [41].

When a small structure is located on top of a considerably larger emitter, the total FEF is assumed to be the product of the structures' individual FEFs, which is known as Schottky's conjecture [29]. However, the FEF is significantly overestimated by this assumption, if the height of the top protrusion is larger than the width of the bottom structure [43, 44].

In general, the apex FEF depends on the detailed shape and thus, charge distribution at the

emitter's surface and the above listed equations can only be considered as approximations for simplified emitter shapes, namely any surface roughness on top of the emitter can cause modifications of the apex FEF. Additionally, the detailed emitter shape may change over time through FE-initiated effects, such as thermally activated surface diffusion [1, 38, 45]. Furthermore, the emitter is supposed to be placed on a perfectly flat surface and the counter electrode is assumed to be at sufficient distance from the cathode, namely the emitter height is much smaller than the inter-electrode spacing $\left(\frac{h}{d} \ll 1\right)$ [38, 45]. Nevertheless, the above presented emitter models are commonly employed for rough estimation of the FEF from emitter shape, as for example equation 2.22 was already used for ZnO NWs [46] as well as for CNTs [47].

Nanoemitters

For emitter radii larger than 100 nm, the electric field on the surface of the emitter is assumed to be uniform and the 1D model of the VPB is sufficient. However, for smaller tip dimensions and especially for apex widths comparable to the VPB thickness, namely for apex radii of less than 10 nm, the electric field on the emitter's surface becomes inhomogeneous. Then, the three-dimensional (3D) Schrödinger equation has to be solved for an asymmetric VPB to acquire the electric potential at the surface of the emitter. Numerical calculations by Fursey *et al.* revealed that the emission current density even decreases for emitter radii smaller than the width of the VPB, which is contrary to the geometrical field enhancement effect [1]. Note, atomic scale surface roughness and variation of the work function over the emitter apex do not account for such significant variations from the 1D approximation of the VPB and are consequently not causing considerable deviations from the FN model [1, 48].

For quasi-1D nanoemitters (wire-like structures), the electron supply for FE can be affected by spatial confinement through the emitter dimensions. The spatial constriction causes discretization of the electron energy levels, which can lead to separation of the continues electron supply into sub-bands. Hence, the free electron model and emission in thermal equilibrium (instantaneous replacement of emitted electrons) are no longer valid assumptions. For transverse confinement in ideal metallic NWs, namely the emission direction is aligned normal to the geometrical confinement, the total ECD was found to decrease for transverse emitter dimensions of less than 5 nm. Thus, there is a trade-off between a high FEF caused by a large aspect ratio and the spatial confinement of the emitter's electron supply. The ECD can be maximized for an optimum relation between transverse emitter width and the overall emitter geometry as a function of the applied electric field [49].

2.2.2 Multi-Apex Arrays

Single tip emitters provide only a small emission current at relatively high applied voltages limited by their intrinsic electron supply. Additionally, the FE current is often unstable over time because of unavoidable, FE-initiated morphology variations during the electron emission process. The microstructure of the cathode is affected by thermally activated surface migration of atoms and by bombardment with residual gas ions accelerated by the high electric field, for instance. These changes of emitter shape alter the local electric field and result in considerable modification of FE current because of the exponential dependence of the current density on F_l. Since the emission current is limited and the single-apex field emitter is vulnerable to failure, multi-apex arrays came in focus for fabrication of efficient FE electron sources [2]. FEAs consist of a large number of single emitters randomly distributed or regularly ordered over a macroscopic area A_M that is much larger than the emitting area of the individual field emitters. The macroscopic ECD J_M behaves as average current density taken over the whole cathode area as function of the applied (macroscopic) field F_M [50]. FE-initiated shape modifications of single emitters in an array cause typically no significant change of FE behavior because of the statistical distribution of the ECD over the entire cathode area [1].

Emission Area

The determination of the actual emission area is complex even for a single emitter with defined surface facets, as it is a function of the applied electric field and may change over time because of FE-initiated emitter modifications [1, 51]. For FEAs, the approximation of the emission area is even more complicated, as the ratio of field emitters actually contributing to the total ECD is uncertain because there are no identical emitters in a realistic array. The surface area that is emitting electrons is usually much smaller than the overall macroscopic area of the cathode A_M, as the emission occurs predominantly from the apex regions. To account for the discrepancy between the actual emission area A and the macroscopic area, the "area efficiency of emission" α_M was introduced, which is estimated to be much less than unity [50]:

$$A = \alpha_\mathrm{M} \cdot A_\mathrm{M}. \tag{2.29}$$

The subscript of A is omitted here, because there are several approaches in literature for definition of the emission area. Among them, the macroscopic area gives the ratio of emission current I_e to the total macroscopic ECD: $A_\mathrm{M} = \frac{I_\mathrm{e}}{J_\mathrm{M}}$. Whereas, the so called notional emission area is used to relate the emission current to the ECD that is characteristic for the entire cathode: $A_\mathrm{n} = \frac{I_\mathrm{e}}{J_\mathrm{c}}$. The denomination "characteristic" refers to the area of origin of the largest ECD for a given voltage (*e.g.* sharpest emitter) that mainly determines the emission current

from the cathode. Reviews of diverse theoretical constructs for description of the emission area can be found elsewhere [52, 53].

Screening

If two emitters in an electric field are positioned close to each other, the equipotential lines between the adjacent conductive structures are deformed by mutual electrostatic depolarization, also known as electrical field screening (see Figure 2.4). The screening effect causes a decrease in local electric field on the surface of neighboring emitters, which is reflected in suppression of the FEF. The ratio of the FEF for an emitter in a two-dimensional (2D) array γ_{FEA} to the FEF for the same isolated single emitter γ_0 is often given as follows [29, 54]:

$$\frac{\gamma_{FEA}}{\gamma_0} = 1 - \exp\left(a\left(\frac{b}{h}\right)^c\right), \tag{2.30}$$

with emitter height h and inter-emitter spacing b. The values for a and c were derived by several authors through fitting equation 2.30 to data from simulated FEAs and strongly depend on the emitter and array dimensions. Some numbers for the two parameters a and c are shown in Table 2.1 for ordered as well as for randomly distributed field emitters.

In general, the total ECD from a FEA can be raised by increasing the emitter density. However, at some point the FEF becomes suppressed by electrical field screening, which leads to

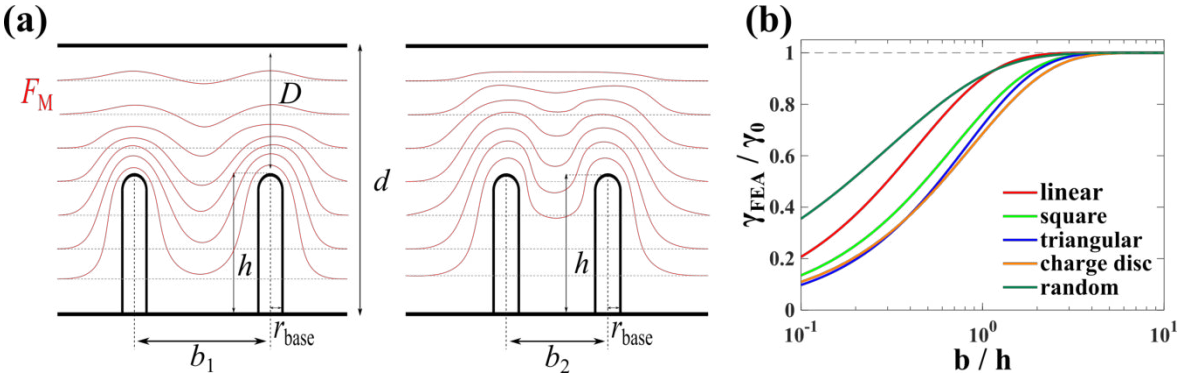

Figure 2.4: (a) Schematic illustration of the electrical field screening effect for two adjacent emitters. If the distance b between two conductive emitters with height h is reduced ($b_1 > b_2$), the equipotential lines between them are raised and their curvature around the apex is reduced. Figure freely adapted from [29]. **(b)** The ratio of the FEF for an emitter in an array to the FEF for the isolated emitter is shown in dependence on the emitter distance-to-height ratio according to equation 2.30. Note, the x-axis is in logarithmic scale to accentuate the trend with variation of b/h. The values from Table 2.1 for different emitter arrangements were used (emitter line, square and triangular unit cell, shielding in charge disc model and randomly distributed emitters) and the emitter length was set to $h = 50$ µm. Regardless of the model, electrical field screening becomes negligible for emitter distances that are larger than four times the emitter height.

Emitter distribution	a	c
Line of emitters [29]	-2.3172	1.00
Square unit cell [29]	-1.4500	1.00
Triangular unit cell [29]	-1.2650	1.09
"Charge discs" in ordered array [41]	-1.1586	1.00
Randomly distributed emitters [54]	-2.4100	0.74

Table 2.1: Parameters a and c for equation 2.30 that is used to evaluate the influence of electrical field screening on the FEF. The following emitter distributions are considered: A linear arrangement of emitters, ordered arrays of emitters with square and triangular unit cell [29, 55], ordered conical emitters modeled as "charge discs" [41] and conical shaped, randomly distributed field emitters as a function of the average spacing between nearest neighbors [54].

the reduction of the ECD with further increase of emitter density. Thus, the ECD can be maximized by optimizing the inter-emitter spacing b. For instance, Nilsson *et al.* and Smith *et al.* suggested an inter-emitter spacing of two times the emitter height for CNTs, since the current density was reduced for smaller emitter separations [56, 57]. Further, Harris *et al.* reported the shielding to be negligible for emitter tip-to-tip distances of 2.4 and of 2.6 times the emitter height for a triangular unit cell and for a square arrangement, respectively [58]. As a consequence, the ideal emitter density and thus, the optimum spacing, are a function of the applied electric field. For lower F, closer separations are favored, but for higher electric fields, the ECD benefits from larger emitter spacing. Note, finite arrays have an additional field enhancement effect at the edges of the FEA because of the reduced number of next neighbors [29, 55].

The screening factor s_{FEA} is another measure for the degree of electrical field screening that varies from 0 for high density FEAs to 1 for isolated emitters. The following formula is given for derivation of the FEF for a tapered emitter in an array [39, 40]:

$$\gamma_{\mathrm{FEA}} = s_{\mathrm{FEA}} \cdot \gamma_{\mathrm{apex}}(5). \tag{2.31}$$

The expression $\gamma_{\mathrm{apex}}(5)$ for an isolated single emitter is given by equation 2.26.

Typically, the dimensions of single structures in an array exhibit statistical variation because there are no identical emitters in reality. Especially additional nanostructures on the apex of the emitter can have a huge influence on FE and therefore, the current usually does not scale with the number of emitters or with the macroscopic emission area. Simulations showed that the total ECD from a realistic cathode, which considers emitter size variations within the array, is usually dominated by a very small number of the sharpest emitters in weak electric fields. However, with increasing electric field, emitters with larger tip radius start gradually contributing to the macroscopic ECD. Therefore, assuming only one constant FEF

for the whole FEA can be deficient [29].

2.3 Nonmetal Emitter Materials

Herein, the general intrinsic differences of semiconductors from metal emitters are listed that have a potential effect on the FE characteristics. Further, zinc oxide is considered as field emitter and the impact of intense electric fields on its material properties is discussed.

2.3.1 Semiconductors

In contrast to metals, the valence band (highest occupied band) and conduction band (lowest unoccupied band) of a semiconductor are separated by the energy gap E_g. Electrons can be excited thermally into the conduction band already at room temperature, which generates a finite electrical conductivity [28]. The total ECD from a semiconductor is the sum of contributions from conduction band, valence band and surface states [25], namely electronic states near the surface that result either from recombination mechanisms caused by the finite nature of the crystal or from layers of adsorbates [59]. Especially surface recombination is much more common for semiconductors than for metals because of strong directional bonding between the atoms [25]. A list of semiconductor features that affect FE and can lead to deviations from FN theory, is given in the following:

- **Energy band structure**: The emission current depends on a relatively small number of electrons thermally excited into the conduction band because of the separation of valence from conduction band by the energy gap [4].

- **Doping**: For intrinsic semiconductors, electrical charges are only generated by thermal excitation of electrons. Through addition of small portions of impurities, doping can modify the charge density of a semiconductor considerably [28]. Intense electric fields showed to have different impacts on n-type (donor impurities) compared to p-type (acceptor impurities) semiconductors, which correlate with the respective location of the Fermi energy level and the corresponding energy band alignment at the bulk-vacuum interface (see Figure 2.5) [1].

- **Electric field penetration and band bending**: Typically, the large number of charge carriers in a metal shields its interior from the external electric field. However, the electric field can percolate through the surface of a semiconductor because of the smaller density of charge carriers near the surface. As a result, the energy bands at material-vacuum interface are deformed [1, 60]. The energy band diagrams of n- and p-type semiconductors under the influence of intense electric fields are shown in Figure 2.5.

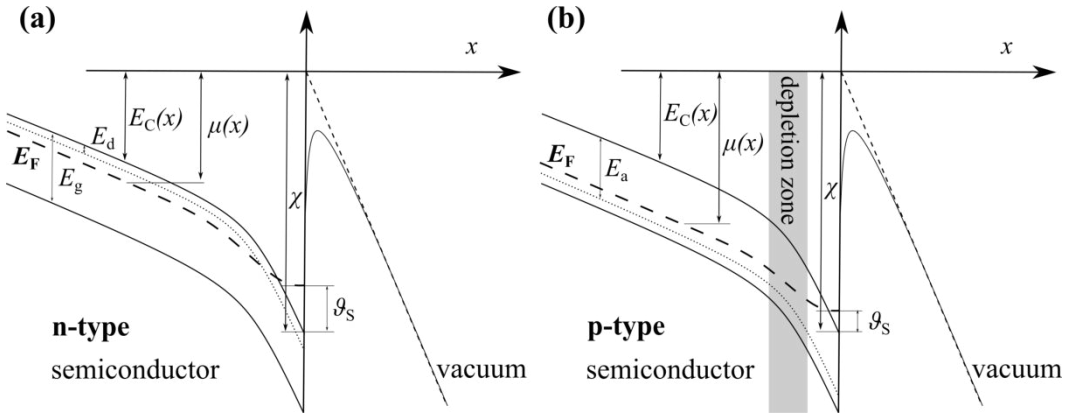

Figure 2.5: Energy band diagrams of **(a)** n- and **(b)** p-type semiconductors at material-vacuum interface in strong electric field, with Fermi energy E_F (dashed lines), position-dependent energy at bottom of the conduction band $E_C(x)$, electron affinity χ (energy difference between vacuum level and bottom of conduction band) and the electrochemical potential $\mu(x)$ (energy difference between vacuum level and Fermi level). E_a and E_d are the energies at acceptor and donor level referred to the bottom of the condition band, respectively. Further, ϑ_S describes the distance of conduction band bottom relative to Fermi level at the semiconductor's surface and is called degeneration parameter. In strong electric fields, the energy bands are deformed near the surface, which leads to formation of a zone depleted of carriers for p-type emitters, but such a region is usually not formed in n-type emitters. Figure freely adapted from [1, 61].

- **Equilibrium electron emission**: FE is assumed to be in thermal equilibrium, namely emitted electrons are immediately replaced by charge carriers from the bulk. For sufficiently low current densities, equilibrium electron emission is a valid approximation also for emission from semiconductors. Yet, it is rather unlikely for surface states to be in thermal equilibrium with energy bands in the bulk [25].
- **Emitter surface cleaning**: Cleaning of the material's surface prior to FE is a critical issue for semiconductors because ad-layers can strongly distort the measurement results by shielding the material's surface from the electric field. However, processes to clean the surface—for instance by heating—can lead to irreversible changes of the emitter material. The most effective cleaning method is proposed to be desorption of surface adsorbates by intense electric fields under high vacuum conditions [1].

The theoretical description of FE from semiconductors is much more complicated than for FE from metals because of the effects listed above. For low ECDs and thus, in low electric fields, the FE curve from semiconductors usually follows the FN prediction. With increasing electric field, the carrier concentration near the emitter's surface is modified by electric field penetration leading to deviations from FN theory. Often, a saturation of current density from semiconductors can be observed for intense electric fields as electron emission is mainly limited by the supply of charge carriers to the near-surface region. For n-type semiconductors,

the carrier concentration gradually decreases away from the surface, whereas for p-type materials, a depletion region forms directly in the near-surface area (see Figure 2.5) [1]. In general, there is no simple formulation for FE from semiconductors like the FN equation 2.9. However, several approaches were developed to predict the ECD from nonmetals. For instance, Stratton gave a general model that considers electron emission by FE separately from conduction and valence band of semiconductors [62] and more recently, Bhattacharya *et al.* provided a summary of theoretical models for FE from specific semiconductor nanostructures, which additionally take into account quantum confinement effects [63].

2.3.2 ZnO Emitters

Zinc oxide is a II-VI compound semiconductor, which has a wide band gap in the ultraviolet spectral range and piezoelectric properties. The band gap width of the transparent conductive oxide is approximately 3.37 eV at room temperature. Typically, ZnO forms a wurtzite type structure with tetrahedral coordination, namely each zinc ion has four oxygen neighbor ions in a tetrahedral arrangement and conversely. In a crystal matrix, the tetrahedrons are stacked in bi-layers consisting of zinc and oxygen layers, which are arranged in a hexagonal wurtzite lattice structure with a distinct axis (c-axis) [64]. A summary of ZnO material properties is given in Table 2.2. ZnO structures can be synthesized by a variety of techniques—such as vapor phase transport (CVD, thermal evaporation, pulsed laser deposition), wet chemical growth, electrochemical deposition and template assisted methods—and a multitude of shapes can be generated (tube-, wire-, tetrapod-, sheet-like structures) [22]. Typically, as-grown ZnO has n-type conductivity because of intrinsic defects or by incorporation of hydrogen, which acts as donor in ZnO and is present in almost all growth environments. The band gap of ZnO can be tailored by doping during the growth process, however, stable p-type conductivity is difficult to achieve. The compensation of dopants is related to the positions of conduction and valence band relative to the vacuum level and generally increases with widening of the band gap. Acceptors tend to be compensated since the valence band in ZnO has a very low energy relative to the vacuum level [64]. Additionally, the conductivity of the surface is highly sen-

	ZnO
ϕ_{ZnO} [46]	5.30 eV
χ_{ZnO} [41]	3.60 eV
$E_{\mathrm{g,ZnO}}$ [64]	3.37 eV
$T_{\mathrm{m,ZnO}}$ [64]	2242 K

Table 2.2: Work function ϕ_{ZnO}, electron affinity χ_{ZnO}, energy band gap $E_{\mathrm{g,ZnO}}$ at room temperature and melting temperature $T_{\mathrm{m,ZnO}}$ of zinc oxide.

sitive to the presence of adsorbates as well as to the annealing in different atmospheres. The formation of surface states may cause generation of a surface electron accumulation layer, which influences the material's electrical properties [65].

ZnO structures are attractive FE electron sources as they can be grown with a large aspect ratio and thus, can have a considerable FEF. In addition, the oxide surface is resistant to degradation by reactions with residual gases, the fabrication costs are comparatively low and the material exhibits good thermal stability [22, 66]. If an electric field is applied to the ZnO structure, it penetrates into the semiconductor and supplies additional electrons to the surface area. Typically, the band bending causes the bottom of the conduction band to get below the Fermi level by a magnitude of about 0.1 eV, which enhances the surface electronic density. The band bending is assumed to be sufficient for ZnO to have metallic properties in the presence of electric fields that allow for FE [41]. Often, a work function value of 5.3 eV is used for FE related calculations. However, this value might not be appropriate anymore in high electric fields, as the effective work function decreases from its bulk value equal to the amount of band bending [41, 60]. McCarthy *et al.* reviewed the work function values utilized in literature for c-axis oriented ZnO field emitters [46]. The work function varies considerably with the crystal face and additionally, work function and band bending are a function of time during FE because of surface reconstruction, defect creation or gas adsorption processes. The authors claim that the value of 5.3 eV is more appropriate for polycrystalline ZnO and potentially for disordered ZnO NW assemblies. However, for electron emission from the conduction band, a work function value between 3.3 eV and 4.5 eV is suggested and for electron emission from the valence band, a value of 7.9 eV is recommended [46].

Additionally, it is well known that surface impurities and adsorbates may shield the material's interior from the electric field. For high ad-layer coverage density, the emission might even originate from the surface states rather than from the conduction or from the valence band of the ZnO [22, 60].

Typically, the FE from ZnO emitters follows a linear behavior in the region of low electric fields. However, the region of high electric fields is characterized by deviations from the linear trend, which can have several reasons. Often, the formation of vacuum space charge near the cathode's surface is proposed to limit the increase of emission current in high electric fields [46]. Furthermore, experimentally observed non-linearity is attributed to the saturation of electron emission from the conduction band because of the limited generation rate for charge carriers inside the semiconductor [60, 67]. Moreover, the intermixing of emission from conduction and valence band can be an explanation for distinct features of the FE current in high electric fields [68].

The electrical resistance of the ZnO structure is another important factor for FE because it is related to the conductivity and thus, to the electron supply and to the magnitude of Joule heat-

ing by FE current flow. When the emitter material has a high electrical resistance, the FE properties are usually poor and the risk for electrical breakdown through local self-heating and subsequent material vaporization, is enhanced. Therefore, in addition to an uniform emitter size distribution, a homogeneous conductivity is crucial for reliable FE electron sources [69].

2.4 Analysis of Field Emission Data

This section deals with the matching of experimental FE data with theoretical predictions, which is far from being trivial for a number of reasons. In FE studies, the current I_m is measured as a function of the applied (measured) voltage V_m between emitter and an opposing electrode, rather than the ECD as a function of the local electric field because the *J*-*F* relation is usually not accessible experimentally. For FE data analysis, the emission current I_e and corresponding voltage V_e are assumed to be equal to the measured current and voltage, namely any additional contribution to the *I*-*V* curve not originating from the field emitter—such as leakage current or resistance in the measurement path—are disregarded [52]. Theoretically, the emission current is obtained by integration of the ECD over the emitting area. Commonly, the emission current is approximated by multiplication of the overall ECD with the effective emission area A_eff, since the actual surface ratio that contributes to the FE current is typically unknown [4]:

$$I_\mathrm{e} = \int J\,dA \approx J_\mathrm{e} \cdot A_\mathrm{eff}. \tag{2.32}$$

In reality, however, the emission area—as well as the FEF—are a function of the applied voltage and of time, as FE-initiated effects are known to alter the emitter's morphology [29]. Herein, the well-established FN plot is presented, which is commonly used for analysis of experimental FE data from metal-like emitters. Additionally, the recently developed MG plot is considered and the so called "orthodoxy test" will be explained, which can be used to examine the applicability of the previously discussed theory to experimentally acquired FE data.

2.4.1 Fowler-Nordheim Plot

The FN equation 2.9 is linearized according to the form $y = C_\mathrm{FN} + S_\mathrm{FN} \cdot x$. By insertion of equation 2.19 for the conversion from electric field to voltage, of equation 2.20 for the effective FEF γ_eff and of equation 2.32 for the effective emission area A_eff, the linearized FN equation is expressed as follows [4]:

$$\ln\left(\frac{I_\mathrm{m}}{V_\mathrm{m}^2}\right) = \ln\left(\frac{a_\mathrm{FN} A_\mathrm{eff} \gamma_\mathrm{eff}^2}{d^2 \phi}\right) - \frac{b_\mathrm{FN} \phi^{3/2} d}{\gamma_\mathrm{eff}} \cdot \frac{1}{V_\mathrm{m}}. \tag{2.33}$$

To derive physical properties from experimental FE data, the measured current-voltage dependence is plotted in the form of $\ln\left(\frac{I_m}{V_m^2}\right)$ versus $\frac{1}{V_m}$, which is known as FN plot. Slope S_{FN} and intercept C_{FN} of the linearized experimental data are obtained by fitting of a straight line to the FE data in the FN plot. Then, the effective values of the FEF, the emission area and the work function can be derived with the following equations, if one physical property among them is assumed [4]:

$$\gamma_{eff}^{FN} = -\frac{b_{FN}\phi^{3/2}d}{S_{FN}} \text{ and} \tag{2.34}$$

$$A_{eff}^{FN} = \frac{d^2\phi \cdot \exp\left(C_{FN}\right)}{a_{FN}\gamma_{eff}^2}. \tag{2.35}$$

Note, the derived effective values are supposed to be constant during the FE experiment. Therefore, values obtained with this method are apparent and might rather be considered as rough estimates for the emitter's general FE performance. Nevertheless, the simplified FN model has often been used in the last decades for the analysis of *I*-*V* curves from single ZnO emitters [70] as well as from large arrays of ZnO field emitters with nanorod- [40, 71], nanowire- [72–75] and needle-like shapes [76] or with differently shaped ZnO structures [68, 77, 78]. For ZnO emitters, typically a constant work function value of 5.3 eV is assumed for calculation of the effective FEF, which is often used to assess the efficiency of the studied FE electron source [68, 70–72, 76–78].

2.4.2 Recent Developments in Field Emission Data Analysis

"Technically Complete" FN Type Equation

The elementary FN equation 2.9 disregards some fundamental physical effects of FE from metallic emitters. Therefore, the so called "technically complete" FN-type FE equation was introduced to describe the local ECD [79]:

$$J = \lambda a_{FN}\frac{F^2}{\phi}\exp\left(-\frac{\mu b_{FN}\phi^{3/2}}{F}\right). \tag{2.36}$$

The parameter μ accounts for deviations from the triangular barrier shape model and the pre-exponential parameter λ merges several correction factors for effects regarding electron supply, temperature, atomic wave function, the material's band structure, and a correction for the tunneling probability. For realistic situations, it is not possible to give exact values for the correction factors. However, estimates based on their underlying physical effects were provided by Forbes *et al.* [50, 79]. The latest approximated range for the multiplicative correction factor in the pre-exponent is $0.005 < \lambda < 14$ [30]. Equation 2.36 is given in a

generalized form, but for a specific barrier shape like the SN barrier, μ is given by ν_F (equation 2.16). The parameter in the exponent has usually the largest impact on the derived ECD. For instance, the predicted J is enhanced by a factor of about 100 when the SN barrier is considered instead of the simple triangular VPB [52, 79]. If electron tunneling through the SN barrier is assumed, the so called slope correction function $s_F(y)$ needs to be added for calculation of the effective FEF because of the electric field dependence of $\nu_F(y)$ [52]:

$$\gamma_{\text{eff}}^{\text{SN}} = -\frac{b_{\text{FN}}\phi^{3/2}s_F(y)d}{S_{\text{FN}}}. \tag{2.37}$$

Similar to equation 2.16 for $\nu_F(y)$, an approximation for $s_F(y)$ is available [33]:

$$s_F(y) \approx 1 - \frac{1}{6}y^2. \tag{2.38}$$

The slope correction function $s_F(y)$ varies within the FE-relevant range ($0 < y < 1$) between 1 and 0.833, but is in practice often set to 0.95 [52] or for simplicity to unity [80–82].

Orthodoxy Test

The so called orthodoxy test was introduced some years ago to evaluate the reliability of physical values derived from experimental FE data. Orthodoxy of the emission data, namely $I_m = I_e$ and $V_m = V_e$, is given when the current is solely provided by tunneling of electrons through the SN barrier. Thus, the image charge effect as well as the slope correction function are considered. Further, the work function is supposed to be constant over the emitting area and the applied voltage is assumed to be uniform across the emitting surface. However, the relation between measured and emission data can be distorted by a number of effects, such as leakage currents and electrical resistance in the measurement path, formation of vacuum space charge, FE-induced temperature variations of the emitter material, electric field-dependent changes of the emission area, energy band bending and quantum confinement in nanoscale emitters [83].

For application of the orthodoxy test, the MG equation 2.14 is transferred into a scaled form with the help of the scaled barrier field $f = y^2$ that considers the Nordheim parameter y, which was already introduced by equation 2.17. The ratio of the local electric field to the reference field F_R that is needed to reduce the height of the SN barrier completely to zero—which corresponds to the material's work function ϕ—is here expressed as follows [83]:

$$f \equiv \frac{F}{F_R} = c^2\frac{F}{\phi^2}. \tag{2.39}$$

Then, the scaled equation for the ECD can be written as [83]:

$$J = \theta(\phi) f^2 \cdot \exp\left(-\nu_{\mathrm{F}}(f) \cdot \frac{\eta(\phi)}{f}\right), \tag{2.40}$$

with the work function-dependent values:

$$\eta(\phi) = \frac{b_{\mathrm{FN}}\phi^{3/2}}{F_{\mathrm{R}}} = \frac{b_{\mathrm{FN}}c^2}{\phi^{1/2}} \approx \frac{9.8362}{\phi^{1/2}} \left[\mathrm{eV}^{1/2}\right] \text{ and} \tag{2.41}$$

$$\theta(\phi) = \frac{a_{\mathrm{FN}}F_{\mathrm{R}}^2}{\phi} = \frac{a_{\mathrm{FN}}\phi^3}{c^4} \approx 0.7434\ \phi^3 \left[\mu\mathrm{A}/\left(\mathrm{nm}^2 \cdot \mathrm{eV}^3\right)\right]. \tag{2.42}$$

The relevant value for the orthodoxy test, namely the (dimensionless) extracted scaled barrier field, is given by [83]:

$$f^{\mathrm{extr}} = -\frac{s_{\mathrm{F}}(f)\eta(\phi)}{S_{\mathrm{FN}} \cdot \frac{1}{V_{\mathrm{m}}}}, \tag{2.43}$$

with the slope correction function for the SN barrier $s_{\mathrm{F}}(f) \approx 1 - \frac{1}{6}f \approx 0.95$ and the slope S_{FN} derived from the linearized data in the FN plot. To perform the orthodoxy test, the scaled barrier field is extracted from the experimental FE data in the FN plot for the first and for the last data point that are used for the linear fit. Thus, the corresponding values from the x-axis of the FN plot, namely the reciprocal values of the measured voltages, are considered [83–85]. The derived range ($f_{\mathrm{min}}^{\mathrm{extr}}$–$f_{\mathrm{max}}^{\mathrm{extr}}$) is then compared to the work function-dependent thresholds given by Forbes [83].

Extracted values outside the expected limits indicate that the measured FE data was influenced by effects beyond the theory of electron tunneling through the SN barrier. As a consequence, physical values derived from the FN plot may be unreliable. Note, for values of f^{extr} below the expected range, the theoretical ECD would actually be too low to be measured in practice. Furthermore, for values above the maximum threshold, the predicted ECD is in reality high enough to cause significant emitter self-heating, which eventually leads to emitter failure. Since its introduction in 2013, the orthodoxy test was used by several authors for a variety of field emitter types, such as sharp ZnO NWs [86], CNTs [87] and titanium oxide nanorods [88].

Murphy-Good Plot

Experimental FE data in the FN plot can exhibit a slight curvature in the region of high electric fields, namely for small values of $\frac{1}{V_{\mathrm{m}}}$, because of the dependence of $\nu_{\mathrm{F}}(y)$ on the electric field. Therefore, the derivation of intercept and slope from the linearized FE data in the FN plot can be distorted. Recently, the so called MG plot was developed with the intention to enhance the reliability for extraction of physical values from experimental FE data. The formula for the

MG plot has the form of $\ln\left(\frac{I_m}{V_m^\kappa}\right)$ versus $\frac{1}{V_m}$ with $\kappa \equiv (2-\frac{\eta(\phi)}{6})$ and is written as follows [85]:

$$\ln\left(\frac{I_m}{V_m^\kappa}\right) \approx \ln\left(A_{eff}\cdot\theta(\phi)\cdot\exp(\eta(\phi))\cdot\frac{1}{V_R^\kappa}\right) - \eta(\phi)V_R\frac{1}{V_m}. \tag{2.44}$$

Slope and intercept are given by:

$$S_{MG} = -\eta(\phi)V_R = -b_{FN}\phi^{3/2}\zeta_C \text{ and} \tag{2.45}$$

$$\exp(C_{MG}) = A_{eff}\cdot\theta(\phi)\cdot\exp(\eta(\phi))\cdot\frac{1}{V_R^\kappa}. \tag{2.46}$$

With the relation $\exp(C_{MG})\cdot|S_{MG}|^\kappa = A_{eff}\cdot\theta(\phi)\cdot\eta(\phi)^2\cdot\exp(\eta(\phi))\cdot\eta(\phi)^{-\eta/6}$ and if the work function is assumed, the voltage conversion length ζ_C^{MG} (ratio of reference measured voltage V_R to reference electric field F_R) and the effective emission area A_{eff}^{MG} can be calculated by the following equations [85]:

$$\zeta_C^{MG} = -\frac{S_{MG}}{b_{FN}\phi^{3/2}} \text{ [nm]}, \tag{2.47}$$

$$A_{eff}^{MG} = \Lambda_{MG}\cdot\exp(C_{MG})\cdot|S_{MG}|^\kappa \text{ [nm}^2\text{]}. \tag{2.48}$$

The factor Λ_{MG} is the emission area extraction parameter and is defined as:

$$\Lambda_{MG}(\phi) \equiv \frac{1}{(a_{FN}b_{FN}^2\phi^2)\cdot\exp(\eta(\phi))\cdot\eta(\phi)^{-\eta(\phi)/6}} \left[\text{nm}^2/\mu\text{A}\right]. \tag{2.49}$$

The effective FEF can finally be obtained from the following relation [30, 85]:

$$\gamma_{eff}^{MG} = \frac{d}{\zeta_C^{MG}}. \tag{2.50}$$

Equation 2.43 can also be used for application of the orthodoxy test to experimental FE data in the MG plot. However, the slope correction function $s_F(f)$ is set to unity for determination of the scaled barrier field, since the MG plot exclusively considers emission through the SN barrier [89].

2.5 Surface Ad-Layers

FE strongly depends on the properties of the near-surface region of the emitter material. Therefore, any kind of surface modification, such as the unintentional adsorption of molecules or the deliberate deposition of thin films, has potential influence on the FE properties. To estimate the impact of thin surface ad-layers, a modification of the apparent work function is assumed rather than a change of the overall emitter shape. The simplified *I-V* relation for an

emitter with adsorbates (ad) is given by [25]:

$$I = C_{\mathrm{ad}} V^2 \exp\left(\frac{S_{\mathrm{ad}}}{V}\right), \tag{2.51}$$

with the slope S_{ad} and the intercept C_{ad} of the linearized *I-V* curve in the FN plot. If FE data is available from the "clean" structure (cl), namely without surface ad-layers, the ratio of slopes extracted from FN plot can be used to derive information regarding the electronic nature of the surface modification. Under the assumptions that neither the emission area nor the FEF change considerably—which is valid for tip radii much larger than the ad-layer thickness—and with a known work function value for the clean emitter surface ϕ_{cl}, the apparent work function for the adsorbate-covered emitter ϕ_{ad} can be derived by [25]:

$$\phi_{\mathrm{ad}} = \phi_{\mathrm{cl}} \left(\frac{S_{\mathrm{ad}}}{S_{\mathrm{cl}}}\right)^{2/3}. \tag{2.52}$$

The surface coverage is generally difficult to evaluate since the temperature and the sticking coefficient of the material and of the adsorbates are typically unknown. Moreover, the determination of the work function modification from FE data is complex because the coverage with foreign species usually changes during the FE measurement, which is driven by the strong electric fields and by local emitter self-heating. Therefore, fluctuations in emission current are often attributed to surface diffusion of adsorbed species [25].

Besides the variation of the apparent work function of the emitter material, resonant tunneling through virtual energy levels provided by the adsorbed atoms is proposed to be another reason for the change of FE properties caused by ad-layers. Typically, such surface states are modeled by attractive potential wells near the emitter's surface, which alter the effective width of the VPB and therefore, affect the electron tunneling probability [4, 90]. The FE properties of the coated emitter can be enhanced compared to its pristine version by tuning of the ad-layer thickness [91].

2.6 Flexible Substrates

Usually, field emitters are placed on flat bulk substrates and the spacing d between cathode and adjacent electrode remains constant. For emitters located on a flexible base, additional effects might occur as the electric field on the emitter's surface strongly depends on the inter-electrode spacing.

First, the time scale of the distance variation towards the opposing electrode can be of interest. Only if the substrate's displacement variation is slower than the electron tunneling time, the VPB can be assumed to be static and the FE is supposed to be an adiabatic process.

The tunneling time, which is defined as the mean time of interaction between the tunneling electron and the VPB, is estimated to be in the femtosecond range [1].

Second, a flexible substrate, namely a free-standing membrane, can be deformed deliberately by an external force, such as by a differential pressure or by an electrostatic field. Typically, the relation between the differential pressure applied to one side of the membrane and the maximum displacement ξ_{max} in the center of the membrane, is given by [17, 92]:

$$P(\xi_{max}) = C_1 \frac{t_M \sigma_M}{a_M^2} \xi_{max} + C_2(\nu_M) \frac{t_M E_M}{a_M^4} \xi_{max}^3. \tag{2.53}$$

Here, a_M is one half of the side length of the square membrane, t_M is the membrane's thickness, E_M is the Young's modulus, ν_M is the Poisson's ratio and σ_M is the residual stress of the membrane. $C_1 = 3.45$ and $C_2(\nu_M) = 1.994$ (1 - $0.271\nu_M$) are parameters that were derived for the analytical description of the deflection of a square membrane by an external load and showed to be in good agreement with experimental results for silicon nitride membranes [92]. In FE experiments, the membrane-electrode distance becomes a function of the applied voltage and thus, electric field and electrode spacing affect each other mutually. The following relation between electrostatic pressure P_{el} and applied voltage V_m was formulated for a simple parallel-plate measurement configuration [14, 93]:

$$P_{el} = \frac{\varepsilon_0}{2d^2} V_m^2, \tag{2.54}$$

with vacuum permittivity ε_0. The distance d between emitter and opposing electrode is a function of the applied voltage and can be expressed as follows [17]:

$$d(V_m) = d_0 - \xi_{avg}(V_m) = d_0 - 0.48375 \cdot \xi_{max}(V_m). \tag{2.55}$$

Here, d_0 gives the initial emitter-electrode distance at zero electric field and ξ_{avg} is the average displacement across the entire surface of the membrane [17]. The maximum deflection of the membrane ξ_{max} can be derived as a function of the applied voltage V_m when $P(\xi_{max})$ in equation 2.53 is replaced by 2.54 [17, 93]. The obtained displacement-voltage relation can finally be used in a modified form of the FN equation to determine the effect of a flexible emitter base on the FE current [17]:

$$I_m(d(V_m)) = a_{FN} A_M \frac{\gamma^2 V_m^2}{(d(V_m))^2 \phi} \exp\left(-\frac{b_{FN} d(V_m) \phi^{3/2}}{\gamma V_m} \right). \tag{2.56}$$

Third, if a FEA is placed on a flexible substrate, the apparent emitter distribution might be modified by the deformation of its base. On the one hand, by convex bending of the cathode towards the electrode, the electrical field screening among neighboring emitters can

be reduced because their tip-to-tip distance is increased. Thereby, the onset of FE can be shifted to lower applied voltages. This effect was reported by several authors, mostly using flexible polymeric substrates [87, 94, 95]. On the other hand, the emission area that is actually contributing to FE, namely the number of emitting structures, can be affected by membrane deflection, which is attributed to the modification of the electric field distribution on the cathode's surface caused by the substrate's displacement [87, 94, 95].

3 Field Emission Measurement Setup

The reproducibility of FE measurements is an indispensable prerequisite for comparison of different FE cathodes. On the one hand, repeatable measurements of *I-V* curves from identical emitters have to be ensured to allow for the detection of deliberate surface modifications, such as thin film deposition or to study FE characteristics as a function of the cathode's synthesis conditions. On the other hand, any parasitic influence from the measurement setup itself has to be eliminated or at least identified for further data analysis. Otherwise, the measured current and applied voltage are not equal to the actual emitted current and corresponding voltage [52]. Herein, the basic principle of FE measurements is introduced and possible reasons for electrical breakdown are discussed, which is the dominant source for field emitter destruction [1]. Three FE setups are presented as used for sample characterization in this thesis. Based on one FE setup that was built within a Master's thesis[1], the different setup components were strongly modified with the following central intentions: First, reduced risk for electrical discharge during FE experiments and second, increased reproducibility of the *I-V* curves. Partly, the setup optimization was conducted during a Bachelor's thesis[2]. After the aforementioned setup adjustments were implemented, the same tailor-made emitter sample was employed as calibration probe for the three FE setups.

3.1 Field Emission Measurement

The basic FE setup consists of the emitter structure (cathode) placed on a supporting substrate and the opposing anode, which are jointly encapsulated in vacuum [4]. A negative voltage is supplied to the emitter and the absolute value is gradually increased, while the current is measured at the grounded anode. For reaching electric fields in the FE typical range of 1–10 V/nm, the cathode-anode distance needs to be as small as possible but still wide enough to guarantee electrical insulation of the two electrodes. For a spacing of 100 µm, inconceivable voltages of 100 kV up to 1000 kV would be needed to permit FE from a flat metal surface. To facilitate

[1] Christian Henkel, *Characterization of diamond nanomembranes by field emission for a detector in mass spectrometry of large proteins*, research group of Prof. Blick, supervised by Chris Thomason (2016) [96]

[2] Leutrim Pacarizi, *Optimization of a setup for field emission measurements of nanomembranes*, research group of Prof. Blick, supervised by Stefanie Haugg (2018) [97]

electron emission, field emitters are usually designed with sharp apexes to cause amplification of the local electric field by the geometrical field enhancement effect (section 2.2.1) and thereby, to enable FE before electrical discharge occurs in the small inter-electrode gap of the capacitor-like assembly [29]. For instance, an apex FEF of 500 would allow for FE in the experimentally feasible voltage range of 200 V to 2000 V for 100 µm electrode separation.

Often, a diode-type cathode-anode configuration is used for FE measurements because of its simple implementation. Nevertheless, the direct coupling of the FE current to the anode potential limits the controllability of the emission current, which is impractical for many applications. Consequently, a control electrode is introduced between cathode and anode in devices with integrated FE electron sources, such as miniature X-ray tubes, FE displays or for construction of high-brightness electron sources [98–101]. The control electrode in the triode-type configuration extracts electrons independently of the anode voltage and allows for *in situ* control of the FE current. Further, the spacing between cathode and control electrode can typically be reduced compared to the cathode-anode distance in the diode-type arrangement, which enables FE at lower applied voltages [102, 103]. Since the first realization of gated FEAs in 1968 by Spindt *et al.* [104, 105], numerous variations of the triode-type assembly were tailored with respect to the specific application [106]. In this thesis, a triode-like electrode arrangement was used for the *I*-*V* curve measurements with a fine metal grid posing as control electrode as it was described by Park *et al.* [17, 18]. The general procedure of the FE measurement is illustrated in Figure 3.1. On the one hand, the triode-type configuration promotes large emission currents at lower voltages. However, on the other hand, the risk for electrical discharge between cathode and grid is enhanced by the typically smaller inter-electrode spacing [107]. Thus, it is essential to consider the mechanisms leading to electrical breakdown for realization of reliable FE electron sources.

Electrical Breakdown

FE measurements are performed in ultra-high vacuum, however, electrical discharge can occur and cause irreversible destruction of the emitter. If a critical electric field is reached, the dielectric medium in the electrode gap abruptly looses its insulating properties and a considerable increase in current flow, caused by plasma formation, can be noted [108]. In contrast to a conventional electrical breakdown in a gaseous atmosphere—with the breakdown voltage directly related to the electrodes' distance and the system pressure (Paschen's law)—the gas density in vacuum is not sufficient to sustain electron avalanches solely by particle collisions in the electrode gap [109]. For a pressure below 10^{-4} Torr ($\approx 1.33 \cdot 10^{-4}$ mbar) no significant dependence of the breakdown voltage on the inherent pressure is observed anymore because the mean free path of particles is typically much larger than the inter-electrode spacing. Thus, collisions of emitted electrons with residual gas molecules become unlikely [110, 111]. For

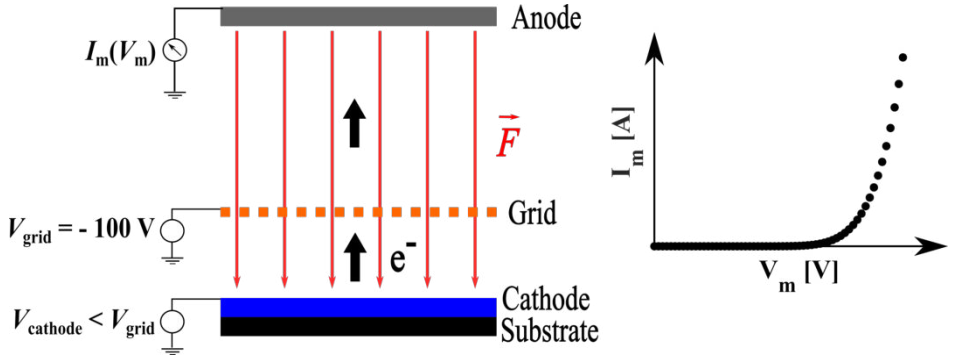

Figure 3.1: Schematic of the FE measurement in triode-type configuration (left side). The cathode (blue) sits on top of a substrate (black) and the control electrode (orange) is located in a distances of several hundred micrometers from the cathode, while the grid-anode separation is in the millimeter range. First, the control electrode—here constituted of a metal grid—is set to a constant negative potential V_{grid}. Second, the absolute value of the negative voltage at the field emitter sample V_{cathode} is raised, and third, emitted electrons are accumulated at the anode (gray). The current I_{m} is consecutively measured as a function of the applied voltage $V_{\text{m}} = |V_{\text{cathode}} - V_{\text{grid}}|$ (graph on the right side). The electric field $\vec{F}$ between the electrodes is indicated by red arrows pointing from anode to cathode and the reverse direction of the electron current is sketched by black arrows.

a vacuum gap of 100 µm width between two planar electrodes, namely without deliberate geometrical enhancement of FE, a breakdown voltage of around 10 kV is suggested by experimental results in literature [110].

Vacuum breakdown is mainly generated by FE-initiated mechanisms and by the local interaction of intense electric fields with electrode surfaces [110]. Considering a clean emitter without any adsorbed species in ultra-high vacuum, emitter self-heating is the dominant source for electrical arcing. The local temperature raise by the interplay of Joule and Nottingham effects (see section 2.1.2) can lead to vaporization of emitter material followed by ionization processes promoted by the electric field [112]. In reality, adsorbed species populate the emitter's surface, which produce secondary effects that lower the threshold for electrical breakdown further. On the one hand, charged particles can be liberated from the cathode side by emission of gaseous adsorbates facilitated by the intense electric fields or through the aforementioned local emitter self-heating. On the other hand, bombardment of the opposing electrode with emitted electrons can cause local heating and subsequently, release of electrode material as well as gas desorption from the control electrode or from the anode, which is followed by an electrical discharge [108, 113]. Typically, a short rise in pressure is observed with the occurrence of an electrical breakdown due to vaporization of electrode material [108]. Another source for vacuum breakdown are charged, loosely bound particles that can be dragged across the vacuum gap by the electric field. According to the "clump" theory, the impact energy released by theses particles when impinging onto the opposing electrode

can lead to local temperature increase and consequently to material release, which provokes electrical discharge in the vacuum gap [110].

3.2 Field Emission Setups

This section presents a detailed description of the FE setups in the configuration used for *I-V* curve measurements in this thesis. For clarity, this part is divided into three subsections as displayed in Figure 3.2 with respect to the main components of a FE setup: First, the high vacuum chamber (sketched in red), second, the sample mounting (blue) and third, the data acquisition (green).

3.2.1 Vacuum Chamber

Side and top views of the three FE setups are displayed in chronological order with regard to their time of construction (from 2016 to 2019) in Figure 3.3. The first setup on the left, in the following called "ISO setup", was assembled within a Master's thesis[3] in the research group of Prof. Blick (CHyN, UHH) [96]. A 6-way ISO-K cross forms the vacuum chamber with the measurement flange on the top port fixed by claw clamps and sealed by an elastomer O-ring, as it is typical for the ISO-K clamping flange system [114]. The setup is placed on an optical table and a base pressure of $2{\cdot}10^{-6}$ mbar is maintained by an EXPT pumping station, consisting of a nEXT300 turbomolecular pump and a nXDS10i dry scroll vacuum pump (Edwards Vaccum). For exchange of the FE sample, an external rotary vane pump (UNO 5, Pfeiffer Vacuum) is employed for evacuation of the chamber from atmospheric level to a pressure below $5{\cdot}10^{-2}$ mbar before the valve towards the turbomolecular pump is opened. Thereby, the shut down of the turbomolecular pump for mounting a new FE sample is avoided. The pressure levels are monitored with a compact cold cathode gauge (IKR 251) coupled to a measurement unit (TPG 262, both from Pfeiffer Vacuum).

The vacuum chamber of a time-of-flight mass spectrometer (Voyager-DE STR, JBI Scientific) was used to set up a second FE system. The load lock chamber can be separated from the high vacuum part of the mass spectrometer by a gate valve for convenient exchange of the measurement flange. In this FE system, called "Voyager", a base pressure of about $5{\cdot}10^{-7}$ mbar is obtained, measured by a compact full range gauge (PKR 250) and read out by the corresponding measurement unit (TPG 251 A, both from Pfeiffer Vacuum). For FE sample mounting, the small load lock chamber is evacuated with the help of a rotary vane pump (Trivac D4B, Leybold) to a pressure below $5{\cdot}10^{-3}$ mbar before the gate valve is opened

[3] Christian Henkel, *Characterization of diamond nanomembranes by field emission for a detector in mass spectrometry of large proteins*, supervised by Chris Thomason (2016) [96]

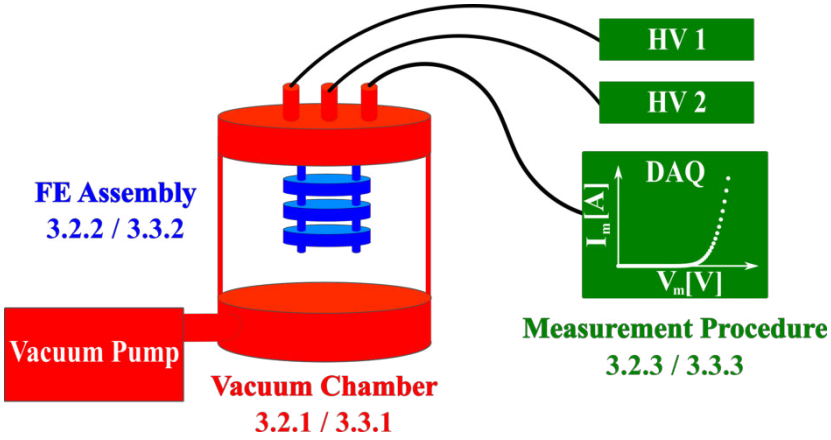

Figure 3.2: The three basic components of the FE setup are shown schematically as guidance for the present section and for the following one, which addresses the setup optimization. First, the vacuum chamber (red), second, the FE measurement assembly in triode configuration (blue) sitting on a vacuum flange and third, the measurement procedure regarding two high voltage (HV) power supplies and data acquisition (DAQ, green), are considered. The subsection numbers that refer to the particular setup components are given in the Figure.

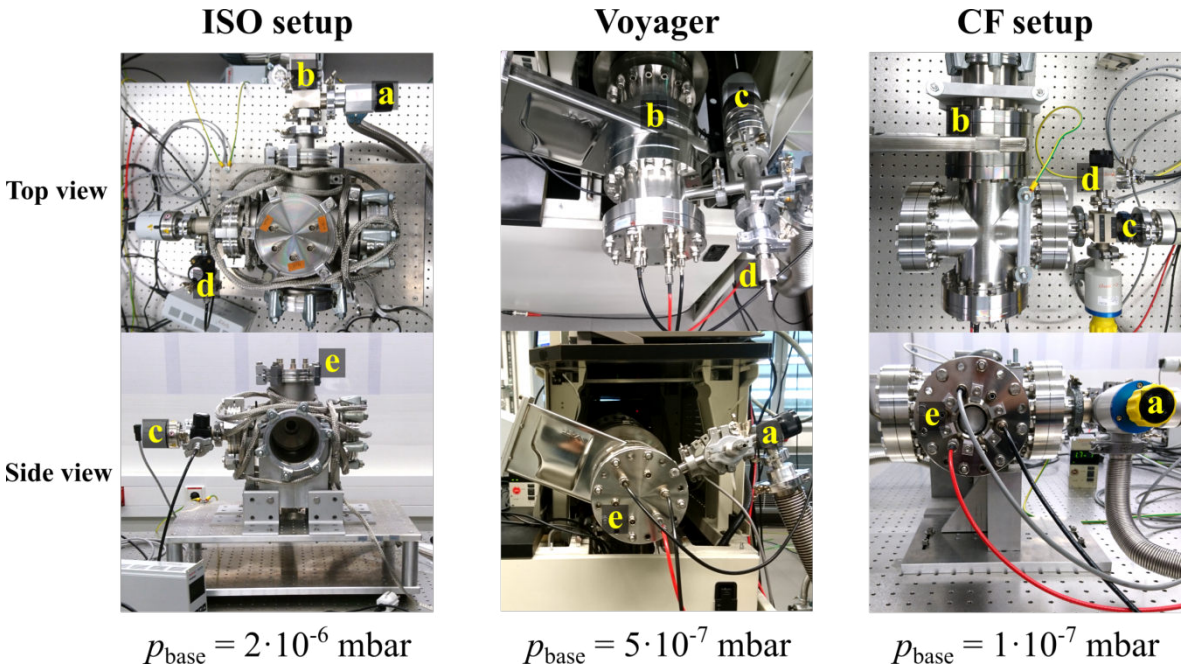

Figure 3.3: The outer appearance of the three FE setups is shown in chronological order with regard to their time of construction (from 2016 to 2019) from left to right: ISO setup, Voyager and CF setup with a base pressure (p_{base}) of $2 \cdot 10^{-6}$ mbar, $5 \cdot 10^{-7}$ mbar and $1 \cdot 10^{-7}$ mbar, respectively. The two latter ones were set up within this thesis. To each of the high vacuum chambers, ports are connected to external rough pumps (a), which are used for initial chamber evacuation when mounting a new FE sample before the respective connections to the turbomolecular pumps are opened (b). Additionally, there are ports for vacuum gauges (c), for ventilation valves (d) and for the measurement flanges (e).

to the time-of-flight chamber. In the mass spectrometer, the pressure is maintained by two turbomolecular pumps (Turbo-V 250 MacroTorr and TV 301 Nav. Pump, both from Varian), which are backed by a dry scroll vacuum pump (nXDS10iC, Edwards Vacuum).

The third setup, named "CF setup", was mainly assembled from ConFlat® compatible vacuum components, proving lower leak rates compared to the ISO-K flange system. CF components are usually sealed by a flat gasket from oxygen-free copper, which is irreversible deformed by the knife-edge on the flange's vacuum side [114]. For the exchangeable measurement flanges of the CF setup as well as of the Voyager, reusable elastomer gaskets are utilized instead. A 4-way CF-cross forms the load lock, which is separated by a gate valve from the turbomolecular pump (TMH 261 P, Pfeiffer Vacuum) and the corresponding rotary vacuum pump (E1M18, Edwards Vacuum). A base pressure of $1{\cdot}10^{-7}$ mbar is detected by a compact full range gauge (PKR 250) that is combined with a measurement unit (TPG 251, both from Pfeiffer Vacuum, formerly Balzers). For FE sample exchange, the load lock chamber evacuation is performed to a pressure below $5{\cdot}10^{-2}$ mbar with the same rotary vane pump that is used for the ISO setup. Despite different flange systems are used for the FE setups, the FE assembly itself on the corresponding measurement flange can easily be exchanged as demonstrated in the next section.

3.2.2 Field Emission Assembly

This section is thought to give an instruction for consistent mounting of FE samples, critical to reproduce *I-V* curves from the same field emitter sample as well as for comparison of different cathodes. The FE assembly presented here—namely the emitter-grid-anode stack—was tailored for the measurement of FEAs on bulk substrates as well as on free-standing membranes. The FE assembly shown in Figure 3.4 is electrically insulated from the measurement flange by a cylindrical PTFE (polytetrafluoroethylene) pedestal (sketched in light brown), while insulating PEEK (polyetheretherketone) screws and nuts (dark brown) are used for fixation of the electrode stack.

First, the emitter (blue) on the substrate (black) is attached to the center of a PTFE disc (light brown) by placing small droplets of silver conductive paste (G3303B, Plano GmbH) underneath the four edges of the substrate (red). Second, a thin metal electrode ring (green, about 50 µm thick) is placed around the sample and a single-side metal-coated PTFE foil (gray, metal coating displayed in yellow) with a centered cutout for the field emitter structure is used to provide electrical contact from the cathode's surface to the electrode ring. On the one hand, the PTFE spacer defines the distance between emitter and adjacent electrode. Therefore, the applied electric field and the obtained FE properties from experimental data are highly dependent on the PTFE sheet thickness. On the other hand, the foil serves as electrical insulation of the emitter from the grid electrode. Hence, the spacer thickness is

chosen to enable FE from the cathode under test within a feasible voltage range, but it is selected as large as possible to provide sufficient electrical insulation. In this thesis, the spacer thickness was varied between 50 µm and 500 µm. Note, the size of the central square hole in the PTFE spacer can easily be tailored with respect to the dimensions of the FE sample by laser cutting of the foil. To compensate the height of the sample's substrate and as additional insulation, PTFE rings are added around the cathode (height compensation, sketched in light brown). For substrates with 300 µm thickness, a 250 µm PTFE ring is used and for 525 µm wide samples, one sheet of 250 µm and one of 100 µm height are combined. The thickness of the height compensation is chosen to be smaller than the actual substrate height to provide sufficient electrical contact through the metallized PTFE spacer to the cathode by mechanical compression. Third, the control electrode (orange) is added, which consists of an electroformed nickel grid (59 lines per centimeter (lpc), Precision Eforming) spanned over a central square hole of a copper disk and fixated with silver conductive paste. After the control electrode is placed on the stack with the mesh facing towards the cathode, another annual electrode is added for voltage supply (dark orange) and the emitter-grid assembly is secured with PEEK nuts. Note, for a reproducible compression of the PTFE spacer, a torque wrench with a force of 0.1 Nm is used for mounting. Fourth, the anode (light gray) is added to the assembly in the distance of 2.4 mm, which is defined by the thickness of the spacer PEEK nuts. Finally, the anode metal plate is attached by another set of those.

Each of the electrode rings is connected with a stainless steel screw to a cable that is plugged into one of the push-on connectors on the vacuum side of the electrical feedthroughs

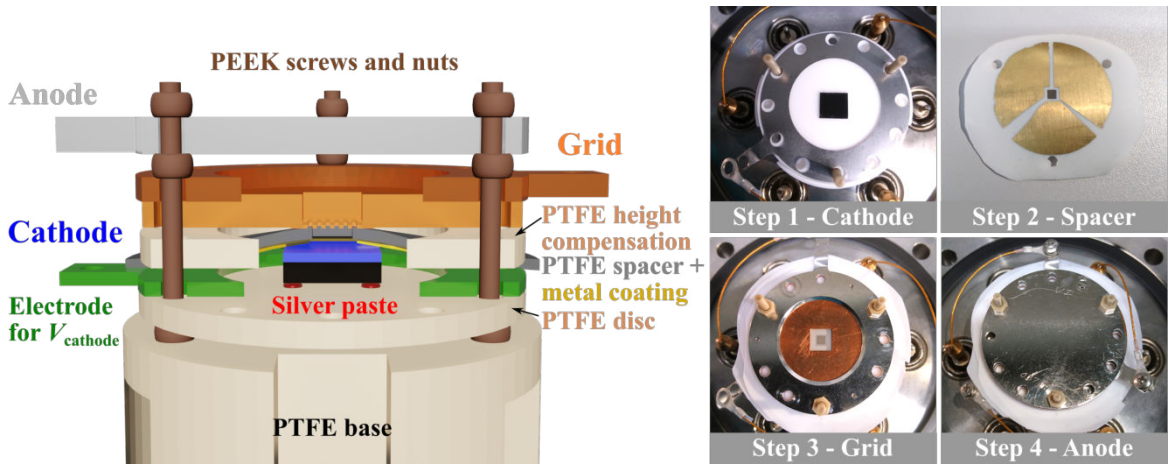

Figure 3.4: The sketch on the left presents a cross section through the FE assembly and the photographs on the right show top views of the four main assembly parts: The cathode fixated with silver conductive paste to a PTFE disk (step 1), the metal-coated side of the laser cut PTFE foil (step 2), the grid (step 3) and the anode (step 4). All assembly components are secured by PEEK nuts on the PTFE base, which is mounted on one of the FE measurement flanges.

in the measurement flange. The Kapton® insulated wires are suited for HV operation in vacuum (UHV KAP301, Allectra GmbH). Last but not least, electrical insulation of the three electrodes to each other is verified by a resistance measurement via a multimeter, before the FE assembly—mounted with the PTFE socket to either a KF or a CF flange—is transferred to one of the vacuum chambers. Additional explanations for material choices and preparation methods for the individual segments of the FE assembly are given in section 3.3.2.

3.2.3 Measurement Procedure

Herein, the voltage supply, DAQ, and measurement procedure, executed by a LabVIEW program, are presented. The electric field between emitter and grid is supplied by HV power supplies (PS350, Stanford Research Systems) connected to the miniature high voltage (MHV) connectors of the electrical feedthroughs on the atmosphere side of the measurement flange. Grid as well as cathode are coupled to the HV power supplies by HV suited cables (Lemo HV 9 kV/0.6 mm, arnnotec GmbH) with MHV connectors for attachment to the measurement flange and with safe high voltage (SHV) plugs for connection to the power supplies [114].

To exclude measurement artifacts from the DAQ system, two different arrangements were applied to measure the FE current. The first method uses a transimpedance amplifier (DLPCA-200, Femto Messtechnik GmbH) to convert the measured currents in the order of picoampere to signals in the millivolt range. The amplifier is connected by a coaxial cable to the anode via an electrical feedthrough in the measurement flange. An amplification factor of $G = 10^9$ V/A is used (low noise setting, full bandwidth, direct current (DC) mode) with the amplifier's input connected to ground. The signal is guided via a BNC rack (NI BNC-2090A) to the network card (PCIe-6363, both from National Instruments). To attain the output current at a specific applied voltage, a large number of samples is integrated to suppress statistical error sources. Hence, for the measurement type that uses the current amplifier, the FE current is determined by $I_\mathrm{m} = \frac{1}{N \cdot G} \sum_{\mathrm{i}=1}^{\mathrm{N}} V_{\mathrm{m,i}}$, with $N = 2 \cdot 10^6$ samples, with a sampling rate of 10^6 samples/s and with $V_{\mathrm{m,i}}$ as single voltage data points [96]. For the second method, a picoammeter (model 6485, Keithley) is used to directly measure the FE current with an integration time of one second per $I_\mathrm{m}(V_\mathrm{m})$ value. The time the input signal is acquired is set to 50 Power Line Cylces (PLCs) with 1 PLC corresponding to an integration time of 20 ms for 50 Hz line frequency [115].

Most of the FE measurements in the ISO and the CF setup were conducted with the amplifier method, whereas the picoammeter was mainly used for measurements in the Voyager. Note, interchange of DAQ techniques is possible without circumstances or loss of measurement accuracy. The LabVIEW program that is utilized to control the measurement execution follows the sequence schematically displayed in Figure 3.5. Herein, the details about the *I-V* curve acquisition are specified to refine the generalized description that was given in

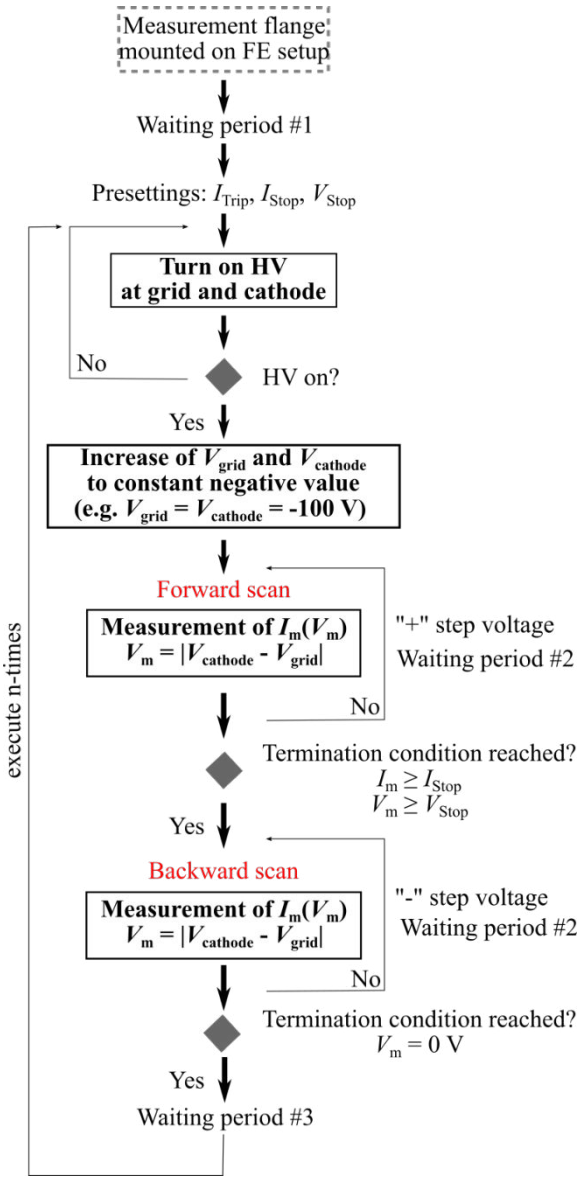

Figure 3.5: The flow chart illustrates the steps executed by the LabVIEW program after mounting the measurement flange with the FE sample on one of the setups. The program allows for the unattended measurement of n subsequent *I-V* curves from one sample after a waiting period #1. First, a trip current I_{trip} is set for the HV power supplies and a maximum applied voltage V_{stop} as well as a threshold output current I_{stop} are established as termination conditions for the FE measurements. Second, the HV is switched on at grid and cathode power supply verified by measuring the voltages. In case of failing to turn on the HV, the process is repeated. The grid voltage is increased step wise to a constant negative value, followed by raise of the cathode voltage $V_{cathode}$ to the same negative potential. Third, the absolute value of $V_{cathode}$ is increased by equidistant voltage steps and a value for I_m is acquired for each V_m after waiting period #2. When reaching one of the termination conditions, the forward scan is aborted and the backward scan is initialized. Fourth, I_m is measured as a function of V_m that is gradually decreasing back to zero applied voltage. After another waiting period #3, the program is executed again, until a specified number of *I-V* curves is acquired.

the beginning of this chapter in section 3.1. Unless otherwise stated, the characterization conditions listed in Table 3.1 were supplied to the LabVIEW program for the *I-V* curve measurements. In general, the waiting periods #1 – #3 are introduced to provide sufficient time for discharging of the FE assembly after voltage increase/decrease and thereby, to prevent falsification of the measured current by the alternating current (AC) signal that can pass through the capacitor-like electrode arrangement when the applied voltage is changed and to reduce the risk of electrical breakdown. The maximum current at grid and cathode power supply is defined by the trip current I_{trip}, which causes the voltage to drop immediately to zero when exceeded by the occurrence of an electrical discharge in the FE assembly. Detailed explanation for parameter selection is given in the next section.

Parameter	Value
V_{grid}	-100 V
Step voltage	2 V
Waiting period #1	72 h
Waiting period #2	3.785 s
Waiting period #3	1 h
I_{trip}	0.1 mA

Table 3.1: Summary of the characterization conditions used in the LabVIEW program that is controlling the FE measurements. The grid voltage V_{grid} is set to a constant negative value and the step voltage corresponds to the voltage value increase (decrease) in the forward (backward) scan before a current value is acquired. Waiting period #1 and #3 describe the elapsed time between the sample is mounted in the vacuum chamber and the initial FE measurement, and the duration between subsequent *I*-*V* curve measurements, respectively. The time between voltage step and current measurement is given by waiting period #2.

3.3 Setup Optimization

Electrical breakdown between small gaps is a severe issue for FE examinations, risking measurement device and emitter destruction [1]. Bulk cathodes can suffer from immense structural changes, but still be emitters at all, however with altered FE characteristics. In contrast, nanostructured emitters and nanomembranes are immediately destroyed when hit by an arc discharge. This sensitivity stresses the need for optimization of the FE measurement setup. To compare the influence of emitter surface modifications—such as coating, surface group termination and aspect ratio—on FE properties, a consistent assembly of the emitter in the FE setup is the prerequisite to provide constant electrode spacing and as a consequence, control over the applied electric field. This section discusses the modifications applied to the ISO setup to enhance the reproducibility of *I*-*V* curves and to lower the risk of electrical breakdown. For transparency, the structure of this chapter follows the sketch that displays the three main FE setup components (vacuum chamber, FE assembly, DAQ) in Figure 3.2. Note, only the sum of all of the aforementioned improvements will enable the experimentalist to fully control the measurements in a reliable manner. The improvements are not setup related and hold true for all FE setups used in this thesis.

Unless otherwise stated, the onset voltage $V_{\text{m}}^{\text{onset}}$ and the corresponding macroscopic electric field $F_{\text{M}}^{\text{onset}}$ are defined by the first current data point $I_{\text{m}}^{\text{onset}}$ above a $10\,\sigma$ threshold and only the forward scan of the FE measurement is presented and considered for data analysis. The standard deviation σ is derived from the normal distribution of the measured current values between 20 % and 50 % of the total range of applied voltages, to exclude artifacts from electrical charging in the low voltage region and from the exponential current increase

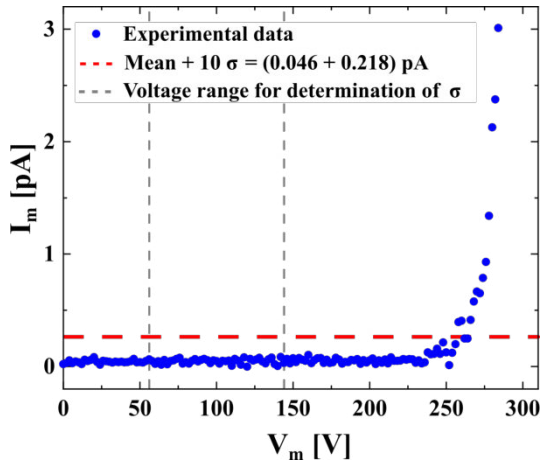

Figure 3.6: The measured current I_m is shown as a function of the applied voltage V_m from a ZnO NW sample. A normal distribution of the I_m values from the range of 20–50 % of the total number of voltage data points of the forward scan (emphasized by the vertical dashed gray lines) is employed to determine the standard deviation σ. Then, the first value I_m^{onset} above the 10 σ threshold (horizontal dashed red line) is used to determine the corresponding onset voltage V_m^{onset}. The conversion to macroscopic electric field F_M^{onset} is subsequently performed by division through the cathode-grid distance, which is defined by the PTFE spacer thickness. For the presented measurement, the following onset values were determined: $V_m^{onset} = 258$ V corresponding to $F_M^{onset} = 2.58$ V/µm for $d = 100$ µm.

by FE for higher voltages. Exemplary, the onset determination is shown in Figure 3.6. In literature, often a turn-on field is defined by the emission current density (ECD) being larger than 10 µA/cm^2 [86, 116] and a threshold field is defined by the ECD overcoming a value of 10 mA/cm^2, which is typically needed for effective excitement of a phosphor pixel in FE displays [116]. On the one hand, there is no unifying definition for these values, since the turn-on field as well as the threshold field are sometimes also set to 0.01 µA/cm^2 [76] and to 1 mA/cm^2 [71], respectively. On the other hand, the conversion from measured current to ECD is uncertain because the real emission area is typically unknown especially for nano- and microstructured emitters [4]. For analysis of *I-V* curves within this thesis, the onset voltage is defined by the measured current overcoming the data set-dependent 10 σ limit and thereby, being clearly distinguishable from background noise. Note, for comparison of field emitter samples measured with different cathode-grid distances, the onset voltage derived from the *I-V* relation is always converted to the macroscopic onset field.

3.3.1 Vacuum Chamber - Modifications

In the framework of this thesis, the Voyager and the CF setup were built as additional FE measurement systems. Further, the minimum duration for proper outgassing of the complete FE assembly allowing for reproducible measurements was determined to be 72 h and

the influence of the system pressure on *I-V* curves was investigated in a range of $3{\cdot}10^{-7}$ to $1{\cdot}10^{-5}$ mbar. Both setups (Voyager, CF setup) consist mainly of CF flanges, which proved a lower leak rate compared to the ISO-K flange system used to build up the older ISO setup [114]. The lower base pressures attained in the new setups can additionally be explained by the Voyager system being pumped by two turbomolecular pumps and the CF setup having a smaller vacuum chamber volume compared to the ISO setup (Figure 3.3). As stated in the beginning of this chapter, the influence of the pressure in a vacuum gap on the breakdown voltage was reported to be insignificant for values below $1.33{\cdot}10^{-4}$ mbar [110, 111] and thus, no effect of the base pressure on the breakdown probability would be expected for the three FE setups ($p_{\text{base}} = 1{\cdot}10^{-7}$ to $2{\cdot}10^{-6}$ mbar). However, the pressure is not measured in the small gap between the closely stacked cathode-spacer-grid arrangement, where outgassing—the release of gaseous species from materials in vacuum without additional external stimulation [117]—from the emitter structure, the dielectric inter-electrode material or other components of the FE assembly can increase the amount of particles locally. In addition, polar water molecules tend to bond chemically (exchange of a valence electron) or physically (van der Waals forces) to all kinds of materials that were previously exposed to air, which prolongs the evacuation time [118]. Desorption and ionization of those gases and water molecules within the small gap promoted by strong electric fields during the FE measurement can enhance the risk of electrical sparking considerably.

On the one hand, the high impact of the outgassing duration on the FE measurement, namely the time between sample mounting in vacuum and the first *I-V* curve acquisition, was distinct for a CNT sample that was kept in high vacuum for a long time (Figure 3.7 (a), plotted in red). After this time, no shift in onset field for FE was observed for subsequent measurements, whereas 12 h after mounting in vacuum, the initial rise of emission current from noise level strongly varied and high current pulses were noted (Figure 3.7 (a), plotted in blue). Elsewhere, those current fluctuations are attributed to dynamic modulations of the adsorbate distribution on the emitter's surface through desorption, adsorption, and diffusion processes, which are initiated by intense electric fields and by effects arising from the FE current flux [119]. For practical reasons, a minimum necessary outgassing time was determined by a series of FE experiments to reduce the impact of adsorbed surface molecules on *I-V* curves. A ZnO NW sample was measured three times each after 24 h (plotted in black), after 48 h (orange) and after 72 h (green) in vacuum of the ISO setup (Figure 3.7 (b)). After 3 days, no significant variation in onset of FE was observed within the series of three measurements and the occurrence of sudden current fluctuations was reduced. Since the test was executed in the setup with the highest base pressure ($2{\cdot}10^{-6}$ mbar), this minimum outgassing period of 72 h was implemented for all three FE setups. Methods for degassing the system, such as vacuum bakeout, glow discharge or ultraviolet radiation, to name a few, could potentially be

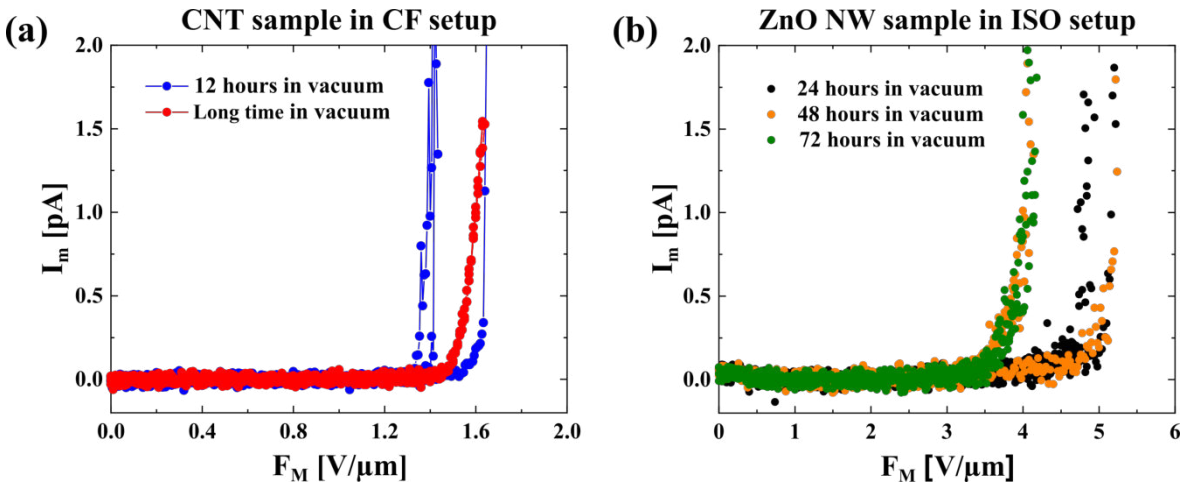

Figure 3.7: (a) The measured current I_m is shown as a function of the macroscopic field F_M for three subsequent measurements from CNT field emitters after 12 hours (blue) and after an extended time (red) in vacuum (CF setup). The derived onset fields for 12 hours and for the longer outgassing time are $F_M^{onset}(12\,h) = 1.5\,V/\mu m \pm 8.9\,\%$ and $F_M^{onset}(long) = 1.5\,V/\mu m \pm 0.4\,\%$, respectively. **(b)** Three subsequent FE measurements from ZnO NWs, each after 24 h (black), 48 h (orange), and 72 h (green) in vacuum (ISO setup) are shown. The following onset field values were derived: $F_M^{onset}(24\,h) = 4.8\,V/\mu m \pm 8.3\,\%$, $F_M^{onset}(48\,h) = 4.0\,V/\mu m \pm 14.2\,\%$ and $F_M^{onset}(72\,h) = 3.7\,V/\mu m \pm 2.8\,\%$. The minimum necessary outgassing time was determined to be 72 h as the variation of the onset field for subsequent measurements is significantly reduced. For convenient comparison of the onset fields, the setup- and DAQ system-dependent offsets and slopes were subtracted from the raw FE data prior to data analysis (see 3.3.3 for detailed explanation).

employed to reduce the outgassing time further [118]. However, the sensitivity of the nanostructured samples to, for instance, high temperature or arcing has to be considered because it can lead to irreversible and irreproducible modifications of the emitter [1].

On the other hand, the pressure in the vacuum chamber could have an impact on the shape of *I-V* curve. At higher base pressures, effects such as a modification of the emitter geometry through sputtering with residual gases or adsorption of molecules occur with higher probability [2]. Further, adsorption of residual gases promoted by the electric field showed to change *I-V* curves by modifying the material's effective work function, which was demonstrated in studies with deliberate gas injection [120, 121]. For that reason, the CF setup was used to examine the influence of system pressure in a range of $3.1 \cdot 10^{-7}$ mbar to $1.1 \cdot 10^{-5}$ mbar as shown in Figure 3.8. For each vacuum level, which was set by closing the gate valve towards the turbomolecular pump until a desired steady-state pressure was reached by system-inherent leakage, the FE measurement was executed for the same ZnO NW sample. The pressure in the measurement chamber increased presumably by material outgassing and permeation through gaskets, while the pumping force was reduced. In the studied pressure range, no significant variation of the onset field as a function of the system's pressure is detected. This

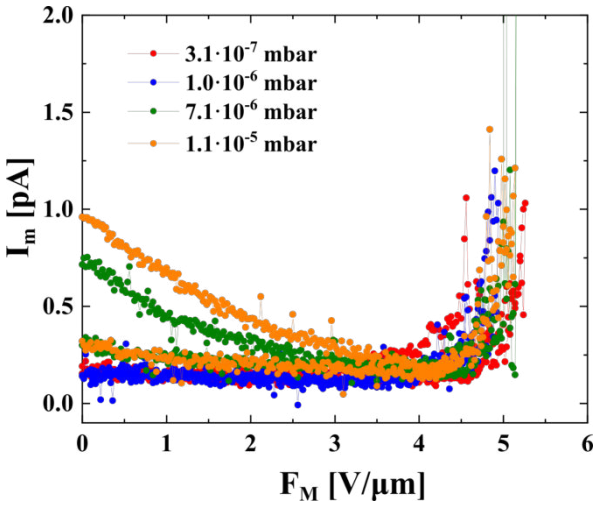

Figure 3.8: The forward and backward scan of the measured current is shown in dependence on the applied electric field for different pressures in the CF setup. The pressure was set to the following values: $p = 3.1 \cdot 10^{-7}$ mbar (red), $p = 1.0 \cdot 10^{-6}$ mbar (blue), $p = 7.1 \cdot 10^{-6}$ mbar (green) and $p = 1.1 \cdot 10^{-5}$ mbar (orange). The mean onset field of the four shown measurements was determined to be $F_{\mathrm{M}}^{\mathrm{onset}} = 4.6$ V/µm $\pm$ 6.6 %.

observation leads to the conclusion that the impact of adsorption/desorption processes may be negligible for the relatively low applied electric fields in the examined high vacuum range provided by the utilized FE setups. However, a gradually increase of I_{m} was found for the backward scan becoming more dominant with higher pressure values. Such a current slope can be attributed to the accumulation of charges in the capacitor-like FE assembly during the gradual voltage decrease of the backward scan. Ionized residual molecules may build up a layer of charged particles between the cathode-spacer-grid stack and may alter the effective finite resistance of the dielectric medium leading to an increase of the leakage current. In good agreement, but in other context, FE current enhancement through higher system pressure was ascribed to formation of a positive ion charge layer on the cathode's surface by ionization of gas molecules [122]. In summary, a lower vacuum level is favored because less disturbance by gas molecules interacting with intense electric fields is expected. Nevertheless, with a consistent outgassing time and in the pressure range of our FE setups, no influence on the forward scan of the *I-V* curves is observed.

3.3.2 Field Emission Assembly - Modifications

This section presents changes that were applied to the individual segments of the FE assembly, following the sequence of the sample mounting routine as described in section 3.2.2 and as emphasized in Figure 3.9. Most of the measurements presented in this subsection were

carried out in a scope of a Bachelor's thesis[4] in the research group of Prof. Blick (CHyN, UHH). All FE measurements were executed in the ISO setup utilizing a SiN coated Si piece as cathode, with a step voltage of 5 V/step and measuring with the transimpedance amplifier. Note, no emission is expected from a smooth SiN surface because an electrical field of at least 1000 V/µm (= 1 V/nm) would be necessary to permit FE without any field enhancing geometry, which is not feasible in our setups [4]. Therefore, FE-initiated electrical breakdown is not expected and the maximum electric field that can be applied to study the FE properties is mainly limited by the dielectric breakdown strength of materials used in the FE assembly. With a maximum voltage of 5 kV from the HV power supplies and a minimum cathode-grid distance of 50 µm defined by the available spacers, the maximum applied macroscopic field is restricted to 100 V/µm. The observation of a sudden strong current rise was defined as termination condition for the measurements, which is characteristic for occurrence of an electrical breakdown [108]. In addition, the voltage at emitter and grid power supplies dropped to zero, if the current flowing between the electrodes exceeded the maximum possible trip current of I_{trip} = 5.25 mA. For convenient comparison of the FE breakdown measurements, the setup-

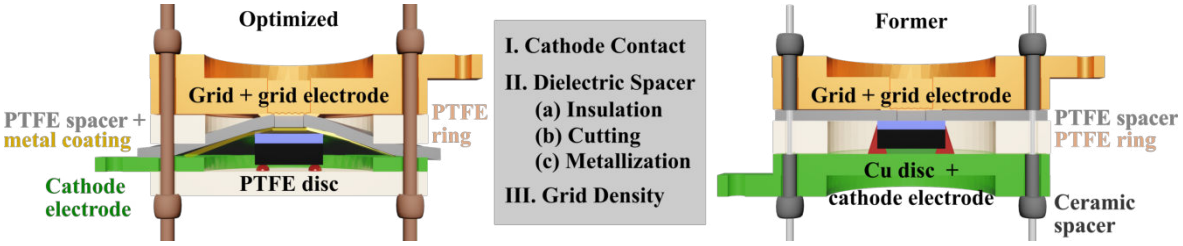

Figure 3.9: Comparison of optimized and former cathode-grid stack as guidance for this section. Separate parts are used to discuss the influence of first, the cathode contact method, second, the dielectric spacer—considering the material used for electrical insulation, the cutting technique and the metallization method—and third, the grid density. The **optimized assembly** consists of the cathode (sketched in blue) fixated with silver conductive paste (red) to a PTFE disk (light brown), the metal ring for voltage supply to the cathode (green), the PTFE spacer (gray) with gold coating (yellow) on the side facing towards the cathode, a PTFE ring as height correction (light brown) chosen with respect to the substrate's thickness (black), the grid and a corresponding metal electrode for voltage supply (both shown in orange). In contrast, in the **former assembly**, the cathode was fixated to a copper plate (green), the electrical contact was provided by silver conductive paste (red) applied to the sides of the sample and a reversed sequence of PTFE spacer (gray) and height correction (light brown) was used. Additionally, the optimized configuration is fixed by insulating PEEK screws and nuts (dark brown) to avoid any risk of shortening, while the previous arrangement was assembled with metal screws, which were electrically shielded by ceramic spacers (dark gray) from the conductive parts of the assembly.

[4] Leutrim Pacarizi, *Optimization of a setup for field emission measurements of nanomembranes*, supervised by Stefanie Haugg (2018) [97]

and DAQ system-dependent offset and slope were subtracted from the raw data prior to further analysis (see 3.3.3 for detailed explanation).

I. Cathode Contact

Herein, two methods for the electrical contact to the cathode on top of a substrate are compared, namely a metallized polymeric foil (optimized version) and silver conductive paste (former version). Often, the use of semiconducting substrates is inevitable due to sample processing, but proper voltage supply is sometimes not feasible across the substrate towards the field emitter's base, caused by formation of a certain energy barrier at the metal-substrate interface in dependence of the substrate's doping level [107].

For the optimized version, the sample's surface is directly contacted from above by a gold layer on the polymeric foil. The voltage supply is provided through the metal electrode ring over the metallization on the polymeric spacer to the cathode. For the former version, the silver suspension (G3303B, Plano GmbH) is applied along the sample's sides as close as possible to the cathode to provide electrical contact from the copper plate towards the field emitter structure [96]. However, several disadvantages of this method could be identified: Silver paste on top of the cathode has to be avoided in any case, as it can potentially form an additional emission site, which can falsify the *I*-*V* curve and can promote electrical breakdown. However, if the silver paste is not applied close enough to the top surface, the electrical contact may be insufficient. In this case, the measured voltage would not be equal to the actual voltage supplied to the field emitter. Moreover, this method lacks reproducibility especially between different experimentalists.

For comparison of both contact methods, a silicon-on-insulator (SOI) sample (from microfab Service GmbH) was utilized that constitutes of a highly-doped Si film on a Si substrate, separated by a buried oxide layer. The sheet resistance of the n-type Si surface layer was determined to be about 86 Ω/sq with a four-point probe station measured in van der Pauw geometry [123, 124]. From the resistiviy of approximately 0.0013 Ω·cm for the 149 nm thick n-type Si layer, a heavy phosphorus dopant density that is larger than 10^{19} cm^{-3} can be estimated [125]. Note, the thickness of the Si film was given by the manufacturer. Figure 3.10 presents the voltage-current relation for both contact techniques. The metallized polymeric foil shows an Ohmic behavior, which is revealed by the linear fit (Figure 3.10 (a)). In a wide range of p- to n-type doping, the work function of silicon was reported to vary between 4.7 eV and 4.9 eV [126], which is smaller than the work function of 5.1 eV for gold [27]. Typically, the energy bands bend upwards at the metal-semiconductor interface when the n-type semiconductor has a smaller work function value than the metal [127]. The linear behavior of the herein examined gold-silicon contact indicates that the doping concentration of the n-type semiconductor (SOI sample) is sufficiently high to enable tunneling of electrons through the

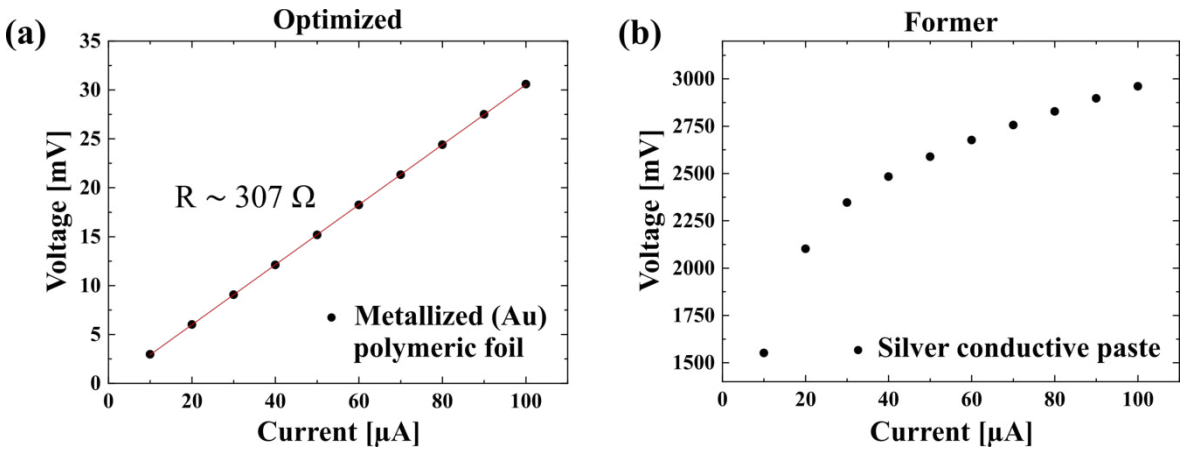

Figure 3.10: The voltage-current relation was measured for the optimized and former electrical contact techniques with a four-point probe station. A current was supplied to the respective cathode electrode (see Figure 3.9) and the corresponding voltage was measured at the surface of the SOI sample. **(a)** An Ohmic trend is observed for the optimized contact version, which is verified by the linear fit (red line). For the gold sputtered polymeric foil contact, a resistance of about 307 Ω is derived from the reciprocal slope of the fit. **(b)** A non-linear dependence of the measured voltage on the supplied current is observed for the former silver paste contact technique.

thin potential barrier at the semiconductor-metal interface [128].

When the work function of the metal is smaller than the value of the n-type semiconductor, the energy bands would bend downwards at the interface and an Ohmic behavior could appear [127]. However, a non-linear voltage-current dependence is observed for the silver contact to the n-type SOI sample although the work function of the metal (4.26 eV for silver [27]) is lower than the suggested range for Si (4.7–4.9 eV [126]), which indicates that the silver-silicon junction is disturbed by additional effects (Figure 3.10 (b)). Firstly, this non-Ohmic behavior may appear because the silver paste was not applied close enough to the cathode on top of the substrate and additionally, the influence of the electrical contact from the copper plate through the silicon substrate is uncertain. Even so the substrate's conductivity is low, a considerable leakage current through the Si substrate cannot be excluded. Secondly, silver tends to react with oxygen or sulfur when exposed to air leading to formation of a silver oxide or a silver sulfide surface layer [129]. In addition, the silver suspension consists of individual particles that provide a huge surface area for chemical reactions. Depending on the temperature and on the exposure time, surface layers of silver oxide or of silver sulfide may form and cause—together with the possible oxide layer on the SOI sample—a thick interfacial layer that impedes the electrical contact. Presumably, the non-linear behavior of the silver contact method is caused by a mixture of the above described effects. In conclusion, the probe station measurements indicate that the gold coated dielectric foil provides a reduced contact resistance, which is not dependent on the dexterity of the experimentalist and is thus, the

preferred contact method. However, the silver paste contact is not applicable for consistent sample examination of semiconductor substrates because of its lack of reproducibility.

II. Dielectric Spacer

Besides adsorbates that may be attached to the surface of the dielectric spacer, sublimation of the material is another source for particles in vacuum that can provoke electrical breakdown. Sublimation of a solid occurs when the material's vapor pressure is higher or comparable to the vacuum pressure in the system. Thus, the number of materials suitable for ultra-high vacuum operation is severely limited [130]. This section discusses the applicability of selected polymeric foils as dielectric spacer between emitter and grid electrode.

(a) **Insulation**

The following materials were examined as electrical insulators in the cathode-grid gap because of their high dielectric strengths and low outgassing rates as summarized in Table 3.2: Kapton® (polyimid), PEEK, and PTFE. The insulating materials were tested with silver paste as contact method (former version) for the SiN coated sample to avoid uncertain influences from the metallization process, such as the reduction of the breakdown voltage by the preparation of the contact layer (see item (c)). Figure 3.11 presents the FE measurements that were used to experimentally determine the breakdown fields for the different dielectric foils. The onset of electrical breakdown, characterized by a high negative current rise, occurred for Kapton® and for PTFE at an applied electric field of about 25 V/µm, while the measurement with PEEK was stopped around 26.5 Vµm to prevent damage of the transimpedance amplifier.

The experimental results for PEEK and PTFE agree well with their values for the dielectric strength given in Table 3.2, which is the maximum electric field a material can withstand before electrical discharge occurs [131]. However, the maximum measured electric field for Kapton® (25 V/µm) is 8.2 times smaller than the value given in the data sheet, indicating that other mechanisms may be responsible for electrical discharge than simple failure of the dielectric medium. On the one hand, Kapton® has a total mass loss (TML) that is 4-times and 58-times higher compared to PEEK and PTFE, respectively. The TML is a figure used by the National Aeronautics and Space Administration (NASA) to examine the suitability of materials for operation in space, gathered in a large database over the last decades [132]. Note, the outgassing behavior is described in literature also by the outagssing rate, which is defined as "quantity of gas leaving per unit time per unit of exposed geometric surface, [...] at a specified time after the start of evacuation" [117]. These values vary considerably in literature for similar materials because the outgassing rate is highly sensitive to the material's history,

Material	Dielectric strength [V/µm]	TML [%]	Compressive strength [MPa]
Kapton®	205 [134]	0.96	186 [135]
PEEK	23 [136]	0.26	125 [136]
PTFE	22–24 [137]	0.02	3.9–4.9 [137]

Table 3.2: Dielectric strength, total mass loss (TML) and compressive strength for 100 µm skived PTFE foil (by High-tech-flon), 100 µm PEEK 381G film (by RS PRO) and 75 µm Kapton® HN (by DuPont™). The TML data was taken from [132] for comparable materials, namely for "Teflon FEP Tube 0.02", for "TML victrex peek 50g brown 0.26" and for "TML Kapton 200HN Polyimide film, 0.96".

namely baking, exposure to air or coating [133]. On the other hand, accumulation of charges on the surface of the dielectric medium exposed to a high electric field can promote electrical surface flashover. Discharge occurs typically with a higher probability in a layer of desorbed gases on the insulator's surface than through the bulk dielectric. The outgassing behavior and the surface conditions have a strong influence on the formation of such a charge layer, which can ease electrical breakdown [111, 138]. Thus, the reduced breakdown field observed for Kapton® may be correlated with the larger TML value compared to the ones for PEEK and for PTFE. To conclude, a maximum electric field of 50 V/µm could possibly be applied with our equipment together with

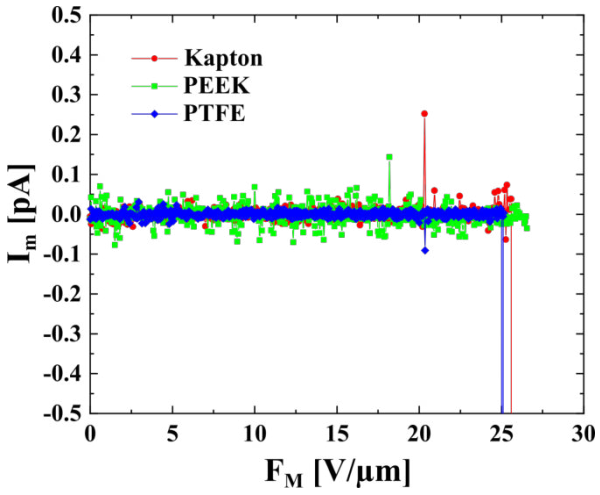

Figure 3.11: For experimental determination of the breakdown field for the three dielectric materials (Kapton®, PEEK and PTFE), FE measurements were executed until breakdown occurred (except for PEEK), which is identified by a large current spike. The three insulators showed a breakdown field of about 25 V/µm. Since the Kapton® layer has a thickness of 75 µm, the breakdown voltage is only 1925 V. For PEEK and for PTFE (each 100 µm), a maximum applied voltage of 2655 V and of 2505 V were reached, respectively. Note, the former cathode contact method, hand-cut dielectric foils and 32.7 lpc grids were used for the presented measurements.

a 100 µm thick insulating spacer, but is limited to around 25 V/µm by the material's dielectric strength and outgassing behavior.

(b) **Cutting**

Initially, the polymeric foils were cut by hand with a cutter knife. This method lacks for accuracy, which is especially important for assembly of large free-standing membrane samples. If the dielectric foil touches a nanomembrane accidentally because the square opening is not exactly placed in the center of the foil, the membrane is immediately destroyed. Therefore, the applicability of cutting the dielectric spacers with the help of a CO_2 laser (MM200-Flex, Optec laser micromachining systems) was investigated. After laser cutting of Kapton®, a distinct black crystalline structure was found on the cutting edges and its conductivity was verified by a multimeter measurement. The polyimid film tends to carbonize in the area just outside the laser beam where not enough heat is transferred to vaporize the material. Thus, laser cut Kapton® cannot be used as spacer because it electrically connects emitter and grid electrode and the current flowing between the power supplies would exceed the trip current immediately. Potentially, the carbonized residues could be removed by ultrasonication in solvent [139], but deliberate liquid exposure would increase the outgassing duration for the polyimid film considerably. Therefore, Kapton® is not considered as spacer material from here on, because accurate cutting is essential for consistent *I-V* curve measurements as the emission current depends on the exposed emission area [4].

PTFE conducts not enough heat to overcome its melting temperature outside the laser path to cause carbonization [139] and thus, no related color changes were observed for this material as well as for PEEK. However, the breakdown measurements showed strong emission current fluctuations and revealed reduced breakdown fields. The corresponding measurements can be found in the Bachelor's thesis by Pacarizi [97]. Since this study was performed before optimization of the outgassing time (see Figure 3.7), the duration of approximately 12 h between mounting the sample in vacuum and the breakdown measurement was apparently not sufficient to allow for proper desorption of gaseous species possibly incorporated during the laser cutting process.

(c) **Metallization**

Since silver paste is not applicable as electrical contact to the cathode, the influence of metallization on the breakdown strength of PEEK and of PTFE was studied. In a first approach, the polymers were sputtered with 30 nm Au using a sputter coater (K550X from Emitech). During the deposition process, the edges of the polymeric foils were covered with scotch tape to reduce the risk for direct electrical contact between cathode and grid through the metal film. The PEEK and PTFE foils had an appearance similar

to the second step in Figure 3.4. The sputter coated films reduced the breakdown voltage significantly, which may have been caused by local weakening of the dielectric strength of the material by bombardment and by implementation of gold atoms. Therefore, the second approach used a more gentle physical vapor deposition (PVD) process. The metal was evaporated by an electron beam (e-beam) and condensed on the PEEK and PTFE by forming a thin layer [140]. A shadow mask from PTFE was tailored with the CO_2 laser to cover the edges of the polymeric foils. This holder enabled metallization of four spacers simultaneously in the PVD system (PLS 500 by Balzers-Pfeiffer) with 5 nm titanium serving as adhesive layer followed by 50 nm of gold as electrode. Figure 3.4 shows a photograph of such a metallized PTFE spacer. The breakdown fields, determined for the second PVD technique, were also reduced compared to the uncoated dielectric foils as shown in the Bachelor's thesis by Pacarizi [97]. However, the sequence of insulation and electrode layers in between the first PTFE disc and the grid electrode was not fully developed at the time of this study. Note, for recent acquisitions, no degradation of the dielectric foil through metallization by e-beam evaporation is observed, as shown in the next part.

In conclusion, PTFE and PEEK showed similar performances. Finally, PTFE was chosen over PEEK because it is commercially available in a larger thickness variety. Electrical breakdown can be enhanced through the accumulation of charged particles in between polymeric foils. Therefore, it is more convenient to use one polymeric foil having the final intended thickness, instead of adding up several layers to obtain the wanted spacer width. To prevent variation of the applied electric field by compression of PTFE during assembly, as it has a lower compressive strength compared to Kapton® and to PEEK (see Table 3.2), a torque wrench was used to fixate the nuts that hold the cathode-grid stack in place.

III. Grid Density

Herein, nickel meshes with different grid densities (see Table 3.3) were tested as material for the control electrode. The commercial grids offer high transmission rates with exceptional

Grid density [lpc (lpi)]	**Transmission** [%]	**Manufacturer**	**Part number**
27.6 (70)	90	Precision Eforming	MN17
32.7 (83)	80	Industrial Netting	-
59 (150)	73	Precision Eforming	MN28

Table 3.3: The properties of the tested nickel meshes were taken from [141] and from [97]. Note, the grid densities are displayed in lines per centimeter (lpc), but were given in lines per inch (lpi) by the manufacturers.

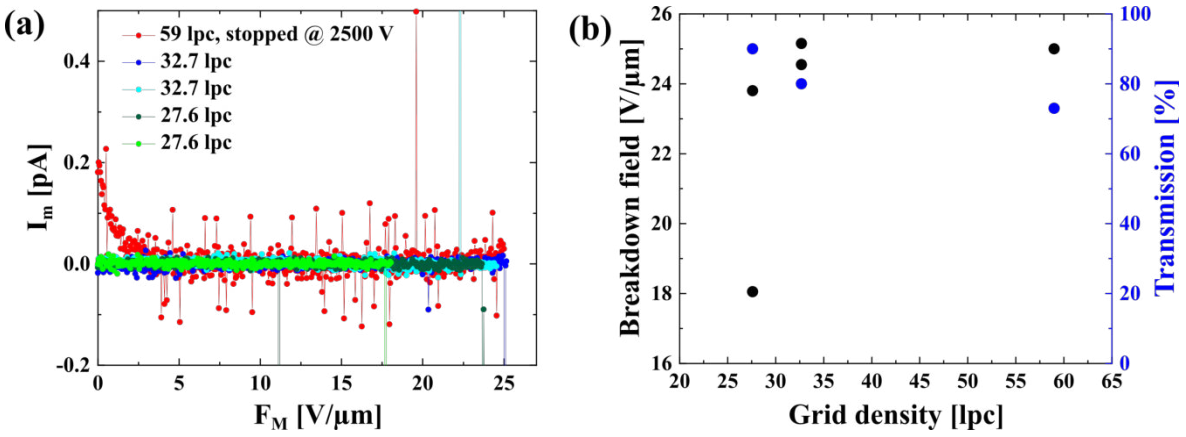

Figure 3.12: (a) Several FE (breakdown) measurements are shown for different grid densities. Measurements with a grid density of 27.6 lpc (displayed in light and dark green) and of 32.7 lpc (light and dark blue) are displayed, which were combined with hand cut, 100 µm thick PTFE spacers and silver paste contacts. The breakdown measurement with 59 lpc (red) was performed with the final FE assembly configuration, namely with a laser cut, 100 µm thick PTFE spacer, which was metallized by e-beam evaporation. **(b)** The observed breakdown fields (black) as well as the grid transmission (blue) are plotted in dependence on the grid density. For less dense meshes, the breakdown field varied strongly with every new grid preparation, however, for a higher grid density and in the final configuration, a maximum applied electric field of about 25 V/µm was obtained.

uniformity and were fabricated by electrodeposition [141]. As shown in Figure 3.12, a lower grid density caused reduction as well as stronger variation of the breakdown field. Therefore, the fixation of the mesh with silver paste onto the copper plate is less consistent for the 27.6 lpc grid because deformation can easily occur and bending towards the emitter reduces the cathode-grid distance unintentionally. Using a mesh with a larger density results in enhanced reproducibility of the maximum electric field, while the transmission rate remains in an acceptable range.

IV. Conclusion of Assembly Optimization

In conclusion of this section, the FE assembly composition was chosen to be a laser cut PTFE spacer, which is metallized by e-beam evaporation combined with a 59 lpc nickel mesh as grid electrode (as shown in Figure 3.4). The corresponding (breakdown) measurement in this configuration is plotted in red in Figure 3.12 (a). In our FE setups, a macroscopic electric field of 25 V/µm can safely be applied to the FE cathode. Further increase may be possible, however, it risks the damage of the field emitter sample and of the measurement devices.

3.3.3 Measurement Procedure - Modifications

A LabVIEW program from earlier work[5] was strongly modified during this thesis. For the former FE program, it was necessary to attend the time-consuming *I-V* acquisition for intervening in case of an electrical breakdown to prevent destruction of measurement devices. The following modifications were applied to enable consistent and unattended *I-V* curve measurements.

(a) For protection of measurement devices and emitter sample, the trip current at the HV power supplies is always set to 0.1 mA and a maximum current I_{stop} is chosen prior to the measurement as termination condition to prevent FE-initiated electrical discharge by excessive electron current. Due to the possible occurrence of current fluctuations—especially during the initial examination, caused by desorption of surface molecules—a specified number of counts above the stop current is allowed by the program. This setting prevents an early cancellation of the *I-V* examination before the actual electron emission by FE occurs.

(b) Further, the execution of a number of subsequent *I-V* curves with equal waiting period between the single measurements is possible. It was studied, if the waiting period between subsequent measurements has an impact on the appearance of the *I-V* curves by charge accumulation within the FE assembly. However, no significant modification of the onset field by the waiting period was observed as shown in Figure 3.13. Thus, the shortest tested pause time of 1 h is feasible. Note, the HV is shut off after each measurement to allow for complete discharging of the FE assembly.

(c) Additionally, the switching-on of the HV has to be verified at the beginning of each measurement in a loop of several FE examinations because communication failures between the power supplies and the DAQ system frequently occur. If the HV is off, the measurement is canceled and restarted again by initiation of the HV.

In the beginning of this chapter, the strong impact of the relation between measured and actual emitted current and corresponding voltages on proper data analysis was already mentioned [52]. Possible sources for distortion of this relation can originate from the FE measurement setups, FE assemblies and DAQ systems. Reasons for deviations of measured from emission values are additional resistance and capacitance in the measurement path of the electron current, which is illustrated by a replacement circuit in Figure 3.14 (a).

[5] Christian Henkel, *Characterization of diamond nanomembranes by field emission for a detector in mass spectrometry of large proteins*, research group of Prof. Blick, supervised by Chris Thomason (2016) [96]

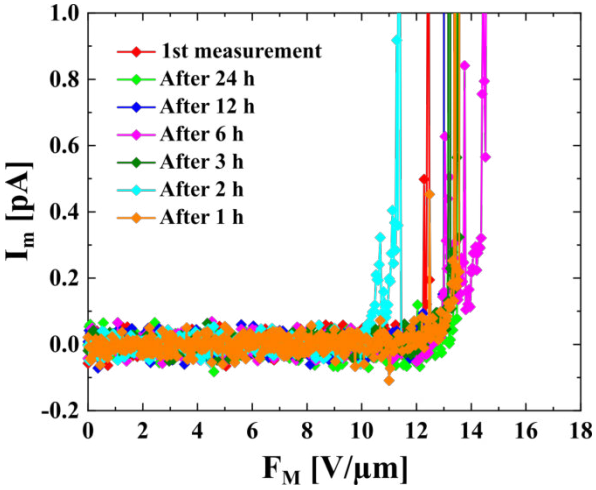

Figure 3.13: The waiting period between several subsequent FE measurements was reduced step wise from 24 h down to 1 h. The FE measurements were carried out for a ZnO NW sample (d = 50 µm) in the Voyager setup with the picoammeter. No significant influence is observed that would indicate a dependence of *I-V* curve appearance on the elapsed time between subsequent measurements. The onset fields for the shortest waiting period (1 h) and for the pause times between 3–24 h vary only by 2 % around a mean value of 13 V/µm. Stronger variation of the onset field—as for the 2 h waiting period—may rather be generated by FE-initiated changes of the cathode's surface constitution caused by self-heating and associated mechanisms, such as the release of adsorbed species.

The three electrode plates form two capacitors in series, which consist of the cathode-grid stack (C_{c-g}) with the PTFE as dielectric material and the grid-anode stack (C_{g-a}) with vacuum as dielectric medium. With the relation $C = \varepsilon_0 \varepsilon_r \frac{A}{d}$ and the plate dimensions given in the sketch (A - area of circular electrode, d - electrode separation), the capacitance of the grid-anode stack was determined to be C_{g-a} = 7.5 pF, with the relative permittivity ε_r(vacuum) = 1. The capacitance of the PTFE filled (ε_r(PTFE) = 2.1) cathode-grid arrangement was calculated to be C_{c-g}(PTFE) = 380 pF [131]. The cutout in the center of the PTFE spacer for the field emitter structure, which has a maximum size of 36 mm^2 in this thesis, is not taken into account here. The consideration of the centered opening would lead to a slight reduction of the total value for C_{c-g} since the relative permittivity is smaller for vacuum than for the PTFE sheet. The resistance of the PTFE foil is about $R_{c-g} = \rho_{el} \cdot \frac{d}{A} \approx 5 \cdot 10^{14}\,\Omega$ with the electrical resistivity of ρ_{el}(PTFE) = 10^{18} Ω·cm [131]. The resistance of the grid-anode stack is assumed to be even larger because there are basically no charge carriers to conduct the current in vacuum and thus, no considerable leakage current is expected. Furthermore, the capacitance of the parallel-plate stack is known to have no considerable influence on the DC emission current of interest [143]. Note, the waiting period between voltage step and current measurement (waiting period #2, subsection 3.2.3) is contained in the LabVIEW program to exclude the AC signal passing through the capacitor structures when the applied voltage is changed [96].

However, additional resistances in series to the FE current path may originate from cable and contact resistances or the intrinsic resistance of the emitter. On the one hand, the series resistances are associated with non-linearity in the FN plot at high electric fields [52, 144]. On the other hand, the additional resistance in the current path can lead to a distortion of the whole *I*-*V* curve as shown in Figure 3.14 (b) (plotted as gray dots). Therefore, the offset and slope—derived from the low voltage region before onset of FE—were always subtracted from the raw FE data prior to further analysis with the intention to remove the part of the measured current that does not originate from the FE process itself. The general assumption is that the offset is introduced by the DAQ method, namely by the transimpedance amplifier or by the picoammeter, and the slope is caused by the total resistance in the path of the measured current [96]. From the reciprocal slope of the linear fit in Figure 3.14 (b), a total resistance of $R_{\mathrm{total}} = 2.9 \cdot 10^{15}\ \Omega$ was calculated for the FE assembly. The derived resistance is 5.8 times larger than the previously estimated value for the cathode-grid gap $R_{\mathrm{c-g}}$, which may be caused by a combination of contact resistance in the FE assembly and series resistance of the cables.

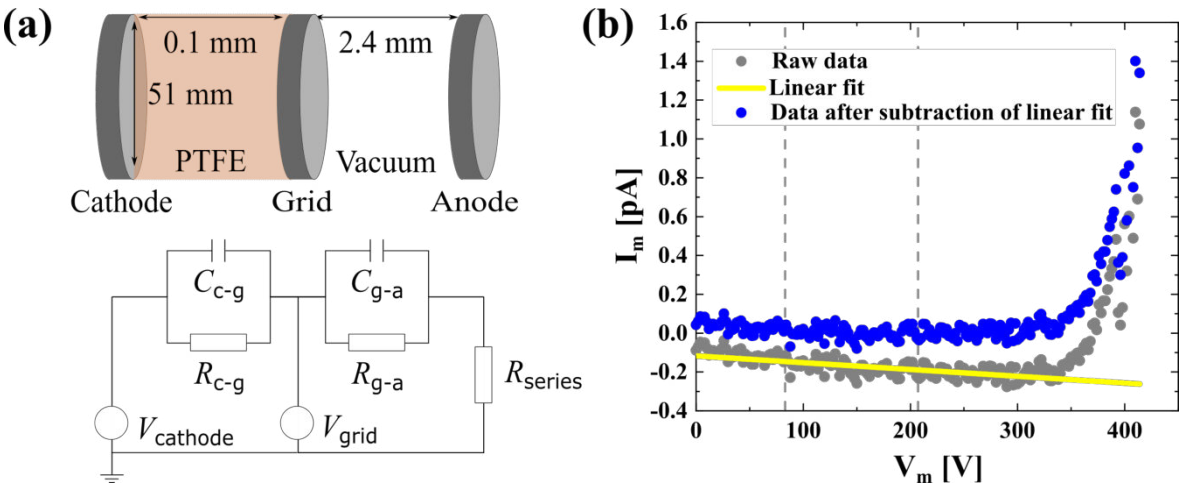

Figure 3.14: (a) The replacement circuit of the FE assembly—consisting of cathode, grid and anode—is shown, which is freely based on [142]. The three elements consist of conductive plates with lateral dimensions much larger than their inter-electrode spacing and resemble two capacitor structures in series ($C_{\mathrm{c-g}}$, $C_{\mathrm{g-a}}$). Additionally, resistances parallel to the path of the electron current ($R_{\mathrm{c-g}}$, $R_{\mathrm{g-a}}$) as well as in series (R_{series}) may exist [52]. **(b)** A FE measurement from a ZnO NW sample is used to exemplify the subtraction of offset and slope that are unintentionally introduced by resistances in the FE current path. First, a linear function (yellow line) is fitted to the raw data (gray dots) in the range of 20–50 % of the total number of applied voltage values (marked by vertical dashed gray lines). Second, the linear function is subtracted from the complete data set and the obtained, corrected *I*-*V* curve (blue dots) is subsequently used for further data analysis. In the present case, the linear function was determined to be: $I_{\mathrm{m}} = -0.117\,[\mathrm{pA}] - 0.00035 \cdot V_{\mathrm{m}}\,[\mathrm{pA/V}]$.

3.4 Setup Calibration and Data Analysis

To conclude this chapter, an array of randomly ordered ZnO NWs on p-doped Si bulk substrate was used as calibration probe for the three optimized FE setups with a PTFE spacer of 100 µm thickness. Four subsequent measurements were performed under the optimized conditions presented in section 3.2 in each FE setup, which are shown in Figure 3.15 (a). For the ISO and the CF setup, the amplifier and for the Voyager setup, the picoammeter were used to acquire the FE data. Furthermore, the general characterization conditions given in Table 3.1 were applied. The sample was first measured in the CF setup, subsequently, in the Voyager and finally in the ISO setup. The FE data was analyzed using MATLAB® (MathWorks®) and the measurements were plotted with OriginPro® (OriginLab® Corporation).

Clearly, the first measurement in each setup (depicted as empty circles) has a larger onset field compared to subsequent measurements. The onset field of the initial measurement in the first setup (CF setup, red empty circles) shows a deviation of 3.62 V/µm from the mean onset field of the three subsequent measurements (red filled circles). Yet, this deviation between first and subsequent measurements reduces to 0.59 V/µm and to 0.35 V/µm in the Voyager (plotted in green) and the ISO setup (plotted in blue), respectively. The magnitude of onset

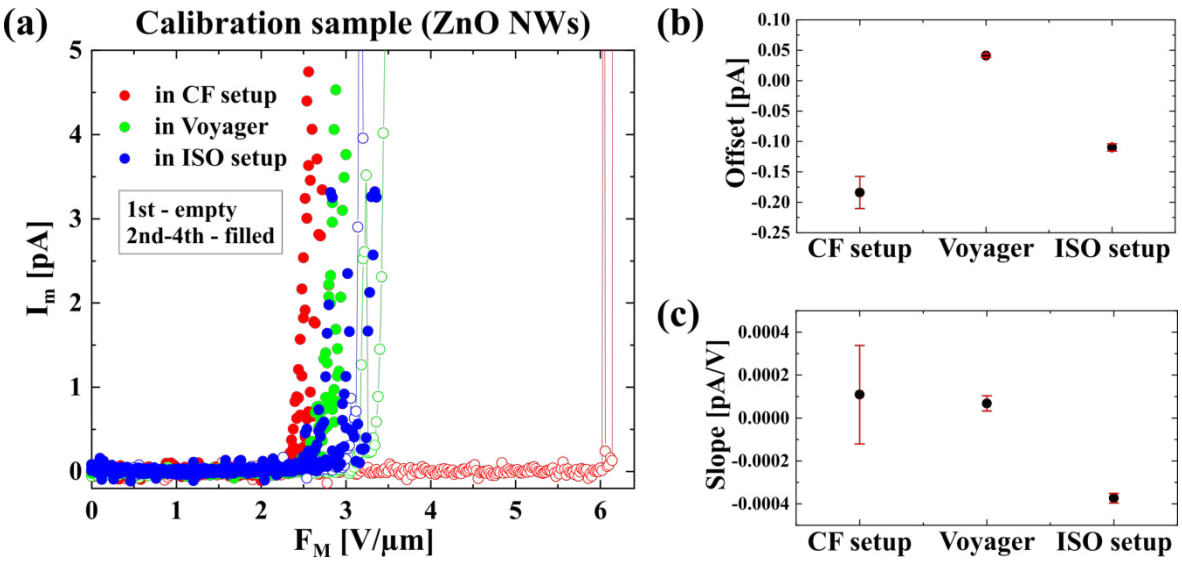

Figure 3.15: (a) The measured current from the calibration probe is displayed as a function of the macroscopic electric field. The FE sample was measured in each setup four times, utilizing the same 100 µm laser cut and metallized PTFE sheet as well as the same 59 lpc grid. The sample was first measured in the CF setup (red), than in the Voyager (green) and finally in the ISO setup (blue). The respective initial measurement is emphasized by the empty circles. For each of the FE measurement setups, the mean values **(b)** of the offset and **(c)** of the slope are shown that were derived from the raw FE data for subtraction prior to further data analysis (see Figure 3.14). The extracted values are arranged from low to high base pressure FE setup from left to right.

field shift seems to scale with the exposure time of the sample to ambient conditions, as the measurement in the CF setup (red) was carried out after prolonged storage of the sample in air. However, for each transfer between FE setups, the sample was exposed to air for less than one hour.

Since ZnO NWs have a huge surface area and are known for their high sensitivity to ad-atom attachment—making them attractive candidates for gas sensing applications [66]—different amounts of adsorbed species are assumed to explain the observed variation of the magnitude of onset field shift. As no considerable onset shift is observed among the subsequent measurements in each FE setup, it is supposed that ad-layers desorb during the initial FE scan, which is promoted by the strong local electric field [25]. The adsorbates may alter the electronic properties of the surface region for the initial FE acquisition, which possibly affects the apparent work function of the emitter material. Therefore, values for the apparent work function of the adsorbate covered material were derived by comparison of linearized FE data in the FN plot before (1st) and after ad-layer desorption (2nd–4th measurement) [25]. Assuming a work function value of 5.3 eV for $\phi_{\mathrm{cl}} = \phi_{\mathrm{ZnO}}$ [46], and with S_{ad} and S_{cl} being the slope extracted from the FN plot of the first measurement and the mean slope determined from the second to the fourth measurement, the following apparent work function values were derived with equation 2.52: ϕ_{ad}(Voyager) = 4.7 eV and ϕ_{ad}(ISO setup) = 2.7 eV. Note, the severely limited number of data points above the $10\,\sigma$ threshold for the initial measurement in the CF setup prevents the determination of a value for ϕ_{ad}. The apparent work function values obtained from the FE measurements in the two others setups are lower than supposed for the "clean" emitter surface. However, the onset fields are larger for both initial measurements, which is contrary to the theoretical expectation that a lower work function value facilitates electron emission (see Figure 2.1). As already mentioned in section 2.5, the herein used method to determine the impact of adsorbates on FE is only a rough estimation because of the probable complexity of the ad-layer constitution [25]. Possibly, the adsorbates shield the surface of the ZnO NWs from the applied electric field, which causes the observed onset field increase for the ad-layer covered emitters [1]. As a consequence, the initial FE measurement after mounting the sample in vacuum will be excluded from further data analysis in the next chapters.

The mean onset fields of the second to the fourth measurement in the different setups were determined to be 2.4 V/µm ± 2.5 % in the CF setup ($1{\cdot}10^{-7}$ mbar), 2.6 V/µm ± 2.3 % in the Voyager setup ($5{\cdot}10^{-7}$ mbar), and 2.7 V/µm ± 6.0 % in the ISO setup ($2{\cdot}10^{-6}$ mbar). Note, the FE data analysis is always carried out for each *I*-*V* curve separately to calculate the mean and standard deviation for a group of subsequent measurements. The onset voltage variation is smaller than 2.5 % for measurements in the setups with pressures below 10^{-6} mbar, but the deviation for subsequent acquisitions is notably larger in the ISO setup. Since the same

DAQ method (transimpedance amplifier) was used in CF and ISO setup, the higher system pressure is most likely the reason for the observed current fluctuations in the ISO setup. More gaseous residues are expected in the vacuum chamber of the ISO setup, which can interact with the field emitter's surface during the FE measurements and modify the cathode's shape by sputtering with residual gas ions. The increased occurrence of local modifications of the cathode's constitution is consequently reflected by stronger variations of the emission current in the ISO setup than in the other FE setups [2, 25]. Comparing the onset fields of the ZnO NWs in all three setups, a mean value of 2.6 V/µm was found under exclusion of each of the initial measurements. Besides the impact of adsorption/desorption processes, the variation around the mean onset field can be caused by FE-induced surface modifications, such as emitter self-heating, thermally activated surface diffusion and the corresponding local electronic and structural changes of the cathode [1]. In conclusion, however, the mounting procedure and the measurements under optimized conditions showed to be highly reproducible for all three setups.

As announced in the previous section, the setup-dependent offset and slope were subtracted from the data for convenient comparison of the *I*-*V* curves and prior to extraction of onset values as well as before further FE data analysis. The mean values of offset and slope were extracted from the raw FE data according to the description given in Figure 3.14 and are displayed in Figure 3.15 (b) and (c) for each of the FE setups. Since the same FE assembly and sample were used for all the measurements, variations of offset and slope are not associated with resistances in the FE assembly itself or with the intrinsic resistance of the cathode. Rather, the DAQ methods and the different base pressures seem to generate the observed deviations. The offset of the *I*-*V* curve changes from a mean value of -0.18 pA in the CF setup to -0.11 pA in the ISO setup, both measured with the amplifier. However, for the measurement with the picoammeter in the Voyager, a much smaller positive offset of 0.04 pA was derived. The offset for the amplifier measurement can easily be adjusted with the amplifier's built-in potentiometer. Therefore, the offset is supposed to be mainly determined by the measurement device type [145]. The slopes of the raw FE data for CF setup and for Voyager were determined to be about $1.1 \cdot 10^{-4}$ pA/V and $0.7 \cdot 10^{-4}$ pA/V, respectively, and $-3.7 \cdot 10^{-4}$ pA/V for the measurement in the ISO setup. Since CF and ISO setup used the same current amplifier for the FE measurements, the different slope values may be attributed to the higher base pressure in the ISO setup. Presumably, the observation can be associated with the accumulation of charges in the FE assembly formed by ionized residual gas molecules, which modify the resistance of the current path. The impact of base pressure on the *I*-*V* curves was already studied in the CF setup (see Figure 3.8) and is in good agreement with the herein observed variations.

On a first glance, simple subtraction of the linear fit from the raw data may be an oversimplified approach to treat the FE data. The correction has possibly an effect on the intercept C_{FN} and slope S_{FN} extracted from the linearized experimental data in the FN plot and therefore, also on the subsequently derived effective values γ_{eff}^{FN} and A_{eff}^{FN}. Exemplary, the effective FEFs were derived for the second to the fourth measurement in the Voyager setup following the description in section 2.4. For the raw and the corrected data, values of γ_{eff}^{FN}(raw) = 1653 ± 337 and of γ_{eff}^{FN}(corrected) = 1473 ± 277 were derived, respectively. Note, the difference of the values is only $\Delta\gamma_{eff}^{FN}$ = 180, which is smaller than the variations of the effective FEFs for subsequent measurements that are given by their standard deviations. Thus, the change by the line subtraction is within the error boundaries of subsequent measurements in the same setup and has no significant influence on the analysis of the experimental FE data.

In addition, the subtraction of the linear function from the raw data prior to data analysis is necessary for a consistent data comparison from different setups because they introduce various offsets and slopes to the *I*-*V* curves (see Figure 3.15 (b) and (c)). Especially for the raw data having a negative offset when measured with the current amplifier, the data has to be corrected before linearization because of the natural logarithm on the y-axis of the FN plot. Moreover, it is usually not possible to identify the magnitude of the separate contributions to the overall resistance and the series resistance typically does not scale with the electrode plate distance. Therefore, the analysis of the *I*-*V* data is advised in literature rather than the prior conversion to the macroscopic electric field [143]. Herein, the conversion to the macroscopic field is done for comparison of cathodes measured with different emitter-grid distances after the extraction of onset values and after derivation of effective values from the FN plot.

In conclusion, the FE measurements from the identical sample showed to be reproducible within the boundaries of unavoidable, FE-initiated cathode modifications. In the present section, the FE measurements were terminated below an emission current of 10 pA because only the onset values were of interest for comparison of the three FE setups. To detect the maximum possible emission current from the field emitters in the following chapters, three initial FE measurements are stopped at an emission current of 5 pA. Then, the maximum allowed emission current that functions as termination condition for the FE acquisition, is gradually increased for every subsequent measurement until the repeated occurrence of electrical breakdown prevents a further raise. By this procedure, adsorbates that may still remain on the emitter's surface—but do not lead to a notable change of FE properties—can desorb in a controlled manner, which was found to lower the risk for electrical breakdown considerably and corresponds to emitter surface cleaning induced by an electric field in vacuum [1].

4 ZnO Emitters - Sputter Shadow Mask

Flexible nanomembranes (NMs) used as FE electron sources have the potential to be employed in displacement sensing devices as described in chapter 1. However, FE from plain NMs is unlikely within a feasible range of applied voltages because the field enhancement effect generated by the natural surface roughness of the membrane material is negligible. As exemplified in section 3.1 of the previous chapter, an applied voltage of more than 100 kV across an emitter-grid distance of 100 µm would be needed to allow for FE from a flat metal emitter, which is not possible in our FE setups.

Herein, ZnO FEAs were directly grown on NMs for geometrical enhancement of the local electric field. Basically, there are two approaches for the CVD of ZnO NWs, namely the vapor-solid (VS) and the vapor-liquid-solid (VLS) approach [64]. In contrast to the VLS method, no catalyst is needed for the VS growth, which is beneficial to the application of fragile membranes as substrates, since additional processing steps for catalyst generation—risking NM destruction—can be omitted. However, the aspect ratio of the VS grown ZnO nanowhiskers is usually much lower than for structures generated by the VLS process. Hence, the VS growth impedes the production of efficient field emitters that would provide emission currents as large as possible at minimized applied electric fields [22]. Figure 4.1 presents the morphology and the FE properties of ZnO nanowhiskers grown without any catalyst in our previous work [23] and constitutes the starting point for the development of techniques for the catalyst-assisted ZnO NW growth compatible with NM substrates.

In the present chapter, a sputter shadow mask is used to affect the constitution of a thin gold film during deposition on commercially bought Si NMs as well as on in-house fabricated SiN NMs. In the following, the synthesis steps for the field emitter samples are explained and then, the morphology analysis of the ZnO structures as well as the investigation of their FE properties are presented separately for the two substrate types.

4.1 Sample Fabrication

Herein, a fine metal mesh was placed in a 3D-printed holder posing as shadow mask for deposition of gold on the surface of NMs prior to the growth of ZnO NWs. The usage of this mask permits the deposition of a gold layer that allows for the formation of catalyst particles

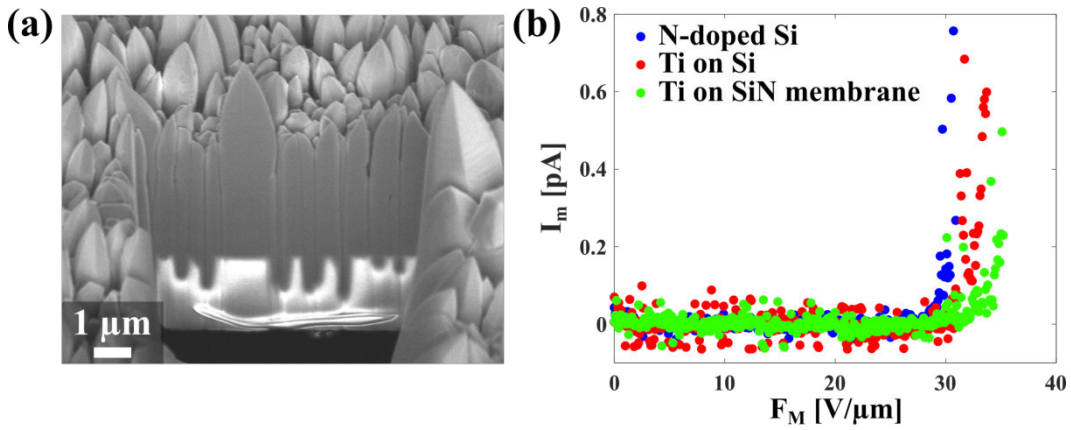

Figure 4.1: (a) SEM images of the ZnO nanowhiskers grown with the VS mechanism (catalyst-free) on a 1500 nm thick, titanium (Ti) coated SiN membrane. The arrays of densely packed, crystalline nanowhiskers exhibit a maximum aspect ratio of about 16. Note, thinner membrane substrates were destroyed during the growth process possibly by stress that was induced by the ZnO structures or by the elevated temperatures (580 °C) in combination with the long growth duration (20 h). **(b)** FE measurements of VS grown ZnO structures on n-doped Si (plotted in blue), on Ti coated Si (red) and on a 1500 nm thick, Ti coated SiN membrane (green) are shown. The macroscopic onset field varies in a range of 30 V/µm to 35 V/µm for the examined FE samples. Figure adapted from [23].

by dewetting—known as agglomeration of thin solid films by surface diffusion well below the material's melting point, driven by surface energy minimization [146]—which is induced by the elevated temperatures during the ZnO growth process. The 3D-printed holder avoids the physical contact of the metal grid with the NM and thereby, prevents the damage of the substrate. Firstly, the substrate preparation, which involves also the NM fabrication, secondly, the catalyst deposition and thirdly, the ZnO growth process are presented in the following.

4.1.1 Substrate Preparation

On the one hand, commercial Si membranes made from n-doped SOI wafers by microfab Service GmbH were utilized as substrates for the ZnO growth. Each 10x10 mm^2 sample chip incorporates four circular, freely suspended Si NMs, which have a diameter of 2 mm each and a thickness of about 149 nm according to the manufacturer. The mean sheet resistance of (61 $\pm$ 23) Ω/sq was obtained by the measurement of four SOI samples with a four-point probe station in van der Pauw geometry [124]. The measured sheet resistance is higher than the value provided by the manufacturer of 36.5 Ω/sq, which may be explained by oxidation of the Si surface caused by the storage in ambient conditions for several years.

On the other hand, SiN membranes were fabricated in-house from commercially bought (100) Si wafers coated with SiN on both sides by low-pressure chemical vapor deposition (LPCVD). The substrate height of about 300 µm was determined with a caliper gauge and the

SiN thickness and refractive index of about 100 nm and of 2.231, respectively, were measured with a spectroscopic ellipsometer (SENpro from Sentech Instruments GmbH). Figure 4.2 shows images of the two NM types and Table 4.1 summarizes characteristics of the substrates.

The membrane fabrication from the SiN covered Si wafers involves three main steps. First, the backside of a 10x10 mm^2 sample chip is masked by photolithographic techniques. The positive photoresist Microposit™ S1813™ G2 is spin coated onto the sample chip for 60 s with a spin speed of 4000 rpm and an acceleration of 10000 rpm/s. Prior to deposition of

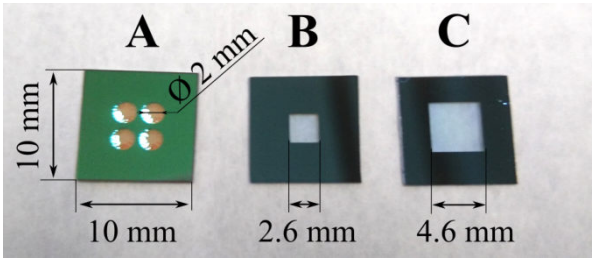

Figure 4.2: Photographs of the two different substrate types, namely Si and SiN NMs. The circular Si membranes in the SOI sample (**A**) are bending upwards. The membrane bulging as well as the buckling at the edges of the NMs may be caused by compressive stress that is typically introduced at the interface between the top Si film and the buried oxide layer of the SOI sample [147]. The square, in-house prepared SiN NM samples (**B** and **C**) are shown for two different membrane sizes and appear to be flat, which correlates well with the tensile tendency of the residual stress in LPCVD SiN [148].

	Si NM	**SiN NM**
NM properties		
Shape	Circular	Square
Lateral size [mm]	2 (diameter)	2.6 / 4.6
Thickness [nm]	149	100
Sheet resistance [Ω/sq]	61 ± 23	$>10^{19}$
Substrate properties		
Dimensions [mm^2]	10x10	10x10
Height [mm]	0.4	0.3

Table 4.1: Summary of the characteristics for the two different NM types that were used as substrates. The diameters of the circular Si NMs as well as the side lengths of the square SiN NMs were determined from microscopic images. The thickness of the Si NMs was given by the manufacturer and for the SiN NMs it was measured by ellipsometry. The sheet resistance of the Si NMs was measured with a four-point probe station. For the insulating LPCVD SiN, the sheet resistance was determined from the resistivity of SiN ($>10^{14}$ Ω·cm [140]) divided by the membrane's thickness (10^{-5} cm).

the photoresist mask, the sample is cleaned by rinsing it in acetone, isopropanol, and finally drying it with gaseous nitrogen. After spin coating, the sample is baked for 60 s at 115 °C on a hot plate. Subsequently, a square window of 3 mm or of 5 mm side length is exposed for 5 s to channel 2 (23.0 mW/cm^2, wavelength 405 nm) of the MJB4 mask aligner (from SÜSS MicroTec SE) and then, the sample is rinsed for 55 s in Microposit™ MF-319 Developer to remove the photoresist from the exposed area. The photoresist mask is finalized by a hard bake step for 90 s at 90 °C on a hot plate.

Second, the SiN layer on the backside of the sample is removed from the area that is not covered by the photoresist mask by inductively coupled plasma-reactive ion etching (ICP-RIE) using a plasma etcher system (SI500 from Sentech Instruments GmbH). Prior to the dry etch step, photoresist residues are carefully removed from the front side, namely the NM side, with an acetone-soaked cotton bud to allow for sufficient thermal contact between the sample and the aluminum carrier in the ICP-RIE. Else, excessive heat accumulation through ion bombardment in the plasma etcher causes a notable damage of the photoresist mask. The LPCVD SiN is etched with a rate of (439 $\pm$ 24) nm/min for 40 s using the following recipe in the ICP-RIE: 50 sccm sulphur hexafluoride (SF_6), 5 sccm oxygen (O_2), 2 Pa pressure in the reaction chamber, 23 °C electrode temperature, 400 W ICP power and 50 W radio frequency power (see summary in section A.2). Intentionally, it is etched deeper into the sample than the SiN thickness to guarantee access to the Si underneath for the subsequent wet chemical etching step. Note, for uniform dry etching, Si dummy pieces are assembled as frame around the sample because otherwise the rim of the probe is etched faster than its center, which is presumably caused by an inhomogeneous plasma distribution at the edges of the substrate.

Third, by etching with aqueous potassium hydroxide solution (KOH, 30 %, 80 °C) the Si is anisotropically removed until the SiN layer on the front side of the sample chip, namely the NM, is reached. The sample is fixated in a PTFE holder—which was tailor-made for the respective substrate size of 10x10 mm^2 and can incorporate up to five samples—and is etched for 4.5 h to ensure complete removal of the Si from the SiN membrane. Etch rates of about 77 µm/h for (100) Si and of (1.6 $\pm$ 0.8) nm/h for the LPCVD SiN under constant stirring of the KOH solution, which promotes the removal of reaction products from the sample, were observed. The etch rate of Si and of LPCVD SiN in 30 % KOH at 80 °C were determined from the time it takes to etch completely through the substrate and with the help of ellipsometry, respectively [149]. The side length of the resulting SiN membrane is about 0.42 mm smaller than the initial opening defined in the backside of the sample because of the different etch rates for the crystal planes in Si, which leads to generation of an inverse pyramidal shape with an inclination angle of 54.74 ° [140]. For simplicity, the smaller and the larger SiN NM sizes (see B and C in Figure 4.2) are in the following referred to as 3x3 mm^2 and as 5x5 mm^2, respectively. After removal of the sample from the PTFE holder, the chemical reaction is

terminated in water. Subsequently, the sample is rinsed in a first beaker with ultra pure water (taken from the Milli-Q® Integral 5 device) and afterwards, it is soaked for at least 12 h in a second beaker with ultra pure water to allow for the dissolution of KOH residues. Finally, the sample is rinsed in methanol and dried on a hot plate at 300 °C to accelerate the solvent evaporation and prevent the formation of residues on the membrane's surface. Note, the sample is hold with tweezers in a tilted manner above the hot plate to prevent the gathering of solvent and thereby, to avoid generation of residues on the flexible membrane part of the substrate. The described cleaning sequence is referred to as "membrane cleaning recipe" and is summarized in section A.2 in the appendix.

4.1.2 Catalyst Deposition

In our previous work, it was found that the ZnO growth process yields only a small number of nanowhiskers on a thick gold (Au) film, whereas the density of NWs with large aspect ratio considerably increases at the edges of the gold film. Figure 4.3 shows the differently pre-treated areas on a n-doped Si piece after ZnO growth. The sample was coated with gold (sputter coater K550X from Emitech) for 60 s and, unless otherwise stated, with a current of 20 mA, which yields a deposition rate of (19.5 ± 0.9) nm/min. A 2x2 mm^2 square in the center of the sample was covered by a Kapton® film to prevent gold deposition in this area. The enhanced NW aspect ratio was noted at the transition region from the gold covered area to the uncoated Si substrate (Figure 4.3 C). On the one hand, the film thickness presumably decreases gradually at the gold-silicon interface because of a certain degree of step coverage that is typical for deposition by sputtering [140]. Thus, the formation of particles that can act as catalytic sites for NW growth may be promoted in the transition area, since the average particle diameter and dewetting temperature are known to decrease simultaneously with the film thickness [146]. On the other hand, particle agglomeration occurs predominantly at

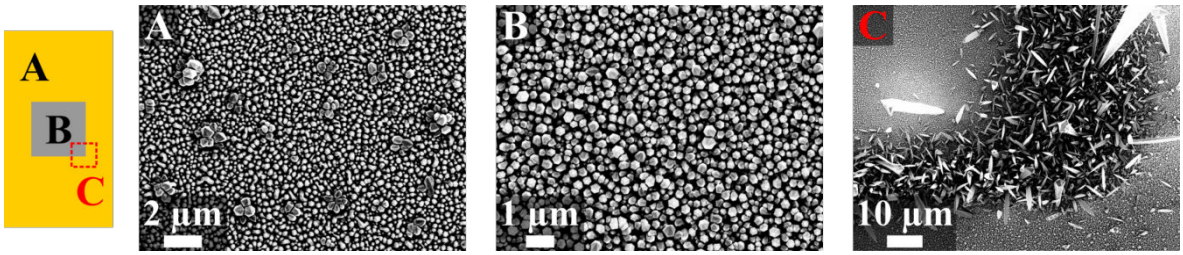

Figure 4.3: Illustration of a n-doped Si substrate (sketched in gray) with a gold layer (yellow) that was deposited by sputtering. A 2x2 mm^2 area in the sample's center was covered with a polymeric film during deposition. On the Au layer (**A**) as well as on the n-doped Si (**B**), nanowhiskers with low aspect ratio were grown. However, considerably larger NWs were generated in the transition region between Au film and n-doped Si substrate (**C**). The SEM images were taken by Carina Hedrich (supervised hourly student) with the Supra 55 by Zeiss.

existing holes or at film edges [146]. However, simple coverage with a polymeric film is not directly applicable to NMs, as the deliberate edge formation is limited to a small area of the total surface of the substrate and physical contact of the mask with the NM must be avoided in any case to prevent its destruction.

Instead, a sputter shadow mask was developed that consists of a 3D-printed holder (printed with the Ultimaker 2, Extended+) and a grid (59 lpc nickel mesh from Precision Eforming, Table 3.3), which is fixated with silver conductive paste to the holder as shown in Figure 4.4. For catalyst deposition, the shadow mask was placed on top of the substrate before the sample was sputtered with gold for 60 s. After deposition, the mask was carefully lifted up from the substrate and a slight color change of the grid covered part could be observed. Subsequently, the sample was used for the ZnO growth with the catalyst film as deposited. The 3D-printed holder itself can be reused, but the metal mesh has to be exchanged as the additional gold layer presumably widens the grid lines, which would cause a different sputtering pattern for subsequent depositions. The apparent gold film thickness was found to be reduced to 5.9 nm with application of the sputter shadow mask compared to the film thickness of 17.8 nm without the shielding (measured by ellipsometry on Si). Besides the film thickness reduction, edges in the gold film may possibly be generated by the shielding through the grid wires that can act as additional sites for particle agglomeration. The usage of a copper mesh as mask for sputter coating was reported elsewhere before, but with the grid mask in contact with the bulk substrate, which was merely used to define the catalyst deposition area rather than for the modification of the film constitution [150, 151]. Moreover, the deposition of gold catalyst sites through mask patterns, such as metal nanotube membranes [152], nanopores formed in anodized aluminum oxide [153] and monolayers of polystyrene spheres [154], can be found in literature. In contrast to our sputter shadow mask approach, none of these methods is directly applicable to the free-standing membranes because the masks would be in contact with the substrate's surface.

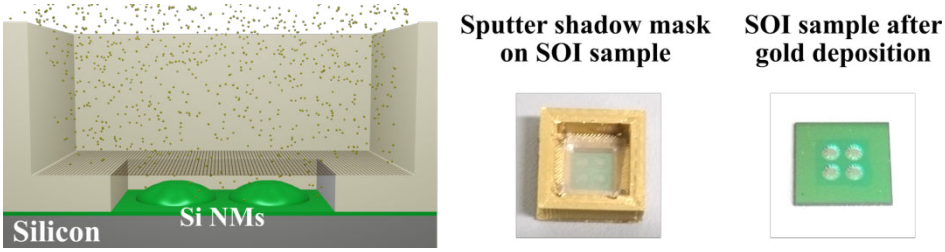

Figure 4.4: The grid is located about 1 mm above the SOI substrate, as indicated in the schematic cross section picture through the sputter shadow mask on the left side. In the center, a photograph of the 3D-printed holder aligned on a substrate is shown and on the right side, the SOI sample is displayed after sputter deposition. The color of the central, 6x6 mm^2 area has slightly changed compared to the sample's frame that was shielded by the holder during the deposition process.

4.1.3 ZnO Growth Process

Vapor phase transport is a common method for the growth of ZnO NWs. The gaseous precursors zinc (Zn) and oxygen (O_2) are guided by a transport gas, typically an inert gas such as argon (Ar) or nitrogen (N_2), towards the substrate. ZnO structures are formed by condensation and oxidation of the precursor substances on the substrate's surface, which is controlled by the temperature gradient in the reaction chamber. For the VLS type CVD mechanism, metal nanoparticles are distributed over the substrate's surface prior to the ZnO growth. The precursor material is absorbed at the catalyst particle surface, diffuses into the gold dot, and causes melting of the alloy below the melting points of its components by an eutectic reaction. When the precursor concentration inside the metal particle reaches supersaturation, precipitation of ZnO occurs at the particle-substrate interface, which leads to the growth of the ZnO structure. Hence, dimensions and positions of ZnO structures can be controlled to some degree by the initial size and distribution of the catalyst particles [22, 64, 155]. The CVD growth usually allows for lower process temperatures than required for the ZnO NW deposition by thermal evaporation and additionally, yields higher purity ZnO structures compared to the solution based growth methods. However, the growth temperature can be reduced further by employing a metal organic precursor as zinc source for the CVD process. A typical precursor for the MOCVD of ZnO is zinc acetylacetonate ($Zn(acac)_2$), which is a white powder with a melting temperature that varies around 137 °C in dependence on the precursor's degree of hydration [24].

Herein, the same process parameters were used for the catalyst covered substrates as optimized for the VS growth in the study by Hedrich *et al.* [23]. Zinc acetylacetonate hydrate powder (from Sigma-Aldrich) and oxygen were used as precursors for the growth process, which was performed in a horizontal three-zone tube furnace (OTF-1200X-III-UL, MTI corporation). The growth oven is shown schematically in Figure 4.5 (a). In preparation of the ZnO growth process, 2.4 g of the precursor powder were evenly distributed in a ceramic boat, which was subsequently placed in the middle of the first heating zone. The substrate was positioned in the front-third of a second ceramic boat and a thin SiN/Si hard mask was placed on top of the sample to limit the ZnO deposition to the desired area. Note, further explanation for the tailor-made hard mask is given below. After the substrate loaded ceramic boat has been placed in the beginning of the third heating zone, the quartz tube was evacuated below a pressure of $1.8{\cdot}10^{-1}$ mbar before initialization of the growth process. Constant argon (100 sccm, purity 5.0) and oxygen gas flows (83 sccm, purity 5.0) were introduced 1 h after start of the heating process, which yielded a pressure of about (5.7 ± 1.1) mbar in the quartz tube during the ZnO deposition. The mean and standard deviation of the chamber pressure were determined from the values of 84 deposition processes. Figure 4.5 (b) shows the individual temperature profiles of the ZnO growth process for each zone of the tube furnace. In a

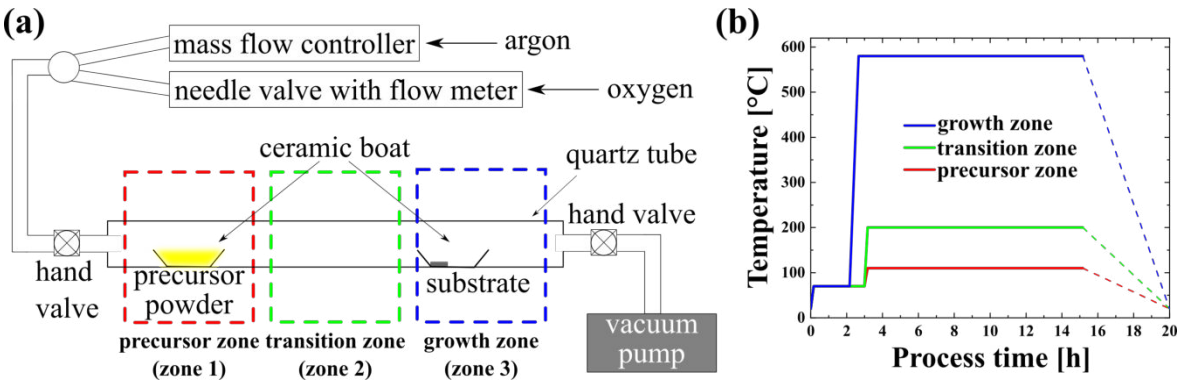

Figure 4.5: (a) A sketch of the three-zone tube furnace is shown that was used for the ZnO growth. **(b)** The temperature profiles of the first (red), second (green) and third heating zone (blue)—namely the precursor, transition and growth zone—are presented for the standard growth process in dependence on the elapsed time in hours. The cooling time is indicated by dashed lines, since the profile of the natural cooling depends on the ambient temperature. Figure freely adapted from [23].

first step, all three zones were heated to 70 °C and the temperature was held constant for 2 h to promote desorption of residues from the chamber walls and from the substrate. Second, the temperature in the third zone (growth zone) was increased to 580 °C (growth temperature) in a time period of 30 min, while the temperatures in the first and second heating zones were kept at 70 °C. Third, the sublimation of the zinc containing precursor was initialized by rising the temperature within 10 min to 110 °C in the first zone (precursor zone) and simultaneously, the temperature in the second zone (transition zone) was set to 200 °C. Typically, the growth process was executed for 12 h, followed by natural cool-down of the system. Unless otherwise stated, the "standard process" of the ZnO growth refers to the above described process conditions and is summarized in section A.2 in the appendix.

For intentional restriction of the deposition area, a tailor-made SiN/Si hard mask was developed that can withstand the elevated growth temperatures and is thin enough to allow for undisturbed precursor gas flow towards the substrate's surface. Additionally, the mask is easily removable from the sample after ZnO deposition and it is reusable. Common mask techniques, such as photoresists or polymeric foils do not fulfill those requirements because typically they have lower melting temperatures than required for CVD and may outgas when heated in vacuum, which can lead to unwanted chemical reactions in the tube furnace. Herein, the thin hard mask consists of a SiN layer on thinned Si substrate, which has a total thickness of about 100 µm. For fabrication, a 300 µm thick Si (100) wafer with 100 nm LPCVD SiN on both sides was initially cut into a square piece that has a lateral size about 1 mm larger on every side than the respective NM substrate to provide an overlap. Then, a square window was defined in the photoresist on the substrate's backside and subsequently, the SiN was re-

moved from the exposed area by dry etching according to the detailed description given in section 4.1.1. Note, the square opening in the center of the hard mask was chosen larger than the NM dimensions to avoid physical contact with the free-standing film. After the ICP-RIE step (see recipe in section A.2), the sample was cleaned from photoresist with the remover AR 300-70 (from Allresist GmbH) and then, the SiN layer on the front side of the substrate was removed completely by another dry etch step for 40 s. Afterwards, the Si was etched away from the exposed front side and simultaneously from the backside through the window in the SiN film by etching in aqueous KOH (30 %, 80°C) for a duration of 2.5 h. The chemical reaction was terminated in a water bath and subsequently, the hard mask was cleaned in ethanol and dried with gaseous nitrogen.

For the ZnO growth, the mask was placed on the substrate posing as frame for the membranes to spatially limit the deposition area to the center of the sample as shown in Figure 4.6. SEM images of the different areas on the SOI sample reveal that large ZnO NWs were only formed in the center of the substrate that was exposed by the SiN/Si hard mask (Figure 4.6 a). Further, the amount of ZnO deposit gradually decreases in the transition region from ex-

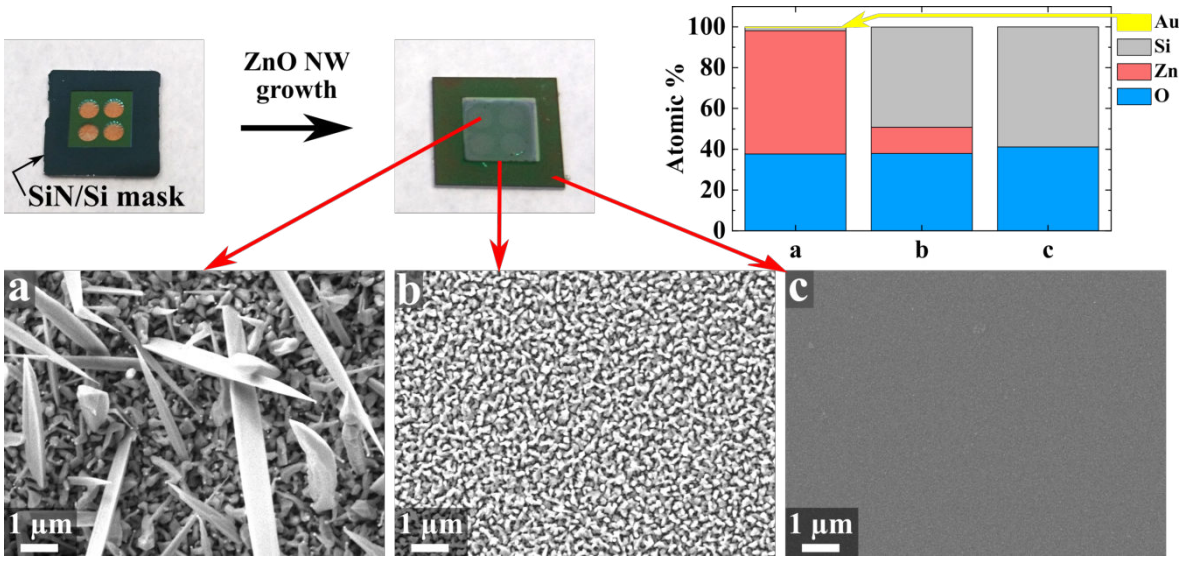

Figure 4.6: The top row on the left side shows a photograph of the tailor-made SiN/Si hard mask placed on a SOI sample before ZnO growth. Afterwards, a white film is observed in the area that was exposed by the hard mask. The SEM pictures in the bottom row display the three different zones on the sample after ZnO deposition, namely the NM area with large ZnO NWs (a), the transition region between exposed and covered area, which exhibits a film of low ZnO structures (b), and the frame around the NW array without visible deposit (c). The bar chart in the top row on the right side presents the results from the EDX spectra taken at the positions (a) to (c), which corroborate the observed ZnO distribution. Zinc, oxygen and silicon are detected only in zone (a) and (b), but no zinc is found in zone (c), which demonstrates that the SiN/Si hard mask effectively prevents the ZnO deposition in the intended area. The SEM images and EDX spectra (8 kV, 3 nA) were taken with the Crossbeam 550 by Zeiss.

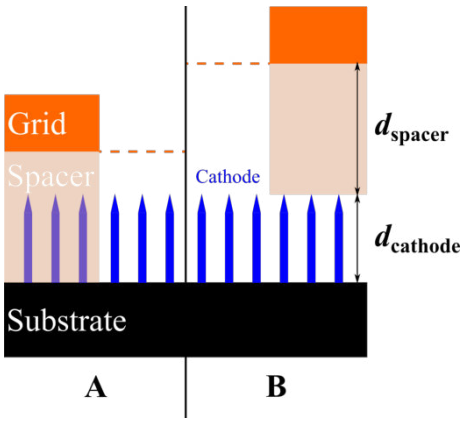

Figure 4.7: Illustration of the two extreme cases when ZnO NWs (sketched in blue) would be located at the edges of the substrate (black). Case (A) depicts the piercing of NWs through the polymeric spacer (light brown), which can lead to the decrease of its breakdown voltage. Case (B) shows the second extreme with the PTFE spacer laying on top of the NWs. The actual distance d_{spacer} between substrate and gird (orange) would be increased by the height of the NWs ($d_{cathode}$), which would falsify the conversion from applied voltage to the macroscopic electric field. In reality, the situation would be a mixture of both cases.

posed to shielded area (Figure 4.6 b) and no ZnO structures were formed beneath the SiN/Si frame (Figure 4.6 c). In addition, the observations are supported by the results from energy-dispersive X-ray spectroscopy (EDX). Note, during the growth process, ZnO structures were also formed on the surface of the SiN/Si hard mask. To avoid disturbance caused by the added thickness of the ZnO deposit for a subsequent growth process, the ZnO was removed after each growth process by placing the SiN/Si frame in 45 % KOH solution for 10 min at room temperature, followed by rinsing the sample in water, then in ethanol and finally, drying it with gaseous nitrogen.

The limitation of the deposition area to the center of the sample is needed for a reproducible sample assembly for FE measurements. When ZnO NWs are located at the edges of the sample, they would either pierce through the PTFE spacer or they would increase the cathode-grid distance unintentionally as illustrated in Figure 4.7. In the first case, the perforation of the insulating PTFE foil by NWs would lower the breakdown voltage of the FE assembly by reduction of the distance between emitter and control electrode. In the second case, the uncertain increase of the cathode-grid distance by the NW height in the spacer-substrate contact area would falsify the conversion from applied voltage to macroscopic electric field as well as would affect the determination of effective values from the FN plot (see section 2.4). In summary, the SiN/Si hard mask allows for the selective deposition of ZnO in a CVD process and effectively prevents the growth in the contact area between the PTFE spacer and the substrate.

Typically, a thinner gold film leads to generation of smaller catalyst particles by dewetting at the same temperature, which also facilitates the formation of NWs [146, 151]. Furthermore, the yield of ZnO NWs was reported to be enhanced for gold films thinner than 10 nm [156]. As already mentioned in the previous section, the apparent gold film thickness for a deposition duration of 60 s was reduced from 17.8 nm to 5.9 nm by application of the sputter shadow mask, presumably by deposition of material on the grid wires. For comparison of the effect of

gold film thickness on NW growth, substrates were sputter coated for 60 s with and without using the sputter shadow mask. The SEM images (a) and (b) in Figure 4.8 reveal that the density of large NWs is notably enhanced by application of the shadow mask for catalyst deposition. The minimum possible deposition time (about 22 s) of the utilized sputter coater (K550X from Emitech) yields a gold film thickness of 7.9 nm and is obtained by setting the deposition duration to zero. By application of the sputter shadow mask, the apparent film thickness was reduced to 1.8 nm. Note, for the standard ZnO growth process, it was chosen to use a sputter time of 60 s for the deposition through the shadow mask.

Additionally, the partial shielding of the substrate's surface by the grid wires may affect the constitution of the gold film. A unique pattern formed by deposition through the shadow mask, such as a periodically altered gold film thickness, could not be confirmed by profilometer measurements of the as-deposited gold film. However, an additional effect of the sputter shadow mask on the gold film constitution was verified indirectly: Since regular sputter coating of less than 7.9 nm was not possible, a 5 nm thin gold layer was deposited by PVD (e-beam evaporation) on a fully exposed substrate. Although, the PVD film was thinner than the one that was deposited through the sputter shadow mask for 60 s (5.9 nm), the NW density was obviously enhanced by the less time consuming sputter deposition through the metal grid, as revealed by comparison of the SEM images (a) and (c) in Figure 4.8. This observation suggests local thickness variations of the gold film deposited through the sputter shadow mask, which seems to facilitate the generation of gold particles that act as catalysts and thus, enhances the growth of large ZnO NWs.

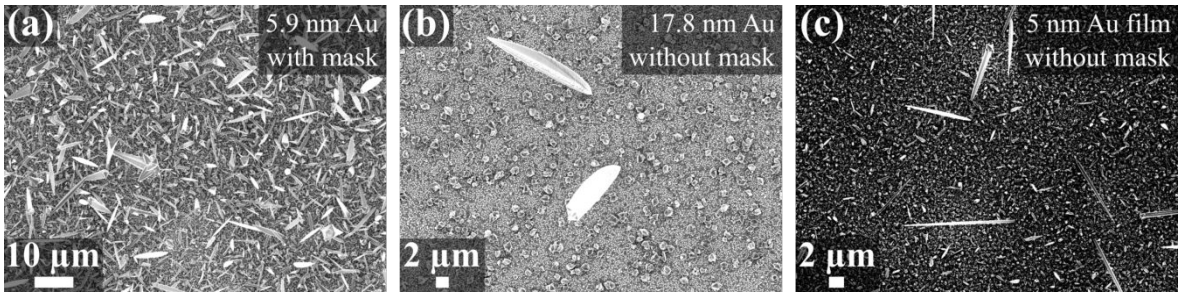

Figure 4.8: Investigation of the effect of the sputter shadow mask on the ZnO NW growth. **(a)** Top view of the ZnO NW array, which was generated with the gold film that was deposited for 60 s through the sputter shadow mask. **(b)** In contrast, only a few large NWs can be found on the entire substrate when the gold film was sputtered for the same deposition duration without using the shadow mask. **(c)** The density of large NWs grown on a 5 nm gold film (e-beam evaporation) appears to be lower in comparison to the NW density that was achieved by catalyst deposition through the sputter shadow mask. Unless otherwise stated, the thicknesses of the gold (Au) films were measured by ellipsometry on bulk silicon. The SEM images in (a) and (b) were taken with the Crossbeam 550 by Zeiss. The SEM image in (c) was taken by Carina Hedrich (supervised hourly student) with the Supra 55 by Zeiss.

4.2 Substrate Type A - Silicon Membranes

Herein, the structure and the FE properties of ZnO NWs grown on Si NMs with the help of the sputter shadow mask are investigated. In the first part, the morphology and FE characteristics are examined for ZnO emitters deposited by the previously explained standard growth process. In the second part, the effect of synthesis parameter modification on the ZnO NW dimensions as well as on the FE properties is studied.

4.2.1 Standard Growth Process - Morphology

For the standard ZnO growth process using the sputter shadow mask for catalyst deposition, an array of randomly ordered wires of different lengths and with various tip shapes was formed over the entire area exposed by the SiN/Si hard mask. Three groups of ZnO structures were identified on the SOI NMs from SEM images as shown in Figure 4.9. First, large

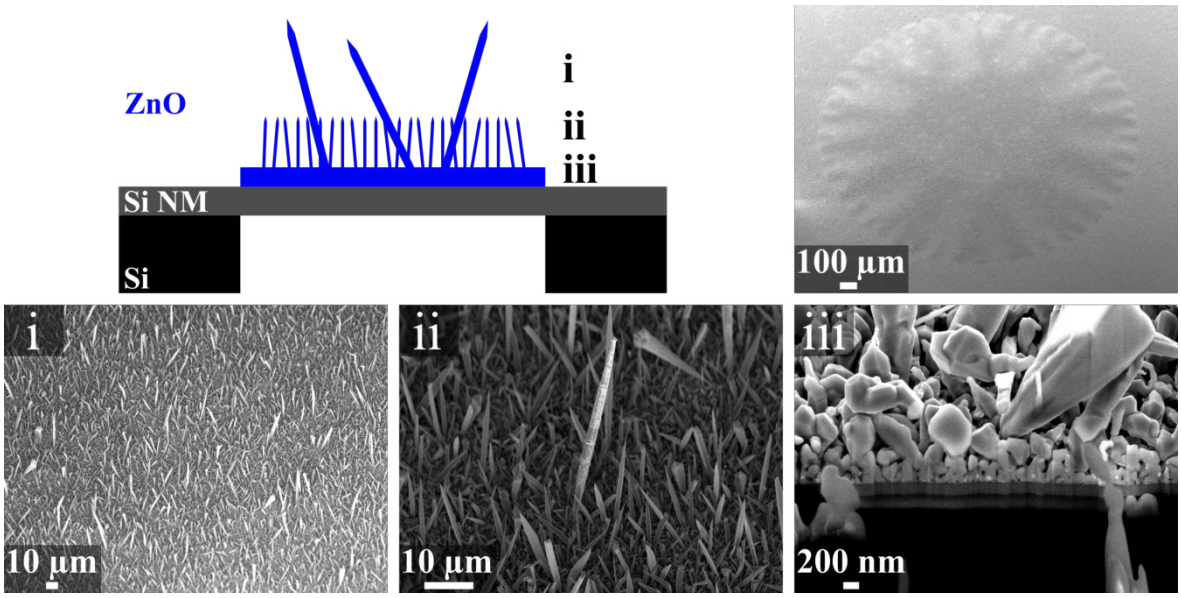

Figure 4.9: Types of ZnO structures grown on Si NMs with the standard ZnO growth process in combination with the sputter shadow mask used for catalyst deposition. The illustration in the top row displays the three kinds of ZnO structures (sketched in blue), namely large, sparsely distributed ZnO NWs (i), shorter ZnO needles with a higher density (ii) and a film of ZnO crystallites (iii). The respective SEM images are shown in the bottom row. The images for (i) present an overview of the ZnO NW arrays and number (ii) shows one large NW in the center surrounded by shorter ZnO needles. The cross section through the substrate in image (iii) reveals the layer of low ZnO crystallites on top of the free-standing membrane. After ZnO growth, the bulging pattern of the Si NM is still visible as shown in the SEM image in the top row. The SEM images were taken under a tilt angle of 54 ° with the Crossbeam 550 by Zeiss. The cross section through the NM was prepared by focused ion beam (FIB) milling (30 kV, 50 pA).

	ZnO NWs on Si NMs
Length (h) [µm]	58 ± 15
Diameter ($2r_{\text{base}}$) [µm]	2.4 ± 0.8
Tilt angle [°]	93 ± 20
Tip diameter ($2r_{\text{apex}}$) [µm]	0.187 ± 0.092
Tip inclination (θ_{apex}) [°]	18.3 ± 17.7
Aspect ratio ($h/(2r_{\text{apex}})$)	310 ± 233
Density [NWs/mm^2]	5963 ± 772

Table 4.2: Summary of ZnO NW dimensions grown on a Si NM. Note, only NWs that stand out from the array because of their height were analyzed (Figure 4.9 i), since they are expected to dominate the FE process [29]. The mean and standard deviation of the different parameters were obtained by measuring the dimensions of 20 separate NWs. The emitter density was determined by counting the number of ZnO NWs larger than 10 µm on six SEM images, which were taken at different locations on the NM with a constant magnification of 10^4.

NWs with different tilt angles and various tip shapes were noted, which are well separated from each other. Second, an array of shorter, needle shaped structures appeared with a higher density and third, a film of densely packed ZnO crystallites was found directly on the Si NM. For analysis of the emitters' morphology, the dimensions of 20 separate, large NWs at the center of one Si NM were determined from SEM images using ImageJ [157]. The results are summarized in Table 4.2 and explanatory notes on the measurement regime are given in section A.3.1 in the appendix. Note, only NWs with an outstanding height (Figure 4.9 i) were considered for the determination of emitter dimensions, as typically the largest NWs of an array dominate the FE process [29]. Additionally, only the NWs at the center of the NM were examined where the displacement of the flexible substrate by the electrostatic field may have the largest extent. Thus, the local electric field is possibly enhanced the most at the membrane's center and consequently, the measured emission current would be mainly determined by the ZnO NWs located there. The cross section through the free-standing Si NM revealed a thickness of about (885 ± 166) nm for the ZnO crystallites (Figure 4.9 iii). The mean and standard deviation were attained from measurements of the crystallite height at six different locations of the cross section.

From here on, only the large NW structures (Figure 4.9 i) are considered as they are supposed to have the largest impact on the FE properties of the emitter array because of their substantial size. The aspect ratio—here defined as the total average length from tip to bottom along the wire (h), divided by the smallest diameter at its apex ($2r_{\text{apex}}$)—was determined to be 310. The random orientation of the wires may be correlated with the crystal surface structure of the Si substrate, since especially polycrystalline as well as amorphous substrates

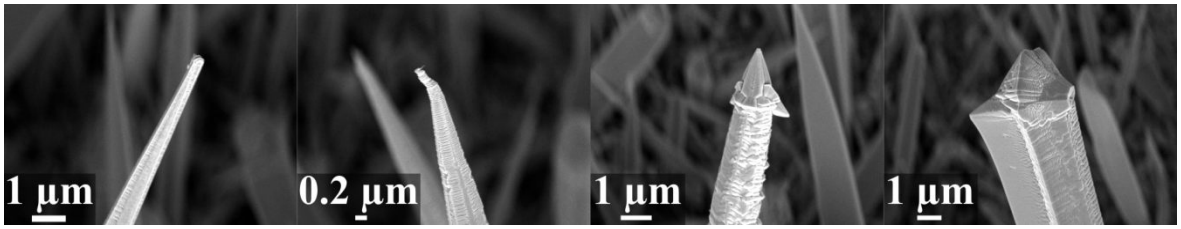

Figure 4.10: A selection of apex shapes from large NWs grown on Si NMs (Figure 4.9 i) are shown. On the one hand, there are NWs having an apex width similar to the wire's overall diameter. On the other hand, tapered NW ends were found, which often exhibit additional secondary wires orientated perpendicular to the wire's growth direction. The SEM images were taken under a tilt angle of 54 ° with the Crossbeam 550 by Zeiss.

are known to promote the generation of randomly oriented NWs [24]. Moreover, a large variety of apex shapes was observed and a selection of the NW tips is shown in Figure 4.10.

The herein observed NW morphology suggests that the growth follows a catalyst-assisted mechanism because the ZnO structures have a remarkably different appearance compared to the catalyst-free, VS grown ZnO nanowhiskers from the study by Hedrich *et al.*, which are displayed for comparison in Figure 4.1 [23]. Additionally, the group of outstanding long NWs (Table 4.2) are at least 10 times larger than the nanowhiskers grown without preceding catalyst deposition. However, the presence of a catalyst does not guarantee a VLS dominated nucleation process. Main indications for the growth by the VLS mechanism are metal particles located at the tips of the NWs and the correlation of the NW diameters with the size of the catalyst droplets [158, 159]. Therefore, the location of gold particles after NW growth was investigated with the help of SEM and EDX to examine the possibly involved nucleation mechanisms for the herein presented ZnO structures.

First, a VLS mechanism is indicated by gold droplets that were identified at the tips of shorter ZnO needles (Figure 4.9 ii) as shown in Figure 4.11. Yet, neither on the tip nor along the large ZnO NWs (Figure 4.9 i) a significant portion of gold could be verified via EDX as exemplary shown in Figure 4.12 (a). On the one hand, it is possible that the catalyst particles at the tips of large NWs have been evaporated during the growth process or that the gold atoms have migrated and were thereby incorporated into the wires, which could explain the absence of gold at the NW tips after growth [158]. In addition, the local gold concentration in the large NWs may have been below detection limits of the EDX device. On the other hand, it may also be an indication that the VLS mechanism is not the predominant growth regime throughout the complete deposition process. Another evidence against a purely VLS driven growth is that the mean NW diameter of (2400 ± 800) nm is significantly larger than the mean diameter of the Au particles, namely (80 ± 33) nm, which were formed by dewetting during the heating ramp of the growth process without subsequent ZnO deposition. The corresponding evaluation of the Au dot array is given in section A.3.2 in the appendix. The

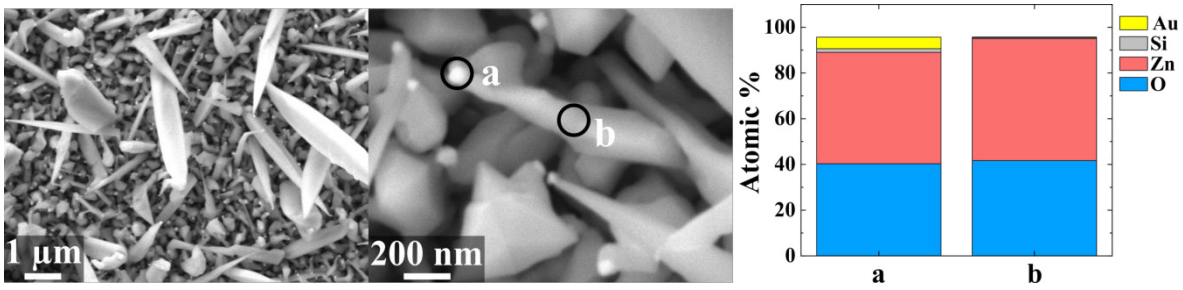

Figure 4.11: Bright particles were found on the low ZnO structures as shown in the SEM image on the left side. The close up SEM image in the center reveals that the bright particles are mainly located at the tips of the short ZnO needles (Figure 4.9 ii). The EDX spectrum, which was taken at the location of the dot that is marked by (a), showed an enhanced amount of gold compared to the spectrum measured at location (b) on the ZnO structure, as summarized in the column chart on the right side. The SEM images and EDX spectra (8 kV, 3 nA) were taken with the Crossbeam 550 by Zeiss.

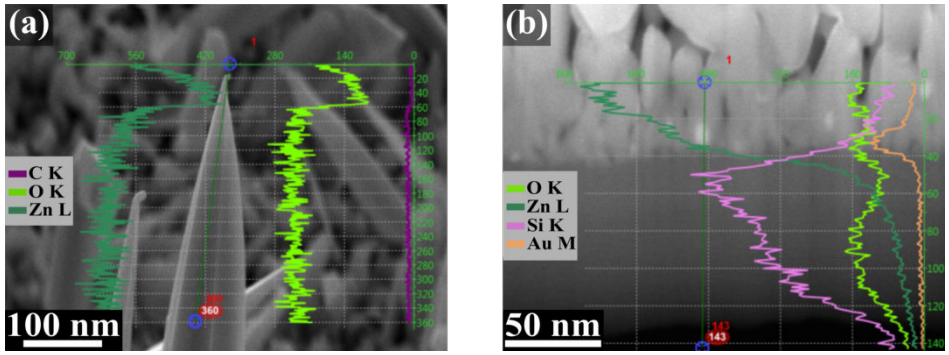

Figure 4.12: (a) For the scan across the apex area of a large ZnO NW, only zinc (dark green) and oxygen (light green) were detected as well as carbon contamination (purple) presumably from the preceding SEM imaging. However, no gold was detected. **(b)** In the cross section through the NW array, several bright particles were observed at the root of ZnO structures. A line scan across such an area showed an increased amount of gold (orange) at the bottom of the ZnO structure. Additionally, the transition from ZnO crystallites to the Si membrane is noted by the decreasing amount of zinc (dark green) and simultaneously increasing intensity of silicon (pink). The SEM images and EDX spectra (8 kV, 3 nA) were taken under a tilt angle of 54 ° with the Crossbeam 550 by Zeiss.

NW expansion in lateral direction may be attributed to the surface diffusion of gold atoms to the sidewalls of the wires during growth, which can act as additional nucleation sites and may also explain the absence of gold at the tips of the large ZnO structures [156].

Second, it was also possible to find gold particles at the roots of the NWs as presented in Figure 4.12 (b), which is supposed to be an evidence for the vapor-solid-solid (VSS) mechanism. For this growth regime, the NW formation is driven by surface diffusion of the precursor substances to the solid gold catalysts that aid the condensation of ZnO. The VSS mechanism was mostly reported for growth processes below the gold-zinc eutectic

temperature of 684 °C, which is in agreement with the herein used growth temperature of 580 °C [155, 158]. In addition, $Zn(acac)_2$ is reported to decompose into ZnO as well as into some carbon-containing species. Therefore, the ZnO vapor rather adsorbs and nucleates on the surface of the gold dots because no chemical reaction between ZnO and Au is expected [160]. In summary, there are indications for the VLS as well as for the VSS growth regime. Thus, it is assumed that a mixture of both mechanisms causes the formation of the observed ZnO structures. Further investigation of the different growth stages as well as a detailed element analysis of the gold droplets to detect possible alloying would be necessary to identify the predominant growth mechanism, which may also change over time [155, 161].

Time dependent changes of the growth process with $Zn(acac)_2$ as precursor substance were also reported elsewhere [24]. According to Baxter *et al.*, the formation of a polycrystalline film during the initial phase of the growth process, the subsequent NW growth after dehydration of the $Zn(acac)_2$ and finally the formation of secondary wires after its decomposition to ZnO, is expected for the used precursor [24]. The herein observed layer of ZnO crystallites may be formed during an early stage of the growth process. Therefore, the generation of the low, densely packed ZnO film (Figure 4.9 iii)—which most probably provides no contribution to the FE current—may be inevitable due to the correlation of its growth with the variation of the precursor constitution over time. Also for other precursor combinations, a similar dependence of the ZnO morphology on the zinc vapor supersaturation was reported. High supersaturation promotes the growth of 2D crystals in the initial stage of the growth process, whereas a reduced precursor concentration in the gas phase facilitates the growth of NWs in a later stage [162].

Moreover, a striking variety of apex structures was noted for the large NWs, as shown in Figure 4.10. The so called screw dislocation mechanism may be responsible for their appearance, as conical tip shapes with spiral morphology are characteristic for this growth regime. Typically, the growth rate is much faster along the dislocation line than in the radial direction, which favors the growth of sharp cones [68]. Since the screw dislocation is known to appear for low zinc supersaturation, this mechanism may be present during a later stage of the NW growth when most of the precursor is already consumed [159]. Furthermore, the formation of secondary NWs perpendicular to the growth axis was noted. The generation of secondary wires was also observed for the usage of $Zn(acac)_2$ by Baxter *et al.* who attributed the specific apex appearance to the anhydrated state of the precursor in a final stage of the growth process [24].

In conclusion, the notable diversity of ZnO shapes and variety of NW dimensions may be correlated with the broad distribution of gold particles (see section A.3.2), with the possible mixture of different growth mechanisms as well as with the time dependent change of the precursor constitution.

4.2.2 Standard Growth Process - Field Emission Measurements

Herein, the FE properties of the ZnO NW arrays deposited on the Si NMs by the standard growth process were investigated. For consistency of the FE measurements, the *I-V* curve acquisition was executed according to the detailed routine explained in section 3.4. Specific characterization conditions relevant to the present study are listed in Table 4.3. Furthermore, the FE data analysis was performed following the description that is also given in section 3.4.

For investigation of the reproducibility of the field emitter synthesis with the sputter shadow mask, the macroscopic onset fields were determined for three separate samples according to the description given in Figure 3.6 of chapter 3 and the results are summarized Figure 4.13. The derived onset fields from three separate samples (Si-NM-1 to Si-NM-3) vary within their

ZnO NWs on Si NMs - Characterization conditions	
d	250 µm
A_M	36 mm^2
PTFE height compensation	250 µm
FE measurement setup	Voyager

Table 4.3: Summary of specific characterization conditions used for *I-V* curve acquisition for the ZnO emitters on Si NM substrates in the Voyager FE setup with the picoammeter. The emitter-grid distance d was defined by the thickness of the PTFE foil that separates both electrodes, and the macroscopic emission area A_M was defined by the square 6x6 mm^2 cutout in the PTFE foil exposing the ZnO NW array (see section 3.2.2 for details on the FE assembly).

Si NMs – Onset fields

Sample no.	d [µm]	F_M^{onset} [V/µm]
Si-NM-1	300	1.8 ± 0.1
Si-NM-2	250	2.0 ± 0.1
Si-NM-3	250	2.0 ± 0.1

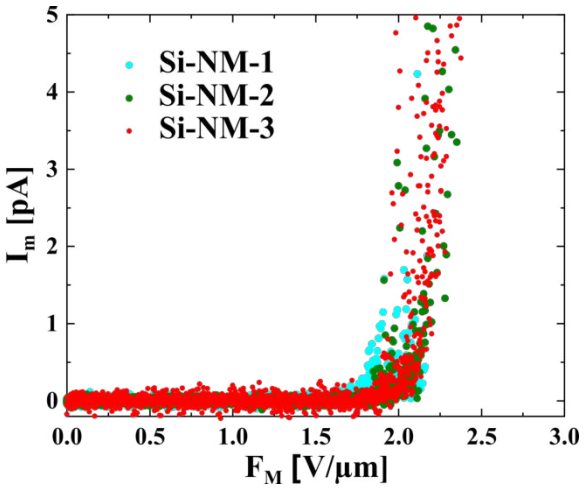

Figure 4.13: Summary of the macroscopic onset fields F_M^{onset} for three samples with ZnO NW arrays grown on Si NMs. The mean and standard deviations of the macroscopic onset fields were derived from six subsequent *I-V* curves from each sample according to the explanation given in Figure 3.6 and in section 3.4.

standard deviations around a mean value of about 1.93 V/µm, which indicates a remarkable repeatability of the herein used synthesis route for the ZnO emitters on the Si NM substrates.

For determination of the maximum possible emission current that can be extracted from the ZnO emitters on the Si NMs, the termination current was step wise increased as described in section 3.4. Note, only sample Si-NM-3 is considered for further data analysis. After an electrical discharge occurred during the 7th FE measurement that triggered the trip current of the power supplies, a modification of the *I-V* curve shape was observed for the subsequent measurements as shown in Figure 4.14 (a) (compare red to blue curves). The low threshold current that initiated the immediate voltage trip at the power supplies (see section 3.2.3 for details) prevented the destruction of the membrane substrate and preserved an operational FE sample. The mean onset field shifted from (2.0 ± 0.1) V/µm before electrical discharge (2nd–7th, plotted in red) to a slightly larger mean value of (2.3 ± 0.1) V/µm (8th–11th, plotted in blue), which may indicate a permanent modification of the shape or of the electronic surface constitution of the ZnO emitters by the electrical discharge.

The largest emission current of 73.8 nA from sample Si-NM-3 was obtained at an applied voltage of 942 V, which corresponds to a macroscopic ECD of 0.21 µA/cm^2 at a macroscopic electric field of 3.8 V/µm, as presented in Figure 4.14 (b). The macroscopic emission area (36 mm^2, Table 4.3) is defined by the area that was exposed by the central cutout in the PTFE

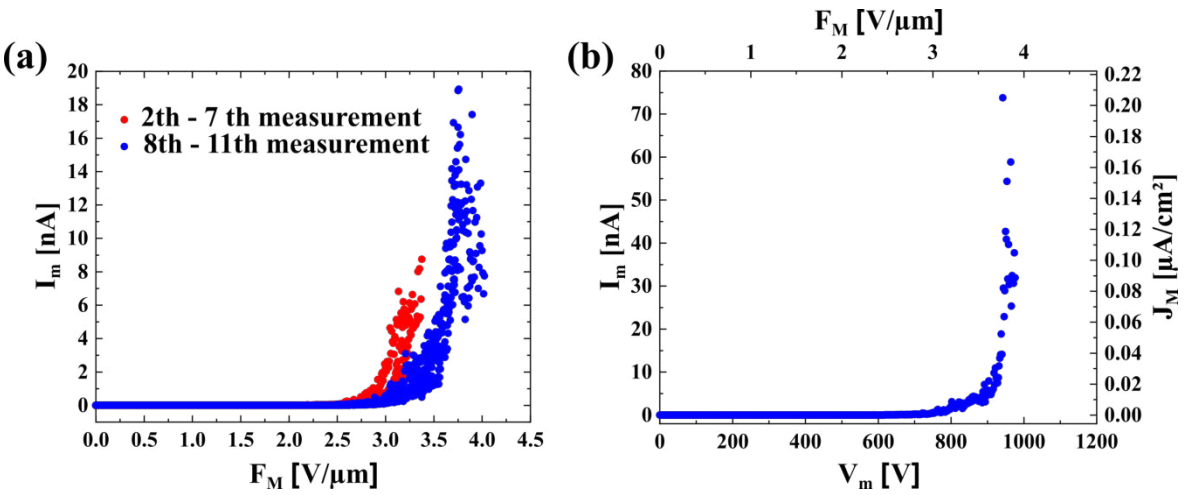

Figure 4.14: (a) Several *I-V* curves from Si-NM-3 are shown with step wise increasing maximum emission current functioning as termination condition for the FE measurements. The 7th measurement was stopped by an electrical discharge and the corresponding voltage trip at the power supplies. Afterwards, the appearance of the emission curves was irreversible changed (compare red to blue). **(b)** The maximum current from the ZnO NWs on Si NMs was reached by sample Si-NM-3. For comparison of the FE properties to other measurement configurations in literature, I_m was converted to the macroscopic ECD J_M by division through A_M= 0.36 cm^2, which is plotted at the right axis, whereas the macroscopic electric field is presented at the top axis for d = 250 µm.

spacer. Thus, a contribution to the emission current from ZnO NWs that were not located on the Si NMs is possible, since the total membrane area of 12.6 mm^2 is smaller than the exposed area (4 membranes per sample with 2 mm diameter each, see Figure 4.2). Note, it is not feasible to solely expose the NM area, as physical contact between the flexible base and the PTFE spacer has to be prevented in any case as indicated in section 3.3.2.

Further emission current rise was not possible because the power supplies tripped repeatedly for additional attempts to reach higher emission currents. On the one hand, the limitation of the emission current may be related to the adhesion of the ZnO structures on the substrate. When charged material can be dragged across the emitter-grid gap by the strong electric field, electrical discharge can be provoked [110, 163]. On the other hand, localized Joule heating may cause the melting and subsequent vaporization of emitter material, which generates a source for electrical breakdown in the vacuum gap between emitter and grid [69].

The *I-V* curves were analyzed using the FN as well as the MG plot according to the description in section 2.4. For investigation of the impact of the electrical discharge on the FE properties, the *I-V* curves from Si-NM-3 were analyzed separately before and after the onset shift. Note, only the FE measurements were considered showing an emission current larger than 5 nA, namely starting from the 5th measurement, to provide a sufficient number of data points for the linear fit above the respective onset value. Exemplary, the linearized FE data from the high current measurement from sample Si-NM-3 is displayed in Figure 4.15. For extraction of slope $S_{\mathrm{FN/MG}}$ and intercept $C_{\mathrm{FN/MG}}$ from both plot types, linear functions (yellow lines) were fitted to the FE data (blue dots) above the onset voltages. Under the

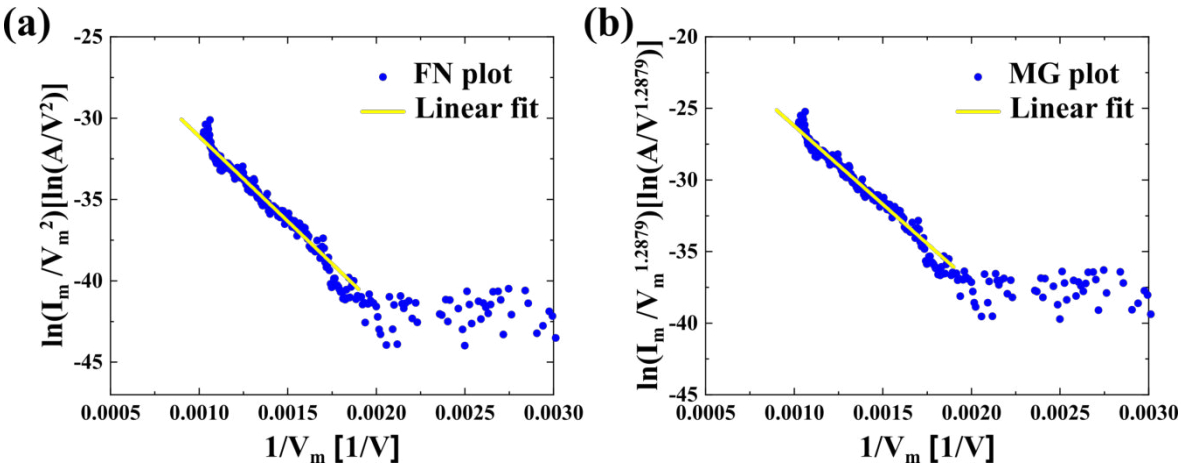

Figure 4.15: (a) FN and **(b)** MG plot of the *I-V* curve shown in Figure 4.14 (b) from sample Si-NM-3. The data is linearized according to the relation $\ln\left(\frac{I_\mathrm{m}}{V_\mathrm{m}^\kappa}\right)$ versus $\frac{1}{V_\mathrm{m}}$. The values for the exponent on the y-axis are: $\kappa = 2$ for the FN plot and $\kappa \approx 1.2879$ for the MG plot, with $\phi_{\mathrm{ZnO}} = 5.3$ eV, $\eta(\phi) \approx 4.2726$ and $\theta(\phi) \approx 1.1068 \cdot 10^{-4}$ A/nm^2. For extraction of slope and intercept, a line (yellow) is fitted to the data above the onset voltage.

assumption that a work function of 5.3 eV can be applied for the randomly distributed ZnO NW emitters [46], an effective field enhancement factor (FEF) γ_{eff} as well as an effective emission area A_{eff} were extracted from each of the *I-V* curves (5th–11th measurement). The mean effective FEFs are summarized in Table 4.4 with respect to the measurements before (5th–7th) and after electrical discharge (8th–11th) occurred and the corresponding onset field shift was noted (Figure 4.14 (a), compare red to blue).

Before onset shift, the effective FEF results in a value of 2056 ± 236 and reduces only slightly to 1864 ± 129 after the electrical discharge. The impact of the slope correction function for calculation of $\gamma_{\text{eff}}^{\text{SN}}$—originating from assuming an image charge affected SN barrier instead of a simple triangular barrier—is negligible, as it lowers the effective FEF only by 5 %. The values for the effective FEF extracted from the MG plot are similar to the ones derived from the FN plot, namely 1966 ± 218 before and 1780 ± 119 after onset shift. In summary, the impact of the electrical discharge on the geometrical field enhancement effect of sample Si-NM-3 seems to be low, since the derived effective FEFs before and after onset shift vary within their standard deviations for the FN as well as for the MG plot analysis.

The effective emission areas from FN and MG plot (equation 2.35 and 2.48) are well below square micrometers, which suggests FE from only a small part of the total exposed area. For the FN plot analysis, the effective emission area changes from 217 nm^2 (5th–7th) to 110 nm^2 (8th–11th) with occurrence of the electrical breakdown. It may indicate a change of emission area by the sudden discharge, possibly by material evaporation from the ZnO emitters. For the MG plot analysis, an emission area extraction parameter of Λ_{MG} = 19.415 nm^2/A

ZnO NWs on Si NMs - FN and MG plot results

	γ_{eff}	$\gamma_{\text{eff}}^{\text{SN}}$	R^2
FN plot			
5th–7th	2056 ± 12 %	1953 ± 12 %	0.97 ± 2 %
8th–11th	1864 ± 7 %	1770 ± 7 %	0.98 ± 1 %
MG plot			
5th–7th	1966 ± 11 %	-	0.97 ± 1 %
8th–11th	1780 ± 7 %	-	0.98 ± 1 %

Table 4.4: Effective values extracted from FN and MG plot for the 5th–7th (before discharge) and for the 8th–11th measurement (after discharge) from sample Si-NM-3. The effective FEFs γ_{eff} for FN and MG plot were calculated with the equations 2.34 and 2.50, respectively. The effective FEF assuming the SN barrier $\gamma_{\text{eff}}^{\text{SN}}$ is derived by additional multiplication of γ_{eff}^{FN} with the slope correction function $s_{\text{F}}(y) \approx 0.95$ according to equation 2.37. The coefficients of determination R^2 are close to unity and show only small variation for subsequent measurements, which indicates that the FE data in FN and MG plot is well described by the linear fit.

(equation 2.49) was calculated with the work function of 5.3 eV for ZnO. The effective areas derived from the MG plot of the FE data are up to 90 times smaller compared to the FN plot results. Typically, considerably larger ECDs are predicted by the MG model than by the FN equation that considers FE through the triangular barrier (see Figure 2.2 (b)). Thus, the extraction of smaller effective emission areas for the same measured *I*-*V* dependence is expected, because the MG plot analysis exclusively assumes emission through the SN barrier, which is reduced by the image charge effect [85].

Since neither the total apex area of the emitters nor the number of the randomly distributed ZnO NWs that actually contribute to the emission current are known, it is not feasible to estimate if the extracted emission areas match expectations derived from the emitters' morphology. Compared to the macroscopic emission area of 0.36 cm^2 = $3.6{\cdot}10^{13}$ nm^2, the area efficiency of emission (equation 2.29) would be less than $\alpha_M = 6{\cdot}10^{-12}$. In general, the extracted emission area values vary more than 70 % for subsequent measurements from the same emitter array, which indicates a poor reproducibility for the extraction of A_{eff}.

The area extraction is known to be highly sensitive to any curvature of the linearized FE data in the high field region, namely on the left side of the FN/MG plot. For the emission through the SN type barrier, a curvature of the linearized data is expected because of the dependence of $v_F(y)$ on the electric field. The MG plot was established to straighten out this effect and thereby, to allow for a more precise determination of the emission area [85]. However, for the FE measurement from sample Si-NM-3 that is linearized in Figure 4.15 (b), an upwards curvature of the data is still visible in the high field region of the MG plot. This observation indicates that effects beyond the MG FE model may be responsible for the noted non-linearity [85]. Hence, the MG plot may be used as further evidence for the presence of influences beyond the SN barrier and to identify the regions of experimental FE data that may be dominated by additional effects. In conclusion, the effective emission area is not considered further in this thesis, since the extracted values vary considerably for every new measurement from the same emitter sample and thus, may be unreliable.

To conclude the FE data analysis, the scaled barrier fields for the orthodoxy test were extracted with equation 2.43 from the FN plot for the first value above the onset of FE and for the data point at the highest applied voltage for each of the FE measurements. Considering the 5th–11th measurement, a mean minimum scaled barrier field of 0.21 $\pm$ 0.01 and a mean maximum value of 0.34 $\pm$ 0.03 were derived. Therefore, the FE data passed the orthodoxy test, since the experimentally determined values f_{min}^{extr}–f_{max}^{extr} are within the so called apparently reasonable range of 0.14 to 0.43 given for work function values between 5.0 eV and 5.5 eV [83]. This result may indicate the viability of our FE measurement conditions and the reliability of the effective FEFs extracted from the experimental FE data [80, 82].

For comparison of the effective FEFs extracted from the FE data to the emitters' morphology, theoretical values for the apex FEF were derived. Since the structure of the ZnO NWs was investigated by SEM after the FE measurements, only the effective FEF from sample Si-NM-3 is considered after electrical discharge occurred, namely the mean result of 1864 ± 129 for the 8th–11th measurement given in Table 4.4 is contemplated for comparison. For calculation of the theoretical FEF with different models (see section 2.2.1), the NW dimensions from Table 4.2 were used. The bases of the large wires are in general larger than the width of the apexes and therefore, the "hemi-ellipsoid on a plane" model (A), the equation that includes a factor for the base in dependence on the emitter shape (B) and the charge disc model (C) were used to calculate the apex FEF. In addition, one model was applied that includes the inclination angle of tapered emitters and the emitter tip-to-electrode distance (D). The results of the different models vary considerably from 179 to 2428 as shown in Table 4.5. The three models (A)–(C) only take into account the width and height of the emitters and the calculated FEFs are all lower than the effective value derived from the FE data. However, the result from model (D) is only 23 % larger than the effective FEF that was experimentally derived for sample Si-NM-3, namely 1864 ± 129.

In general, a number of prerequisites for application of the theoretical FEF models are not fulfilled by the experimentally investigated ZnO NWs on the Si NMs. First, the condition of $\frac{h}{d} \ll 1$ may not be given by our measurement configuration, as the relation results in a value of about 0.23. Therefore, the influence of the opposing grid electrode may need to be considered. Second, the models for the apex FEF assume a perfectly flat emitter substrate [38], however, the shape of our flexible NM base may have a dependence on the applied voltage. Thus, the membrane bulging would introduce an additional factor to the total FEF, since the emitter-grid distance possibly decreases with increasing applied voltage [164]. Third, the actual apex dimensions may be much smaller than found in the SEM images because of detection

ZnO NWs on Si NMs - Theoretical FEFs

Model number	Equation number	Value
(A)	$\gamma_{\mathrm{apex}}(3)$ (2.23)	654
(B)	$\gamma_{\mathrm{apex}}(4)$ (2.25)	179
(C)	$\gamma_{\mathrm{c-disc}}$ (2.27)	608
(D)	$\gamma_{\mathrm{apex}}(5)$ (2.26)	2428

Table 4.5: The theoretical values for the apex FEF calculated from the average NW dimensions, taken from Table 4.2, are shown. For model (B), a factor of $\alpha_{\mathrm{base}} = 0.88$ was used for conical shaped emitters and for model (C), equation 2.28 was applied for calculation of $R_{\mathrm{c-disc}} = 0.095\,\mu\mathrm{m}$. For model (D), the tip inclination of 18.3 ° and the emitter tip-to-grid distance of $D = d - h = 250\,\mu\mathrm{m}$ - $58\,\mu\mathrm{m} = 192\,\mu\mathrm{m}$ were used.

limits and other analysis methods, such as TEM, would be needed to determine the actual tip diameters. In addition, with focus on the various complex tip shapes observed for the ZnO NWs (Figure 4.10), a multiplicative FEF similar to the Schottky's conjecture may apply to the investigated emitters (see section 2.2.1) [29]. The combination of the described effects may cause the discrepancy between the effective FEF derived from the FE data and the results from the theoretical models (A)–(C). However, the FEF calculated with model (D) that considers the mean tip inclination and the emitter tip-to-grid distance $D = d - h$, is comparable to the effective FEF derived from the FE data. Hence, the position of the opposing electrode may have a significant impact on the geometrical field enhancement effect in our FE measurement configuration. Furthermore, the consideration of additional details regarding the emitters' shape, such as the inclination angle, leads to a better agreement between the theoretical model and the value extracted from the experimental FE data.

The previously discussed models assume isolated single emitters. Therefore, the potential influence of electrical field screening on the FE properties is assessed in the following. In a randomly distributed emitter array, it is only possible to roughly estimate an average spacing between nearest neighbors. Applying the NW density of 5963 NWs/mm^2 for ZnO structures that are larger than 10 µm from Table 4.2, one NW would stand on a square area of about 168 µm^2. Assuming that the NWs are located in an ordered array with square unit cell of the same density, the average distance between NWs would be b = 13 µm. The FEF of an isolated emitter is predicted to be reduced by up to 56 % through the mutual shielding in the ZnO FEA, when equation 2.30 is applied with the parameters a = -2.41 and c = 0.74 for a randomly distributed emitter array [54]. According to the models that were contemplated for the generation of Figure 2.4 (b), the screening becomes negligible for average emitter distances that correspond to four times the emitter height. Therefore, an average distance of 232 µm is suggested for the large ZnO NWs that have a mean emitter height of 58 µm (see Table 4.2). With the average NW distance of 232 µm, a hypothetical NW density of 19 NWs/mm^2 would lead to a negligible screening effect according to the theoretical models. However, only a rough estimation of the electrical field screening effect is possible by the previous analysis, since the large ZnO NWs are highly tilted, vary considerably in height (Figure 4.9 i), and the number of emitters actually contributing to the emission current is unknown and may increase with rising electric field [29].

In Figure 4.16, the measured FE data from Figure 4.14 (b) is compared to the theoretical curves plotted according to the FN equation 2.9 for the triangular (plotted in red) and according to the MG equation 2.14 for the SN barrier (light blue for s_F = 0.95, green for $s_F(y)$). The effective parameters that were extracted from the displayed experimental *I-V* curve, namely γ_{eff}^{FN} = 1997 and A_{eff}^{FN} = 55.9 nm^2, were used to plot the theoretical curves. The experimen-

tally measured FE data (blue dots) follows the theoretical prediction that assumes electron emission through the triangular vacuum potential barrier (VPB, red) in the low field region as shown in Figure 4.16 (a). However, the high field region of the FE data is characterized by a steeper rise of the emission current with increasing electric field. The corresponding FN plot in Figure 4.16 (b) emphasizes that the FE data from the ZnO NWs follows a linear trend for low electric fields. The non-linear tendency is observed for voltages above 833 V, which corresponds to a value of 0.0012 [1/V] on the x-axis of the FN plot.

Such a non-linearity in the high field region of the FN plot from n-type ZnO emitters was earlier attributed to the saturation of emission current from the conduction band because of the limited charge carrier generation rate in the semiconductor. With further increase of the electric field, the magnitude of energy band bending can be sufficient to allow for electron emission from the valence band of ZnO, which causes again a steep rise of the emission current [61, 67]. Herein, the absolute value of the slope was determined to be 10434 V (between 0.0012 [1/V] and 0.0017 [1/V]) from the linear, low-field region. With increasing electric field, the absolute current slope first reduces to 6450 V (0.0011 [1/V]–0.0012 [1/V]) and then, increases again to an absolute value of 27988 V ($1/V_m < 0.0011$ [1/V]). No considerable change of the geometrical shape of the emitters is assumed for transition from low to high field region. Thus, the effective FEF from the linear low field region, namely $\gamma_{eff}^{FN} = 1997$, was used to derive an estimate for the work function in the high field region. An apparent work function value of 10.2 eV was found for the enhanced slope (27988 V) of the high field

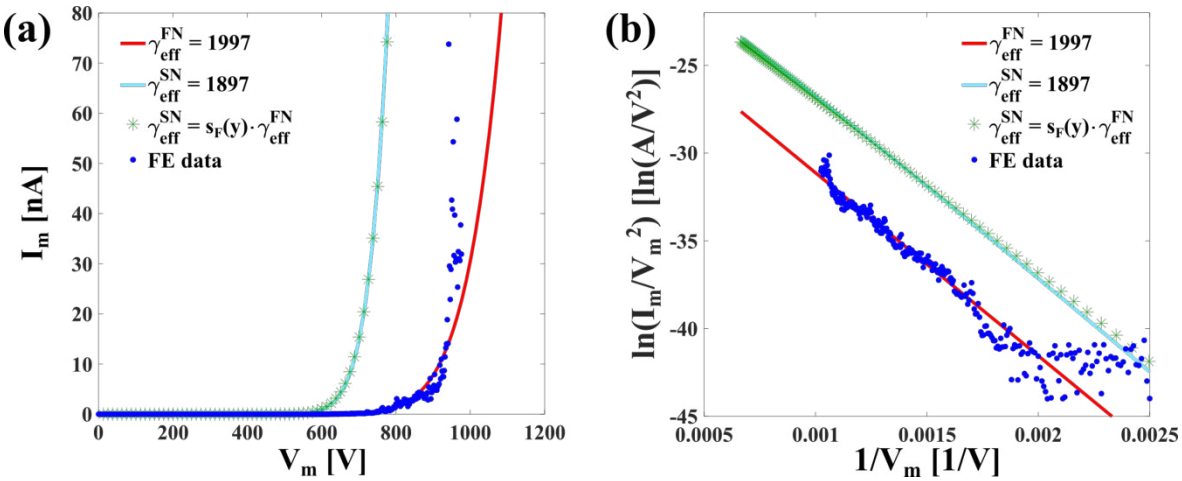

Figure 4.16: (a) The *I-V* curves and **(b)** the corresponding linearized data in the FN plot are displayed for the experimental FE data from sample Si-NM-3 (blue dots), which was shown in Figure 4.14 (b), and for theoretical models. The values extracted from the FN plot of the measured FE data ($\gamma_{eff}^{FN} = 1997$, $A_{eff}^{FN} = 55.9\,nm^2$) were used to plot the *I-V* curves according to the FN equation 2.9 for the triangular barrier (plotted in red) and according to the MG equation 2.14 for the SN barrier with $\gamma_{eff}^{SN} = 0.95\cdot\gamma_{eff}^{FN} = 1897$ (light blue) and with $\gamma_{eff}^{SN} = s_F(y)\cdot\gamma_{eff}^{FN}$ (green asterisks).

region ($1/V_m < 0.0011$ [1/V]) of the FN plot. The increase of the apparent work function value in the high field region is in agreement with observations in literature and suggests the electron emission from energy levels below the conduction band minimum, which may be an indication for emission current contribution from the valence band [67].

Two theoretical curves for the SN barrier model are shown in Figure 4.16, namely with the FEF derived by multiplication of $\gamma_{\mathrm{eff}}^{FN}$ with the constant slope correction factor of 0.95 (light blue) and by employment of the electric field-dependent function $s_{\mathrm{F}}(y)$ (green asterisks) according to the equations 2.37 and 2.38 (see section 2.4 for further explanation). The deviation between the two approaches that consider the SN barrier, is negligible. However, the difference between the theoretical curves plotted with the MG equation for the image charge affected VPB and the measured *I*-*V* curve is significantly larger than the deviation between the FN model (for the triangular barrier) and the experimental results. This observation is explained by the larger ECD that is predicted by the MG FE equation compared to the result for the fundamental FN formula, as it is exemplified in Figure 2.2. Division of the theoretical curves through a factor of 76 would lead to an overlap of the prediction by the MG equation with the experimental data in the linear low field region. Thus, for the measured *I*-*V* curve, an effective emission area of 0.74 nm^2 is predicted by consideration of the SN barrier. As previously noted in this chapter, the comparison of the effective emission area to the actual emission area of the ZnO NWs is prevented by the uncertain ratio of emitters that contribute to the FE current.

Both models neglect the dependence of the FEF and of the emission area on the electrical field because its local variation is typically unknown [4, 29, 165]. Additionally, the Si NMs show notable bulging patterns already at zero electric field (see Figure 4.9). Thus, the membranes are presumably displaced gradually towards the grid electrode, which corresponds to the reduction of d as a function of the applied voltage [164]. In conclusion, the local shape of the VPB may be highly complex for the sharp ZnO emitters and the mutual cancellation of various effects may lead to the observed agreement of the experimental FE data with the fundamental FN model [34, 79].

4.2.3 Synthesis Parameter Variation

Herein, one parameter of the standard synthesis recipe for ZnO emitters on Si NMs, which is described in the sections 4.1.2 and 4.1.3, was changed at a time and the dimensions and the FE properties for each of the FEAs were investigated. For all field emitter samples, the sputter shadow mask was used for catalyst deposition. The FE acquisition as well as the FE data analysis were executed following the description in section 3.4 and the specific characterization conditions given in Table 4.3 were used. The following four parameters were varied: First, the deposition time for the thin gold layer, second, the growth time for the NW

array, third, the precursor temperature and fourth, the substrate position in the boat.

As shown in Figure 4.17, the decrease of the deposition time for the gold film from 60 s (standard, shown in black) to about 22 s (green) caused a reduction of the onset field by 15 %. The duration of roughly 22 s corresponds to the minimum possible deposition time, which was obtained by adjustment of the turning knob for the sputter time to zero (sputter coater K550X from Emitech). The SEM images present sections of the ZnO NW arrays for both samples and are ordered here—as well as for the subsequent synthesis parameter variations—from low to high onset field from left to right. The mean NW length of (33.2 ± 10.6) µm, which was found for the 22 s deposition time, is longer than the NW length of (18.3 ± 8.2) µm generated by the standard process. For all investigated parameter variations, estimates for the NW lengths were derived from the respective SEM images using ImageJ [157]. In addition, the mean effective FEF for the shorter sputter time, namely 3276 ± 1174, is larger than the value of 1864 ± 129 obtained for the standard process with the longer gold sputter duration. Therefore, the geometrical field enhancement effect is larger for the ZnO NWs grown with the shorter catalyst deposition time, which is in good agreement with the observed reduction in onset field as well as with the increase in NW length.

By decreasing the sputter time from 60 s to the minimum possible sputter time of about 22 s, the apparent thickness of the gold film deposited through the sputter shadow mask was reduced from 5.9 nm to 1.8 nm. The gold particle size is known to decrease with the thickness of the metal film, when the same dewetting temperature is applied [146, 151]. Thus,

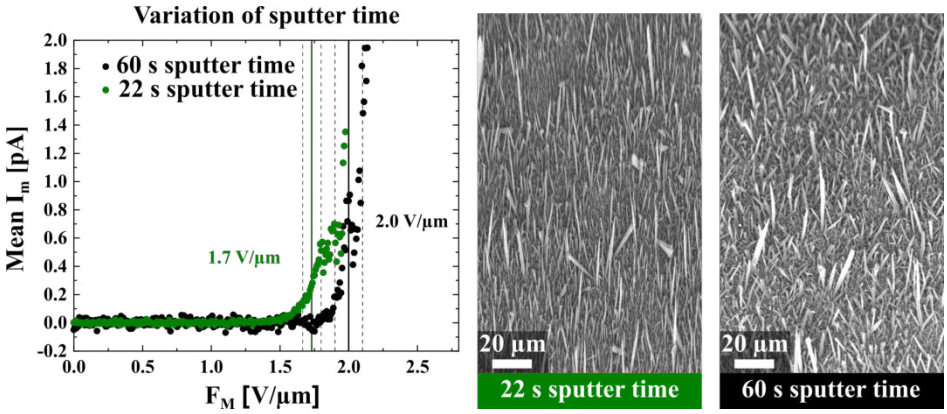

Figure 4.17: The mean of several subsequent measurements from ZnO NWs grown on Si NMs are shown for the standard growth process that uses a gold deposition time of 60 s (black) and for the minimum possible sputter time of about 22 s (green). The mean onset fields and the standard deviations are highlighted by the solid and by the dashed lines, respectively. The onset field is (2.0 ± 0.1) V/µm for 60 s and (1.7 ± 0.1) V/µm for 22 s sputter time. The SEM images show sections of the ZnO NW arrays for both samples. Note, the black FE data as well as the respective SEM image, which shows the results for the standard growth process, are used as reference in all subsequent parameter sets. The SEM images within this section were taken under a tilt angle of 54 ° with the Crossbeam 550 by Zeiss.

the formation of smaller particles is expected for dewetting of the thinner gold film. The state of supersaturation by incorporation of zinc and oxygen in the catalyst particles can be reached faster for smaller particle diameters, which may lead to an accelerated initiation of the NW growth by precipitation of precursor material [156]. Hence, the enhanced NW length obtained for the shorter gold deposition time may be caused by an earlier start of the NW generation than for the standard growth process for the constant growth time of 12 h. Note, the FE data of the 2nd–7th measurement from sample Si-NM-3 (see Figure 4.14 (a)) was used as reference that represents the standard growth process. For determination of the mean effective FEFs, only *I-V* curves were included with R^2 larger than 0.2 for the linear fit to the FE data in the FN plot to solely consider measurements that have a sufficient number of data points above the onset field.

The ZnO growth time in the tube furnace was increased from 6 h to 9 h and finally to 12 h. The onset field decreased by about 39 % for increase of the growth time from 6 h (red) to 12 h (black), as shown in Figure 4.18. However, the onset field was only slightly lowered between 9 h (orange) and 12 h growth duration and the respective standard deviations overlap. The observed FE properties are supported by the emitter lengths found for the separate samples. The mean NW length increases with rising growth time from (8.9 ± 3.4) µm for 6 h to (19.4 ± 7.8) µm for 9 h. The NW length for the standard process using a growth time of 12 h, namely (18.3 ± 8.2) µm, is within the standard deviation of the NW length for the 9 h growth process. Note, it is only feasible to examine a relatively small region of the total exposed emission area (A_M = 36 mm^2) and it is impossible to determine which of the wires actually contribute to the FE current. Therefore, the derived NW dimensions have to be considered as rough estimates for the overall array dimensions and are intended to be used for

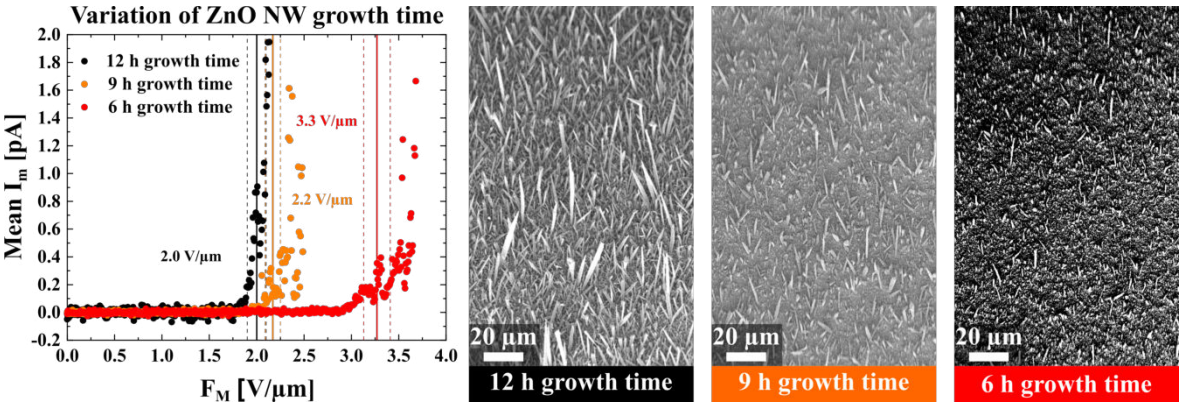

Figure 4.18: Variation of the growth time for the ZnO NW array from 6 h (red) to 9 h (orange) and in comparison to the standard process with 12 h (black). With increasing growth duration, the macroscopic onset field drops from (3.3 ± 0.1) V/µm to (2.2 ± 0.1) V/µm and finally to the reference value of (2.0 ± 0.1) V/µm.

the relative comparison of emitter lengths in this section. In general, the high onset field for 6 h growth is determined by the strongly reduced NW length and the similar onset fields for 9 h and 12 h growth are correlated with their comparable NW dimensions.

The herein used precursor $Zn(acac)_2$ was reported to decompose with preceding growth process [24]. In the initial stage, the hydrated precursor causes predominantly the formation of 2D ZnO structures, whereas the anhydrated $Zn(acac)_2$ in a later stage of the growth process facilitates the generation of 1D wire shapes. For a longer process duration, the formation of secondary wires was reported in correlation with further decomposition of the precursor [24]. This behavior fits well to our observations for the time dependence of the ZnO deposition, as for the 6 h process already short structures were formed. However, the growth of long NWs seems to be dominant between a growth time of 6 h and 9 h. For the increase from 9 h to 12 h, only a small reduction in onset field was observed. Presumably, the growth in vertical direction is almost completed after 9 h and a longer growth duration causes only further shaping of the NW tips, for instance, by initial growth of secondary wires. Hence, the slightly lower onset field for the standard growth process may be explained by a relativity small impact on the overall morphology of the ZnO emitters between 9 h and 12 h growth time.

The third parameter variation considers the precursor temperature and the results are presented in Figure 4.19. The increase of the precursor temperature to 130 °C (blue) lowered the onset field by about 45 % in comparison to the FE measurements from the sample grown with the standard process (black), namely with a precursor temperature of 110 °C. In contrast, the reduction of precursor temperature to 90 °C (turquoise) resulted in a 3.9 times larger onset field than found for the reference sample. The NW length increased from (5.6 ± 1.8) µm to (18.3 ± 8.2) µm and then to (38.1 ± 13.2) µm with rising precursor temperature. The consid-

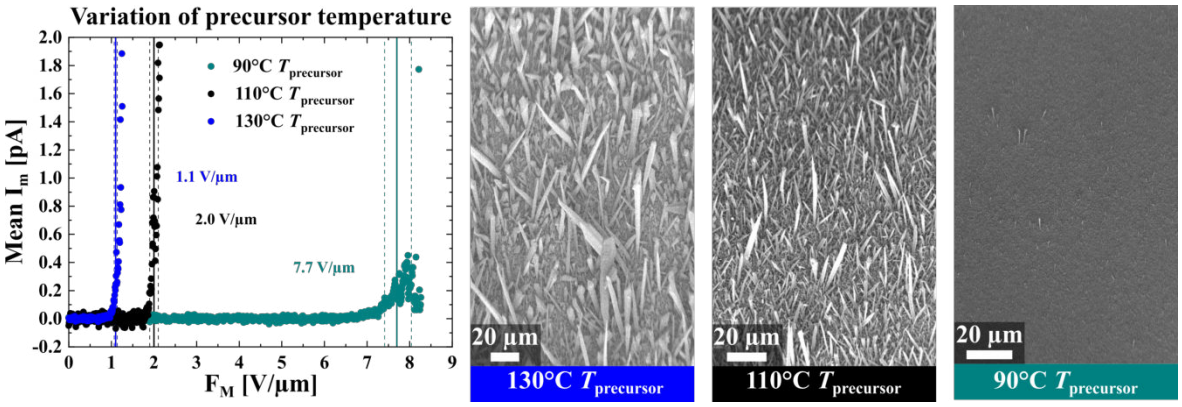

Figure 4.19: Variation of the precursor temperature from 90 °C (turquoise) to 110 °C (black) up to 130 °C (blue). With increasing precursor temperature, the macroscopic onset field decreases significantly from (7.7 ± 0.3) V/µm for 90 °C to (2.0 ± 0.1) V/µm for 110 °C and finally down to (1.1 ± 0.1) V/µm for 130 °C.

erable increase in NW length for the 130 °C precursor temperature is assumed to be the main reason for the notable reduction in onset field.

On the one hand, the dehydration process of the precursor described by Baxter *el al.* may be accelerated by the elevated temperature (130 °C) in the first heating zone of the tube furnace, which can lead to a faster initialization of the 1D NW growth [24]. Hence, longer NWs can be formed for the higher precursor temperature compared to the reference sample (110 °C) within the constant growth duration of 12 h. On the other hand, the precursor dehydration may be decelerated for the 90 °C in the precursor zone. Thus, the NW formation is rarely initiated within the 12 h deposition time, as the 1D wire growth is known to be the dominant regime for the anhydrated state of the $Zn(acac)_2$ precursor.

Finally, the substrate position in the ceramic boat was altered and the FE properties were investigated. The Si NM sample (with catalyst) was placed behind another plain Si NM substrate (without catalyst), which yields a shift of about 1 cm away from the beginning of the growth zone. The onset field for this sample (purple) was found to be 1.5 times higher than for the standard process (black) with only one substrate placed in the beginning of the growth zone (Figure 4.20). The NW length of (18.3 ± 8.2) µm for the standard process reduced only slightly to (15.8 ± 10.0) µm for the changed placement of the sample. In addition, the effective FEF was determined to be 1011 ± 367, which is about 46 % lower compared to the value derived for the reference sample. Note, on the plain Si NM substrate (without catalyst), a homogeneous layer of densely packed, low aspect ratio ZnO nanowhiskers was observed. The structures showed an appearance similar to the ZnO nanowhiskers grown in the study by

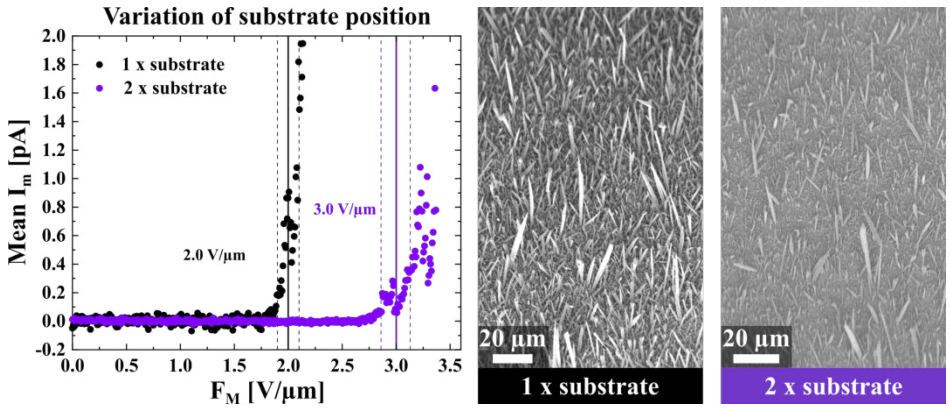

Figure 4.20: The placement of another sample in front of the NM substrate and the corresponding increase in distance from the beginning of the growth zone caused an increase in onset field (purple) compared to the standard process (black) with only one substrate placed in the beginning of the ceramic boat. The macroscopic onset field increased from (2.0 ± 0.1) V/µm to (3.0 ± 0.1) V/µm by the enlarged distance of the substrate from the beginning of the growth zone.

Hedrich *et al.* [23] and as presented in Figure 4.1.

The CVD growth process of ZnO NWs is known to be highly sensitive to the substrate's position relative to the precursor source as well as to the substrate's temperature [23, 159]. Elsewhere, the increase of the substrate's distance from the precursor boat was reported to cause a decrease in NW length [166]. Therefore, the herein observed increase in onset field may be caused by the combination of the increased distance from the precursor source boat and the change of the substrate's temperature by modification of its position in the growth zone.

As a summary for this study, the onset fields of the investigated ZnO emitter samples are compared to the change of the mean NW length and of the effective FEF with variation of the synthesis conditions in Figure 4.21. As shown in Figure 4.21 (a), the onset field increases with decrease of the mean NW length, because of the expected corresponding decrease of the geometrical field enhancement effect. Hence, the lowest onset field is observed for the longest ZnO NWs and vice versa. This result is further supported by the effective FEFs that were derived from the experimental FE data for each synthesis parameter set. Figure 4.21 (b) shows that the effective FEF behaves contrary to the onset field, namely the lowest onset field correlates with the largest FEF and the other way around. Thus, the relative NW lengths of the ZnO emitters agree well with the trend of the macroscopic onset fields and of the effective FEFs, which possibly enables the prediction of the field emission behavior from emitter dimensions for further synthesis parameter variations. This observation indicates the reliability and reproducibility of the FE acquisitions in our optimized FE measurement configuration that is presented in chapter 3.

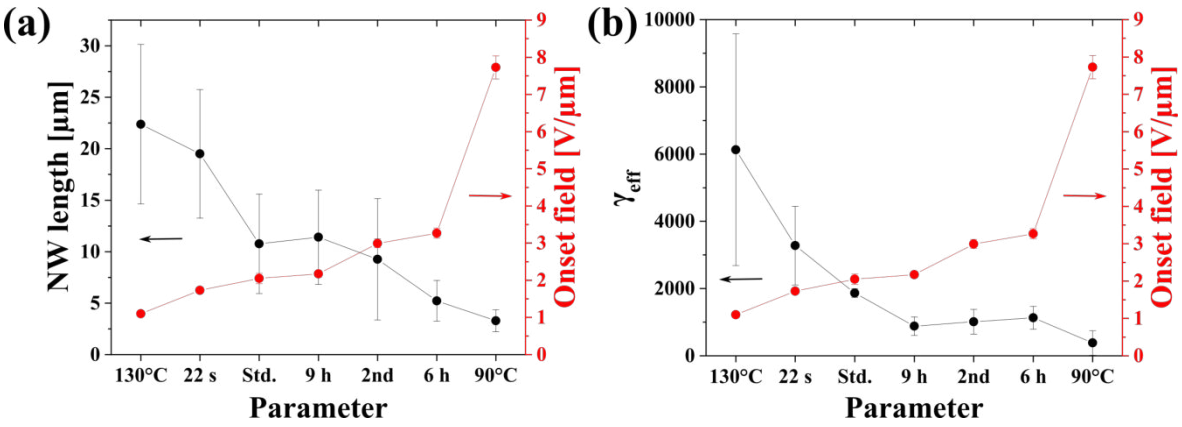

Figure 4.21: The onset field (red) is plotted as a function of the varied synthesis parameter from lowest to highest value from left to right. For comparison, the mean NW length (black) is presented in **(a)** and the effective FEF (black) is shown in **(b)**. Note, "Std." refers to the standard growth process, "2nd" to the position variation in the ceramic boat and the other FE samples are labeled according to the respective synthesis parameter that was altered.

4.3 Substrate Type B - Silicon Nitride Membranes

Herein, the substrates for the ZnO growth were replaced by square SiN NMs (former section 4.2 used Si NMs). The residual stress of LPCVD SiN films can be tailored over a wide range from tensile nature with a magnitude of +1 GPa to compressive stress of about -100 MPa by variation of the precursor gas flow ratios. Usually, silicon-rich films are used for fabrication of membranes because of their low residual stress of around +200 MPa [140, 148, 167]. Low-stress SiN NMs are often employed as vacuum windows for X-ray spectroscopy or as sample holders for TEM, as these flat and chemical inert membranes have a certain strength against static load and are transparent to visible light as well as to X-rays and electrons [168]. Since the NM fabrication was conducted in-house from commercially bought, SiN coated Si wafers (see section 4.1.1), the membrane dimensions can be scaled up easily, which is an advantage compared to the predefined size of the Si NM substrates. In the first part, the dimensions of the ZnO emitter array grown on a SiN NM are examined and the FE properties are investigated. In the second part, the possible impact of the membrane size on the FE properties is studied.

4.3.1 Standard Growth Process - Morphology

Herein, the ZnO structures grown on a 100 nm thick, 3x3 mm^2 SiN NM were investigated. Note, the sputter shadow mask was applied for catalyst deposition (60 s sputter time) prior to the ZnO growth according to the "standard process" (section 4.1.3). Similar to the ZnO shapes that were formed on the Si NMs (Figure 4.9), an array of randomly distributed ZnO NWs of different length were obtained, as shown in Figure 4.22. Large, sparsely distributed ZnO NWs were noted (Figure 4.22 i), which are surrounded by smaller ZnO needles (Figure 4.22 ii). Further, the cross section through the membrane, which was obtained by FIB milling, revealed the existence of a layer of densely packed ZnO crystallites directly on the

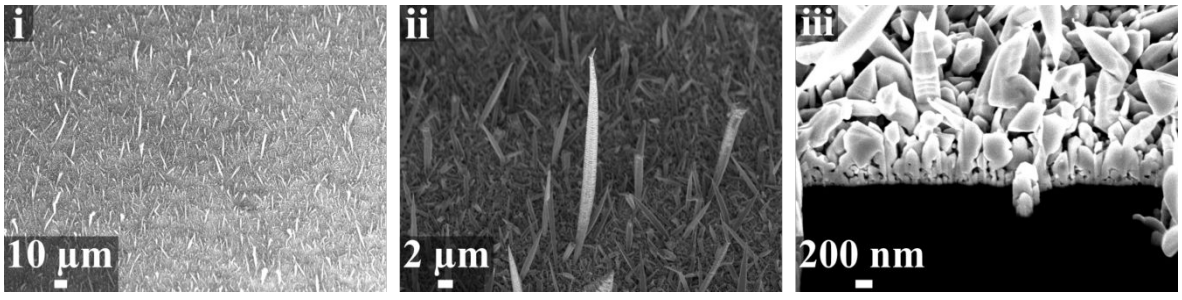

Figure 4.22: Large, sparsely distributed ZnO NWs (i), shorter ZnO needles with a higher density (ii) and a film of ZnO crystallites (iii) were grown on the SiN NM. The cross section through the membrane was prepared by FIB milling (30 kV, 50 pA) and the SEM images were taken under a tilt angle of 54 °, both with the Crossbeam 550 by Zeiss.

free-standing membrane substrate (Figure 4.22 iii). The NM itself is not visible in the given cross section because of the poor material contrast between the insulating SiN film and the free space below the membrane. The mean dimensions were derived from SEM images of 20 outstanding, well separated NWs using ImageJ [157] according to the description given in section A.3.1 and are summarized in Table 4.6. The average height of the ZnO crystallites was determined to be (825 $\pm$ 157) nm, with the mean and standard deviation derived by measuring at nine different locations in the cross section image. The dimensions observed for the ZnO NWs on the SiN NM are similar to the values found for the ZnO emitters on the Si NM within their standard deviations (section 4.2.1, Table 4.2), which indicates the reproducibility of the catalyst-assisted MOCVD process. Additionally, the change from highly-doped Si to the insulating SiN as substrate seems to have no considerable influence on the emitter morphology. Therefore, similar ZnO growth mechanisms are expected on the SiN substrates as already discussed in section 4.2.1 for the Si NMs.

It was possible to identify gold droplets on the tips of shorter wires (Figure 4.22 ii) as shown in Figure 4.23, which is presumed to be an evidence for the VLS growth regime [159]. However, it was not possible to detect any significant amount of gold at the tips of large NWs (Figure 4.22 i) or along them, as exemplarily displayed in Figure A.3 (a) in the appendix. In contrast to the Si NM substrates, it was not possible to find gold dots in the cross section image at the root of the ZnO structures (Figure A.3 (b) in the appendix), which would be an indication for a VSS driven growth mechanism [158]. On the one hand, the amount of remaining gold at the NW roots may be below detection limits. On the other hand, gold droplets were apparently not located at the small area of the cross section, but may be present at other

	ZnO NWs on SiN NMs
Length (h) [µm]	50 ± 9
Diameter ($2r_{\text{base}}$) [µm]	2.3 ± 0.6
Tilt angle [°]	90 ± 16
Tip diameter ($2r_{\text{apex}}$) [µm]	0.150 ± 0.072
Tip inclination (θ_{apex}) [°]	24.2 ± 23.2
Aspect ratio ($h/(2r_{\text{apex}})$)	333 ± 220
Density [NWs/mm^2]	4810 ± 548

Table 4.6: Summary of ZnO NW dimensions grown on a SiN NM. Similar to the analysis for the Si NMs, the mean and standard deviation of the different parameters were acquired by measuring 20 separate, large NWs and the NW density was determined by counting the number of ZnO structures larger than 10 µm on six separate SEM images, which were taken at different locations on the NM and with a constant magnification of 10^4.

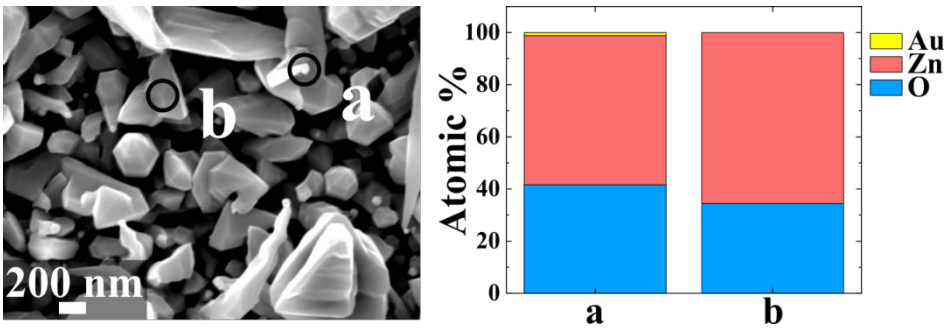

Figure 4.23: Gold was detected by EDX at the bright dot at the wire's tip that is marked by (a). In contrast, no gold was found on the ZnO at area (b). The SEM image and EDX spectra (8 kV, 4.7 nA) were taken with the Crossbeam 550 by Zeiss.

Figure 4.24: Selection of tip shapes found for the ZnO NWs grown on a SiN membrane. The SEM images were taken under a tilt angle of 54 ° with the Crossbeam 550 by Zeiss.

locations. Moreover, a variety of tip shapes was noted for the large NWs (Figure 4.22 i) as demonstrated by the selection presented in Figure 4.24. In addition to conical shaped tips and secondary structures grown perpendicular to the wire's growth direction, reoriented growth axes were observed, which may indicate a screw dislocation mechanism [68].

4.3.2 Standard Growth Process - Field Emission Measurements

Herein, the FE properties from a sample with ZnO NWs grown on a 3x3 mm^2 SiN NM were investigated. All FE measurements were carried out and analyzed according to the description in section 3.4 with the specific characterization conditions listed in Table 4.3.

The onset fields for two subsequent mountings of the same FE sample in the Voyager setup are given in Figure 4.25. The mean onset field for FE from the as-deposited sample (1st mounting, plotted in purple) as well as for the second mounting after previous FE measurement (2nd mounting, black) are shown. A reduction of onset field from the first to the second mounting of 0.5 V/µm is found. Note, the onset fields were determined for the 2nd–5th measurement after mounting the sample in vacuum and for emission currents below the microampere range to exclude FE-initiated effects as far as possible. Yet, a considerable number of measurements was executed for the 1st mounting that may have changed the FE properties of the examined sample irreversible. Furthermore, the ZnO NWs were investigated by SEM between the two mountings in the FE setup. Consequently, the change of the

SiN NMs - Onset fields

Mounting	d [µm]	F_M^{onset} [V/µm]
1st	250	2.0 ± 0.1
2nd	250	1.5 ± 0.1

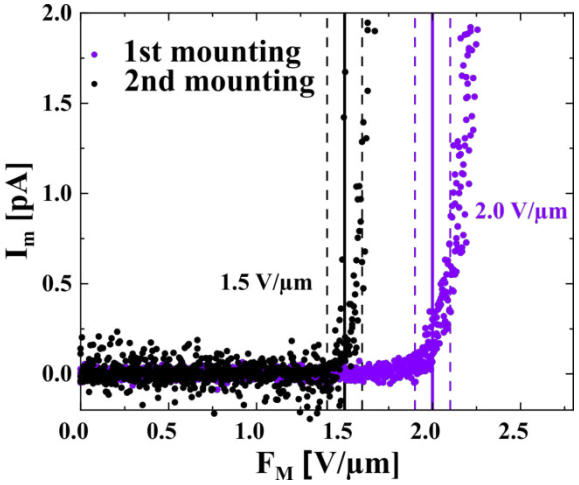

Figure 4.25: The mean onset field for FE was derived from four subsequent measurements from the ZnO emitters on the SiN NM for the 1st mounting of the as-deposited sample (purple) and for the 2nd mounting after previous FE acquisition and SEM imaging (black).

local structure and of the surface electronic properties between 1st and 2nd mounting cannot be excluded and may explain the observed onset field shift.

To investigate the maximum possible emission current from the ZnO emitters grown on the SiN NM, the highest allowed emission current that functioned as termination condition for the FE measurements, was gradually increased for the 2nd mounting of the FE sample. A notable shift in onset field compared to the preceding *I-V* curves occurred when the measured current reached the microampere range as summarized in Figure 4.26 (a). From the mean value of 1.5 V/µm, the onset field increased further in the following measurements up to 2.5 V/µm. Note, the applied electric field was held constant for 3 h when the emission current reached a predefined value in the microampere range, to test the emission stability of the emitters for the 5th, the 7th and the 9th measurement, which will be discussed in detail later in this section (see Figure 4.28). Additionally, an electrical discharge occurred during the 8th measurement accompanied by immediate voltage trip at the power supplies. Hence, the extended emission from the ZnO NWs at a constant applied field as well as the electrical breakdown led to a notable shift of the onset field for the respective subsequent FE measurement, which indicates a modification of the cathode's physical properties. Typically, FE-initiated structural modifications of the cathode are attributed to the local resistive self-heating caused by large emission currents, and the subsequent melting and vaporization of emitter material (see section 2.1.2) [1, 29].

Furthermore, the effective FEFs were derived from the FN plot for each of the FE measurements. The mean value of 2349 ± 226 for the 2nd–5th measurement is shown in Figure 4.26 (a) in gray. For comparison, the single values for the 6th–9th measurement are

presented, which exhibit a decreasing trend down to 993 (9th). Note, the orthodoxy test was passed for all measurements (2nd–9th), because the range of the mean extracted scaled barrier fields (equation 2.43) of 0.17 ± 0.03 to 0.27 ± 0.07 is in the apparently reasonable range between 0.14 and 0.43 [83]. As expected from theory, the FEF behaves contrary to the onset field because a larger geometrical field enhancement effect typically leads to a lower macroscopic electric field that is needed to allow for FE. The considerable modification of the FEF compared to the initial value (from 2nd–5th measurement) may be another evidence for the impact of the extended current emission at constant applied field as well as of the electrical discharge on the geometrical shape of the ZnO emitters. In agreement with the previous analysis for Si NM substrates (section 4.2.2), the effective FEFs derived from the respective MG plots are comparable to those found with the FN plot. Therefore, the MG plot analysis is not discussed further.

For determination of the effective FEF values, the FE data was linearized as presented in Figure 4.26 (b) for the 6th–9th measurement. For all four curves, the data shows a linear behavior after onset of FE in the low field region (1st slope), but a non-linear trend for high electric fields (low $1/V_m$, 2nd slope). Therefore, the linearized data was divided into two segments (low and high field region), which were analyzed separately. A change in slope was not observed for the 2nd–5th measurement, since the FE acquisitions were terminated before reaching the high field region. Hence, only the 1st slope (yellow fit) was considered for

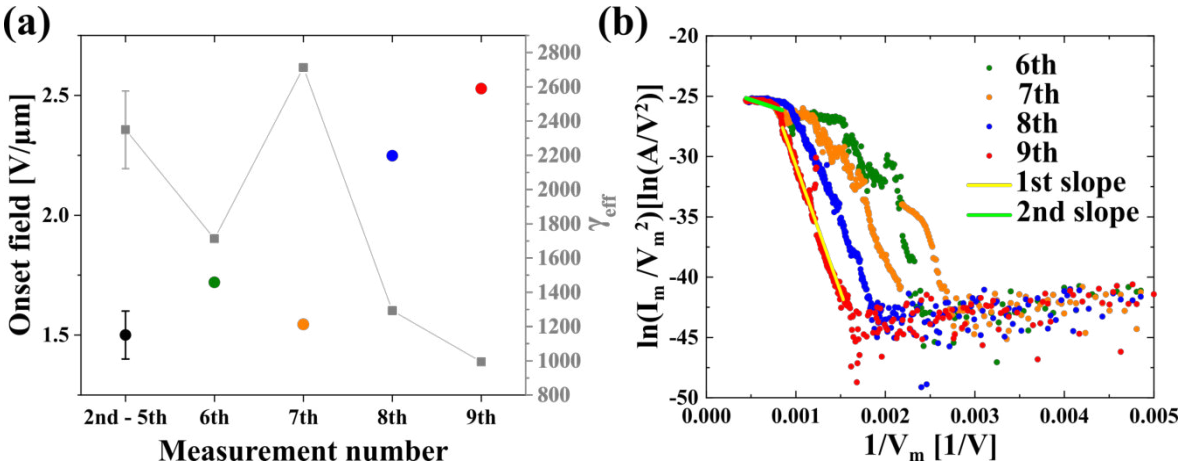

Figure 4.26: (a) The mean onset field of the 2nd–5th measurement (2nd mounting, plotted in black), as well as the single values derived for each of the *I-V* curves from the 6th–9th measurement (green, orange, blue, red) are shown. Additionally, the effective FEFs were derived from the linear part of the FE data in the FN plot (gray). **(b)** The 6th–9th FE measurement (green, orange, blue, red) are presented in the FN plot. Shifts of the onset field to higher values (lower $1/V_m$) become apparent for every further measurement, which was attributed to FE-initiated modifications of the emitters' physical properties. The linearized FE data can be divided into the low field region (1st slope, yellow line) and the high field region (2nd slope, green line), which is exemplarily highlighted for the 9th measurement.

the previous FE data analysis that is summarized in Figure 4.26 (a). The 2nd slope (green fit), which is indicated in Figure 4.26 (b), was examined for the measurement numbers 6th–9th. However, unrealistic large FEFs of 4705 up to 41478 were derived from the 2nd slope, which emphasizes that the FN theory cannot be applied in the high field region. This interpretation is also supported by the extracted values for the orthodoxy test (equation 2.43) performed for the 2nd slope. The extracted scaled barrier fields of 3.3 ± 4.3 and of 6.0 ± 7.6 from the high field region are far beyond the apparently reasonable range for ZnO emitters (0.14–0.43) [83].

In conclusions, only the effective FEFs derived from the low field region (1st slope) of the FE data in the FN plot are assumed to be reliable and are applied for comparison to theoretical calculations in the following. The mean FEF of the ZnO NWs on the SiN NM of $2349 \pm 10\,\%$ is comparable to the value extracted for the ZnO emitters on the Si NMs, namely $2056 \pm 12\,\%$ (section 4.2.2, Table 4.4). Therefore, the FE properties of the ZnO emitters seem to be independent of the herein investigated substrate types in the low field region.

For comparison of the effective FEFs to the emitter morphology, theoretical models were used to calculate the apex FEFs from the dimensions of the ZnO NWs given in Table 4.6. The theoretical FEF values are summarized in Table 4.7. The values determined with the models (A)–(C) are smaller compared to the mean effective FEF of 2349 ± 226 derived from the 2nd–5th FE measurement. The theoretical value of 2500 from model (D) is the closest to the experimentally extracted FEF. Thus, the combined consideration of the tip inclination and the emitter tip-to-grid distance for calculation of an apex FEF seems to yield a better agreement with the experimental FE data than the models (A)–(C), which was also observed and discussed in more detail for the ZnO emitters on Si NMs in section 4.2.2 (see Table 4.5).

Further, the impact of electrical field screening on the FE properties was estimated. A mean distance between nearest neighbors of about $b = 14.4\,\mu m$ was derived from the NW density

ZnO NWs on SiN NMs - Theoretical FEFs

Model number	Equation number	Value
(A)	$\gamma_{apex}(3)$ (2.23)	545
(B)	$\gamma_{apex}(4)$ (2.25)	169
(C)	γ_{c-disc} (2.27)	652
(D)	$\gamma_{apex}(5)$ (2.26)	2500

Table 4.7: The theoretical values for the apex FEF are shown, which were calculated with the average NW dimensions from Table 4.6. For model (B), a factor of $\alpha_{base} = 0.88$ was used for conical shaped emitters and for model (C), equation 2.28 was applied for calculation of $R_{c-disc} = 0.077\,\mu m$. For model (D), the tip inclination of 24.2 ° and the emitter tip-to-grid distance of $D = 200\,\mu m$ were used.

of 4810 NW/mm^2 (see section 4.2.2 for detailed description). For randomly distributed wires in an array, the FEF of an isolated single emitter would be reduced by 62 % (equation 2.30 with a = -2.41, c = 0.74) [54]. Note, the NW density was determined from ZnO structures larger than only 10 µm. Hence, the FE may originate from much larger and well-separated emitters because the mean NW length was found to be 50 µm (see Table 4.6). According to the theoretical models shown in Figure 2.4 (b), a distance between emitters that equals four times the NW height would lead to a negligible screening effect. Therefore, a mean NW distance of 200 µm and thus, a theoretical NW density of 25 NW/mm^2 is supposed to eliminate the electrical field screening among neighboring, 50 µm long emitters in an array.

Figure 4.27 (a) shows the two subsequent *I-V* curves with the highest emission currents reached for the ZnO emitters on SiN NMs, namely the 8th (blue) and 9th (red) measurement. A maximum current of 50.9 µA at a voltage of 2248 V was obtained, which corresponds to a macroscopic ECD of 141.5 µA/cm^2 at a macroscopic electric field of 9.0 V/µm (9th, red). The reduction of the current slope in the high field region becomes obvious when the FE data is plotted on a logarithmic scale, which is displayed in Figure 4.27 (b).

In contrast to the observations for the ZnO NWs on Si NMs in the last section (Figure 4.16), no distinct increase of the emission current slope is observed after the initial decrease in

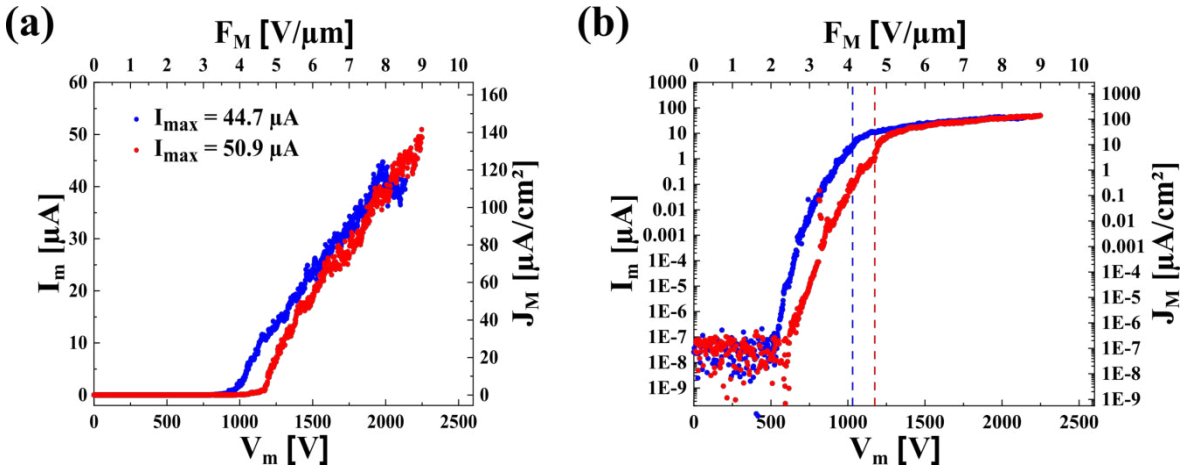

Figure 4.27: (a) The FE data for two subsequent measurements, namely the 8th (blue) and the 9th (red) one, is plotted for the measured current in dependence on the measured voltage (left and bottom axis) as well as for the macroscopic ECD and for the macroscopic electric field (right and top axis). For the conversion, the emitter-grid distance and the macroscopic emission area of 250 µm and of 0.36 cm^2 were used, respectively. In the 8th measurement, a maximum current of 44.7 µA (124.2 µA/cm^2) at a voltage of 1980 V (7.9 V/µm) was obtained. In the 9th sweep, a maximum current of 50.9 µA (141.5 µA/cm^2) at a voltage of 2248 V (9.0 V/µm) was detected. **(b)** Herein, the two *I-V* curves are plotted for a logarithmic y-axis. For both samples, a distinct change of the slope is observed for macroscopic electric fields larger than 4.1 V/µm, which is marked by the vertical dashed lines.

the high field region in the present section. The transition to the high field region for the ZnO NWs on the Si NM substrate was characterized by a reduction of the current slope in a narrow field region, followed by an enhanced rise of emission current. This observation was attributed to the saturation of the emission current from the conduction band of ZnO and the subsequent onset of electron emission from the valence band, possibly enabled by energy band bending caused by the increasing electric field [46, 67]. However, for the ZnO emitters on the SiN NMs, only a considerable reduction of emission current slope with rising electric field is noted. Since the same preparation methods for the ZnO NWs were used and the NW dimensions showed to be comparable for both membrane types, the different conductivity of the substrates may have an impact on the FE properties in the high field region. Probably, the limited charge carrier supply of the insulating SiN substrate impedes a considerable rise of emission current in the high field region as it was observed for the highly-doped Si NM substrates. Hence, only the saturation of emission current from the conduction band may be detected here, which was attributed to the limited charge carrier generation rate inside the semiconductor [61, 67].

Additionally, it is most likely that vacuum space charge is formed in front of the cathode that shields the emitters' surface from the applied electric field. Thus, the intensity of the electric field becomes dependent on the local ECD [2, 46]. This explanation can be corroborated by experimental observations for the high field region. At an applied voltage of 2250 V, a current of 83 µA was displayed at the cathode's power supply, which is about 38 % larger than the maximum current measured at the anode. In addition, the voltage at the grid's power supply showed a bias of -643 V at the same applied voltage instead of the defined -100 V. Therefore, it is supposed that the vacuum space charge is the predominant mechanism that causes the observed non-linearity in the high field region and probably impedes the observation of other, energy band related effects.

Presumably, the grid plays an important role for the accumulation of vacuum space charge. The utilized 59 lpc nickel mesh has a transmission of 73 % (see Table 3.3), which may explain the significant difference between the detected current at the cathode's power supply and the current measured at the anode. Therefore, it may be necessary for reliable measurements of larger currents in future, to modify the transmission rate of the grid. Note, the exchange of the grid is not trivial, as it needs to be stiff and flat for proper distance control towards the cathode as it was already discussed for the FE assembly modifications in section 3.3.2. For future applications, the usage of tailor-made meshes from metallized silicon nitride on a wider silicon support grid may be beneficial, as good mechanical stability was reported for those grids and their transmission rate can be adjusted to some extend. However, a trade-off between a maximum transmission and an uniform distribution of the electric field has to be considered [169, 170]. Another approach is the insertion of an additional electrode between

emitter and grid, which is used to focus the beam of emitted electrons to reduce electron losses at the grid electrode. The current that reached the anode was reported to be 2.6 times larger for this tetrode arrangement compared to the results for the conventional triode-type configuration [171].

Finally, the stability of the emission current from the ZnO NWs was investigated by applying a constant field when reaching a predefined measured current. After obtaining a current value of 1 µA, of 10 µA and of 50 µA, respectively, the field was held constant for 1440 steps with a waiting period of 3720 ms before acquiring a current value, which is combined with 10 PLCs defined for the picoammeter that adds the waiting period of 200 ms to the total time between two measurement points. Therefore, the current was acquired for a total time of around 94 min at one constant applied field. After this period, the electric field was further increased, until the defined threshold current is reached again and then, the field is held constant a second time for the same duration. Figure 4.28 displays the mean emission current at the three different predefined current levels. The percentage standard deviation reduces with increasing current level from 1.2 µA ± 8.3 %, to 14.7 µA ± 5.4 % and finally to 51.2 µA ± 2.9 %, which indicates the reduction of current fluctuations with rising emission current. Furthermore, a slight increase of the emission current within the initial 10 min was noted at the three current levels. For the largest emission current of 51.2 µA, the applied voltages at the power supplies dropped to zero after 12 min, but the NM substrate was still intact after the measurement. Probably, the actual emitted current was above the trip current

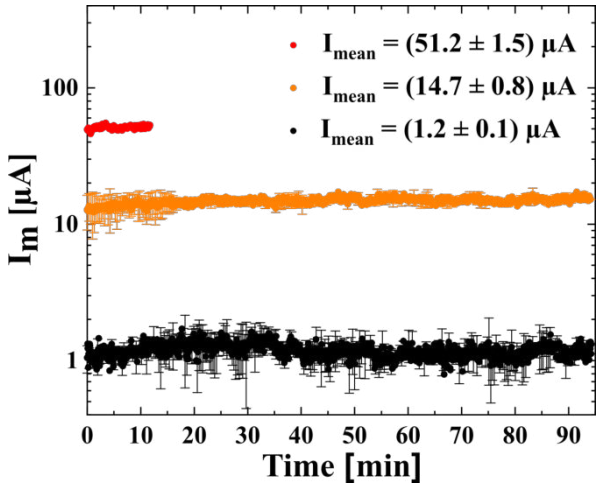

Figure 4.28: The emission current was recorded two times for 94 min each at a constant macroscopic field of (3.12 ± 0.02) V/µm (5th measurement, black), of (5.24 ± 0.02) V/µm (7th, orange) and of 9 V/µm (9th, red). The error bars display the standard deviations from the mean emission current that was determined from the two subsequent measurements at each of the above given electric fields. For clarity, only every fifth error bar is shown.

of 0.1 mA, which was defined as switch-off condition for the high voltage of the power supplies (see section 3.2.3). Hence, less current reached the anode than it was emitted by the cathode, which was caused by the limited transmission of the grid electrode. The low trip current threshold led to an early cancellation of the measurement at 51.2 µA, but was not increased further since it would risk the destruction of the fragile NM substrate by an electrical breakdown.

The observed current increase within the first 10 min as well as the enhanced stability of the emission current with rising current level, are attributed to the desorption of adsorbates from the ZnO surface. In an initial stage of the measurement, adsorbates may shield the interior of the ZnO from the applied electric field, which would reduce the local electric field on the surface of the emitter. Consequently, the magnitude of energy band bending would be lower and thus, the FE current is reduced compared to an ad-layer free ZnO emitter. However, with increasing emission current, the desorption of ad-layers is promoted by the resistive self-heating of the emitters in vacuum, which may correlate with the observed increase of FE current within the first 10 min [1]. Additionally, emission current fluctuations are often attributed to the variation of the adsorbate coverage over time. The current stability was elsewhere reported to increase with emitter temperature, since the desorption of ad-atoms is promoted by the local self-heating [47]. Thus, the observed stability enhancement with rising emission current may be caused by the simultaneous increase of the FE-induced emitter heating (see section 2.1.2) and the correspondingly reduced occurrence of adsorption processes.

In summary, the variation of onset fields as well as of the effective FEFs (summarized in Figure 4.26) may indicate that the ZnO structures are altered during each of the high current measurements by FE-induced mechanisms, such as local self-heating and related effects like surface diffusion [1]. Furthermore, the maximum macroscopic field of 9 V/µm = 0.009 V/nm multiplied by the effective FEF of 993 (9th measurement) would correspond to an intense local electrical field of 8.9 V/nm. The image charge affected SN barrier is theoretically pulled down by about $\Delta\phi_{SN}$ = 3.6 eV through the local electric field (see section 2.1.2), which would enhance the probability for electrons being also emitted above the barrier and contribute to the measured emission current.

The ZnO NWs were investigated by SEM imaging before and after the high current and stability measurements, namely before and after the 2nd mounting of the FE sample. Yet, no considerable morphology changes were observed for the ZnO NWs or their apexes. Since the detailed micro- and nanostructure at emission site defines the FE properties as discussed in section 2.2.1, the FE-initiated emitter modifications may be below detection limits of the SEM. Future analysis of the emitters with other techniques, such as X-ray diffraction (XRD) or TEM would be needed to reveal the effect of high emission currents on the crystallographic

nature of the wires and on the detailed apex shapes as well as dimensions of single emitters, respectively [69, 72, 76].

Besides structural changes, the observed impact of high emission current on the FE properties of the ZnO emitters may also be attributed to the change of the electronic surface constitution and thus, to the modification of the apparent work function of the emitter material by thermally induced desorption of ad-layer substances [25]. In this thesis, only the *I-V* curve shift between the initial measurement after mounting the sample in vacuum and the subsequent one was directly attributed to the influence of adsorbates on the emission current (see section 3.4 for details). However, it is certainly possible that unknown species are still bound to the ZnO emitters, since only considerable heating can typically promote the desorption of the entire ad-layer. Furthermore, the smallest amounts of gaseous species adsorbed on the emitter's surface can lead to a considerable change of its FE properties, which was demonstrated by other researchers by investigation of the emission patterns for adsorption/desorption and surface diffusion processes of ad-layer molecules using field emission microscopy [25, 172, 173].

4.3.3 Membrane Size Variation

Herein, the lateral size of the 100 nm thick SiN membrane that was used as substrate for the ZnO emitters, was varied and the FE properties were compared. SiN coated bulk Si samples were used as substrate for the ZnO NW growth as reference for comparison to the 3x3 mm^2 and to the 5x5 mm^2 SiN NMs. Note, two separate samples were considered for each substrate size that was examined. For each of the samples, four subsequent FE measurements from the as-deposited ZnO emitters, namely the 2nd–5th measurement, were analyzed according to section 3.4 and the specific characterization conditions from Table 4.3 were applied. Herein, the FE acquisitions were terminated for emission currents below the microampere range to exclude FE-initiated emitter modifications as observed in the last section.

In general, a reduction of the onset field is noted with increasing membrane size, namely it decreases from a mean level of (2.52 ± 0.03) V/µm for bulk, to (2.17 ± 0.24) V/µm for 3x3 mm^2 NMs and finally to (1.28 ± 0.17) V/µm for 5x5 mm^2 NMs. Thus, the onset field is almost reduced by 50 % when the 5x5 mm^2 SiN NM is used instead of a bulk substrate. Furthermore, the effective FEFs show the expected trend that is contrary to the onset field. Therefore, the reduction of the onset field is accompanied by an increase of the effective FEF. From bulk to the largest NM size, the FEF increases from 1521 ± 207 (bulk), further to 2018 ± 160 (3x3 mm^2 NMs) and then to 4006 ± 1743 (5x5 mm^2 NMs).

The displacement of the NM towards the grid electrode, which may be caused by the applied electrostatic field during the FE measurement, is considered as the predominant reason for the enhanced FE properties of the conductive ZnO NWs that stand on a flexible base.

According to other work, the bending of the membrane is increased as a consequence of the rising electrostatic pressure. Thus, the emitter-grid distance becomes a function of the applied voltage [164]. In addition to the geometrical FEF of the ZnO emitters, the NM displacement basically introduces another FEF by the substrate bending, which is a function of the applied voltage and depends on the material properties and dimensions of the NM substrate.

The observation of the enhanced FEF with increasing membrane size—which corresponds to a larger NM displacement for the same applied voltage—is in agreement with the results by Pekarek *et al.* [15]. Their simulations for the displacement of a flexible membrane showed that the maximum possible bending rises with increasing membrane size [15]. Additionally, the geometrical field enhancement effect of the ZnO emitter array may also be raised by the reduction of the electrical field screening among neighboring emitters. Convex bending of the NM towards the grid electrode can cause an increase of the tip-to-tip emitter distances and thereby, lead to a reduction of the electrical screening [94]. However, a reliable estimation of the impact of electrical field screening on the FE behavior of the examined disordered ZnO arrays was not possible, since the ratio of emitters that contribute to FE is unknown and may also change with the applied electric field (see section 4.2.2).

A theoretical model was used to approximate the effect of NM displacement caused by the electrostatic field on the FE current for different membrane dimensions. Square, 100 nm thick membranes with NM areas of 3x3 mm^2 and of 5x5 mm^2 were considered. Additionally, the following material parameters were used that are typical for SiN membranes: A Young's modulus of E_M = 300 GPa, a residual stress of σ_M = 200 MPa and a Poisson's ratio of ν_M = 0.25 [92, 148]. In the first step, the maximum displacement at the membrane's center was calculated in dependence on the applied differential pressure with equation 2.53. As shown in Figure 4.29 (a), the displacement for the same applied pressure is enhanced when the NM is enlarged (compare red to blue) as well as when the NM thickness is reduced (compare green to blue), which is in agreement with the predictions by Pekarek *et al.* [15].

In the second step, the differential pressure was replaced by equation 2.54 to plot the membrane's displacement as a function of the applied voltage in Figure 4.29 (b). The initial membrane-electrode distance for zero electric field was set to d_0 = 250 µm. The tendencies noted for the different membrane sizes and thicknesses in dependence on the applied differential pressure are resembled by the general trends of the maximum membrane displacement observed with increasing voltage.

In the last step, the voltage-dependent NM displacement and the corresponding voltage values were inserted into equation 2.56 to estimate the emission current from emitters on a flexible base. The results are displayed in Figure 4.30 (a). The effect of the NM displacement on the FE current is already noted in the picoampere range and as expected, the NM deflection leads to an earlier rise of the emission current because of the continuous reduction of the

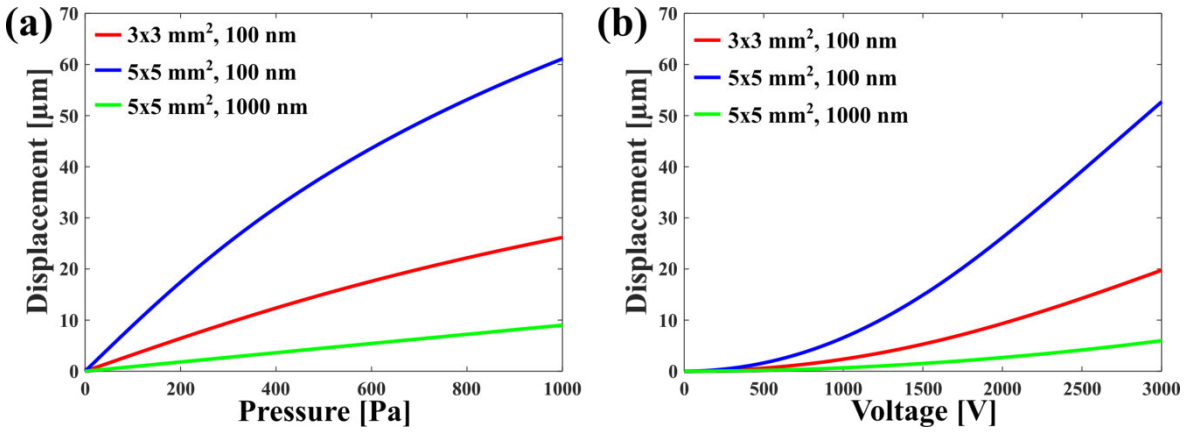

Figure 4.29: (a) Maximum NM displacement as a function of the applied differential pressure according to equation 2.53. The increase of the membrane size from 3x3 mm^2 (red) to 5x5 mm^2 (blue) for the constant NM thickness of 100 nm, leads to a signification increase of the maximum NM displacement for the same external pressure. The 10 times thicker, 5x5 mm^2 NM (1000 nm, green) shows a maximum deflection that is notably smaller than for the reduced NM area of 3x3 mm^2 with 100 nm thickness. **(b)** Maximum NM displacement as a function of the applied voltage (equation 2.54) for the membrane sizes of 3x3 mm^2 (100 nm, red), of 5x5 mm^2 (100 nm, blue) and of the thicker 5x5 mm^2 NM (1000 nm, green).

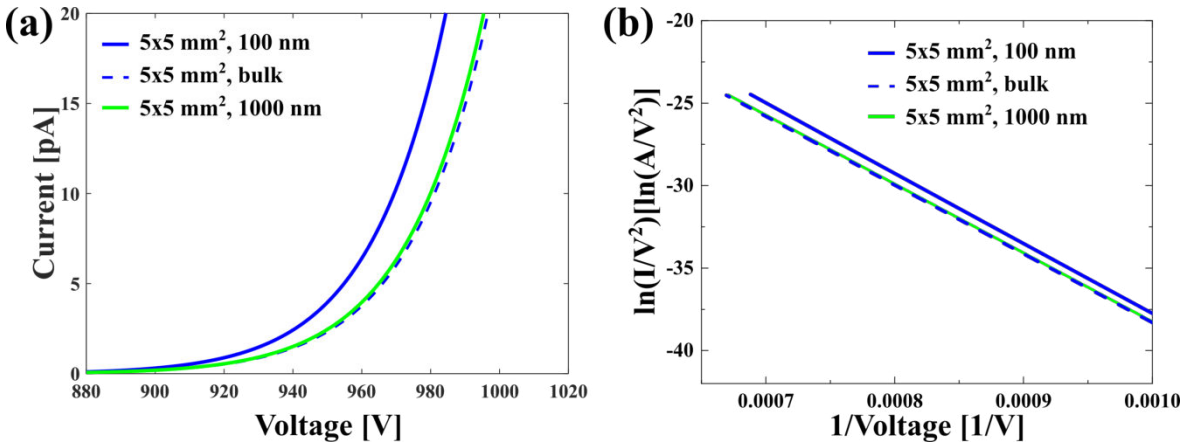

Figure 4.30: (a) Emission current as a function of the applied voltage plotted according to equation 2.56 with the voltage-dependent emitter-grid distance, an emission area of 5x5 mm^2, a FEF of 500 and a work function value of 5.3 eV [46]. The NM deflection induced by the electrostatic field causes the emission current to rise at lower applied voltages (solid blue line) compared to the bulk emitter that was plotted according to the FN equation 2.9 with the constant emitter-grid spacing (dashed blue line). Only a slight enhancement of FE current is noted for the 1000 nm thick NM (green) compared to the bulk version. **(b)** The corresponding FN plot shows the linearized data for the three theoretical curves plotted up to an emission current of 50 µA, which was also obtained experimentally (see section 4.3.2, Figure 4.27). With rising applied voltage, the discrepancy between the emission current from the membrane and from the bulk substrate becomes larger and thus, the impact of NM displacement rises with increasing electrostatic pressure.

emitter-grid spacing with increasing applied voltage (compare blue solid to blue dashed line). For the assumption of an emission area of 5x5 mm^2, an emission current of 1 pA is reached at a voltage of 933 V (dashed blue line). When the same area is supposed to be a flexible, 100 nm thick NM, the voltage required to reach 1 pA is reduced by about 1 % (solid blue line). With rising emission current, the impact of the NM displacement on the emission current shows an increasing trend. However, the threshold to obtain an emission current of 1 µA is still only reduced by 2 % by the effect of NM deflection.

Furthermore, the three theoretical *I-V* curves for the emission area of 5x5 mm^2 where linearized in the FN plot in Figure 4.30 (b). With increasing applied voltage, the impact of the NM displacement on the FE properties becomes more pronounced, which is characterized by a stronger deviation between the curve of the membrane and of the bulk substrate for low values of $1/V_m$ (compare dashed to solid blue line). Additionally, a 1000 nm thick SiN NM was considered for comparison to the experimentally studied membranes that were composed of the ZnO crystallites on the SiN films (see section 4.3.1). The thick membrane is presented as green solid line in both Figures 4.29 and 4.30. Clearly, the theoretical emission current from the thicker membrane shows no considerable enhancement compared to the bulk substrate.

In summary, the earlier onset of FE with increasing size of the flexible emitter base is in agreement with our experimental observations. However, the predicted impact of the displacement on the emission current is considerably lower than experimentally observed because the theoretical calculation neglects the detailed structure of the ZnO emitters. On the one hand, the electrical field screening may be reduced for neighboring ZnO NWs by the NM bending, which can enhance the FE current. On the other hand, the local variation of the electric field distribution on the emitter's surface by bending of the complex ZnO-SiN composite membrane may lead to a notable amplification of the emission current in the experiment, which is not considered by the simple deflection model that was used for the theoretical calculations in this section.

4.4 Summary and Discussion

ZnO NW arrays were deposited on Si NMs as well as on SiN NMs by a catalyst-assisted vapor phase transport method using the precursors zinc acetylacetonate hydrate and oxygen. The dimension analysis of the ZnO structures revealed a similar morphology of randomly distributed, tapered wires with sharp tips for both substrate types, which suggests that the substrate has a minor influence on the overall growth process. Field emission was observed for the as-deposited ZnO NWs grown on both substrate types with a similar onset field of 2.0 V/µm for the measured current to overcome a 10 σ threshold from the background noise. For the Si membranes as substrates for the ZnO emitters, the maximum attained macro-

scopic ECD was 0.2 µA/cm^2 at a macroscopic electric field of 3.8 V/µm. The largest ECD of 141.5 µA/cm^2 was obtained for the ZnO NWs grown on the SiN membrane at a macroscopic electric field of approximately 9 V/µm. For comparison to other field emitters in literature, the following two turn-on fields were extracted: F_M^{on1} for the macroscopic ECD overcoming 0.1 µA/cm^2 and F_M^{on2} for J_M larger than 10 µA/cm^2 (section 3.3). For the Si NM and the SiN NM substrates, the first turn-on field is reached at 3.9 V/µm and at 3.3 V/µm, respectively. However, the second turn-on field was only obtained by the sample with the SiN substrate at a macroscopic electric field of F_M^{on2} = 4.1 V/µm. The emitters on the Si NMs did not reach this current level because electrical breakdowns caused early terminations of the measurements. Table 4.8 presents a comparison of the FE results from the ZnO emitters synthesized with the help of the sputter shadow mask on the two different substrate types. In summary, the FE properties of the ZnO NWs on SiN NMs are enhanced with increasing electric field compared to the ZnO NWs on the Si NMs, when the values for F_M^{on1} are compared. This observation may correlate with a larger maximum displacement that is expected for the SiN membranes (100 nm, 3x3 mm^2), because they are thinner and larger than the Si NMs (149 nm, 2 mm diameter) [15].

The stability of the emission current from the ZnO NWs on the SiN NM was demonstrated. It was possible to measure an emission current of 14.7 µA at a constant electric field for 3 h continuously and the fluctuations around the mean current value showed to be less than 6 %. The stability test was aborted manually and thus, the extended measurement of the emission current at constant applied field is most likely. Further increase of the emission current from the ZnO emitters on the SiN NM was mainly limited by the formation of vacuum space charge. To achieve larger emission currents, an increase of the grid transmission would be a first step. Yet, replacing the grid material is not trivial, since the mechanical stability of the control

Sputter shadow mask - Comparison of FE results

Substrate type	F_M^{onset} [V/µm]	F_M^{max} [V/µm]	J_M^{max} [µA/cm^2]	F_M^{on1} [V/µm]	F_M^{on2} [V/µm]
Si NM	2.0 ± 0.1	3.8	0.2	3.9	-
SiN NM	2.0 ± 0.1	9.0	141.5	3.3	4.1

Table 4.8: Herein, the FE properties of ZnO NWs grown on Si NMs (149 nm thick, 2 mm diameter) as well as on SiN NM substrates (100 nm thick, 3x3 mm^2) are summarized. The onset fields F_M^{onset} of the as-deposited FE samples are presented. Furthermore, the maximum obtained ECD J_M^{max} and the corresponding electric field F_M^{max} are shown. The turn-on fields F_M^{on1} and F_M^{on2} are defined by the macroscopic ECD overcoming 0.1 µA/cm^2 and 10 µA/cm^2, respectively. Note, for all results shown here, an emitter-grid distance of 250 µm and a macroscopic emission area of 0.36 cm^2 were utilized.

electrode as well as the uniform field distribution have to be maintained.

For the herein used precursor combination of $Zn(acac)_2$ and oxygen, the FE properties of the ZnO structures were only rarely investigated [23]. Compared to the FE from ZnO nanowhiskers studied by Hedrich *et al.*, the macroscopic onset field was reduced by a factor of about 15 by application of a catalyst. Most of the studies found for the MOCVD utilizing $Zn(acac)_2$ referred to a catalyst-free process [23, 24, 174–177]. Only Wu *et al.* reported on the deposition of a 10 nm thick gold layer prior to the ZnO growth with the precursor $Zn(acac)_2$. The NW growth took place selectively at the gold covered areas, however the FE properties of the nanorod shaped ZnO structures were not investigated in their study [160]. Yet, the FE from ZnO structures is well studied for other precursor combinations. For the growth of nanoneedles by MOCVD using diethylzinc and oxygen as precursors, a turn-on field of 0.85 V/µm at an ECD of 0.1 µA/cm^2 was reported and for vapor phase grown ZnO NWs a value of 6.0 V/µm was found in literature [178, 179]. In addition, for the CVD growth of nanoneedles, a turn-on field of 2.5 V/µm at 10 µA/cm^2 was reported in a review [178]. For the FE from VLS grown ZnO structures, a turn-on field of 1.85 V/µm at 10 µA/cm^2 was mentioned [75]. The turn-on fields of our ZnO NWs are comparable to the turn-on fields given as key parameters in the reviews for ZnO field emitters, which were also grown by vapor phase transport processes but with other precursors. A first investigation of the variation of onset fields with growth parameters showed that the increase of the precursor temperature reduced the required electric field for detectable electron emission almost by 50 %. In a certain combination with a thinner gold film, the onset field may be reduced even further and therefore, also the turn-on field.

The above cited studies were exclusively carried out on bulk substrates. Usually, polymers and carbon fabrics are used as flexible substrates for semiconductor FE cathodes that are made from ZnO, CNTs, Si or diamond. One of the main issues for the growth of emitters on flexible polymers is their poor adhesion, which increases the risk for electrical breakdown provoked by charged particles that can be dragged across the emitter-grid vacuum gap by the electrostatic field (section 3.1). Furthermore, the substrate's low chemical stability in harsh environments prevents the direct growth of emitters by processes that require elevated temperatures. Thus, the available direct deposition processes are limited or a transfer of the emitters to the flexible base needs to be carried out after their previous deposition on another bulk substrate. For ZnO emitters on polymers, turn-on fields of 1.3 V/µm up to 4.2 V/µm for an ECD of 10 µA/cm^2 were reported, which are again comparable to our results [163].

Herein, another group of flexible (carbon-free) substrates has been added. Note, these free-standing inorganic membranes facilitate direct growth of nanostructured field emitters at high temperatures. As a consequence, these kinds of FE samples can be employed in harsh environment and at elevated temperatures.

5 ZnO Emitters - Porous SiO_2 Template

Besides affecting the constitution of a gold film during deposition—as it was done with the sputter shadow mask in the last chapter—structuring of the substrate's surface is another approach to manipulate the catalyst particle distribution, because the dewetting behavior of a thin film typically correlates with the surface structure of the underlying base [146]. The impact of porous substrates on the dewetting of thin gold layers was already shown for porous silicon [180] as well as for pores in anodic aluminum oxide [181].

Herein, a porous SiO_2 template is utilized to guide the catalyst particle formation from a gold film. During the heating ramp of the ZnO growth process, the sputtered gold layer agglomerates into particles while the porous template confines the gold droplets spatially. Therefore, a certain dependence of the catalyst size distribution on the porosity of the SiO_2 film is expected, which may be reflected by the morphology of the ZnO structures as well as by their FE properties. In the first part of this chapter, the sample fabrication is explained with a strong focus on the synthesis route for the porous SiO_2 template on p-doped bulk Si as well as on free-standing SiN membranes. In the second part, the morphology and the FE properties of the ZnO emitters are investigated for both substrate types individually.

5.1 Sample Fabrication

The fabrication process of the FE samples is based on the following four steps: First, the substrate preparation, second, the synthesis of the porous SiO_2, third, the deposition of the thin gold film and fourth, the ZnO growth process. The key aspect of this part is the optimization of the processing route for the porous SiO_2 template on bulk samples as well as its modification for the application on free-standing SiN NMs.

5.1.1 Silicon Oxynitride

A subtractive preparation route based on the approach by Ghazaryan *et al.* was employed for the synthesis of porous SiO_2 films [182]. Silicon oxynitride (SiO_xN_y) was deposited with a plasma-enhanced chemical vapor deposition (PECVD) system (SI 500D from Sentech Instruments GmbH). Subsequently, the SiN_y compounds were selectively removed by wet

etching of the SiO_xN_y in hot phosphoric acid (H_3PO_4) to generate porous films composed of the remaining SiO_x. The refractive indices (RIs), which were measured with a spectroscopic ellipsometer, were used as an indication for the composition of the as-deposited SiO_xN_y as well as for estimation of the porosity of the resulting porous SiO_x. For enhancement of the porosity of the SiO_x, the RI of the SiO_xN_y was increased as much as possible, which corresponds to a rise of the amount of SiN_y compounds that were incorporated in the as-deposited film. In general, the porosity of the SiO_x was determined by the initial composition of the SiO_xN_y film as well as by the etch duration in the H_3PO_4.

As the first step, the PECVD processes for SiO_x and SiN_y were investigated by modification of the precursor gas compositions as shown in Figure 5.1. A gas mixture of argon (Ar, purity 6.0) and silane (5 % SiH_4 (5.0) in He (5.6)) was used with addition of oxygen (O_2, 5.0) for SiO_x and of ammonia (NH_3) for SiN_y deposition. The RIs of the layers were monitored with variation of the O_2 and of the NH_3 flux, respectively. The lowest RI of 1.462 for PECVD SiO_x was obtained for a silane-to-oxygen ratio of 0.24 and is close to the typical literature value for silicon oxide, namely an RI of n_{SiO_2} = 1.46 [183]. For the PECVD SiN_y, a silane-to-ammonia ratio of 0.84 yields a RI of 2.03, which approaches the value for stoichiometric silicon nitride of $n_{Si_3N_4}$ = 2.011 [184]. Note, a pure silan flux of 7.25 sccm was employed for calculation of the gas flow ratios as it corresponds to the total flux of 145 sccm for the utilized gas mixture of 5 % silane in helium. Unless otherwise stated, the measured RI values are given for a wavelength of 632.8 nm. In the second step, ammonia was added as precursor gas to the SiO_x recipe and oxygen was included for the deposition of SiN_y films. As shown in Figure 5.2, the RIs of the SiO_xN_y can be tailored to bridge the gap between the RI values of the pure SiO_x and SiN_y films. In summary, the RI of the as-deposited PECVD film can be adjusted in the range of 1.46 up to 2.13 by variation of the precursor gas flows.

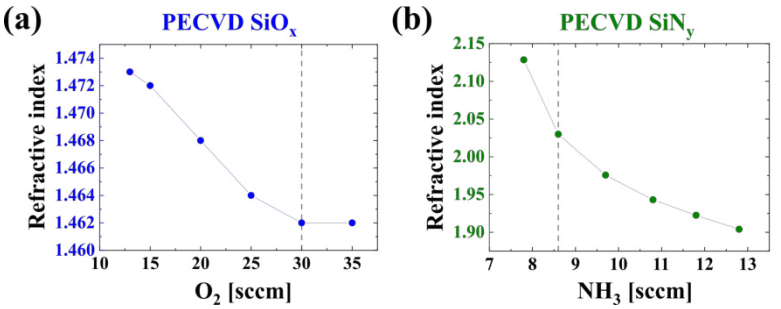

(c)

PECVD recipe	SiO_x	SiN_y
T [°C]	130	130
ICP [W]	450	450
p [Pa]	3	13
5% SiH_4 in He [sccm]	145	145
Ar [sccm]	126	140
O_2 [sccm]	*X*	-
NH_3 [sccm]	-	*Y*

Figure 5.1: RIs in dependence on **(a)** the oxygen flux in the PECVD SiO_x recipe and on **(b)** the ammonia flux in the PECVD SiN_y recipe. The RI decreases for both film types with increasing amount of oxygen and ammonia, respectively. RIs close to the literature values are obtained for the gas flows that are marked by the vertical dashed lines, namely X = 30 sccm for SiO_x and Y = 8.6 sccm for SiN_y. **(c)** The respective deposition recipes are given in the table.

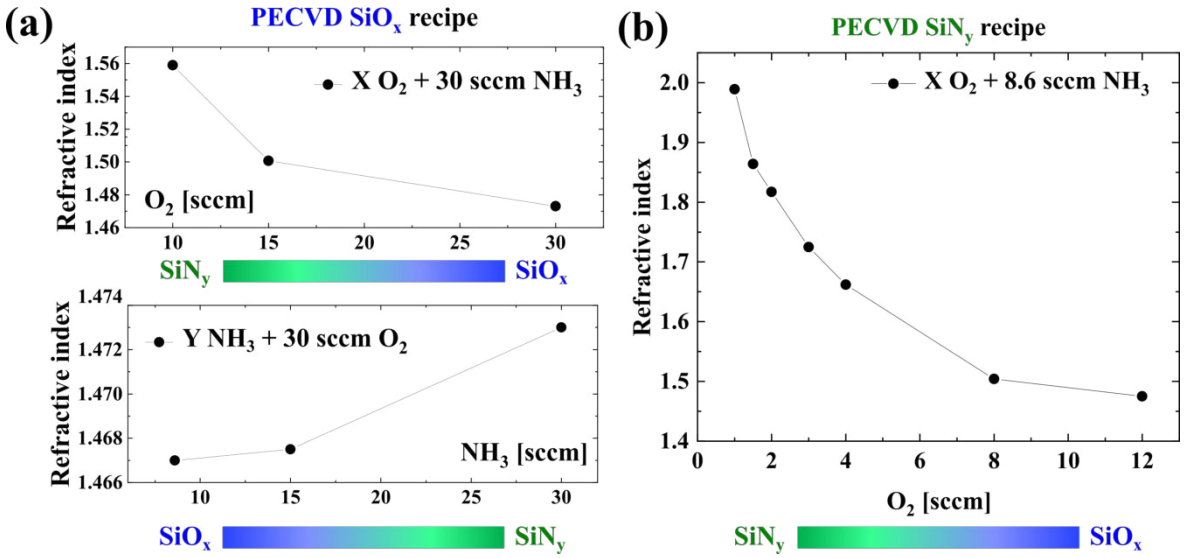

Figure 5.2: (a) The variation of the RI with the SiO_x recipe as starting point was investigated. As shown in the top graph, the RI decreases with increasing oxygen flux while the ammonia flux is held constant at 30 sccm. It indicates that the amount of SiO_x compounds in the SiO_xN_y film is enhanced by rise of the oxygen flow, which is illustrated by the color gradient. In the bottom graph, the contrary behavior is observed for increase of the ammonia flux combined with a constant oxygen flow of 30 sccm. Thus, the rise of the RI with NH_3 flow indicates an increased incorporation of SiN_y compounds. **(b)** For the SiN_y recipe as starting point, a fixed silane-to-ammonia ratio of 0.84 was chosen. By rise of the oxygen flux to 12 sccm, the RI nearly approaches the lowest value obtained for the pure SiO_x recipe.

For the subsequent selective removal of the SiN_y components from the SiO_xN_y films, the samples were etched in extra pure, 85 % ortho-phosphoric acid (Carl Roth GmbH + Co. KG). Typically, silicon nitride is etched in boiling phosphoric acid to obtain reasonable etch rates [185]. A temperature of 158 °C is stated as boiling point by the supplier. Therefore, a reflux condenser was used to maintain the concentration of the aqueous etchant and to reduce fluctuations of the etch rate as suggested in literature [185]. The sample was mechanically clamped in a PTFE holder and kept above the solution during heating in the etch setup that is shown in Figure 5.3 (a). The sample was lowered into the boiling etch bath without the need to open up the glass flask again, which prevents the removal of water vapor from the system. For etch rate determination, SiN_y films deposited according to the optimized conditions were used (see Figure 5.1 (b)). A mean etch rate of (9.0 ± 0.5) nm/min was determined from three SiN_y coated samples. As shown in Figure 5.3 (b), the etch rate for SiO_x is in general one order of magnitude lower than for SiN_y and decreases further with increasing oxygen flux. The SiO_x recipe with 30 sccm oxygen yielded the RI that was closest to the literature value for silicon oxide and showed the strongest resistance in boiling H_3PO_4. Thus, the silicon oxide is from here on referred to as SiO_2 when it was deposited with the optimized parameter set, which is given in Figure 5.1 (a). Comparable etch rates in boiling, refluxed 85 % H_3PO_4

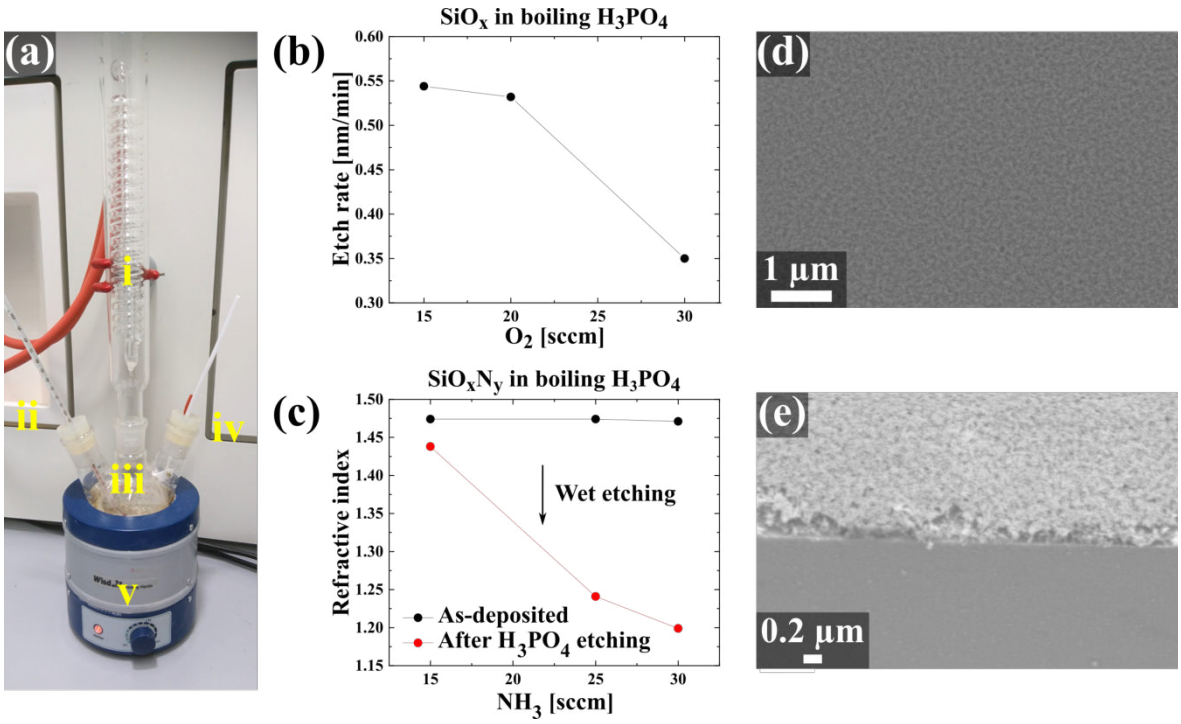

Figure 5.3: (a) H_3PO_4 etch setup consisting of (i) a reflux condenser, (ii) a thermometer, (iii) a three-necked round-bottom flask, (iv) the sample holder and (v) a heating mantle. **(b)** The etch rate for SiO_x in boiling H_3PO_4 decreases with increasing oxygen flux. **(c)** With the SiO_2 recipe (constant oxygen flux of 30 sccm) as starting point, the ammonia flux was varied between 15 sccm and 30 sccm. The RIs of the as-deposited SiO_xN_y (plotted in black) and of the remaining porSiO$_2$ after H_3PO_4 etching (red) are presented. The RIs for the SiO_xN_y vary only in a narrow range around (1.473 ± 0.002). However, the values for the porSiO$_2$ films show a strong decrease from 1.44 down to 1.20 with rising ammonia flux. **(d)** Top and **(e)** side view SEM images of the porSiO$_2$ layer (n_{porSiO_2} = 1.206) that was synthesized with the optimized recipe, namely with a O_2:NH_3 ratio of 30 sccm:30 sccm. The SEM images were taken with the Supra 55 by Zeiss.

can be found in literature, namely about 7 nm/min for silicon nitride and less than 1 nm/min for silicon oxide [185].

Based on the approach stated above, SiO_xN_y layers with large RI—as it was achieved for the SiN_y recipes presented in Figure 5.2 (b)—would principally be used to obtain silicon oxide films with high porosity. However, only the SiO_2 based films showed to be resistant enough in boiling H_3PO_4. Therefore, the SiO_xN_y was deposited with 30 sccm oxygen flux and the additional ammonia flux was varied between 15 sccm and 30 sccm. As shown in Figure 5.3 (c), the RI of the as-deposited film of about 1.47 was reduced by 30 min etching in boiling H_3PO_4 from 1.44 down to 1.20 with increasing ammonia flux. The lowest RI of approximately 1.20 was achieved for a precursor combination of 30 sccm ammonia and 30 sccm oxygen, which is referred to as the optimized PECVD recipe for the synthesis of porous silicon oxide and will be abbreviated by porSiO$_2$ in the following. SEM images of

the optimized porous layer are presented in Figure 5.3 (d) and (e). From the change of the RI from 1.47 (as-deposited) to 1.20 (after wet etching), an apparent porosity of 57 % can be calculated using the formula given in the publication by Yang *et al.* [186]:

$$\text{Porosity} = 100 \cdot \frac{\left(n^2_{\text{porSiO}_2} - n^2_{\text{SiO}_x\text{N}_y}\right) \cdot \left(n^2_{\text{air}} + 2n^2_{\text{SiO}_x\text{N}_y}\right)}{\left(n^2_{\text{porSiO}_2} + 2n^2_{\text{SiO}_x\text{N}_y}\right) \cdot \left(n^2_{\text{air}} - n^2_{\text{SiO}_x\text{N}_y}\right)} [\%]. \tag{5.1}$$

The RI of air $n_{\text{air}} = 1$ as well as of $n_{\text{SiO}_x\text{N}_y}$ and of n_{porSiO_2}, which are the RIs of the as-deposited film and of the porous layer after H_3PO_4 etching, respectively, are considered in the equation. For comparison, Ghazaryan *et al.* determined a porosity of about 55 % for porous silicon oxide that has a RI of approximately 1.2, which is comparable to our result [182]. Further reduction of the RI could not be achieved in the present study. Typically, a strong decrease of the film thickness to less than 10 nm accompanied by an increase of the layer's RI above the initial value of the as-deposited SiO_xN_y were noted for an extended etch duration. These observations may be associated with the collapse of the porous structure.

In conclusion, the SiO_2 based PECVD recipe with an oxygen and ammonia flux of 30 sccm for both gases was used for the synthesis of field emitter samples because the remaining porSiO$_2$ exhibited the strongest RI reduction and thus, the largest apparent porosity.

5.1.2 Porous SiO_2 - Bulk Silicon

For fabrication of the field emitter samples, the SiO_xN_y was deposited selectively only in the center of the sample to limit the growth area for the ZnO emitters and to provide electrical contact through the metallized PTFE spacer directly to the p-doped Si substrate according to the FE assembly described in section 3.2.2. Initially, a 300 nm thermal silicon oxide layer was removed from the p-doped Si wafer by wet etching in buffered hydrofluoric acid (BOE 7:1 from MicroChemicals GmbH) with an etch rate of about 90 nm/min. Afterwards, the p-doped Si wafer was stored in a desiccator, however, the formation of a thin layer of native oxide may not have been prevented, since the sample was exposed to ambient conditions during the further processing steps. The resistivity of the about 525 µm thick, p-doped Si wafer was determined to be 0.005 Ω·cm using a four-point probe station in van der Pauw geometry [124]. The Si samples were cut into pieces of 5x7 mm^2, were cleaned in acetone, in isopropanol, and finally, were dried with gaseous nitrogen. Subsequently, the substrate was masked with photoresist to define the deposition area for the PECVD film. Detailed description of the processing steps are given in section 4.1.1. Here, a 3x3 mm^2 area in the center of the p-doped Si substrate was exposed by the photoresist mask for the deposition of SiO_xN_y by PECVD. The optimized deposition parameters from the last section (30 sccm O_2, 30 sccm NH_3) were applied for a PECVD process duration of 4 min. A mean film thickness

of (91 ± 2) nm and a mean RI of 1.468 ± 0.005 were determined from sixteen separate, as-deposited SiO_xN_y films. The small standard deviations indicate the high reproducibility and uniformity of the PECVD process. The photoresist mask was removed by ultrasonication for 10 min in the remover substance AR 300-70 (from Allresist GmbH), followed by cleaning of the sample in acetone, then in isopropanol, and finally it was dried with gaseous nitrogen.

In the next step, the selective etching of the SiO_xN_y was carried out in the etch setup presented in Figure 5.3 (a). After a heating time of 30 min for 100 ml of the H_3PO_4 in the round-bottom flask, the sample was carefully lowered into the boiling substance. After the etch duration has passed, the sample was immediately transferred to DI water for termination of the chemical reaction, followed by rinsing the probe in ethanol and drying it with nitrogen. The synthesis route for FE samples on bulk substrates is summarized in Figure 5.4.

For the herein used sample configuration, namely the 3x3 mm^2, 91 nm thick film of SiO_xN_y in the center of a p-doped Si piece, the etch time had to be reduced to avoid complete removal or collapse of the $porSiO_2$. In the last section, the PECVD films were deposited without masking parts of the sample. Thus, the edges of the silicon substrates were presumably covered by the CVD process to some extend. However, on the p-doped Si, the faces on the side of the dielectric film were exposed and may have provided additional surface area for chemical

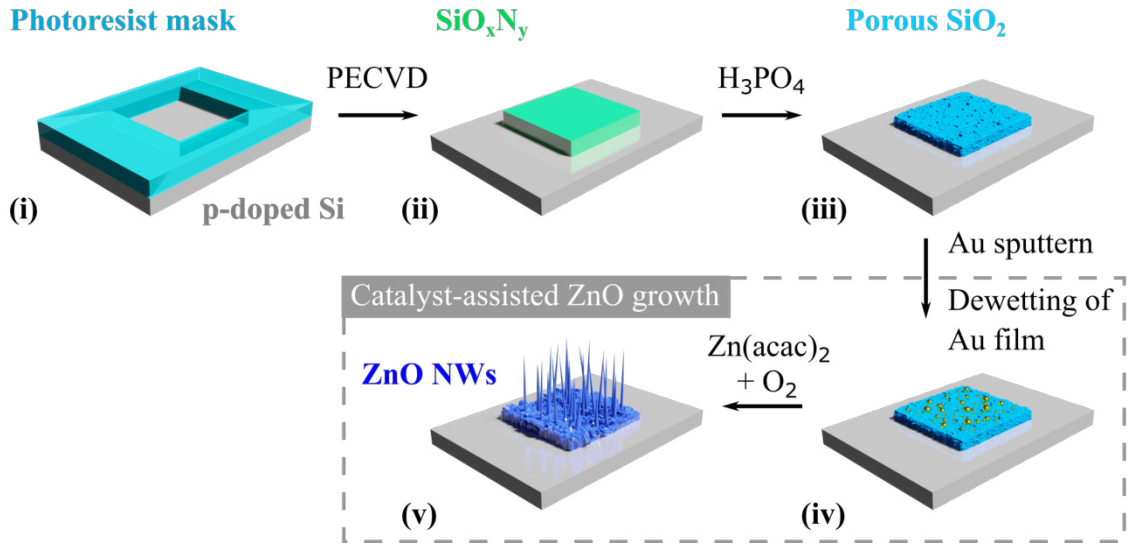

Figure 5.4: Illustration of the synthesis route for the ZnO emitter array using the porous SiO_2. After definition of a 3x3 mm^2 area in the center of the p-doped Si substrate with a photoresist mask (i), the SiO_xN_y is deposited by PECVD, followed by removal of the polymeric mask (ii). Subsequently, the SiN_y compounds are removed from the dielectric film resulting in a porous SiO_2 layer (iii). After sputter deposition of a thin gold film on the $porSiO_2$ coated area, catalyst particle formation during the heating ramp of the ZnO growth process is guided by the underlying porous template (iv), which subsequently allows for the catalyst-assisted formation of ZnO NWs (v).

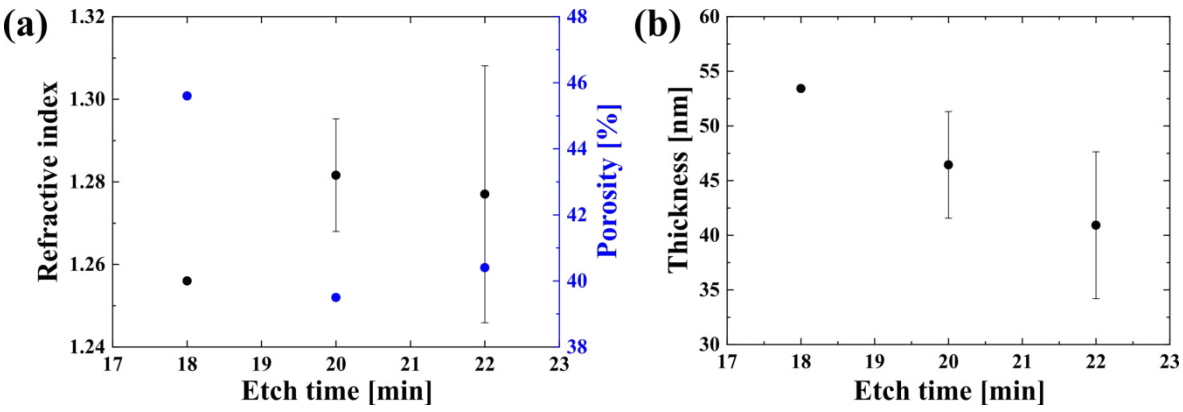

Figure 5.5: (a) The RI (plotted in black) as well as the apparent porosity according to equation 5.1 (blue) are plotted in dependence on the etch time in boiling H_3PO_4. **(b)** The thickness of the remaining porSiO_2 is shown in dependence on the etch time in boiling H_3PO_4. The error bars display the standard deviations from the mean values obtained from several samples that were etched for the same duration.

reaction and for diffusion of the etchant into the SiO_xN_y film. This sample configuration seemed to accelerate the removal of the SiN_y compounds and thereby, led to a faster collapse of the remaining SiO_2 layer.

Figure 5.5 presents the reduced RIs and corresponding apparent porosity values as well as the film thicknesses after etching in boiling H_3PO_4 for an etch duration between 18 min and 22 min. The RI of the porSiO_2 varies between 1.26 and 1.30, but does not show a distinct dependence on the investigated etch times. The apparent porosity varies in a range from 45 % to 36 % from low to high RI. Further, a linear fit to the mean values given in Figure 5.5 (b) revealed that the thickness of the porSiO_2 decreases with a rate of (3.1 ± 0.2) nm/min. Note, etching longer than 22 min results in a large reduction of film thickness as well as in an increase of the RI, which suggests the collapse of the remaining film.

In summary, the RI and the corresponding apparent porosity vary in a narrow range around their mean values of 1.28 ± 0.02 and of (41 ± 4) %, respectively. Therefore, all porSiO_2 layers that were etched for a duration of (20 ± 2) min were used for the subsequent synthesis of field emitter samples.

5.1.3 Porous SiO_2 - Silicon Nitride Membranes

The yield of intact NMs was strongly decreased when the processing route for porSiO_2 on bulk substrates was applied. Typically, the etching process in boiling phosphoric acid was too harsh for the thin membranes or the sudden temperature and ambient condition changes led to destruction of the free-standing thin films when transferred either into the boiling H_3PO_4 or into the DI water for termination of the chemical reaction. Therefore, adjustments of the synthesis route of the porSiO_2 were inevitable for the process transfer to NMs. Note, only

free-standing 3x3 mm^2 SiN membranes were employed as substrates.

First, the deposition of an additional layer of approximately 60 nm SiO_2 was necessary before deposition of the 84 nm thick SiO_xN_y film, to increase the stability of the freely suspended LPCVD SiN for the subsequent wet etching. The optimized PECVD processes for the SiO_2 (see Figure 5.1 (a)) and for the SiO_xN_y from section 5.1.1 were applied successively for 4 min each. Here, the dielectric films were deposited on the entire surface of the substrate without prior masking, since the insulating SiN can obviously not be used as electrical contact for the FE measurements. However, the overlap of the metallized PTFE spacer with the thin ZnO film in the transition region from the ZnO FEA to the substrate (see section 4.1.3, Figure 4.6) provided sufficient electrical contact for the subsequent FE measurements.

Second, the etch setup required modification. The round glass flask in a heating mantle was replaced by a beaker on a hot plate as illustrated in Figure 5.6. The substrate was sitting on a PTFE holder to avoid stress by mechanical clamping and the heads of four PEEK screws, which were assembled on the edges of the rectangular PTFE holder, provided a distance from the beaker's bottom, which was in direct contact with the hot plate. A glass plate was loosely assembled on the beaker to prevent concentration changes by water evaporation during the etching. The sample was heated within the etch substance to avoid sudden temperature changes.

Experimentally, an etch duration of 90 min was determined because the RI of the porSiO_2 could repeatedly be reduced below a value of 1.3. The etch time had to be increased compared to the process for bulk substrates in boiling H_3PO_4, since the temperature of the hot plate was intentionally set below the boiling point of the 85 % H_3PO_4 (158 °C, given by supplier). Moreover, the exact temperature of the etchant is not monitored during the process and thus, the actual temperature of the H_3PO_4 may even be lower than the set temperature of the hot plate. Note, for termination of the etch process, DI water was heated for 2 min on the hot plate (150 °C set temperature) before the sample was transferred from the etchant to the DI water, to avoid sudden temperature changes. For removal of the etch solution, the sample was gently rinsed in the heated DI water for about 2 min, followed by soaking it in a beaker with methanol for the same duration. To accelerate the drying process and especially, to impede

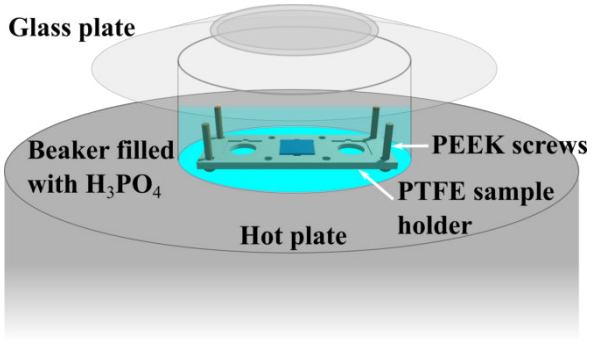

Figure 5.6: The etch setup for porSiO_2 on SiN NMs consisted of a beaker placed in the center of a hot plate that was filled with 30 ml H_3PO_4. The beaker was covered by a glass plate during the etching and the etch process was initiated by setting the cold hot plate to 150 °C. The samples were etched for 90 min in the solution before the chemical reaction was terminated in heated DI water.

gathering of liquid on the flexible membrane, the sample was held in a tilted manner above the hot plate, which was still set to 150 °C.

Since it was not possible to determine the layer thickness and RI from the free-standing NM itself because no adequate fitting model was found for the ellipsometer measurement, the etch rates for SiO_2, for $porSiO_2$ and for LPCVD SiN were determined separately on bulk substrates. The results are summarized in Figure 5.7. For the etch duration of 90 min, a mean RI of 1.29 was obtained for the $porSiO_2$ accompanied by a film thickness reduction of about 21 %. For the pure SiO_2, the film thickness was reduced by about 8 %. However, the SiO_2 was not exposed to the etchant in the final configuration as it was located between the SiO_xN_y film and the LPCVD SiN membrane and was most likely not attacked by the etchant. The thickness of the 100 nm LPCVD SiN decreased to about 38 nm for the 90 min etch time. As expected, the RIs of the SiO_2 and of the LPCVD SiN were not considerably changed by the wet etching. Note, the etch solution has access to the membrane's backside through the hole in the holder and can reduce the thickness of the SiN film further to achieve ultra-thin membranes. The total thickness of the remaining free-standing layer system of $porSiO_2/SiO_2$/LPCVD SiN was estimated to be about 162 nm.

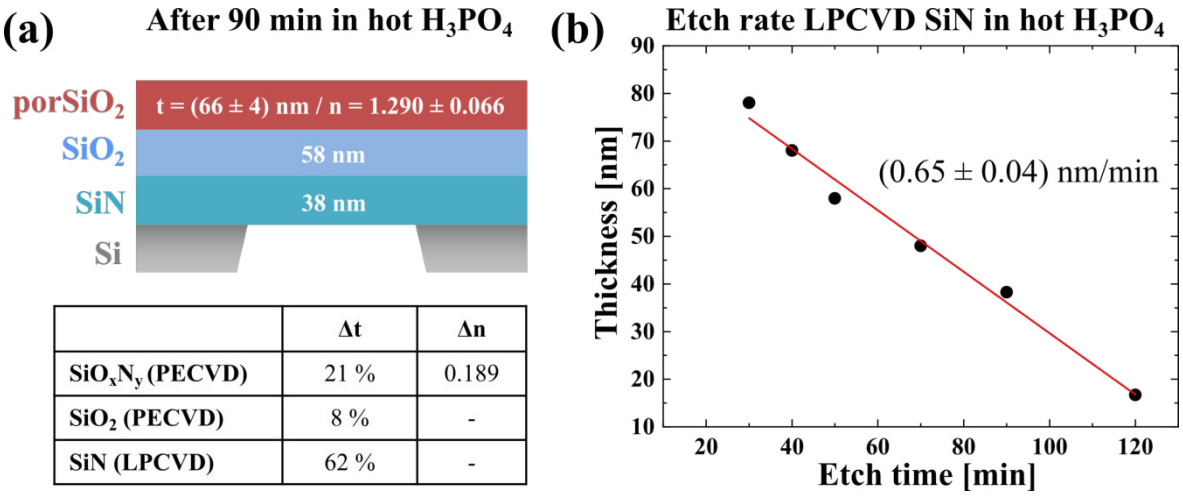

	Δt	Δn
SiO_xN_y (PECVD)	21 %	0.189
SiO_2 (PECVD)	8 %	-
SiN (LPCVD)	62 %	-

Figure 5.7: (a) In the illustration on the top, the layer system of $porSiO_2/SiO_2$/LPCVD SiN is arranged from top to bottom. The mean RI of the porous layer was determined to be 1.29 from two separate samples, which corresponds to an apparent porosity of about 39 % according to equation 5.1. The thickness and RI reductions were determined separately by etching of the as-deposited dielectric films for 90 min in H_3PO_4 on a hot plate that was set to 150 °C. The results are listed in the table on the bottom. **(b)** Even so no reflux condenser was used and the samples were heated within the etchant, the etch rate for LPCVD SiN reveals a linear dependence on the etch time with a slope of 0.65 nm/min.

5.1.4 Catalyst-Assisted ZnO Growth on Porous SiO_2

The gold film was deposited with a sputter coater (K550X from Emitech) for the minimum possible sputter time of about 22 s—obtained by adjusting the turning knob for the deposition time to zero—and with a current of 20 mA. For these parameters, a gold film thickness of (8.2 ± 0.4) nm was measured on silicon for two separate sputter processes using a spectroscopic ellipsometer. Figure 5.8 shows the gold particle distribution on the porSiO$_2$ template after dewetting of the gold film at the ZnO growth temperature of 580 °C. The mean particle diameter of (37 ± 10) nm, which was derived from the SEM image in Figure 5.8 (a) using ImageJ [157], has half the size of the mean diameter that was found for the sputter shadow mask approach ((80 ± 33) nm, section A.3.2). Note, an apparent gold film thickness of about 5.9 nm was measured for the deposition through the sputter shadow mask (see section 4.1.2). However, the mean gold particle diameter is smaller for the dewetting on the porSiO$_2$, which is contrary to the general assumption that a thinner film causes the formation of smaller particles at the same dewetting temperature [146]. This observation indicates that the porous surface leads to a certain size confinement of the gold particles during agglomeration. In general, it was observed elsewhere, that the mean particle diameter decreases for the same gold film thickness when a pre-patterned substrate is used instead of a flat surface [187, 188]. Besides the capillary forces that drive the surface energy minimization process for dewetting, a textured substrate can add another force that facilitates the particle agglomeration. A decrease of the mean gold particle diameter by 43–61 % was reported compared to a flat substrate, which is in good agreement with the herein found mean particle diameter reduction of 54 % on porSiO$_2$ [187, 188].

The sputter coated substrate was subsequently used for ZnO growth according to the stan-

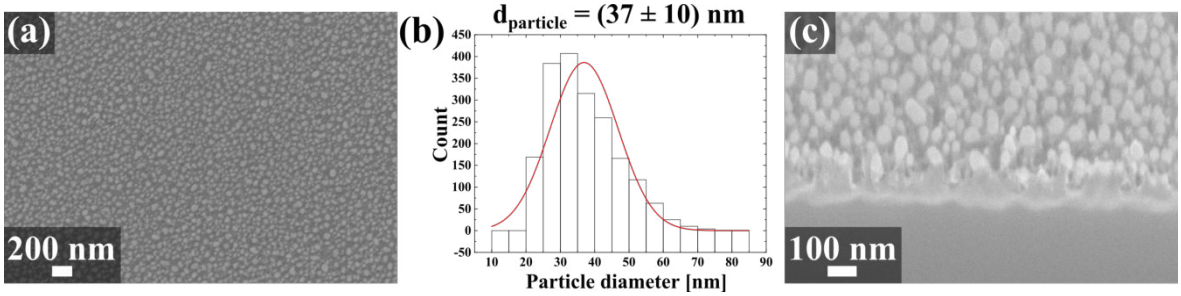

Figure 5.8: (a) Top view of the gold particle distribution on porSiO$_2$ after dewetting of the thin gold film at 580 °C, which corresponds to the ZnO growth temperature. **(b)** A mean particle diameter of (37 ± 10) nm was determined for the densely packed gold dot distribution. **(c)** The cross section through the substrate indicates the location of the gold droplets on the porSiO$_2$ template. The gold particles seem to be sitting rather on top of the porSiO$_2$ layer than in the pores. The SEM image for (a) was taken without tilting of the stage and the cross section for (c) was obtained by FIB milling (30 kV, 50 pA) and imaged under a specimen tilt angle of 54 °, both with the Crossbeam 550 by Zeiss.

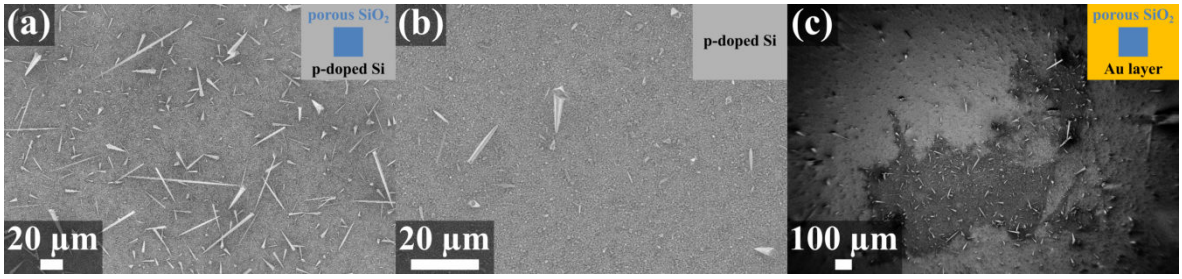

Figure 5.9: (a) The top view of the ZnO NW array grown on a porSiO$_2$ template (p-doped Si substrate) is shown. Large, randomly oriented ZnO NWs are observed across the area defined by the porSiO$_2$. **(b)** Only a few large ZnO NWs are noted on the p-doped Si substrate that was etched in boiling H_3PO_4 but has no porSiO$_2$ layer. **(c)** ZnO structures grown on porSiO$_2$ on top of a gold coated substrate are shown. The initially square dielectric layer was partially removed during the wet etching in H_3PO_4, leading to formation of an inhomogeneous macroscopic emission area. The SEM images were taken with the Supra 55 by Zeiss. The SEM image in (b) was taken by Carina Hedrich (supervised hourly student).

dard growth process described in section 4.1.3. First, the ZnO growth was tested on a plain p-doped Si substrate (without porSiO$_2$) that was etched in boiling phosphoric acid, to investigate if the porSiO$_2$ has a distinct influence on the formation of the ZnO structures. As expected, comparison of the SEM images (a) and (b) in Figure 5.9 shows that the porSiO$_2$ template clearly enhanced the formation of large ZnO NWs in contrast to the plain p-doped Si substrate. Second, besides p-doped Si, other substrate types were tested, namely, Si coated with a 50 nm thick gold layer as well as n-doped Si. However, the adhesion of the SiO_xN_y film on gold was poor, which led to the partial removal of the porSiO$_2$ film during the selective wet etching in H_3PO_4, as shown in Figure 5.9 (c). The adhesion of the dielectric film was not an issue on n-doped Si, yet, the color of this substrate was strongly modified by the wet etching step, which possibly indicates a chemical reaction that changed its surface properties. Such modifications were not observed for the p-doped Si substrate and it provided sufficient adhesion for the dielectric layer to survive the wet etching. In addition, the resistivity of the p-doped Si substrate remained at about 0.005 Ω·cm after etching in boiling phosphoric acid.

5.2 Substrate Type A - Bulk Silicon

Herein, the bulk p-doped Si substrate with porSiO$_2$ was used as base for fabrication of the ZnO FEAs. The morphology of the NWs was investigated for the standard ZnO growth process (see section 4.1.3). Moreover, the FE properties of eleven samples were studied to examine the reproducibility of the utilized synthesis route for the ZnO emitters.

5.2.1 Morphology

After sputter coating of a thin gold film ((8.2 ± 0.4) nm for the minimum deposition time), the ZnO growth was carried out while the exposed p-doped Si around the dielectric film was covered with a 6x10 mm^2 SiN/Si hard mask with a window in the center (up to 4 mm^2) that exposed the gold coated porSiO_2. One quarter of the FEA grown on the porSiO_2 is shown in Figure 5.10 (b). The intended decrease of large ZnO structures towards the edges of the growth area avoids the physical contact of large ZnO NWs with the metallized PTFE sheet as described in Figure 4.7 in section 4.1.3.

An array of randomly ordered ZnO wires was grown on the gold coated porSiO_2. Three groups of ZnO structures were identified as shown by the illustration in Figure 5.10 (a) and by the respective SEM images i to iii. First, large, well separated and highly tilted ZnO wires were observed that stand out from the surrounding structures because of their length (Figure 5.10 i). Second, considerably shorter ZnO needles were distributed across the substrate (Figure 5.10 ii) and third, a layer on the bulk Si substrate was found that is composed of densely packed ZnO crystallites and of the porSiO_2 template (Figure 5.10 iii). The mean dimensions of the ZnO NWs were extracted from several SEM images using ImageJ [157]

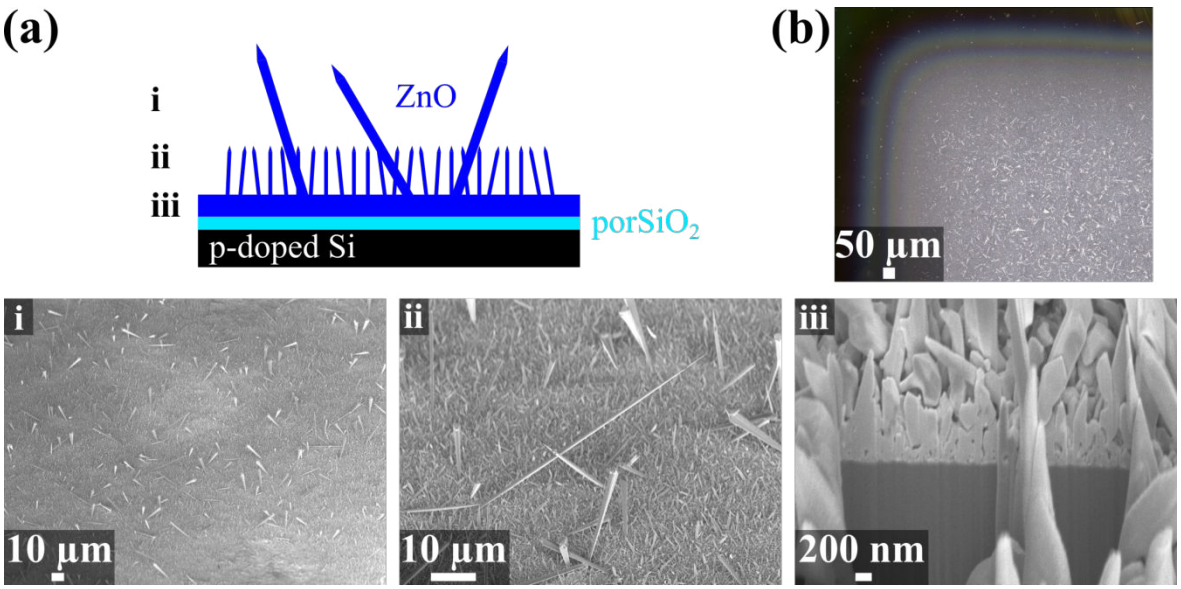

Figure 5.10: (a) The illustration shows the three types of ZnO structures grown on the porSiO_2, namely, large wires protruding from their surrounding structures (i), shorter ZnO needles occurring with a higher density (ii) and the ZnO crystallites on the porous SiO_2 (iii). The corresponding SEM images are shown in the bottom row. The SEM images were taken under a tilt angle of 54 ° and the cross section was obtained by FIB milling (30 kV, 50 pA), both with the Crossbeam 550 by Zeiss. **(b)** The microscopy image presents the distribution of large NWs, which are visible as white, wire-like structures, on a quarter of the porSiO_2 on the p-doped Si substrate (dark background).

according to the description given in section A.3.1 and are summarized in Table 5.1. Note, only large NWs (Figure 5.10 i) were used for the dimension analysis because they are expected to dominate the FE process [29]. An aspect ratio—namely the ratio of NW length to tip diameter—of 446 was found for the examined sample and wires are tilted from a mean angle of 88 ° by about 39 % in various directions. The thickness of the mixture of porSiO$_2$ and ZnO crystallite film was determined to be about (868 $\pm$ 212) nm by measuring at nine different locations using the cross section image shown in Figure 5.10 iii. The thickness of the porSiO$_2$ was determined to be about 48 nm by ellipsometry prior to the ZnO growth process. For the apex shapes of the large NWs, the four variations shown in Figure 5.11 were predominantly observed. Tapered structures with a narrow tip (first image on the left) as well as apexes having a pyramidal shape with a base larger than the wire's diameter (first image on the right) were visible. Moreover, secondary wires were noted that grew perpendicular to the orientation of the NW and a tip inclination of 69 ° with a considerable variation of about 67 % was found among the investigated wires.

ZnO NWs on porSiO$_2$ + p-doped Si	
Length (h) [µm]	49 $\pm$ 19
Diameter ($2r_{\text{base}}$) [µm]	1.7 $\pm$ 0.7
Tilt angle [°]	88 $\pm$ 34
Tip diameter ($2r_{\text{apex}}$) [µm]	0.110 $\pm$ 0.039
Tip inclination (θ_{apex}) [°]	69 $\pm$ 46
Aspect ratio ($h/(2r_{\text{apex}})$)	446 $\pm$ 331
Density [NWs/mm^2]	3390 $\pm$ 325

Table 5.1: Summary of the dimensions found for ZnO NWs grown on porSiO$_2$ on p-doped Si. The dimensions were determined according to the description in section A.3.1 from 20 separate large NWs observed under a specimen tilt angle of 54 °. The density of wires having a length above 10 µm was determined from five separate SEM images that were taken with a constant magnification of 10^4 at different locations of the NW array.

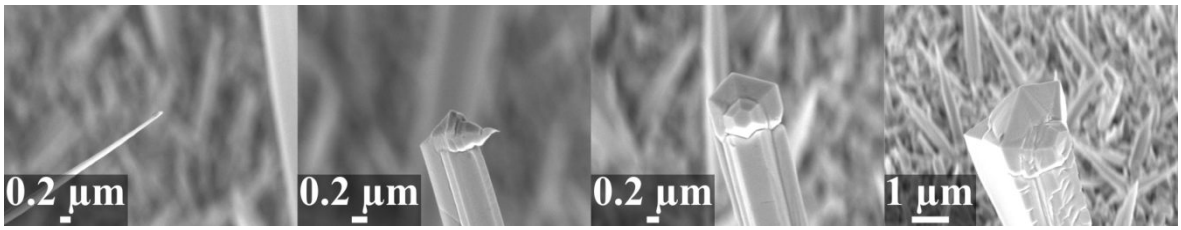

Figure 5.11: The shown apex shapes were repeatedly observed among the NWs of the FEA. Strong variations of the tip width as well as of the tip inclination angle were apparent for the investigated sample. The SEM images were taken under a tilt angle of 54 ° with the Crossbeam 550 by Zeiss.

Compared to the ZnO NWs grown with the help of the sputter shadow mask on NMs from Si and from SiN (see section 4.2.1 and 4.3.1), the mean NW length is similar to the ZnO wires grown on the porSiO$_2$ template. However, the mean tip diameter is reduced for NWs formed on the porSiO$_2$ and therefore, the overall aspect ratio of 446 is larger compared to the values found for Si and SiN membranes in chapter 4, namely 310 (Table 4.2) and 333 (Table 4.6), respectively. In addition, relatively large NW tilt angles as well as substantial tip inclinations were noted for the growth on the porSiO$_2$. The determined NW density of 3390 NWs/mm^2 for structures larger than 10 µm is significantly lower than the values derived for the FEAs in chapter 4, namely 5963 NWs/mm^2 on Si NMs and 4810 NWs/mm^2 on SiN NMs.

Based on the observed similarities for the morphology of the ZnO structures deposited with the help of the porSiO$_2$ and of the sputter shadow mask, a similar mixture of growth mechanisms is expected for the herein studied samples. A catalyst-assisted growth mechanism is indicated by the considerably larger NW dimensions in comparison to the size of the nanowhiskers that were grown by the catalyst-free MOCVD process, which are shown in Figure 4.1. For further analysis of the growth process, the positions of the gold dots after ZnO growth were investigated by SEM and EDX. Firstly, gold droplets were observed on the tips of shorter wires as well as distributed on the ZnO crystallite layer as shown in Figure 5.12, which serve as evidence for a VLS driven growth mechanism. However, it was not possible to identify gold droplets at the tips of large NWs. On the one hand, the absence of the gold at the NW apex may be caused by vaporization of the catalyst particle or its incorporation in the

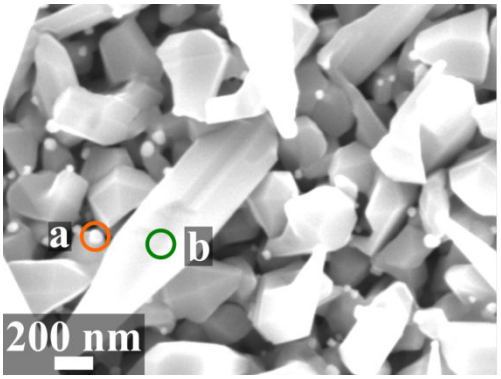

a

Element	Atomic %	Error %
Zn L	55.16	3.67
O K	36.31	7.62
Au M	7.82	4.36

b

Element	Atomic %	Error %
Zn L	48.98	2.92
O K	43.73	6.18

Figure 5.12: Bright droplets were observed on short ZnO structures, which were identified as gold (Au) dots with the point analysis function of the EDX software. An enhanced amount of gold was detected at the position of the bright dot that sits on the ZnO crystallite and is marked by (a). The mean gold dot diameter has almost doubled after NW growth ((62 ± 20) nm) compared to the particle diameter after dewetting without subsequent ZnO growth ((37 ± 10) nm, Figure 5.8), which possibly indicates incorporation or nucleation of precursor materials and correlates with the detection of zinc and oxygen at location (a). In contrast, no gold was detected at the encircled region (b) at the middle of a ZnO structure. The zinc to oxygen ratio at the NW corpus revealed a 1:1 stoichiometry. The SEM image and the EDX spectra (8 kV, 4.7 nA) were taken with the Crossbeam 550 by Zeiss.

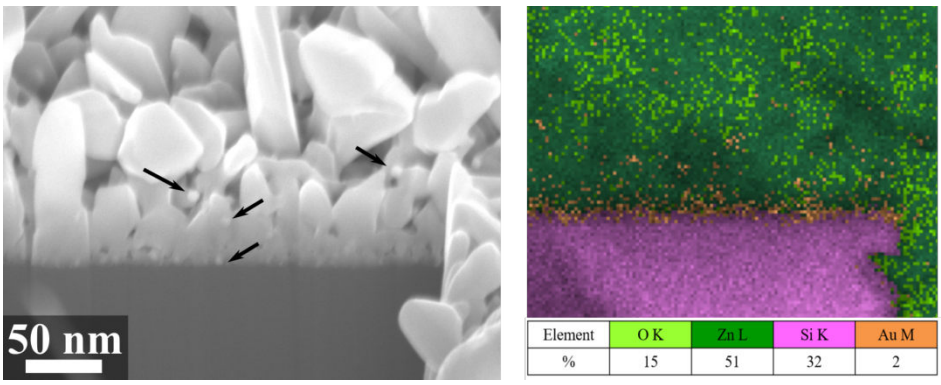

Figure 5.13: The cross section through the substrate (SEM image on the left side) was investigated using the mapping function of the EDX software (right side). Some bright dots—similar to the ones observed on the ZnO crystallites—are visible in the cross section (locations highlighted by black arrows). Gold (displayed in orange) was detected at the root of the ZnO structures as well as at the locations of the bright particles. The SEM image and the EDX spectrum (8 kV, 4.7 nA) were taken under a tilt angle of 54 ° with the Crossbeam 550 by Zeiss.

wire during growth [158]. On the other hand, it may also be a strong evidence that the growth of the large NWs is not safely driven by the VLS mechanism. In addition, the NW diameter of 1.7 µm is 46 times larger than the mean particle diameter after dewetting (see Figure 5.8), which is another indication against a solely VLS driven growth mechanism [158, 159]. Secondly, gold was also detected at the root of the ZnO structures as presented in Figure 5.13, which implies a VSS growth regime [158].

In conclusion, similar NW dimensions and shapes as well as gold dot locations were observed for the ZnO NW synthesis with the standard ZnO MOCVD process by using porSiO$_2$ compared to the sputter shadow mask approach. Therefore, it is assumed that the same mixture of growth mechanisms generated the observed ZnO structures on the porSiO$_2$ as it was discussed in more detail in section 4.2.1. However, a smaller mean tip diameter, a larger aspect ratio and a lower NW density were observed in comparison to the ZnO NWs found in the last chapter for the sputter shadow mask approach. The noted differences are attributed to the effect of the porSiO$_2$ on the gold particle distribution. Furthermore, the smaller apex diameter observed for the herein studied ZnO NWs may be related to the about 50 % smaller gold particle diameter that was found after dewetting of the gold film on porSiO$_2$ compared to the dot size that was generated by the sputter shadow mask technique.

5.2.2 Field Emission Measurements

This section presents the analysis of FE measurements from eleven individual samples with ZnO NWs that were grown on p-doped Si utilizing the porSiO$_2$ template. The FE measurements were carried out according to the instructions given in section 3.4 and with the specific

characterization conditions listed in Table 5.2. The FE data analysis follows the description given in section 2.4 and was executed as explained in section 3.4.

The measurements were carried out over a long time period (2018–2020) and therefore, not all samples were measured under the optimized conditions presented in the sections 3.2 and 3.3. Some field emitter samples were measured multiple times and different emitter-grid distances, namely 100 µm and 250 µm, were used. Additionally, the macroscopic emission area was either defined by a 1.5x1.5 mm^2 or by a 2x2 mm^2 window in the SiN/Si hard mask that was placed on top of the substrate during the ZnO growth process. Furthermore, most of the measurements were carried out at least 72 h after mounting the sample in vacuum to allow for proper outgassing of the FEAs. However, the first sample of this series, namely sample #1, was measured only 24 h after mounting in the ISO setup. This specimen was considered in the analysis as well, because the macroscopic onset field for subsequent measurements varies only by 3 % around the mean value. Before the FE properties of the eleven samples are compared, the effect of modification of the FE characterization conditions is investigated to evaluate the impact on results derived from the FE data analysis.

First, it was tested if there is a change of *I-V* curve shape when the sample is mounted several times, namely not all measurements were taken from as-deposited field emitters. Figure 5.14 shows the FE behavior of a sample that was mounted two times in the ISO setup. The macroscopic onset fields for two subsequent mountings of the same FEA vary within their standard deviations. Thus, FE measurements from as-deposited ZnO arrays as well as from already measured ones were assumed to be comparable. Herein, FE-initiated modifications of the emitter structures may play a minor role as all measurements were deliberately carried out in the picoampere range to detect the onset fields that are characteristic for the as-deposited ZnO NWs. Moreover, the measurements in Figure 5.14 indicate the high repro-

ZnO NWs on porous SiO_2 (p-doped Si) - Characterization conditions	
d	100 µm / 250 µm
A_M	2.25 mm^2 / 4 mm^2
PTFE height compensation	350 µm
FE measurement setup	ISO setup
Step voltage	5 V/step

Table 5.2: Summary of the characterization conditions used for *I-V* curve acquisition for the emitters grown on the porSiO_2 on bulk substrates. The emitter-grid distance d was defined by the thickness of the PTFE foil separating the two electrodes and the macroscopic emission area A_M was determined by the window in the SiN/Si hard mask that was used during the ZnO growth process. All measurements were carried out using the current amplifier in the ISO setup.

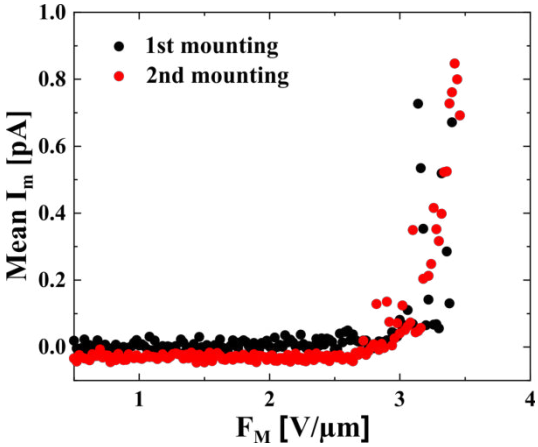

Figure 5.14: *I-V* curves from a sample that was mounted in the ISO setup two times, namely as-deposited (1st mounting, plotted in black) as well as after previous FE acquisition (2nd mounting, plotted in red). Each *I-V* curve shows the average of several subsequent FE measurements for an emitter-grid spacing of 100 µm. The macroscopic onset field of sample #3 was determined to be (3.2 ± 0.1) V/µm for the 1st and to be (3.2 ± 0.1) V/µm for the 2nd mounting.

ducibility of the mounting procedure in the optimized FE assembly.

Second, the impact of the emitter-grid distance on FE measurements was evaluated for three different samples as shown in Figure 5.15. As presented exemplary for one sample in (a), there is a notable variation of the onset field with modification of the spacing between emitter and grid. As stated above, this observation can neither be attributed to the reproducibility of the mounting in the FE assembly nor to modifications of the emitter shape caused by strong current emission through the associated emitter self-heating, since the emission current remains in the picoampere range. In Figure 5.15 (b), the variation of the macroscopic onset field is plotted in dependence on the utilized spacer width for three selected samples. Note, the extracted onset fields are normalized to the values found for $d = 100$ µm to emphasize the onset field variation with respect to the altered spacing.

For all three samples, a non-linear dependence of the onset field on the emitter-grid distance was observed. Based on simulations as well as on experimental results, it was reported elsewhere that the electric field required for FE increases when the spacing d between the two electrodes becomes comparable to the length h of the field emitter [45, 189–191]. Calculations of the electric field distribution revealed that the FEF decreases non-linearly with reduction of the tip-to-counter electrode distance $D = d - h$, which could lead to the corresponding increase in onset field. However, for electrode distances much larger than the length of the emitter, the FEF is independent of the gap width and becomes a constant that is solely determined by the emitter's geometry. Hence, the electric field needed to allow for FE approaches an asymptotic value with increasing inter-electrode spacing [45, 189–191]. These reports agree well with the herein observed increase in onset field with reduction of

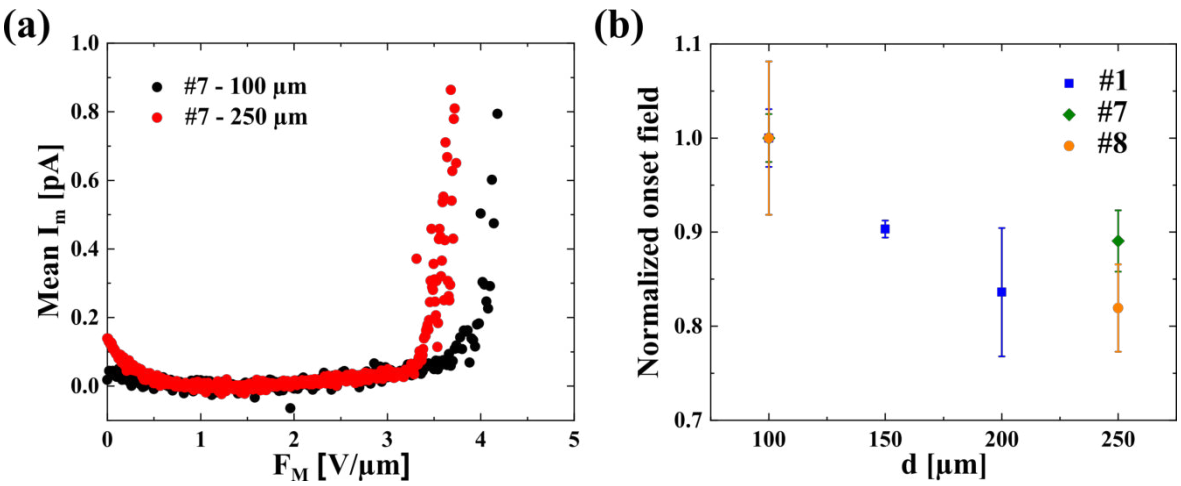

Figure 5.15: (a) The same sample was measured several times with a spacing of 100 µm (plotted in black) and of 250 µm (red). Note, the average of several measurements is shown for both *I-V* curves. The mean macroscopic onset field decreases from (3.9 ± 0.1) V/µm for the smaller spacing to (3.5 ± 0.1) V/µm for the larger one. **(b)** The mean onset fields were extracted for three individual samples from several subsequent measurements and were normalized to the respective value of F_M^{onset} that was found for a spacing of 100 µm for each of the samples. A reduction of the onset field is noted with increasing spacing for all three NW arrays. Compared to FE acquisitions with the 100 µm spacing, an onset field decrease of 18 % was observed for sample #1 measured with 200 µm distance (blue) as well as reductions of 11 % for #7 (green) and of 18 % for #8 (orange) were detected with an electrode separation of 250 µm.

the emitter-grid distance as displayed in Figure 5.15 (b). For the 100 µm spacing and the mean NW length of 49 µm (Table 5.1), the distance *D* between the tips of the emitters and the grid almost equals the mean NW length, which correlates with the noted rise in onset field. Furthermore, the onset field is reduced by up to 18 % when the emitter-grid spacing is increased from 100 µm to 250 µm. Thus, an increase of the derived macroscopic onset field as well as a certain decrease of the FEF have to be considered when a sample was measured with an electrode distance smaller than 250 µm. Most of the samples were examined with the larger distance but the few exceptions are highlighted in the further analysis.

The measurements in chapter 4 were mostly performed with an electrode distance of 250 µm. The lengths determined for the ZnO NWs on the Si NM (58 µm) and on the SiN NM (50 µm) are comparable to the mean value found on the porSiO$_2$. Thus, a possible impact of the grid distance on the FEF and therefore, also on the onset field may be possible. For instance, a decrease of the mean onset field by about 10 % was observed for the increase of the emitter-grid distance from 250 µm to 300 µm in section 4.2.2 (Figure 4.13). Further experiments in the future are suggested to determine the electrode separation that is needed in our measurement configuration to find the constant value of the onset field and thus, to obtain the effective FEF that is solely determined by the emitter dimensions.

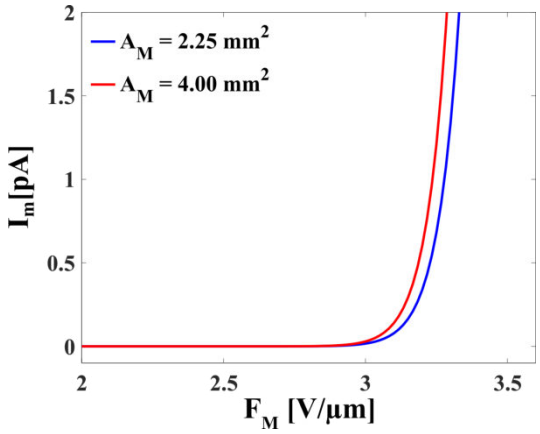

Figure 5.16: The FN equation 2.9 was used to plot the theoretical *I-V* curves for ZnO field emitters with a macroscopic emission area of 2.25 mm^2 (blue) and of 4 mm^2 (red). Further, a work function value of 5.3 eV for ZnO [46], a theoretical FEF of 600 and an emitter-grid spacing of 250 µm were applied.

Third, the macroscopic emission area was varied because SiN/Si hard masks with two different window sizes were used to limit the growth area of the NW arrays to the centers of the p-doped Si substrates. Figure 5.16 shows the theoretical curves according to the FN equation 2.9 for FE from ZnO field emitters for the two different macroscopic emission areas, namely 2.25 mm^2 (plotted in blue) and 4 mm^2 (red). It becomes obvious from the theoretical plot that almost doubling of the emission area causes no significant variation of the *I-V* curve. For instance, the FE current reaches 1 pA at a macroscopic electric field of 3.28 V/µm for 2.25 mm^2 and at F_M = 3.25 V/µm for 4 mm^2. The variation of around 1 % that is theoretically caused by the modification of the emission area is smaller than most of the standard deviations for subsequent experimentally obtained *I-V* curves. Therefore, the samples with different macroscopic emission areas were assumed to be comparable in the further analysis.

Figure 5.17 presents a summary of the mean macroscopic onset fields that were derived from several subsequent measurements from each of the eleven samples. The onset fields vary between 1.4 V/µm for sample #11 up to 7.9 V/µm for #6. The error bars show the relatively low variability for subsequent measurements from the same FE sample. The standard deviations vary only from 1.3 % for sample #3 up to 25 % for #2. It was concluded from the previous analysis of the three characterization conditions that as-deposited and previously measured samples as well as FE cathodes with the herein used emission areas (2.25 mm^2 and 4 mm^2) are comparable. However, the two FEAs examined with 100 µm (marked in blue) would have onset fields that are reduced by up to 18 % when measured with the larger gap distance. For sample #1 and #3, reduced onset fields of 2.4 V/µm and of 2.6 V/µm would presumably occur with a wider emitter-grid spacing, respectively, which are indicated by hollow

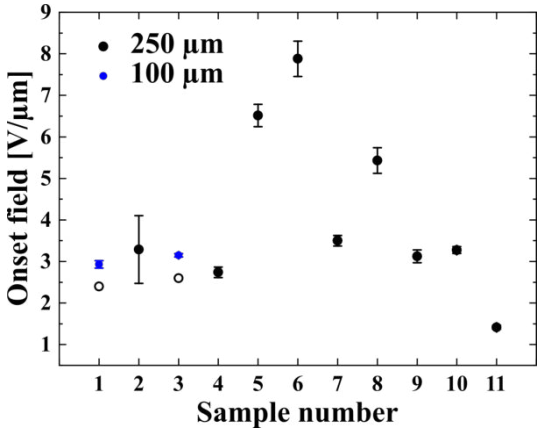

Figure 5.17: Summary of the mean macroscopic onset fields that were extracted for each of the eleven samples from subsequent FE measurements with the error bars showing the standard deviations from the mean values. The samples that were examined with an emitter-grid distance of 250 µm are displayed in black and the ones measured with 100 µm are plotted in blue. The hollow circles indicate the theoretical onset fields when the samples would have been measured with the 250 µm emitter-grid distance.

circles in the graph. About 64 % of the samples (excluding #5, #6, #8, #11) have an onset field of (3.0 ± 0.4) V/µm, which indicates a good reproducibility of the herein investigated synthesis approach for ZnO NWs. By consideration of all eleven samples, a mean onset field of (3.8 ± 1.9) V/µm was derived. Note, the corrected values (hollow circles) from sample #1 and #3 were considered for calculation of the mean values.

5.3 Substrate Type B - Silicon Nitride Membranes

5.3.1 Morphology

The morphology of the ZnO structures grown on the porSiO_2 layer on top of a 3x3 mm² SiN membrane was not investigated in depth, as the formation of ZnO wires was already studied for the porSiO_2 approach for the growth on bulk substrates (section 5.2.1). For NW growth, a SiN/Si hard mask was used to avoid NW formation at the rim of the sample as discussed in section 4.1.3. Figure 5.18 shows an overview image of the NW array as well as the cross section through the membrane substrate. An array of large, randomly distributed and highly tilted ZnO wires was observed. Additionally, smaller needles populated the substrate's surface that appeared with a higher density than the large NWs. A cross section through the NM revealed the layer of ZnO crystallites directly grown on the substrate. The same mixture of growth mechanisms is expected for the herein studied ZnO structures, as it was discussed for the ZnO NWs investigated in the previous chapter in section 4.2.1 as well as in the present chapter in section 5.2.1, since a similar ZnO morphology was observed.

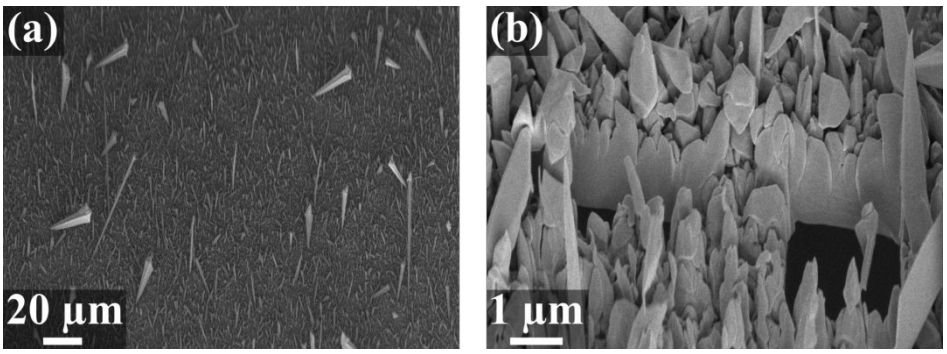

Figure 5.18: (a) Overview of the ZnO NW array grown on the SiN NM with the porSiO$_2$ template. **(b)** A cross section through the free-standing substrate is shown that consists of a stack of porSiO$_2$ on SiO$_2$ on top of a LPCVD SiN NM. The total thickness of the membrane is about 162 nm (see section 5.1.3) and is therefore much thinner than the layer of ZnO crystallites grown on top of the NM. The SEM images were taken under a tilt angle of 54 ° and the cross section was generated by FIB milling (30 kV, 50 pA), both with the Crossbeam 550 by Zeiss.

5.3.2 Field Emission Measurements

The *I-V* curves from three samples with ZnO emitters grown on porSiO$_2$ on 3x3 mm^2 SiN membranes were measured according to the description given in chapter 3.4 with the specific characterization conditions listed in Table 5.3. For comparison, one sample was synthesized on porSiO$_2$ with bulk Si as substrate. The data analysis was executed following the explanation given in the sections 2.4 and 3.4.

The onset fields for all four samples vary within their standard deviations as shown in Figure 5.19 (a). Note, NM substrate #1 is the only sample that was measured in the ISO setup, yet, it shows a similar onset field compared to the other FE probes and emphasizes the mounting reproducibility for the optimized FE setup configuration, which is presented in chapter 3. Fur-

ZnO NWs on porous SiO$_2$ (SiN NM) - Characterization conditions	
d	250 µm
A_M	16 mm^2
PTFE height compensation	250 µm
FE measurement setup	CF setup and ISO setup

Table 5.3: Summary of the characterization conditions used for *I-V* curve acquisition for the emitters grown on SiN NMs with the porSiO$_2$ template. The macroscopic emission area A_M was determined by the 4x4 mm^2 opening in the PTFE spacer. One membrane sample was measured in the ISO setup with the current amplifier (NM #1) and the other three samples (NM #2, NM #3, bulk) were examined in the CF setup (with a picoammeter) after its construction because it provides a lower base pressure.

thermore, the onset fields of all four samples vary less than 10 %, which prove reproducibility of the adjusted synthesis route for the porSiO$_2$ template on NM substrates (see section 5.1.3). The more gentle processing conditions seem to increase the repeatability of the synthesis in contrast to the harsh environment that is provided by the boiling phosphoric acid for bulk substrates (see section 5.1.2). In Figure 5.19 (b), the onset field as well as the effective FEF are plotted for each sample. The herein obtained mean onset field of (1.6 ± 0.1) V/µm is smaller than found for the porSiO$_2$ on p-doped bulk Si ((3.8 ± 1.9) V/µm, Figure 5.17) and is also smaller than the onset field derived for the ZnO emitters grown on the 3x3 mm^2 SiN membrane with the help of the sputter shadow mask, namely (2.0 ± 0.1) V/µm (see section 4.3.2). Note, the macroscopic emission area is increased up to 7 times compared to the porSiO$_2$ on p-doped Si studied in the last section (from 2.25 mm^2 to 16 mm^2). However, the theoretical FE curves plotted with the FN equation 2.9 indicate that the increase in emission area reduces the macroscopic electric field required for an FE current of 1 pA by only 4 % (for γ_{eff} = 600, ϕ_{ZnO} = 5.3 eV, d = 250 µm). Thus, the reduction of onset field for the herein investigated samples is not explained by the increase of the emission area. In the future, a closer examination of the detailed NW morphology is suggested to determine possible reasons for the strongly reduced onset field of the ZnO emitters grown on the porSiO$_2$ membrane substrates.

The FE measurements were further analyzed using the FN as well as the MG plot to extract the effective FEFs according to the description in section 2.4. The FEFs derived with the FN plot vary between 2330 and 3862 as shown in Figure 5.19 (b). For comparison of the bulk with the NM substrates, the results were separately displayed in Table 5.4. Note, only the

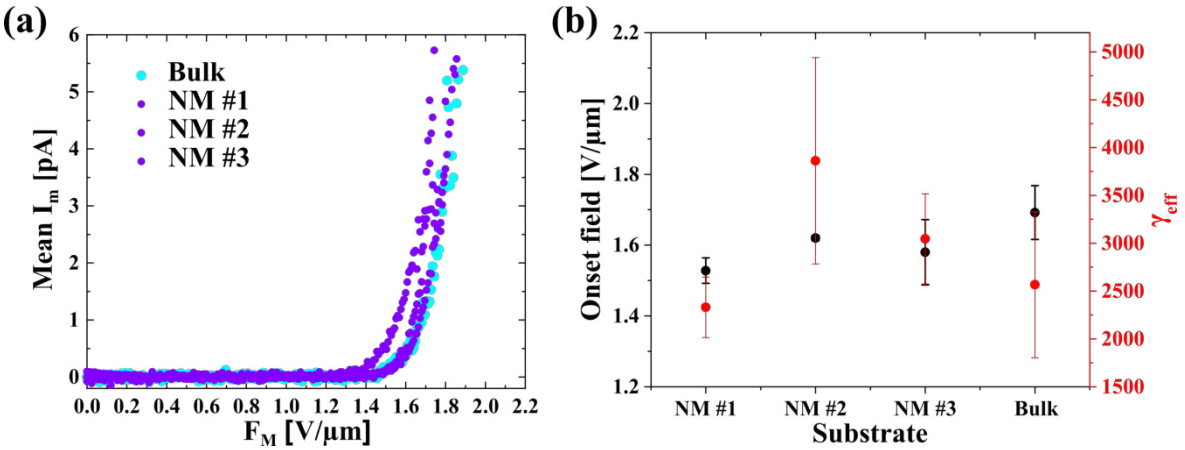

Figure 5.19: (a) The average *I-V* curves derived from several subsequent FE measurements from each of the four samples is presented in dependence on the applied macroscopic electric field. The ZnO emitters were grown on one bulk silicon sample (plotted in light blue), as well as on three separate NM substrates, namely #1, #2 and #3 (plotted in purple). **(b)** The mean values of the onset field (black) as well as of the effective FEF (red) are plotted for the four samples and the error bars present the standard deviations from the mean of subsequent measurements from each sample.

ZnO NWs on porSiO$_2$ (SiN NMs) - FN and MG plot results	
	γ_{eff}
FN plot	
SiN NMs	3079 ± 25 %
Si bulk	2566 ± 30 %
MG plot	
SiN NMs	2929 ± 23 %
Si bulk	2454 ± 29 %

Table 5.4: Summary of the results from FN ($\kappa = 2$) and from MG plot ($\kappa = 1.2879$) for the FE data from ZnO emitters grown on the porSiO$_2$ with SiN NMs and with Si bulk as substrates. The effective FEFs γ_{eff} for FN and MG plot were calculated with equation 2.34 and with equation 2.50, respectively.

extracted values from linear fits with a R^2 value larger than 0.5 were utilized for calculation of the effective FEFs to exclude data sets with an insufficient number of data points above the respective onset voltage. The mean FEF for the membrane substrates is about 17 % larger than the mean value for the bulk substrate. However, the FEFs vary within their standard deviations. Thus, a considerable field enhancement effect from the possible displacement of the flexible NM caused by the applied electrostatic field, is not indicated by the effective FEFs for the herein examined low electric field region, which is characterized by the linear trend of the FE data in the FN plot. Similar to the FN plot analysis, the mean FEF extracted from the MG plot is larger for the membrane substrate than for the bulk one. Yet, the mean values vary again within their standard deviations and are only slightly smaller than the values extracted from the FN plot. Furthermore, the orthodoxy test for the previously considered FE measurements was passed, as the mean minimum and maximum scaled barrier fields (0.23 ± 0.05 and 0.31 ± 0.05) lay within the apparently reasonable range of 0.14–0.43 for ZnO field emitters, which indicates the reliability of the effective FEFs [83].

After investigation of the reproducibility of the *I-V* curves, the FE measurements were executed for NM #2 until termination by electrical breakdown to find the maximum emission current from the ZnO emitters grown on the porSiO$_2$. The largest current of about 1.16 µA—which corresponds to a macroscopic current density of 7.25 µA/cm^2—was reached at a macroscopic electric field of 3.38 V/µm, as shown in Figure 5.20 (a). The turn-on field that is defined by the ECD of 0.1 µA/cm^2, was reached at a macroscopic electric field of about 3.0 V/µm. In an additional experiment, the electric field was held constant at 3.4 V/µm after the emission current exceeded a 1 µA threshold to test the stability of the emission cur-

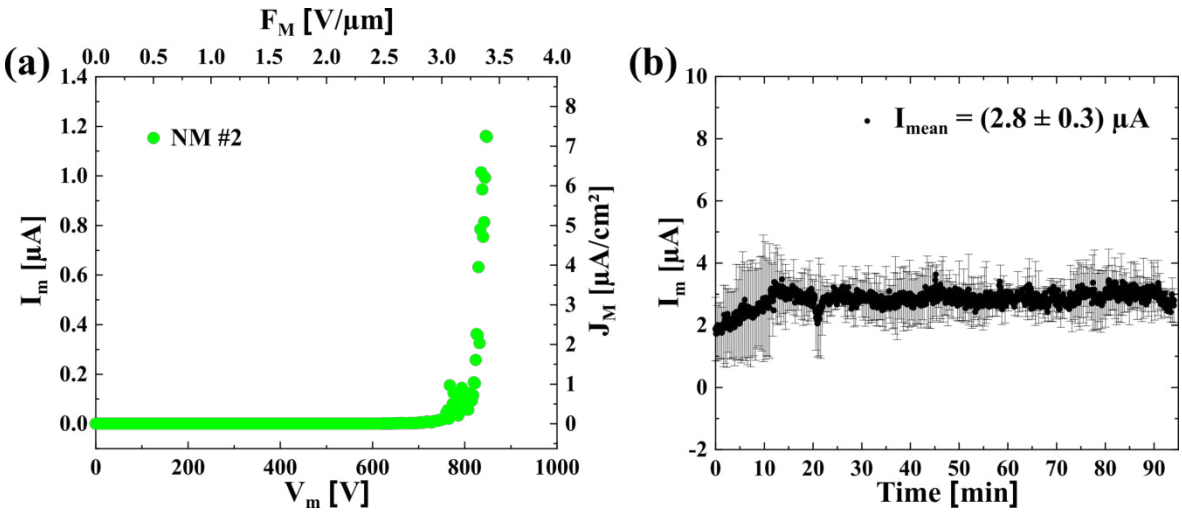

Figure 5.20: (a) The measured current (left y-axis) is shown in dependence on the applied voltage (bottom x-axis) for the ZnO FEA grown on NM #2. The corresponding macroscopic ECD (right y-axis) and macroscopic electric field (upper x-axis) are displayed as well, using the conversion factors $A_M = 0.16\,cm^2$ and $d = 250\,\mu m$. **(b)** The emission current was measured at a constant applied voltage of 848 V (3.392 V/µm) and of 854 V (3.416 V/µm) for 94 min each. The mean emission current of the two successive stability tests is shown and for clarity, the error bars display the standard deviations of every fifth data point only.

rent. As displayed in Figure 5.20 (b), the FE current showed a variation of 11 % around the mean value of 2.8 µA over the total measurement time of 3 h. Similar to the results for the sputter shadow mask approach (ZnO NWs on SiN NM, Figure 4.28), an increase in emission current by about 1 µA was noted within the first 10 min, which was attributed to the resistive self-heating of the emitter. The locally elevated emitter temperature is expected to promote the desorption of adsorbates that have previously shielded the ZnO surface from the electric field. Consequently, the impact of the local electric field on the ZnO was enhanced after ad-layer desorption, which possibly led to the observed increase in emission current [1].

When approaching currents in the microampere range, two distinct features were noted (Figure 5.21 (a)), namely the transition from the linear low field region to the non-linear high field region and the enhanced probability for electrical breakdown. The low threshold of the trip current avoided the destruction of the emitter when an electrical discharge occurred, but still, a modification of the *I-V* curve shape was observed. Figure 5.21 (a) presents the FE measurements before electrical breakdown (2nd–8th, plotted in red) and the change of the FE behavior after electrical discharges occurred (plotted in blue, orange and green). As shown in Figure 5.21 (b), there is no consistent variation of the onset field observed, as shifts to larger and also back to smaller onset values occurred. Additionally, the onset field variation is larger than the standard deviation for the 2nd–8th measurements, which suggests a

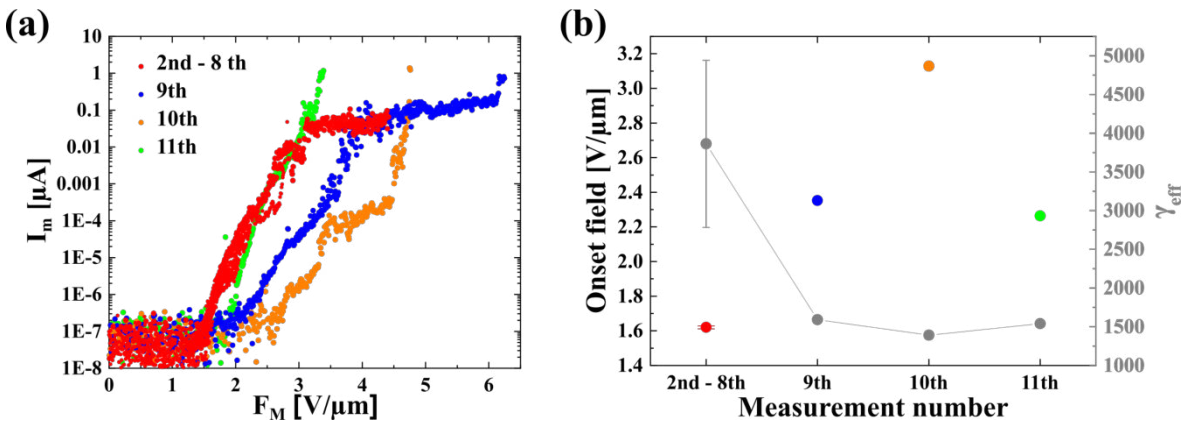

Figure 5.21: (a) *I-V* curves before onset shift for the 2nd–8th measurements (plotted in red) and after the modification through occurrence of electrical breakdowns for the 8th, 9th (blue), 10th (orange) and 11th (green) measurement. The current is shown in logarithmic scale to emphasize the change of the emission current slope with increasing applied electric field. **(b)** The onset field (shown in red) and the effective FEF (gray) are plotted for the initial measurements (2nd–8th) as well as separately for the 9th (blue), 10th (orange) and 11th (green) measurement to visualize the change of the two parameters caused by the electrical discharges.

significant impact of the electrical breakdown on the cathode's constitution. The electrical discharge may alter the shape of the FEA locally or its electronic surface structure, since the associated local heating can promote the desorption of ad-layers that may have shielded the ZnO surface from the applied electric field [1]. Moreover, the variation of the FEF values were plotted in Figure 5.21 (b). The changes of the onset field are accompanied by modification of the effective FEF in the expected direction, namely the increase of the onset field correlates with the reduction of the FEF. In addition, the FEF is nearly reduced by about 50 % after the first electrical discharge. The change of the effective FEF is larger than the range given by the error bar for the 2nd–8th measurement, which indicates a shape modification of the ZnO NWs that contribute to the FE. In summary, the considerable reduction of the FEF and the observed increase of the onset field suggest an unfavorable reshaping of the emitter tips caused by the electrical discharges.

For the previous analysis, only the low field region was contemplated that is characterized by its linear trend in the FN plot as emphasized by the yellow fits in Figure 5.22 (a). For the shown measurements, a decrease of the emission current slope is noted for the transition from low to high field region, which is highlighted by the green fits. The non-linear trend is observed above an applied electric field of 3.1 V/µm and of 3.7 V/µm for the 8th (red) and for the 9th (blue) measurement, respectively. As shown in Figure 5.22 (b) for the two subsequent *I-V* curves, the transition from low to high field region starts about (1.4 ± 0.1) V/µm above the respective onset field of each measurement at a comparable emission current of around

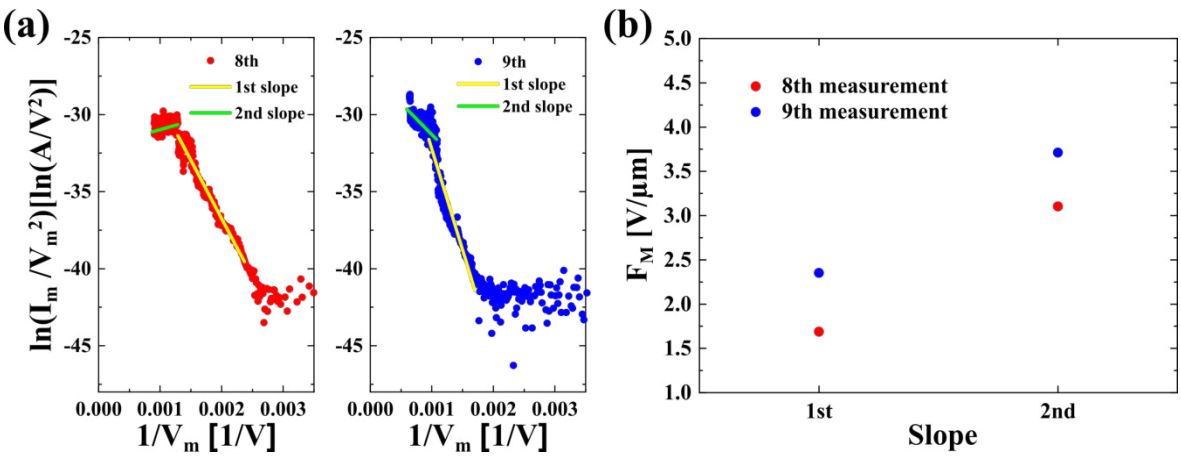

Figure 5.22: (a) The shown FN plots of the 8th (red) and 9th measurement (blue) can be divided into two pars. First, the linear current rise after onset of FE in the low field region (yellow fit) and second, a non-linear trend of the emission current in the high field region (green fit). Additionally, another short steep rise of the emission current is observed for the 9th measurement, which was attributed to the forthcoming electrical breakdown. **(b)** The onset field for FE is given by the values for the 1st slope and the transition from low to high field region is characterized by the macroscopic fields given for the 2nd slope.

(0.031 ± 0.001) µA. The onset field shift between the 8th and 9th measurement was earlier in this section attributed to the effect of electrical breakdown on the emitters' geometrical shape and consequently, on their FE properties. However, the difference between the onset of FE (1st slope) and the transition to the high field region (2nd slope) is not affected by the electrical breakdown. This result suggests that the same effect leads to the observed non-linearity.

The noted decrease of emission current slope may be attributed to the saturation of electron emission from the conduction band because of the limited charge carrier generation rate inside the semiconductor [61, 67]. For the ZnO NWs on the highly-doped Si NMs (section 4.2.2, Figure 4.16), the emission current slope decreased in a narrow voltage range of 76 V (0.0011 [1/V]–0.0012 [1/V]), but increased again at higher electric fields. This observation was supposed to be caused by the contribution from the valence band to the emission current that was enabled by energy band bending, which gradually increases with rising electric field [46, 67].

Herein, the decrease of emission current seems to be the predominant mechanism in the high field regime. In contrast to the observations for the Si NM substrates, the reduction of the emission current slope is noted in a wider range of 0.0009 [1/V]–0.0013 [1/V] (342 V difference) for the 8th and of 0.0006 [1/V]–0.0011 [1/V] (758 V difference) for the 9th measurement. The FE current behavior in the high field region is similar to the results for the ZnO emitters on the insulating SiN NM substrates (see section 4.3.2, Figure 4.27). Therefore, a distinct increase in emission current, as observed for the Si NM substrates in the last chapter,

may be suppressed by the limited charge carrier supply of the herein used insulating substrate (porSiO$_2$ on SiN NM). Additionally, vacuum space charge may have shielded the emitters' surface from the electric field and caused the reduced emission current slope as it was also suggested for the SiN NM substrates in the previous chapter [2, 46].

5.4 Summary and Discussion

A subtractive preparation route for porous SiO$_2$ was established and a minimum RI of 1.2 was obtained that corresponds to an apparent porosity of about 57 %. The SiO$_2$ template was utilized to guide the catalyst particle formation by dewetting of a thin gold film. The generated particle distribution enabled the catalyst-assisted growth of ZnO NWs on bulk substrates and after some adjustments of the synthesis procedure, also on free-standing SiN membranes. The FE properties of the arrays of randomly distributed, several micrometer long ZnO NWs were examined. The adjustment of the selective wet etching process for the thin membranes enhanced the reproducibility of field emitter samples that showed similar FE properties. The mean onset field derived from all samples with the porous SiO$_2$ on 3x3 mm^2 SiN NMs, was determined to be 1.6 V/µm $\pm$ 6 %. In contrast, a mean onset field of 3.8 V/µm $\pm$ 50 % was found for the ZnO emitters grown on the p-doped Si with porous SiO$_2$ that was generated in the boiling phosphoric acid. For the ZnO NWs on the SiN NMs with porous SiO$_2$, it was possible to obtain FE currents in the microampere range and the emission current showed variations of only 11 % at a constant applied field over a total period of 3 h. The turn-on field, defined by a macroscopic ECD of 0.1 µA/cm^2, was already reached at an electric field of 3.0 V/µm, which is within the range of turn-on fields (0.85 V/µm–6.0 V/µm) reported in literature for ZnO emitters grown by vapor phase transport methods on bulk substrates [178, 179].

In Table 5.5, the results of the ZnO NWs on the 3x3 mm^2 SiN membranes with the porous SiO$_2$ template are compared to the FE properties of the ZnO emitters grown on the 3x3 mm^2 SiN membrane with the help of the sputter shadow mask for catalyst deposition (Table 4.8).

SiN NM substrates - Comparison of FE results

Synthesis method	F_M^{onset} [V/µm]	F_M^{max} [V/µm]	J_M^{max} [µA/cm^2]	F_M^{on1} [V/µm]	F_M^{on2} [V/µm]
Porous SiO$_2$ template	1.6 $\pm$ 0.1	3.4	7.3	3.0	-
Sputter shadow mask	2.0 $\pm$ 0.1	9.0	141.5	3.3	4.1

Table 5.5: Summary of the FE properties for ZnO emitters grown on 3x3 mm^2 SiN membranes with the help of the porous SiO$_2$ template or with application of the sputter shadow mask. The turn-on fields F_M^{on1} and F_M^{on2} are defined by an ECD of 0.1 µA/cm^2 and of 10 µA/cm^2, respectively.

The macroscopic onset field and the turn-on field F_M^{on1} are lower for the ZnO field emitters grown on the porSiO$_2$ than for the NWs that were fabricated with the sputter shadow mask. A smaller mean tip diameter as well as a larger aspect ratio were found for ZnO NWs grown on the porous SiO$_2$ compared to the sputter shadow mask technique, as discussed in section 5.2.1. Therefore, the lower electric field values may correlate with a larger geometrical field enhancement effect of the ZnO NWs deposited on the porSiO$_2$. The favorable emitter dimensions are attributed to the smaller mean gold particle diameter that was found for dewetting of a gold film on the porous SiO$_2$, which has half the size of the catalyst dots generated by application of the sputter shadow mask approach (see section 5.1.4).

The larger maximum ECD from the emitters fabricated with the sputter shadow mask was probably caused by the extended outgassing time that was longer than 72 h in combination with a considerable number of previous FE measurements that were executed in the low field region well below the electrical breakdown threshold of our measurement configuration. Hence, the ZnO NWs grown on the porous SiO$_2$ may have the potential to reach the same ECD values after prolonged time in vacuum combined with more low current measurements to promote the desorption of ad-layers, which could reduce the risk for electrical breakdown and thus, prevent the corresponding early termination of the *I*-*V* curve measurements.

6 Conclusion and Future Perspective

In this thesis, the synthesis of ZnO field emitters by catalyst-assisted MOCVD on bulk as well as on free-standing NM substrates was presented. It was possible to find an appropriate combination of deposition parameters for the ZnO growth process, which used the precursor mixture of zinc acetylacetonate hydrate and oxygen, with catalyst particle distributions that allowed for the generation of ZnO NWs having length-to-tip diameter ratios larger than 310. The first approach used a sputter shadow mask that was employed to influence the gold film constitution during sputter deposition and for the second one, a layer of porous SiO_2 was used to affect the catalyst particle agglomeration during the dewetting process. Both catalyst generation techniques, which were tailored for application on freely suspended membranes, enabled the time efficient catalyst distribution on millimeter sized areas. Even the subsequent gold particle formation relied on self-assembly during the heating ramp in the ZnO growth oven, the FE properties of the resulting ZnO emitter arrays showed to be reproducible.

Moreover, a certain dependence of the ZnO NW morphology on the gold particle diameter was suggested by comparison of the two methods. The smaller gold particle diameter formed on the porous SiO_2 correlated with a smaller NW tip diameter as well as an overall larger aspect ratio than it was generated by the sputter shadow mask method. Furthermore, the enhanced NW geometry that was produced on the porous SiO_2 led to the reduction of the electric field that allows for FE from the ZnO emitters. A study on the influence of synthesis parameters and membrane sizes on the emitters' FE properties revealed first approaches to improve their FE characteristics further. A new type of flexible substrate for FEAs has been added by the Si and the SiN nanomembranes that can withstand the elevated growth temperatures in CVD processes and thus, may have the potential to operate in harsh environments. On the basis of the herein determined FE properties, namely the FE current stability over time and the reproducible synthesis of field emitter samples combined with the control over the emission current in the optimized FE measurement configuration, possible future applications for field emitters on free-standing bases and preliminary results are presented in the following.

Sensing Application for Mass Spectrometry

The combination of the matrix-assisted laser desorption/ionization (MALDI) method used

as ion source, with a time-of-flight (TOF) mass analyzer can be applied for analysis of biomolecules, such as peptides and proteins. First, the MALDI technique produces ions in low charge states, which are subsequently accelerated into the adjacent TOF tube, where the ionized molecules are separated according to their mass-to-charge ratio. Finally, the arrival of the ions is sensed by a detector and the flight time of the ionized molecules can directly be related to their mass-to-charge ratio for their identification. In practice, the detection of masses above 100 kDa is mainly limited by the sensitivity of conventional detection systems, such as dynodes and MCPs. Their sensing mechanism typically relies on the generation of secondary electrons provoked by the impinging ions. With increasing ion mass, the secondary electron yield decreases, which leads to a considerable reduction of the detection efficiency and prevents the measurement of heavy biomolecules [192–194].

A nanomembrane detector was proposed to overcome the mass limitation of conventional detectors, since the ion signal is first converted into an electron signal that is subsequently amplified by MCPs. Thereby, the dependence of the secondary electron yield on the ion velocity and thus, on the ion mass, can be circumvented. As explained in the introductory chapter, the nanomembrane detector resembles a FE based displacement sensor with a flexible membrane that functions as FE electron source. Since the field enhancement effect of pristine membranes is solely determined by their surface roughness, the operation voltages and corresponding electric fields are well above 1 kV and 10 V/µm, respectively [17, 19, 21]. Thus, it is necessary to enhance the FE from membranes geometrically to lower the required operation voltages and thereby, to reduce the risk for electrical discharge.

Figure 6.1 shows five SOI samples with twenty NMs in total, which were operated simultaneously in a FE measurement. ZnO NWs have been grown on all five samples with the

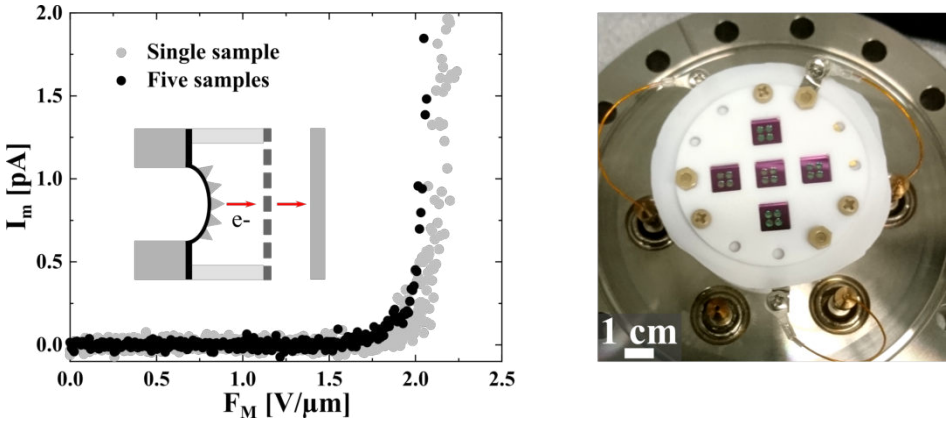

Figure 6.1: Five SOI samples with ZnO NWs were arranged as shown in the photograph on the right side. The FE measurement from the five field emitter samples operating in parallel is shown on the left side (plotted in black). For comparison, several subsequent FE measurements from a single Si NM sample with ZnO NWs are presented (gray, sample Si-NM-3 of section 4.2.2). Both FE experiments were conducted with d = 250µm.

standard growth process by application of the sputter shadow mask technique that was described in chapter 4. The onset field for the five parallel operating FE samples of 1.9 V/µm is within the error boundaries of the onset field for FE from a single sample with ZnO NWs on Si NMs, namely (2.0 ± 0.1) V/µm. This observation indicates the high reproducibility of the herein established ZnO growth process with regard to the FE properties of the samples. The slightly lower onset field may be caused by the enlarged emission area in the arrangement with multiple field emitter samples. This measurement configuration is now ready to be implemented as a detector in a MALDI-TOF system and might pave the way to the measurement of heavy biomolecules at room temperature.

CNTs on Free-Standing NMs for FE

For further enhancement of the FE properties, other emitter materials may be considered like carbon nanotubes. CNTs exhibit extreme aspect ratios that facilitate the emission of electrons by FE at comparable low electric fields. Combined with their high electrical conductivity and their thermal as well as chemical stability, CNTs are known to be excellent FE electron sources [195].

As a proof-of-concept, CNTs were grown in-house by CVD on free-standing Si NMs and the FE properties were determined. As shown in Figure 6.2, emission currents in the microampere range were reached already below an electric field of 2 V/µm. Furthermore, an onset field of (0.86 ± 0.02) V/µm was derived for the CNTs on the Si NM sample from several subsequent measurements. Thus, the onset field was reduced by 50 % through the replacement of ZnO emitters with CNTs. The turn-on field, defined by an ECD of 10 µA/cm^2 (A_M = 0.36 cm^2), was determined to be 1.4 V/µm, which is considerably smaller than found

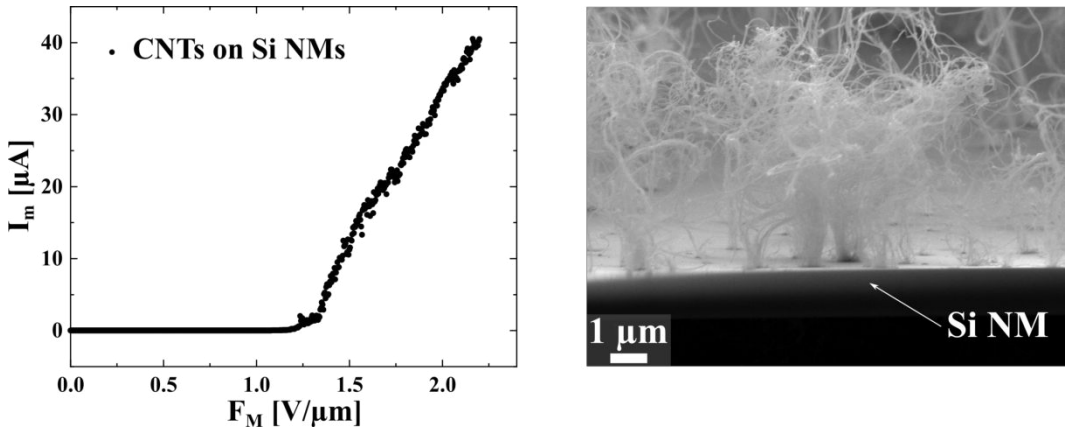

Figure 6.2: The *I-V* curve from CNTs grown on Si NMs is shown on the left side (d = 500µm). A cross section through the free-standing Si NM reveals the random order of the CNTs, which were deposited by CVD on the membrane. The SEM image was taken under a tilt angle of 50 ° with the Crossbeam 550 by Zeiss.

for the ZnO NWs grown on the SiN NM (4.1 V/µm, see Table 4.8). Note, extensive optimization of the recently established CNT deposition process is still needed and may allow for further reduction of the turn-on field.

Si and SiN NMs as Anode

Herein, the universality of the optimized triode-type FE measurement configuration (presented in chapter 3) is demonstrated, as it can also be operated in the diode-type version. Furthermore, the diode-type arrangement allows for the application of a NM as anode. A Si NM sample as well as a gold coated SiN NM were used as collector for the emission current from opposing field emitters on bulk substrates according to the diode-type configuration that is indicated in Figure 6.3 (a). Additionally, the stability of the emission current in this measurement configuration was proven, which is shown in Figure 6.3 (b).

Porous SiO_2 and SiO_xN_y

Further investigation of the porous SiO_2 layers and of the SiO_xN_y films may be of interest because the deposition by PECVD permits the coating of temperature sensitive devices with convenient deposition rates of around 20 nm/min at process temperatures of 130 °C. Typical applications for porous thin films are as anti-reflective coatings that minimize reflection losses or as diffusion membranes for encapsulation of nanostructures for their protection against environmental influences [182, 196]. Furthermore, a wide range of refractive indices can be covered by variation of the deposition conditions for the SiO_xN_y as it was shown

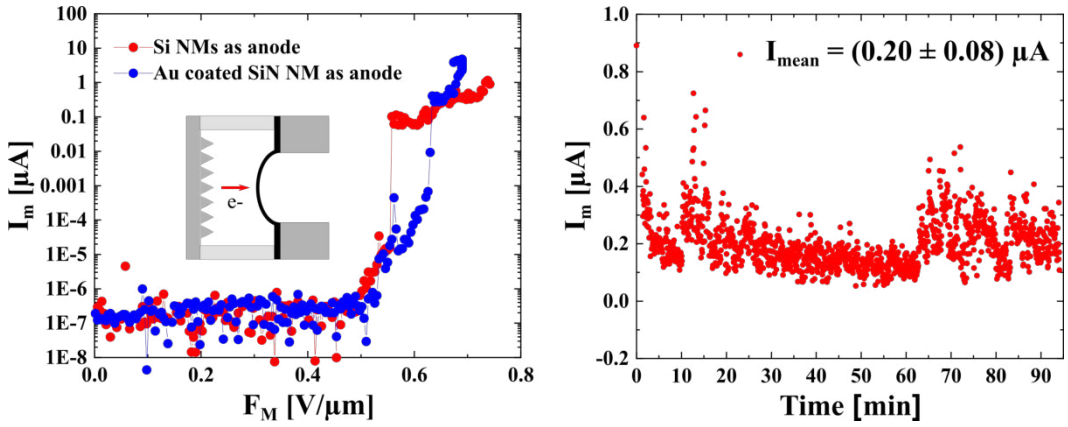

Figure 6.3: Si NMs (plotted in red) and a gold coated SiN NM (blue) were used as anode to measure the FE current from in-house grown CNTs that were deposited on bulk substrates. For the CNT emitters, emission currents in the microampere range are reached well below a macroscopic electric field of 1 V/µm (d = 500µm). Furthermore, the emission current was continuously acquired at the Si NM sample (red) for more than 90 min, as shown on the right side. Extension of the measurement time is most likely possible, since the acquisition was terminated manually.

in chapter 5. Therefore, the optical and electrical properties of SiO_xN_y films can be tailored, which makes them attractive candidates for optoelectronic applications. For instance, SiO_xN_y can be used as a scratch resistant coating for flexible and transparent polymers that are employed as substrates for optoelectronic devices, because of the mechanical strength of the SiO_xN_y and the possibility for adjustment of its optical properties [197].

In this thesis, the foundation for application of ZnO nanostructures on free-standing NMs has been established. The synthesis for the catalyst-assisted MOCVD of ZnO emitters has been optimized and characterization of their FE properties has been performed. Further approaches for improvements have been identified which might pave the way for CVD grown emitters on flexible inorganic membranes for application as pressure sensors or as detectors in mass spectrometry.

A Appendix

A.1 Physical Constants and Field Emission Values

Symbol	Meaning	Value
e	Elementary charge	$1.602\,176{\cdot}10^{-19}$ C
m_e	Electron mass	$9.109\,383{\cdot}10^{-31}$ kg
ε_0	Vacuum permittivity	$8.854\,187{\cdot}10^{-12}$ C/(m·V)
		$8.854\,187{\cdot}10^{-21}$ C/(nm·V)
k_B	Boltzmann constant	$1.380\,649{\cdot}10^{-23}$ J/K
		$8.617\,333{\cdot}10^{-5}$ eV/K
$\hbar = \frac{h}{2\pi}$	Reduced Planck constant	$1.054\,571{\cdot}10^{-34}$ J·s
		$6.582\,119\cdot10^{-16}$ eV·s

Table A.1: Fundamental physical constants taken from the National Institute of Standards and Technology [198].

Symbol	Meaning	Expression	Value
a_FN	FN constant I	$\frac{e^3}{16\pi^2\hbar}$	$1.541\,434\,\mu\mathrm{A{\cdot}eV/V^2}$
b_FN	FN constant II	$\frac{2}{3e}g_\mathrm{e}$	$6.830\,890\,\mathrm{V}/\left(\mathrm{nm}\cdot\mathrm{eV}^{3/2}\right)$
c^2		$\frac{e^3}{4\pi\varepsilon_0}$	$1.439\,964\,\mathrm{nm{\cdot}eV^2/V}$

Table A.2: Basic FE values taken from [4]. The values for a_FN and b_FN were taken from [30].

A.2 Substrate Preparation and ZnO Growth Recipe

Herein, recipes are summarized that were used for the substrate preparation in section 4.1.1 and for the ZnO growth process in section 4.1.3.

ICP-RIE Recipe

The fabrication of a SiN NM (section 4.1.1) involves the opening of a window in the backside of the SiN covered Si sample by ICP-RIE (SI500 from Sentech Instruments GmbH). An etch rate of (439 ± 24) nm/min was determined by ellipsometry for LPCVD SiN.

Parameter	Value
SF_6	50 sccm
O_2	5 sccm
Pressure	2 Pa
Electrode temperature	23 °C
ICP power	400 W
Radio frequency power	50 W

Table A.3: Parameters of the ICP-RIE recipe for the etching of SiN.

Membrane Cleaning Recipe

The following membrane cleaning recipe was used after the etching in aqueous potassium hydroxide solution (KOH, 80 °C, 30 %) to prevent the formation of residues on the membrane's surface.

- Removal of the KOH by transfer of the SiN NM sample in a first beaker with ultra pure water (taken from the Milli-Q® Integral 5 device).
- Leaving the sample in a second beaker with ultra pure water for at least 12 h to allow for the dissolution of KOH residues.
- Gentle rinsing of the sample in methanol.
- Acceleration of the solvent evaporation on a hot plate (set to 300 °C). Note, the sample is hold with tweezers in a tilted manner above the hot plate to prevent the gathering of solvent and thereby, to avoid generation of residues on the flexible membrane part of the substrate.

ZnO Growth Recipe

The standard ZnO growth process uses zinc acetylacetonate hydrate powder (2.4 g, from Sigma-Aldrich) and oxygen (83 sccm, purity 5.0) as precursor substances and argon (100 sccm, purity 5.0) as transport gas. The growth process is performed in a horizontal three-zone tube furnace (OTF-1200X-III-UL, MTI corporation) as described in section 4.1.3.

Preparation:

- The precursor powder is evenly distributed in a ceramic crucible, which is then placed in the middle of the first heating zone.
- The substrate is positioned in the front-third of a second ceramic boat and subsequently, the ceramic boat is placed in the beginning of the third heating zone.
- The quartz tube is evacuated below a pressure of $1.8 \cdot 10^{-1}$ mbar before initialization of the growth process.

Growth process:

Step	Precursor zone	Transition zone	Growth zone
C01 [°C]	20	20	20
T01 [min]	10	10	10
C02 [°C]	70	70	70
T02 [min]	170	170	120
C03 [°C]	70	70	70
T03 [min]	10	10	30
C04 [°C]	110	200	580
T04 [min]	720	720	750
C05 [°C]	110	200	580
T05 [min]	60	60	60
C06 [°C]	20	20	20
T06 [min]	-121	-121	-121

Table A.4: Temperature profile for each zone of the three-zone tube furnace. Note, C0x defines the set temperature and T0x defines the time between subsequent steps. Oxygen and argon are introduced 1 h after initialization of the growth process. The command -121 turns off the heaters, which allows for a natural cool down of the system.

A.3 ZnO Field Emitters - Morphology

A.3.1 Dimension Analysis

All vertical length measurements in the SEM images with ImageJ [157] were subsequently corrected by division through the factor $\cos(\alpha_{stage})$ that considers the tilt angle of the stage, namely $\alpha_{stage} = 54\,°$. Parallel to the tilt axis of the specimen, the object's size is typically not affected, however, perpendicular to the tilt axis, items shown in the SEM image become distorted. The feature of tilt correction from the SEM software is only applicable to objects that are in plane with the specimen. If the tilt correction function is used for a structure of arbitrary 3D orientation, it will cause significant distortion of the image acquired for the object [199]. Hence, the tilt correction function was not applied for imaging of the randomly oriented ZnO NWs. The measured and subsequently corrected values for the NW length have to be treated as rough estimates and are mainly intended for relative comparison of the herein grown ZnO structures.

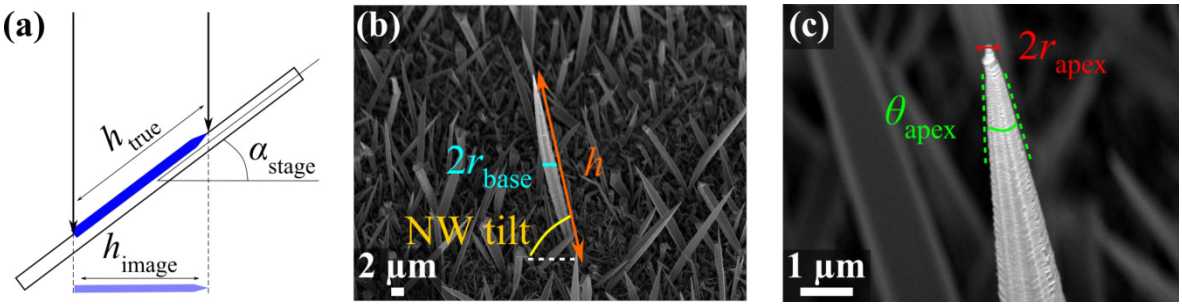

Figure A.1: Explanatory notes on the dimension analysis of the ZnO NWs. **(a)** The image displays the principle of tilt correction. For a tilted specimen, objects appear to be foreshortened in correlation with the tilt angle of the stage (α_{stage}). The observed height of an object (h_{image}) is related to the actual size (h_{true}) by: $h_{true} = h_{image}/\cos(\alpha_{stage})$ [199]. **(b)** The SEM image shows a large ZnO NW grown on a Si NM. The length (h) of the NW, the diameter at the widest position ($2r_{base}$) and the NW tilt angle were determined from one SEM image per NW. **(c)** The tip diameter ($2r_{apex}$) as well as the tip inclination angle (θ_{apex}) were determined from a second close-up image of the wire's tip. The SEM images were taken under a tilt angle of 54 ° with the Crossbeam 550 by Zeiss.

A.3.2 Sputter Shadow Mask - Gold Dot Distribution

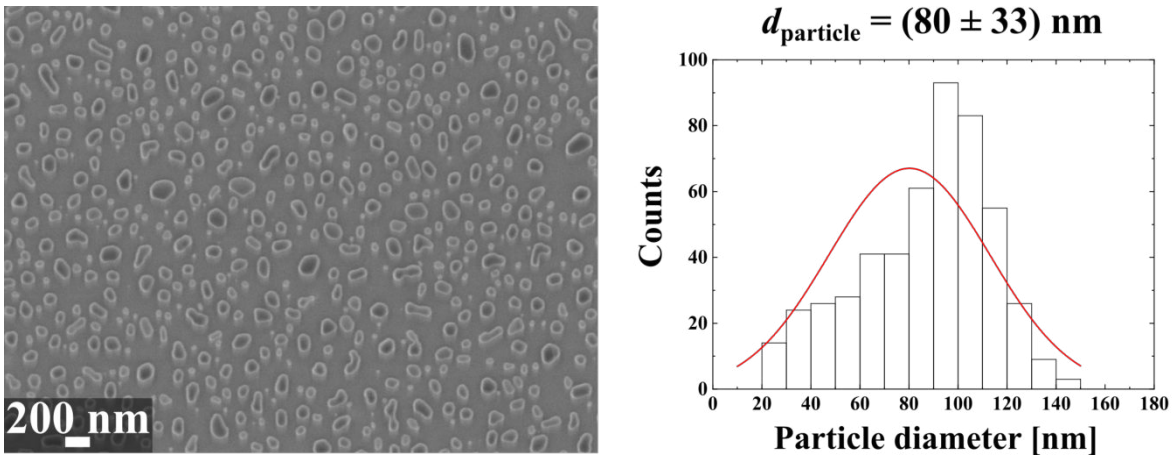

Figure A.2: (a) Gold particle distribution on a Si NM after dewetting of a thin gold film that was deposited through the sputter shadow mask (deposition time: 60 s). The sample was annealed at the ZnO growth temperature of 580 °C. The SEM image was analyzed using ImageJ [157] and the mean gold particle diameter of $d_{particle}$ = (80 ± 33) nm was obtained from the normal distribution of the data shown in the histogram (indicated by the red line). The SEM image was taken with the Crossbeam 550 by Zeiss.

A.3.3 Sputter Shadow Mask - Gold Dot Location

The location of the gold dots after ZnO growth on the free-standing SiN NMs was examined using SEM and EDX.

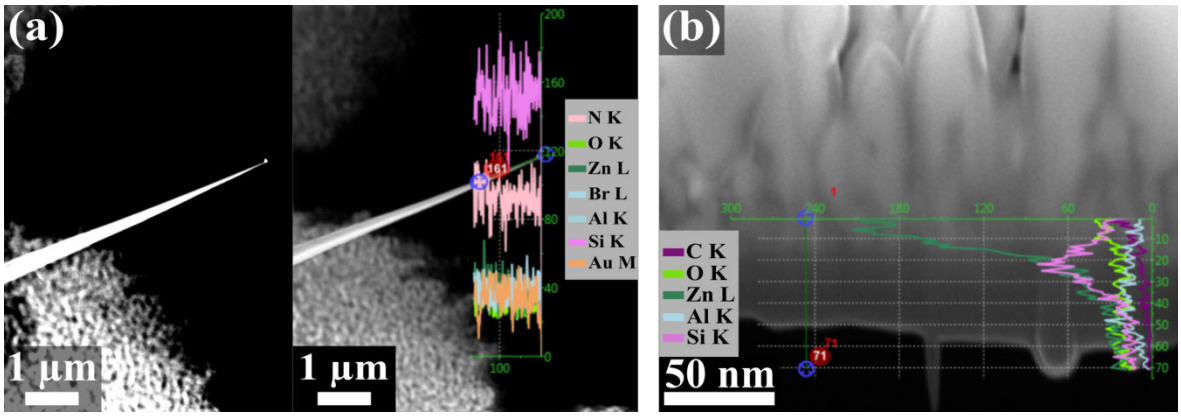

Figure A.3: (a) SEM image of a large NW protruding above a hole in the ZnO film that exposes the SiN NM (black background behind NW tip). A constantly small amount of gold (Au, orange) was detected along the NW that may also originate from the background area. The high silicon (Si, pink) and nitrogen (N, light pink) concentrations are from the exposed SiN substrate, whereas the constant low zinc (Zn, dark green) and oxygen (O, light green) signals originate from the NW. A locally enhanced amount of gold was not detected and the aluminum (Al, light blue) signal was possibly generated by the sample holder because the SiN membrane has a thickness of only 100 nm. The detected bromine signal (Br) may be falsely assigned by the EDX software, because its line is close to the one of aluminum [200]. **(b)** At the cross section through the NM, the transition from the ZnO array to the SiN NM is noted by the sudden drop of the zinc amount (dark green) in the line scan. Gold was neither observed as dots at the roots of the NWs nor detected in the line scan across the ZnO-SiN transition region. The aluminum (light blue) and the carbon (C, purple) signals may originate from the sample holder and from contamination by the preceding SEM imagining, respectively. The SEM images and EDX spectra (8 kV, 3.9 nA) were taken under a tilt angle of 54 ° with the Crossbeam 550 by Zeiss.

Bibliography

[1] G. N. Fursey. *Field emission in vacuum microelectronics*. Kluwer Academic / Plenum Publishers, 1st edition, 2005.

[2] N. Egorov and E. Sheshin. *Field emission electronics*. Springer International Publishing, 1st edition, 2017.

[3] G. Gaertner, W. Knapp, and R. G. Forbes. *Modern developments in vacuum electron sources*. Springer International Publishing, 1st edition, 2020.

[4] S.-D. Liang. *Quantum tunneling and field electron emission theories*. World Scientific Publishing, 1st edition, 2014.

[5] H.-C. Lee and R.-S. Huang. A novel field emission array pressure sensor. *Transducers'91: 1991 International Conference on Solid-State Sensors and Actuators. Digest of Technical Papers. IEEE*, pages 241–244, 1991.

[6] J. C. Jiang, R. C. White, and P. K. Allen. Microcaviy vacuum tube pressure sensor for robot tactile sensing. *Transducers'91: 1991 International Conference on Solid-State Sensors and Actuators. Digest of Technical Papers. IEEE*, pages 238–240, 1991.

[7] H. Liu, K. Wei, Z. Li, W. Huang, Y. Xu, and W. Cui. A novel, hybrid-integrated, high-precision, vacuum microelectronic accelerometer with nano-field emission tips. *Micromachines*, 9(10):481, 2018.

[8] D. Nicolaescu. Modeling of the field emitter triode (FET) as a displacement/pressure sensor. *Applied Surface Science*, 87/88:61–68, 1995.

[9] N. Badi, A. M. Nair, and A. Bensaoula. Field emission pressure sensors with non-silicon membranes. *Applied Surface Science*, 256(16):4990–4994, 2010.

[10] H.-C. Lee and R.-S. Huang. A study on field-emission array pressure sensors. *Sensors and Actuators A: Physical*, 34(2):137–154, 1992.

[11] A. Angelescu, I. Kleps, I. Pavelescu, D. Nicolaescu, O. Nedelcu, M. Avram, N. Samfirescu, and M. Miu. Technology for field emission pressure sensors. *2000 International Semiconductor Conference. 23rd Edition. CAS 2000 Proceedings (Cat. No.00TH8486), IEEE*, 2:437–440, 2000.

[12] K. Qian, T. Chen, B. Yan, Y. Lin, D. Xu, Z. Sun, and B. Cai. Research on carbon nanotube array field emission pressure sensors. *Electronics Letters*, 41(14):824–825, 2005.

[13] W. P. Kang, J. L. Davidson, Q. Li, J. F. Xu, D. L. Kinser, and D. V. Kerns. A novel low-field electron-emission polycrystalline diamond microtip array for sensor applications. *Sensors and Actuators A: Physical*, 54(1-3):724–727, 1996.

[14] S. Taak, S. Rajabali, S. Darbari, and S. Mohajerzadeh. High sensitive/wide dynamic range, field emission pressure sensor based on fully embedded CNTs. *Journal of Physics D: Applied Physics*, 47(4):045302, 2014.

[15] J. Pekarek, R. Vrba, J. Prasek, O. Jasek, P. Majzlikova, J. Pekarkova, and L. Zajickova. MEMS carbon nanotubes field emission pressure sensor with simplified design: Performance and field emission properties study. *IEEE Sensors Journal*, 15(3):1430–1436, 2015.

[16] H. H. Busta, J. E. Pogemiller, and B. J. Zimmerman. The field emitter triode as a displacement/pressure sensor. *Journal of Micromechanics and Microengineering*, 3(2):49–56, 1993.

[17] J. Park, H. Qin, M. Scalf, R. T. Hilger, M. S. Westphall, L. M. Smith, and R. H. Blick. A mechanical nanomembrane detector for time-of-flight mass spectrometry. *Nano Letters*, 11(9):3681–3684, 2011.

[18] J. Park, Z. Aksamija, H.-C. Shin, H. Kim, and R. H. Blick. Phonon-assisted field emission in silicon nanomembranes for time-of-flight mass spectrometry of proteins. *Nano Letters*, 13(6):2698–2703, 2013.

[19] H. Kim, J. Park, Z. Aksamija, M. Arbulu, and R. H. Blick. Ultrananocrystalline diamond membranes for detection of high-mass proteins. *Physical Review Applied*, 6(6):064031, 2016.

[20] J. A. Rogers, M. G. Lagally, and R. G. Nuzzo. Synthesis, assembly and applications of semiconductor nanomembranes. *Nature*, 477:45–53, 2011.

[21] J. Park and R. H. Blick. A silicon nanomembrane detector for matrix-assisted laser desorption/ionization time-of-flight mass spectrometry (MALDI-TOF MS) of large proteins. *Sensors*, 13(10):13708–13716, 2013.

[22] M. Sui, P. Gong, and X. Gu. Review on one-dimensional ZnO nanostructures for electron field emitters. *Frontiers of Optoelectronics*, 6(4):386–412, 2013.

[23] C. Hedrich, S. Haugg, L. Pacarizi, K. P. Furlan, R. H. Blick, and R. Zierold. Low-temperature vapor-solid growth of ZnO nanowhiskers for electron field emission. *Coatings*, 9(11):698, 2019.

[24] J. B. Baxter and E. S. Aydil. Metallorganic chemical vapor deposition of ZnO nanowires from zinc acetylacetonate and oxygen. *Journal of the Electrochemical Society*, 156(1):H52–H58, 2009.

[25] A. Modinos. *Field, thermionic and secondary electron emission spectroscopy*. Springer US, 1st edition, 1984.

[26] R. H. Fowler and L. Nordheim. Electron emission in intense electric fields. *Proceedings of the Royal Society A: Mathematical, Physical and Engineering Sciences*, 119(781):173–181, 1928.

[27] H. B. Michaelson. The work function of the elements and its periodicity. *Journal of Applied Physics*, 48(11):4729–4733, 1977.

[28] R. Gross and A. Marx. *Festkörperphysik*. De Gruyter, 3rd edition, 2018.

[29] K. L. Jensen. *Introduction to the physics of electron emission*. John Wiley & Sons, 2018.

[30] R. G. Forbes. Comments on the continuing widespread and unnecessary use of a defective emission equation in field emission related literature. *Journal of Applied Physics*, 126(21):210901, 2019.

[31] E. L. Murphy and R. H. Good. Thermionic emission, field emission, and the transition region. *Physical Review*, 102(6):1464–1473, 1956.

[32] R. E. Burgess, H. Kroemer, and J. M. Housten. Corrected values of Fowler-Nordheim field emission functions $v(y)$ and $s(y)$. *Physical Review*, 90(4):515, 1953.

[33] R. G. Forbes. Simple good approximations for the special elliptic functions in standard Fowler-Nordheim tunneling theory for a Schottky-Nordheim barrier. *Applied Physics Letters*, 89(11):113122, 2006.

[34] R. G. Forbes and J. H. B. Deane. Reformulation of the standard theory of Fowler-Nordheim tunnelling and cold field electron emission. *Proceedings of the Royal Society A: Mathematical, Physical and Engineering Sciences*, 463(2087):2907–2927, 2007.

[35] F. M. Charbonnier, R. W. Strayer, L. W. Swanson, and E. E. Martin. Nottingham effect in field and T-F emission: Heating and cooling domains, and inversion temperature. *Physical Review Letters*, 13(13):397–401, 1964.

[36] T. Bechtold, E. B. Rudnyi, and J. G. Korvink. *Fast simulation of electro-thermal MEMS: Efficient dynamic compact models*. Springer-Verlag Berlin Heidelberg, 1st edition, 2007.

[37] I. Engle and P. H. Cutler. The effect of different surface barrier models on the Nottingham energy exchange process. *Surface Science*, 8(3):288–306, 1967.

[38] R. G. Forbes, C. J. Edgcombe, and U. Valdrè. Some comments on models for field enhancement. *Ultramicroscopy*, 95:57–65, 2003.

[39] V. Filip, D. Nicolaescu, M. Tanemura, and F. Okuyama. Modeling the electron field emission from carbon nanotube films. *Ultramicroscopy*, 89(1–3):39–49, 2001.

[40] C. Ye, Y. Bando, X. Fang, G. Shen, and D. Golberg. Enhanced field emission performance of ZnO nanorods by two alternative approaches. *The Journal of Physical Chemistry C*, 111(34):12673–12676, 2007.

[41] Z. Zhang, G. Meng, Q. Wu, Z. Hu, J. Chen, Q. Xu, and F. Zhou. Enhanced cold field emission of large-area arrays of vertically aligned ZnO-nanotapers via sharpening: Experiment and theory. *Scientific Reports*, 4(4676):1–7, 2014.

[42] D. Biswas. A universal formula for the field enhancement factor. *Physics of Plasmas*, 25(4):043113, 2018.

[43] J. R. Harris, D. A. Shiffler, K. L. Jensen, and J. W. Lewellen. Investigation of the Schottky conjecture for compound structures modeled with line charges. *Journal of Applied Physics*, 125(21):215307, 2019.

[44] R. Miller, Y. Y. Lau, and J. H. Booske. Schottky's conjecture on multiplication of field enhancement factors. *Journal of Applied Physics*, 106(10):104903, 2009.

[45] C. J. Edgcombe and U. Valdrè. Microscopy and computational modelling to elucidate the enhancement factor for field electron emitters. *Journal of Microscopy*, 203(2):188–194, 2001.

[46] E. McCarthy, S. Garry, D. Byrne, E. McGlynn, and J.-P. Mosnier. Field emission in ordered arrays of ZnO nanowires prepared by nanosphere lithography and extended Fowler-Nordheim analyses. *Journal of Applied Physics*, 110(12):124324, 2011.

[47] N. de Jonge and J.-M. Bonard. Carbon nanotube electron sources and applications. *Philosophical Transactions of the Royal Society A: Mathematical, Physical and Engineering Sciences*, 362(1823):2239–2266, 2004.

[48] G. N. Fursey and D. V. Glazanov. Deviations from the Fowler-Nordheim theory and peculiarities of field electron emission from small-scale objects. *Journal of Vacuum Science & Technology B: Microelectronics and Nanometer Structures Processing, Measurement, and Phenomena*, 16(2):910–915, 1998.

[49] A. A. Patterson and A. I. Akinwande. Elementary framework for cold field emission: Incorporation of quantum-confinement effects. *Journal of Applied Physics*, 114(23):234303, 2013.

[50] R. G. Forbes. Extraction of emission parameters for large-area field emitters, using a technically complete Fowler-Nordheim-type equation. *Nanotechnology*, 23(9):095706, 2012.

[51] W. P. Dyke, J. K. Trolan, W. W. Dolan, and G. Barnes. The field emitter: Fabrication, electron microscopy, and electric field calculations. *Journal of Applied Physics*, 24(5):570–576, 1953.

[52] R. G. Forbes, J. H. B. Deane, A. Fischer, and M. S. Mousa. Fowler-Nordheim plot analysis: A progress report. *Jordan Journal of Physics*, 8(3):125–147, 2015.

[53] E. O. Popov, A. G. Kolosko, M. A. Chumak, and S. V. Filippov. Ten approaches to define the field emission area. *Technical Physics*, 64(10):1530–1540, 2019.

[54] J. Bieker, R. G. Forbes, S. Wilfert, and H. F. Schlaak. Simulation-based model of randomly distributed large-area field electron emitters. *IEEE Journal of the Electron Devices Society*, 7:997–1006, 2019.

[55] J. R. Harris, K. L. Jensen, and D. A. Shiffler. Dependence of optimal spacing on applied field in ungated field emitter arrays. *AIP Advances*, 5(8):087182, 2015.

[56] L. Nilsson, O. Groening, C. Emmenegger, O. Kuettel, E. Schaller, L. Schlapbach, H. Kind, J.-M. Bonard, and K. Kern. Scanning field emission from patterned carbon nanotube films. *Applied Physics Letters*, 76(15):2071–2073, 2000.

[57] R. C. Smith and S. R. P. Silva. Interpretation of the field enhancement factor for electron emission from carbon nanotubes. *Journal of Applied Physics*, 106(1):014314, 2009.

[58] J. R. Harris, K. L. Jensen, D. A. Shiffler, and J. J. Petillo. Shielding in ungated field emitter arrays. *Applied Physics Letters*, 106(20):201603, 2015.

[59] M. Henzler. The origin of surface states. *Surface Science*, 25(3):650–680, 1971.

[60] A. A. Al-Tabbakh. The behavior of the Fowler-Nordheim plot for ZnO-Cu virtual emitter arrays. *Indian Journal of Physics*, 93(1):41–46, 2019.

[61] L. M. Baskin, O. I. Lvov, and G. N. Fursey. General features of field emission from semiconductors. *Physica Status Solidi (B)*, 47(1):49–62, 1971.

[62] R. Stratton. Theory of field emission from semiconductors. *Physical Review*, 125(1):67–82, 1962.

[63] S. Bhattacharya and K. P. Ghatak. *Fowler-Nordheim field emission: Effects in semiconductor nanostructures*. Springer-Verlag Berlin Heidelberg, 1st edition, 2012.

[64] C. F. Klingshirn, B. K. Meyer, A. Waag, A. Hoffmann, and J. Geurts. *Zinc oxide: From fundamental properties towards novel applications*. Springer-Verlag Berlin Heidelberg, 1st edition, 2010.

[65] A. Janotti and C. G. van de Walle. Fundamentals of zinc oxide as a semiconductor. *Reports on Progress in Physics*, 72(12):126501, 2009.

[66] G.-C. Yi, C. Wang, and W. I. Park. ZnO nanorods: Synthesis, characterization and applications. *Semiconductor Science and Technology*, 20(4):S22–S34, 2005.

[67] A. A. Al-Tabbakh, M. A. More, D. S. Joag, I. S. Mulla, and V. K. Pillai. The Fowler-Nordheim plot behavior and mechanism of field electron emission from ZnO tetrapod structures. *ACS Nano*, 4(10):5585–5590, 2010.

[68] N. S. Ramgir, D. J. Late, A. B. Bhise, M. A. More, I. S. Mulla, D. S. Joag, and K. Vijayamohanan. ZnO multipods, submicron wires, and spherical structures and their unique field emission behavior. *The Journal of Physical Chemistry B*, 110(37):18236–18242, 2006.

[69] J. She, Z. Xiao, Y. Yang, S. Deng, J. Chen, G. Yang, and N. Xu. Correlation between resistance and field emission performance of individual ZnO one-dimensional nanostructures. *ACS Nano*, 2(10):2015–2022, 2008.

[70] Y. Huang, Y. Zhang, Y. Gu, X. Bai, J. Qi, Q. Liao, and J. Liu. Field emission of a single In-doped ZnO nanowire. *The Journal of Physical Chemistry C*, 111(26):9039–9043, 2007.

[71] Q. Zhao, H. Z. Zhang, Y. W. Zhu, S. Q. Feng, X. C. Sun, J. Xu, and D. P. Yu. Morphological effects on the field emission of ZnO nanorod arrays. *Applied Physics Letters*, 86(20):203115, 2005.

[72] C. J. Lee, T. J. Lee, S. C. Lyu, Y. Zhang, H. Ruh, and H. J. Lee. Field emission from well-aligned zinc oxide nanowires grown at low temperature. *Applied Physics Letters*, 81(19):3648–3650, 2002.

[73] J. B. Cui, C. P. Daghlian, U. J. Gibson, R. Püsche, P. Geithner, and L. Ley. Low-temperature growth and field emission of ZnO nanowire arrays. *Journal of Applied Physics*, 97(4):044315, 2005.

[74] X. D. Wang, J. Zhou, C. S. Lao, J. H. Song, N. S. Xu, and Z. L. Wang. In situ field emission of density-controlled ZnO nanowire arrays. *Advanced Materials*, 19(12):1627–1631, 2007.

[75] Y. Li, Z. Zhang, G. Zhang, L. Zhao, S. Deng, N. Xu, and J. Chen. Optimizing the field emission properties of ZnO nanowire arrays by precisely tuning the population density and application in large-area gated field emitter arrays. *ACS Applied Materials and Interfaces*, 9(4):3911–3921, 2017.

[76] Y.-K. Tseng, C.-J. Huang, H.-M. Cheng, I.-N. Lin, K.-S. Liu, and I.-C. Chen. Characterization and field-emission properties of needle-like zinc oxide nanowires grown vertically on conductive zinc oxide films. *Advanced Functional Materials*, 13(10):811–814, 2003.

[77] C. X. Xu and X. W. Sun. Field emission from zinc oxide nanopins. *Applied Physics Letters*, 83(18):3806–3808, 2003.

[78] Y. H. Yang, B. Wang, N. S. Xu, and G. W. Yang. Field emission of one-dimensional micro- and nanostructures of zinc oxide. *Applied Physics Letters*, 89(4):043108, 2006.

[79] R. G. Forbes. Physics of generalized Fowler-Nordheim-type equations. *Journal of Vacuum Science & Technology B: Microelectronics and Nanometer Structures Processing, Measurement, and Phenomena*, 26(2):788–793, 2008.

[80] R. S. Devan, V. P. Thakare, V. V. Antad, P. R. Chikate, R. T. Khare, M. A. More, R. S. Dhayal, S. I. Patil, Y.-R. Ma, and L. Schmidt-Mende. Nano-heteroarchitectures of two-dimensional MoS_2@ one-dimensional brookite TiO_2 nanorods: Prominent electron emitters for displays. *ACS Omega*, 2(6):2925–2934, 2017.

[81] P. R. Chikate, K. D. Daware, D. S. Gavhane, Y.-R. Ma, R. J. Choudhary, S. I. Patil, M. A. More, D. M. Phase, S. W. Gosavi, P. M. Shirage, and R. S. Devan. Controlled hetero-architectures of Au-nanoparticles-decorated ZnO nanowires for enhanced field electron emission displays. *ChemistrySelect*, 3(27):7891–7899, 2018.

[82] P. N. Didwal, P. R. Chikate, P. K. Bankar, M. A. More, and R. S. Devan. Intense field electron emission source designed from large area array of dense rutile TiO_2 nanopillars. *Journal of Materials Science: Materials in Electronics*, 30:2935–2941, 2019.

[83] R. G. Forbes. Development of a simple quantitative test for lack of field emission orthodoxy. *Proceedings of the Royal Society A: Mathematical, Physical and Engineering Sciences*, 469(2158):20130271, 2013.

[84] A. G. Kolosko, S. V. Filippov, P. A. Romanov, E. O. Popov, and R. G. Forbes. Real-time implementation of the "orthodoxy test" for conformity of current–voltage characteristics with classical field electron emission theory. *Journal of Vacuum Science & Technology B: Microelectronics and Nanometer Structures Processing, Measurement, and Phenomena*, 34(4):041802, 2016.

[85] R. G. Forbes. The Murphy-Good plot: A better method of analysing field emission data. *Royal Society Open Science*, 6(12):190912, 2019.

[86] P. R. Chikate, P. K. Bankar, R. J. Choudhary, Y.-R. Ma, S. I. Patil, M. A. More, D. M. Phase, P. M. Shirage, and R. S. Devan. Spitzer shaped ZnO nanostructures for enhancement of field electron emission behaviors. *RSC Advances*, 8(38):21664–21670, 2018.

[87] K. Heo, B. Y. Lee, H. Lee, D.-G. Cho, M. Arif, K. Y. Kim, Y. J. Choi, and S. Hong. Carbon and metal nanotube hybrid structures on graphene as efficient electron field emitters. *Nanotechnology*, 27(27):275301, 2016.

[88] R. S. Devan, Y.-R. Ma, M. A. More, R. T. Khare, V. V. Antad, R. A. Patil, V. P. Thakare, R. S. Dhayal, and L. Schmidt-Mende. Promising field electron emission performance of vertically aligned one dimensional (1D) brookite (β) TiO_2 nanorods. *RSC Advances*, 6(101):98722–98729, 2016.

[89] M. M. Allaham, R. G. Forbes, and M. S. Mousa. Applying the field emission orthodoxy test to Murphy-Good plots. *Jordan Journal of Physics*, 13(2):101–111, 2020.

[90] J. W. Gadzuk and E. W. Plummer. Field emission energy distribution (FEED). *Reviews of Modern Physics*, 45(3):487–548, 1973.

[91] C. Henkel, R. Zierold, A. Kommini, S. Haugg, C. Thomason, Z. Aksamija, and R. H. Blick. Resonant tunneling induced enhancement of electron field emission by ultrathin coatings. *Scientific Reports*, 9(6840):1–7, 2019.

[92] D. Maier-Schneider, J. Maibach, and E. Obermeier. A new analytical solution for the load-deflection of square membranes. *Journal of Microelectromechanical Systems*, 4(4):238–241, 1995.

[93] H. Schlicke, D. Battista, S. Kunze, C. J. Schröter, M. Eich, and T. Vossmeyer. Freestanding membranes of cross-linked gold nanoparticles: Novel functional materials for electrostatic actuators. *ACS Applied Materials and Interfaces*, 7(28):15123–15128, 2015.

[94] M. Arif, K. Heo, B. Y. Lee, J. Lee, D. H. Seo, S. Seo, J. Jian, and S. Hong. Metallic nanowire-graphene hybrid nanostructures for highly flexible field emission devices. *Nanotechnology*, 22(35):355709, 2011.

[95] K. J. Sankaran, N. H. Tai, and I. N. Lin. Flexible electron field emitters fabricated using conducting ultrananocrystalline diamond pyramidal microtips on polynorbornene films. *Applied Physics Letters*, 104(3):031601, 2014.

[96] C. Henkel. *Characterization of diamond nanomembranes by field emission for a detector in mass spectrometry of large proteins*. Master's thesis, Universität Hamburg, 2016.

[97] L. Pacarizi. *Optimization of a setup for field emission measurements of nanomembranes*. Bachelor's thesis, Universität Hamburg, 2018.

[98] J.-W. Jeong, J.-T. Kang, S. Choi, J.-W. Kim, S. Ahn, and Y.-H. Song. A digital miniature X-ray tube with a high-density triode carbon nanotube field emitter. *Applied Physics Letters*, 102(2):023504, 2013.

[99] Y. Taniyasu, M. Kasu, and T. Makimoto. Field emission properties of heavily Si-doped AlN in triode-type display structure. *Applied Physics Letters*, 84(12):2115–2117, 2004.

[100] S. Y. Li, C. Y. Lee, P. Lin, and T. Y. Tseng. Gate-controlled ZnO nanowires for field-emission device application. *Journal of Vacuum Science & Technology B: Microelectronics and Nanometer Structures Processing, Measurement, and Phenomena*, 24(1):147–151, 2006.

[101] P. Helfenstein, E. Kirk, K. Jefimovs, T. Vogel, C. Escher, H.-W. Fink, and S. Tsujino. Highly collimated electron beams from double-gate field emitter arrays with large collimation gate apertures. *Applied Physics Letters*, 98(6):061502, 2011.

[102] C. Li, M. T. Cole, W. Lei, K. Qu, K. Ying, Y. Zhang, A. R. Robertson, J. H. Warner, S. Ding, X. Zhang, B. Wang, and W. I. Milne. Highly electron transparent graphene for field emission triode gates. *Advanced Functional Materials*, 24(9):1218–1227, 2014.

[103] J.-W. Kim, J.-W. Jeong, J.-T. Kang, S. Choi, S. Ahn, and Y.-H. Song. Highly reliable field electron emitters produced from reproducible damage-free carbon nanotube composite pastes with optimal inorganic fillers. *Nanotechnology*, 25(6):065201, 2014.

[104] C. A. Spindt. A thin-film field-emission cathode. *Journal of Applied Physics*, 39(7):3504–3505, 1968.

[105] C. A. Spindt, I. Brodie, L. Humphrey, and E. R. Westerberg. Physical properties of thin-film field emission cathodes with molybdenum cones. *Journal of Applied Physics*, 47(12):5248–5263, 1976.

[106] C. M. Marrese. A review of field emission cathode technologies for electric propulsion systems and instruments. *2000 IEEE Aerospace Conference. Proceedings (Cat. No.00TH8484)*, 4:85–97, 2000.

[107] G. Mittal and I. Lahiri. Recent progress in nanostructured next-generation field emission devices. *Journal of Physics D: Applied Physics*, 47(32):323001, 2014.

[108] A. Descoeudres, Y. Levinsen, S. Calatroni, M. Taborelli, and W. Wuensch. Investigation of the DC vacuum breakdown mechanism. *Physical Review Special Topics - Accelerators and Beams*, 12(9):092001, 2009.

[109] D. B. Go and A. Venkattraman. Microscale gas breakdown: Ion-enhanced field emission and the modified Paschen's curve. *Journal of Physics D: Applied Physics*, 47(50):503001, 2014.

[110] R. P. Little and S. T. Smith. Electrical breakdown in vacuum. *IEEE Transactions on Electron Devices*, 12(2):77–83, 1965.

[111] R. Hawley. Vacuum as an insulator. *Vacuum*, 10(4):310–318, 1960.

[112] W. P. Dyke, J. K. Trolan, E. E. Martin, and J. P. Barbour. The field emission initiated vacuum arc. I. experiments on arc initiation. *Physical Review*, 91(5):1043–1054, 1953.

[113] P. A. Chatterton. A theoretical study of field emission initiated vacuum breakdown. *Proceedings of the Physical Society*, 88(1):231–245, 1966.

[114] VACOM® Vakuum Komponenten & Messtechnik GmbH. *VACOM® product catalog*, from `https://www.vacom.de/en/catalog`, accessed on 12.03.2020.

[115] Keithley. *Model 6485 picoammeter, model 6487 picoammeter/voltage source, user's manual, 6487-900-01 Rev. C / March 2011*, from `https://docs.rs-online.com/97f3/0900766b816641c9.pdf`, accessed on 22.03.2020.

[116] F. G. Tarntair, L. C. Chen, S. L. Wei, W. K. Hong, K. H. Chen, and H. C. Cheng. High current density field emission from arrays of carbon nanotubes and diamond-clad Si tips. *Journal of Vacuum Science & Technology B: Microelectronics and Nanometer Structures Processing, Measurement, and Phenomena*, 18(3):1207–1211, 2000.

[117] P. A. Redhead. Recommended practices for measuring and reporting outgassing data. *Journal of Vacuum Science & Technology A: Vacuum, Surfaces, and Films*, 20(5):1667–1675, 2002.

[118] A. Berman. Water vapor in vacuum systems. *Vacuum*, 47(4):327–332, 1996.

[119] K. S. Yeong and J. T. L. Thong. Field emission properties of individual zinc oxide nanowire field emitter. *Journal of Vacuum Science & Technology B: Microelectronics and Nanometer Structures Processing, Measurement, and Phenomena*, 26(3):983–989, 2008.

[120] M. Hajra, C. E. Hunt, M. Ding, O. Auciello, J. Carlisle, and D. M. Gruen. Effect of gases on the field emission properties of ultrananocrystalline diamond-coated silicon field emitter arrays. *Journal of Applied Physics*, 94(6):4079–4083, 2003.

[121] K. Almaksour, M. J. Kirkpatrick, P. Dessante, E. Odic, A. Simonin, H. P. L. de Esch, B. Lepetit, D. Alamarguy, F. Bayle, and P. Teste. Experimental study of the reduction of field emission by gas injection in vacuum for accelerator applications. *Physical Review Special Topics - Accelerators and Beams*, 17(10):103502, 2014.

[122] K. V. Reich, E. D. Eidelman, A. T. Dideykin, and A. Y. Vul'. Determination of an optimal pressure under field emission from diamondlike films. *Technical Physics*, 53(2):261–263, 2008.

[123] L. J. van der Pauw. A method of measuring the resistivity and hall coefficient on lamellae of arbitrary shape. *Philips Technical Review*, 20(8):220–224, 1958.

[124] A. A. Ramadan, R. D. Gould, and A. Ashour. On the van der Pauw method of resistivity measurements. *Thin Solid Films*, 239(2):272–275, 1994.

[125] W. R. Thurber, R. L. Mattis, Y. M. Liu, and J. J. Filliben. Resistivity-dopant density relationship for phosphorus-doped silicon. *Journal of the Electrochemical Society*, 127(8):1807–1812, 1980.

[126] F. G. Allen and G. W. Gobeli. Work function, photoelectric threshold, and surface states of atomically clean silicon. *Physical Review*, 127(1):150–158, 1962.

[127] E. H. Rhoderick. Metal-semiconductor contacts. *IEE Proceedings I - Solid-State and Electron Devices*, 129(1):1–14, 1982.

[128] A. Y. C. Yu. Electron tunneling and contact resistance of metal-silicon contact barriers. *Solid-State Electronics*, 13(2):239–247, 1970.

[129] A. Matikainen, T. Nuutinen, T. Itkonen, S. Heinilehto, J. Puustinen, J. Hiltunen, J. Lappalainen, P. Karioja, and P. Vahimaa. Atmospheric oxidation and carbon contamination of silver and its effect on surface-enhanced Raman spectroscopy (SERS). *Scientific Reports*, 6(37192):1–6, 2016.

[130] K. Jousten. *Thermal outgassing, Report number: CERN-OPEN-2000-274*. Physikalisch-Technische Bundesanstalt, Berlin, Germany, pages 111–126, 1999.

[131] F. Cardarelli. *Materials handbook: A concise desktop reference*. Springer-Verlag London, 2nd edition, 2008.

[132] National Aeronautics and Space Administration (NASA). *Outgassing data for selecting spacecraft materials*, database on `https://outgassing.nasa.gov/`, accessed on 20.03.2020.

[133] K. Battes, C. Day, and V. Hauer. Outgassing rate measurements of stainless steel and polymers using the difference method. *Journal of Vacuum Science & Technology A: Vacuum, Surfaces, and Films*, 33(2):021603, 2015.

[134] DuPont™. *Kapton® HN, polyimide film*, data sheet from `https://docs.rs-online.com/c6e2/0900766b80659d8c.pdf`, accessed on 15.03.2020.

[135] Laminated Plastics. *Polyimide (PI)*, data sheet from `https://laminatedplastics.com/polyimide.pdf`, accessed on 15.03.2020.

[136] Victrex® High Performance Polymers. *Victrex® PEEK 381G*, data sheet from https://www.victrex.com/~/media/datasheets/victrex_tds_381g.pdf, accessed on 15.03.2020.

[137] Standard Fluoromers Pvt. Ltd. *Physical properties of PTFE and filled PTFE products*, data sheet from http://www.standard-ptfe.com/pdf/data-sheet-of-ptfe.pdf, accessed on 15.03.2020.

[138] A. S. Pillai and R. Hackam. Surface flashover of solid dielectric in vacuum. *Journal of Applied Physics*, 53(4):2983–2987, 1982.

[139] Universal Laser Systems. *Plastics overview*, article on https://www.ulsinc.com/material/plastics-overview, accessed on 31.03.2020.

[140] R. Ghodssi and P. Lin. *MEMS materials and processes handbook*. Springer US, 1st edition, 2011.

[141] Precision Eforming. *About electroforming*, article on https://www.precisioneforming.com, accessed on 20.03.2020.

[142] H. Clausert, K. Hoffmann, W. Mathis, G. Wiesemann, and H.-P. Beck. *Das Ingenieurwissen: Elektrotechnik*. Springer Vieweg, 1st edition, 2014.

[143] R. G. Forbes. Why converting field emission voltages to macroscopic fields before making a Fowler-Nordheim plot has often led to spurious characterization results. *Journal of Vacuum Science & Technology B: Microelectronics and Nanometer Structures Processing, Measurement, and Phenomena*, 37(5):051802, 2019.

[144] S. I. Cha, K. T. Kim, S. N. Arshad, C. B. Mo, K. H. Lee, and S. H. Hong. Field-emission behavior of a carbon-nanotube-implanted Co nanocomposite fabricated from pearl-necklace-structured carbon nanotube/Co powders. *Advanced Materials*, 18(5):553–558, 2006.

[145] Femto Messtechnik GmbH. *DLPCA-200, Variable gain low noise current amplifier*, data sheet from https://www.femto.de/images/pdf-dokumente/de-dlpca-200.pdf, accessed on 22.03.2020.

[146] C. V. Thompson. Solid-state dewetting of thin films. *Annual Review of Materials Research*, 42:399–434, 2012.

[147] F. Delachat, C. Constancias, F. Fournel, C. Morales, B. le Drogoff, M. Chaker, and J. Margot. Fabrication of buckling free ultrathin silicon membranes by direct bonding with thermal difference. *ACS Nano*, 9(4):3654–3663, 2015.

[148] J. R. Dwyer and M. Harb. Through a window, brightly: A review of selected nanofabricated thin-film platforms for spectroscopy, imaging, and detection. *Applied Spectroscopy*, 71(9):2051–2075, 2017.

[149] S. Haugg. *Surface modified nanomembranes for field emission based mass spectrometry*. Master's thesis, Universität Hamburg, 2016.

[150] L. Dong, J. Jiao, D. W. Tuggle, J. M. Petty, S. A. Elliff, and M. Coulter. Zno nanowires formed on tungsten substrates and their electron field emission properties. *Applied Physics Letters*, 82(7):1096–1098, 2003.

[151] M. H. Huang, Y. Wu, H. Feick, N. Tran, E. Weber, and P. Yang. Catalytic growth of zinc oxide nanowires by vapor transport. *Advanced Materials*, 13(2):113–116, 2001.

[152] H. J. Fan, W. Lee, R. Hauschild, M. Alexe, G. L. Rhun, R. Scholz, A. Dadgar, K. Nielsch, H. Kalt, A. Krost, M. Zacharias, and U. Gösele. Template-assisted large-scale ordered arrays of ZnO pillars for optical and piezoelectric applications. *Small*, 2(4):561–568, 2006.

[153] H. Chik, J. Liang, S. G. Cloutier, N. Kouklin, and J. M. Xu. Periodic array of uniform ZnO nanorods by second-order self-assembly. *Applied Physics Letters*, 84(17):3376–3378, 2004.

[154] X. Wang, C. J. Summers, and Z. L. Wang. Large-scale hexagonal-patterned growth of aligned ZnO nanorods for nano-optoelectronics and nanosensor arrays. *Nano Letters*, 4(3):423–426, 2004.

[155] M. Kirkham, X. Wang, Z. L. Wang, and R. L. Snyder. Solid Au nanoparticles as a catalyst for growing aligned ZnO nanowires: A new understanding of the vapour-liquid-solid process. *Nanotechnology*, 18(36):365304, 2007.

[156] K. Govatsi, A. Chrissanthopoulos, V. Dracopoulos, and S. N. Yannopoulos. The influence of Au film thickness and annealing conditions on the VLS-assisted growth of ZnO nanostructures. *Nanotechnology*, 25(21):215601, 2014.

[157] C. A. Schneider, W. S. Rasband, and K. W. Eliceiri. NIH image to ImageJ: 25 years of image analysis. *Nature Methods*, 9(7):671–675, 2012.

[158] D. S. Kim, R. Scholz, U. Gösele, and M. Zacharias. Gold at the root or at the tip of ZnO nanowires: A model. *Small*, 4(10):1615–1619, 2008.

[159] A. Menzel, K. Subannajui, R. Bakhda, Y. Wang, R. Thomann, and M. Zacharias. Tuning the growth mechanism of ZnO nanowires by controlled carrier and reaction gas modulation in thermal CVD. *The Journal of Physical Chemistry Letters*, 3(19):2815–2821, 2012.

[160] C. L. Wu, L. Chang, H. G. Chen, C. W. Lin, T. F. Chang, Y. C. Chao, and J. K. Yan. Growth and characterization of chemical-vapor-deposited zinc oxide nanorods. *Thin Solid Films*, 498(1–2):137–141, 2006.

[161] Y. Wu and P. Yang. Direct observation of vapor-liquid-solid nanowire growth. *Journal of the American Chemical Society*, 123(13):3165–3166, 2001.

[162] H. Wan and H. E. Ruda. A study of the growth mechanism of CVD-grown ZnO nanowires. *Journal of Materials Science: Materials in Electronics*, 21:1014–1019, 2010.

[163] S. Chen and W. Yang. Flexible low-dimensional semiconductor field emission cathodes: Fabrication, properties and applications. *Journal of Materials Chemistry C*, 5(41):10682–10700, 2017.

[164] H. Kim. *A diamond nanomembrane detector for proteomics*. PhD thesis, University of Wisconsin–Madison, 2014.

[165] D. Biswas. Field-emission from parabolic tips: Current distributions, the net current, and effective emission area. *Physics of Plasmas*, 25(4):043105, 2018.

[166] E. S. Babu, B. Saravanakumar, G. Ravi, R. Yuvakkumar, V. Ganesh, R. K. Guduru, and S. Kim. Zinc oxide nanotips growth by controlling vapor deposition on substrates. *Journal of Materials Science: Materials in Electronics*, 29:6149–6156, 2018.

[167] C. Yang and J. Pham. Characteristic study of silicon nitride films deposited by LPCVD and PECVD. *Silicon*, 10:2561–2567, 2018.

[168] B. M. Zwickl, W. E. Shanks, A. M. Jayich, C. Yang, A. C. B. Jayich, J. D. Thompson, and J. G. E. Harris. High quality mechanical and optical properties of commercial silicon nitride membranes. *Applied Physics Letters*, 92(10):103125, 2008.

[169] C. Prommesberger, M. Bachmann, F. Düsberg, C. Langer, R. Lawrowski, M. Hofmann, A. Pahlke, and R. Schreiner. Regulation of the transmitted electron flux in a field-emission electron source demonstrated on Si nanowhisker cathodes. *IEEE Transactions on Electron Devices*, 64(12):5128–5133, 2017.

[170] R. Schreiner, C. Langer, C. Prommesberger, R. Lawrowski, F. Dams, M. Bachmann, F. Düsberg, M. Hofmann, A. Pahlke, P. Serbun, S. Mingels, and G. Müller. Semiconductor field emission electron sources using a modular system concept for application in sensors and X-ray-sources. *28th International Vacuum Nanoelectronics Conference (IVNC), Technical Digest*, pages 178–179, 2015.

[171] E. J. Radauscher, K. H. Gilchrist, S. T. di Dona, Z. E. Russell, J. R. Piascik, J. J. Amsden, C. B. Parker, B. R. Stoner, and J. T. Glass. Improved performance of field emission vacuum microelectronic devices for integrated circuits. *IEEE Transactions on Electron Devices*, 63(9):3753–3760, 2016.

[172] E. W. Müller. Elektronenmikroskopische Beobachtungen von Feldkathoden. *Zeitschrift für Physik*, 106:541–550, 1937.

[173] R. Gomer. Field emission, field ionization, and field desorption. *Surface Science*, 299–300:129–152, 1994.

[174] M. Satoh, N. Tanaka, Y. Ueda, S. Ohshio, and H. Saitoh. Epitaxial growth of zinc oxide whiskers by chemical-vapor deposition under atmospheric pressure. *Japanese Journal of Applied Physics*, 38(5B):L586 – L589, 1999.

[175] S.-C. Liu and J.-J. Wu. Low-temperature and catalyst-free synthesis of well-aligned ZnO nanorods on Si (100). *Journal of Materials Chemistry*, 12(10):3125–3129, 2002.

[176] J.-J. Wu and S.-C. Liu. Catalyst-free growth and characterization of ZnO nanorods. *The Journal of Physical Chemistry B*, 106(37):9546–9551, 2002.

[177] V. Khranovskyy and R. Yakimova. Morphology engineering of ZnO nanostructures. *Physica B: Condensed Matter*, 407(10):1533–1537, 2012.

[178] X. Fang, Y. Bando, U. K. Gautam, C. Ye, and D. Golberg. Inorganic semiconductor nanostructures and their field-emission applications. *Journal of Materials Chemistry*, 18(5):509–522, 2008.

[179] C. J. Park, D.-K. Choi, J. Yoo, G.-C. Yi, and C. J. Lee. Enhanced field emission properties from well-aligned zinc oxide nanoneedles grown on the Au/Ti/n-Si substrate. *Applied Physics Letters*, 90(8):083107, 2007.

[180] A. J. Fulton, V. O. Kollath, K. Karan, and Y. Shi. Gold nanoparticle assembly on porous silicon by pulsed laser induced dewetting. *Nanoscale Advances*, 2(2):896–905, 2020.

[181] X. Zhao, U.-J. Lee, and K.-H. Lee. Dewetting behavior of Au films on porous substrates. *Thin Solid Films*, 519(2):706–713, 2010.

[182] L. Ghazaryan, E.-B. Kley, A. Tünnermann, and A. Szeghalmi. Nanoporous SiO_2 thin films made by atomic layer deposition and atomic etching. *Nanotechnology*, 27(25):255603, 2016.

[183] S.-H. Jeong, J.-K. Kim, B.-S. Kim, S.-H. Shim, and B.-T. Lee. Characterization of SiO_2 and TiO_2 films prepared using RF magnetron sputtering and their application to anti-reflection coating. *Vacuum*, 76(4):507–515, 2004.

[184] J. Kischkat, S. Peters, B. Gruska, M. Semtsiv, M. Chashnikova, M. Klinkmüller, O. Fedosenko, S. Machulik, A. Aleksandrova, G. Monastyrskyi, Y. Flores, and W. T. Masselink. Mid-infrared optical properties of thin films of aluminum oxide, titanium dioxide, silicon dioxide, aluminum nitride, and silicon nitride. *Applied Optics*, 51(28):6789–6798, 2012.

[185] W. van Gelder and V. E. Hauser. The etching of silicon nitride in phosphoric acid with silicon dioxide as a mask. *Journal of the Electrochemical Society*, 114(8):869–872, 1967.

[186] P.-Z. Yang, L.-M. Liu, J.-H. Mo, and W. Yang. Characterization of PECVD grown porous SiO_2 thin films with potential application in an uncooled infrared detector. *Semiconductor Science and Technology*, 25(4):045017, 2010.

[187] D. Wang, R. Ji, and P. Schaaf. Formation of precise 2D Au particle arrays via thermally induced dewetting on pre-patterned substrates. *Beilstein Journal of Nanotechnology*, 2:318–326, 2011.

[188] D. Wang and P. Schaaf. Two-dimensional nanoparticle arrays formed by dewetting of thin gold films deposited on pre-patterned substrates. *Journal of Materials Science: Materials in Electronics*, 22:1067–1070, 2011.

[189] H. C. Miller. Change in field intensification factor β of an electrode projection (whisker) at short gap lengths. *Journal of Applied Physics*, 38(11):4501–4504, 1967.

[190] R. C. Smith, R. D. Forrest, J. D. Carey, W. K. Hsu, and S. R. P. Silva. Interpretation of enhancement factor in nonplanar field emitters. *Applied Physics Letters*, 87(1):013111, 2005.

[191] K.-F. Hii, R. R. Vallance, S. B. Chikkamaranahalli, M. P. Mengüc, and A. M. Rao. Characterizing field emission from individual carbon nanotubes at small distances.

Journal of Vacuum Science & Technology B: Microelectronics and Nanometer Structures Processing, Measurement, and Phenomena, 24(3):1081–1087, 2006.

[192] A. El-Aneed, A. Cohen, and J. Banoub. Mass spectrometry, review of the basics: Electrospray, MALDI, and commonly used mass analyzers. *Applied Spectroscopy Reviews*, 44(3):210–230, 2009.

[193] W.-P. Peng, S.-W. Chou, and A. A. Patil. Measuring masses of large biomolecules and bioparticles using mass spectrometric techniques. *Analyst*, 139(14):3507–3523, 2014.

[194] R. Liu, Q. Li, and L. M. Smith. Detection of large ions in time-of-flight mass spectrometry: Effects of ion mass and acceleration voltage on microchannel plate detector response. *Journal of the American Society for Mass Spectrometry*, 25(8):1374–1383, 2014.

[195] F. Giubileo, A. di Bartolomeo, L. Iemmo, G. Luongo, and F. Urban. Field emission from carbon nanostructures. *Applied Sciences*, 8(4):526, 2018.

[196] H. K. Raut, V. A. Ganesh, A. S. Nair, and S. Ramakrishna. Anti-reflective coatings: A critical, in-depth review. *Energy & Environmental Science*, 4(10):3779–3804, 2011.

[197] Y. Shi, L. He, F. Guang, L. Li, Z. Xin, and R. Liu. A review: Preparation, performance, and applications of silicon oxynitride film. *Micromachines*, 10(8):552, 2019.

[198] National Institute of Standards and Technology (NIST). *Fundamental physical constants*, database on `https://physics.nist.gov/cuu/Constants/index.html`, accessed on 21.06.2020.

[199] J. I. Goldstein, D. E. Newbury, J. R. Michael, N. W. M. Ritchie, J. H. J. Scott, and D. C. Joy. *Scanning electron microscopy and X-ray microanalysis*. Springer-Verlag New York, 4th edition, 2018.

[200] D. E. Newbury and N. W. M. Ritchie. Performing elemental microanalysis with high accuracy and high precision by scanning electron microscopy/silicon drift detector energy-dispersive X-ray spectrometry (SEM/SDD-EDS). *Journal of Materials Science*, 50(2):493–518, 2015.

Danksagung

Abschließend möchte ich mich bei allen Personen bedanken, ohne die diese Arbeit nicht möglich gewesen wäre. Ich bedanke mich hiermit bei:

Prof. Dr. Robert H. Blick für die Betreuung dieser Dissertation und für die Möglichkeit zur Arbeit an vielseitigen Projekten in den letzten Jahren, sowie für die Übernahme des Erstgutachtens der Dissertation.

Dr. Robert Zierold für die wissenschaftliche Unterstützung in den letzten Jahren. Darüber hinaus möchte ich mich für das ausführliche Korrekturlesen und für die Einwilligung zur Teilnahme an der Disputationsprüfung bedanken.

Prof. Dr. Zlatan Aksamija für die Einwilligung zur Übernahme des Zweitgutachtens der Dissertation.

Prof. Dr. Jochen Liske und Prof. Dr. Alexander Lichtenstein für die Einwilligung zur Teilnahme an der Disputationsprüfung.

Carina Hedrich für die Unterstützung bei der Probenherstellung und für die Anfertigung von SEM Bildern im Rahmen ihrer Tätigkeit als studentische Hilfskraft. Außerdem möchte ich mich für das Korrekturlesen von Teilen der Dissertation bedanken.

Leutrim Pacarizi für die Hilfe bei der Optimierung des FE Setups im Rahmen seiner Bachelorarbeit.

Jann Harberts, Dr. Chithra H. Sharma, Dr. Pai Zhao und Isabel González Díaz-Palacio für das Korrekturlesen von Teilen der Dissertation. Außerdem möchte ich mich bei Dr. Parisa Bayat für die gemeinsame Zeit während der ersten Hälfte meiner Doktorandenzeit bedanken.

Thomas Finger, Matthias Hein und Bojan Bosnjak für die technische Unterstützung und für die Betreuung von Geräten in den Laboren und im Reinraum.

Schließlich möchte ich mich bei der gesamten Arbeitsgruppe HB für die schöne Zeit in den vergangenen Jahren bedanken.

Ein besonderer Dank geht an meine Eltern, meine Schwester und meine Großeltern für die stetige Unterstützung.

Eidesstattliche Versicherung / Declaration on Oath

Hiermit versichere ich an Eides statt, die vorliegende Dissertationsschrift selbst verfasst und keine anderen als die angegebenen Hilfsmittel und Quellen benutzt zu haben.

Die eingereichte schriftliche Fassung entspricht der auf dem elektronischen Speichermedium.

Die Dissertation wurde in der vorgelegten oder einer ähnlichen Form nicht schon einmal in einem früheren Promotionsverfahren angenommen oder als ungenügend beurteilt.

Hamburg, den 26.05.2021

Stefanie Haugg